Technische Universität München
TUM School of Natural Sciences

Determination of the impurity density profile and charge carrier mobilities in a point-contact germanium detector using a novel Compton Scanner

Felix Hagemann

Vollständiger Abdruck der von der TUM School of Natural Sciences der Technischen Universität München zur Erlangung eines **Doktors der Naturwissenschaften (Dr. rer. nat.)** genehmigten Dissertation.

Vorsitz: Prof. Dr. Alejandro Ibarra

Prüfende der Dissertation:

1. Hon.-Prof. Dr. Allen C. Caldwell
2. Prof. Dr. Lothar Oberauer

Die Dissertation wurde am 21.05.2024 bei der Technischen Universität München eingereicht und durch die TUM School of Natural Sciences am 02.07.2024 angenommen.

Felix Hagemann

Abstract

High-purity germanium detectors are crucial detectors for a wide range of nuclear and particle physics experiments. A detailed understanding of their performance, and in particular the ability to precisely predict their performance using simulations, is essential for achieving best results. Accurate simulations for high-purity germanium detectors rely on precise information about the impurity density profile of the detector and charge carrier mobilities in germanium. Typically, the information provided by the detector manufacturer or in the literature is very limited, resulting in large uncertainties in the simulation output. In this thesis, the impurity density profile and the charge carrier mobilities in a p-type germanium segmented point-contact detector are determined using data from a novel Compton Scanner. Capacitance measurements and Compton images of undepleted volumes of the detector suggest a strong radial decrease in the impurity density in the last centimeter close to the surface. The hole-drift anisotropy was larger and the electron-drift anisotropy was smaller than the prediction using widely used mobility parameters and charge-drift models. Updated values for the charge-carrier mobilities in germanium and their temperature dependence are determined and an improved electron-drift model is proposed.

Zusammenfassung

Hochreine Germaniumdetektoren spielen eine entscheidende Rolle in einer Vielzahl von Kern- und Teilchenphysikexperimenten. Ein detailliertes Verständnis des Verhalten solcher Detektoren und insbesondere die Fähigkeit, dieses Verhalten mit Hilfe von Simulationen möglichst genau vorherzusagen, sind für die optimale Auswertung von Messdaten essentiell. Präzise Pulsformsimulationen für hochreine Germaniumdetektoren hängen stark von genauen Informationen über das Dotierungsprofil und die Ladungsträgermobilitäten im Detektor ab. In der Regel sind die vom Detektorhersteller bereitgestellten oder in der Literatur vorhandenen Informationen sehr limitiert. Dies führt zu großen Unsicherheiten bei Simulationsergebnissen. In dieser Arbeit werden das Dotierungsprofil und die Ladungsträgermobilitäten in einem segmentierten p-Typ Germanium Punktkontaktdetektor mithilfe eines neuartigen Compton Scanners bestimmt. Kapazitätsmessungen und direkte Abbildungen der nicht verarmten Bereiche im Detektors deuten auf eine starke radiale Abnahme des Dotierungsprofils im letzten Zentimeter nahe der Oberfläche hin. Im Vergleich zu häufig verwendeten Literaturwerten wurden kleinere Loch- und größere Elektronendriftanisotropien gemessen. Aktualisierte Werte für die Ladungsträgermobilitäten in Germanium und deren Temperaturabhängigkeiten wurden bestimmt und ein verbessertes Elektronendriftmodell vorgeschlagen.

Publications

Part of the results obtained within the framework of this thesis were already published in scientific journals and are publicly available:

Corresponding author, peer reviewed

I. Abt, C. Gooch, **F. Hagemann**, L. Hauertmann, D. Hervas Aguilar, X. Liu, O. Schulz, M. Schuster, A.J. Zsigmond: *A novel wide-angle Compton Scanner setup to study bulk events in germanium detectors*, Eur. Phys. J. C **82**, 936 (2022)
DOI: 10.1140/epjc/s10052-022-10884-y

Author, peer reviewed

I. Abt, F. Fischer, **F. Hagemann**, L. Hauertmann, O. Schulz, M. Schuster, A.J. Zsigmond: *Simulation of semiconductor detectors in 3D with SolidStateDetectors.jl*, J. Instr. **16**, P08007 (2021)
DOI: 10.1088/1748-0221/16/08/P08007

I. Abt, C. Gooch, **F. Hagemann**, L. Hauertmann, X. Liu, O. Schulz, M. Schuster, A.J. Zsigmond: *Identification and simulation of surface alpha events on passivated surfaces of germanium detectors and the influence of metalisation*, Eur. Phys. J. C **82**, 1119 (2022)
DOI: 10.1140/epjc/s10052-022-11064-8

I. Abt, C. Gooch, **F. Hagemann**, L. Hauertmann, X. Liu, O. Schulz, M. Schuster: *Bayesian inference of high-purity germanium detector impurities based on capacitance measurements and machine-learning accelerated capacitance calculations*, Eur. Phys. J. C **83**, 352 (2023)
DOI: 10.1140/epjc/s10052-023-11509-8

I. Abt, C. Gooch, **F. Hagemann**, L. Hauertmann, D. Hervas Aguilar, X. Liu, O. Schulz, M. Schuster, A.J. Zsigmond: *Temperature dependence of the electron-drift anisotropy and implications for the electron-drift model*, J. Instr. **18**, P10030 (2023)
DOI: 10.1088/1748-0221/18/10/P10030

Table of contents

1 Introduction

Germanium detectors have maintained their pioneering status as leading-edge radiation detectors for over 60 years [1]. They are used to detect particle interactions from a few eV to several MeV with an excellent energy resolution and a detection efficiency close to unity, allowing for investigations of physics processes over a wide range of energies.

High-purity germanium detectors are deployed in many physics experiments worldwide. Several collaborations [2–6] deploy germanium detectors with sub-keV energy thresholds to search for weakly-interacting massive particles in the MeV mass parameter space. Such detectors are also used to study the nature of neutrinos, e.g. in detecting coherent elastic neutrino-nucleus scattering [7–9] or searching for neutrinoless double-beta decay of ^{76}Ge [10–12]. Moreover, germanium detectors are used to study the structure, shape and decay modes of atomic nuclei [13–16], to screen materials in underground laboratories [17–19], to measure the element composition on the surfaces of planets and moons in our solar systems [20–26], to image astrophysical sources [27], to monitor radiation exposure and in other medical applications [28]. Understanding germanium detectors and their performance has an impact in many areas of physics.

The working principle of germanium detectors in most of these applications is based on ionization [29]. Part of the deposited energy is used to excite bound electrons, thereby also creating vacancies in the covalent bonds of the germanium crystal, so-called holes. The electric field in the germanium detector leads to the separation and subsequent collection of the electrons and holes on electric contacts placed on the detector surface. The time evolution of the charges induced on the contacts during the charge collection, so-called pulses, are typically read out using low-noise charge-sensitive preamplifiers.

Analyzing the shapes of the pulses does not only allow for the determination of the deposited energy with an excellent resolution but also for an insight into the event topology, i.e. where the energy was deposited in the detector and what the properties of the particles causing the event were. This additional information allows for efficient identification of background events in rare-event searches [30–32] which is crucial for improving the sensitivity in next-generation experimental efforts [33].

The largest uncertainties, which strongly influence the charge-carrier drift and, hence, the recorded pulse shapes, are due to the restricted knowledge on the impurity density profile of a given detector and the charge-carrier mobilities in germanium. It is not trivial to study both influences independently using pulse shape analysis alone as the length and shapes of the pulses are given by an interplay of the two. However, impurity densities can be estimated from capacitance measurements [34], and charge-carrier mobilities can be studied via the temperature dependence of pulse shapes [35, 36].

The goal in this thesis is to determine both, the impurity density profile of a large-volume germanium detector and the charge-carrier mobilities in germanium, independently using a novel Compton characterization technique. The techniques developed and the knowledge gained should be generally applicable.

The thesis is structured as follows:
Chapter 2 uses neutrinoless double-beta decay as a case study to motivate the use of germanium detectors in rare-event searches. The basic working principle of germanium detectors and our current understanding of charge-carrier drift in germanium are presented in chapters 3 and 4, followed by their implementation in the simulation software package SolidStateDetectors.jl [37] in chapter 5. Chapter 6 introduces the p-type segmented point-contact detector that was used as a test detector for this thesis, followed by the characterization of its read-out electronics in chapter 7. The determination of the impurity density profile of the detector based on capacitance-voltage measurements is presented in chapter 8. The novel wide-angle Compton Scanner to study bulk events in germanium detectors [38] and its hardware and software upgrades performed within the framework of this thesis are presented in chapter 9. In chapter 10, a novel method to determine the impurity density profile through Compton imaging of the development of the depleted volume with increasing bias voltage is presented. The procedure to create pulse shape libraries from Compton Scanner data is explained in chapter 11. A novel method to extract charge-carrier mobilities for electrons and holes and their temperature dependence using the pulse shape library from data and the improved impurity density profile is introduced in chapter 12. The results presented in this thesis are summarized in chapter 13 and will improve the input to pulse shape simulation frameworks and, thus, improve background identification techniques for rare-event searches.

2 Physics motivation

In this chapter, neutrino physics and, in particular, neutrinoless double-beta decay are used as a case study to motivate the use of germanium detectors in fundamental research. After giving an introduction to the history of neutrino physics and to neutrinoless double-beta decay, the "Large Enriched Germanium Experiment for Neutrinoless $\beta\beta$ Decay", LEGEND, is presented.

2.1 History

2.1.1 Radioactive decay

An isotope ${}^{A}_{Z}\mathrm{X}$, consisting of A nucleons, i.e. Z protons and $A-Z=N$ neutrons, will eventually decay if there is a daughter isotope with a lower mass. In 1935, C.F. Weizsäcker proposed a semi-empirical formula [39] to estimate the mass of nuclei, $M(A,Z)$, based on the nuclear liquid drop [40] and nuclear shell models [41]:

$$\begin{aligned} M(A,Z) &= NM_n + ZM_p \\ &\quad - a_\mathrm{v}A + a_\mathrm{s}A^{2/3} + a_\mathrm{c}Z(Z-1)A^{-1/3} + a_\mathrm{a}(A-2Z)^2A^{-1} + \delta. \end{aligned} \tag{2.1}$$

The mass of a nucleus is not simply given by the sum of the neutron and proton masses, M_n and M_p, but also reflects the binding energy resulting from interactions between the nucleons. In Weizsäcker's model, the last five terms in Eq. (2.1) describe the dominant nucleon binding mechanisms. The parameters a_v, a_s, a_c and a_a, describe the magnitude of volume, surface, Coulomb and asymmetry energy. The last parameter δ, accounting for spin couplings between the nucleons, depends on whether N and Z are odd or even:

$$\delta = \begin{cases} +\Delta, & \text{for odd-odd nuclei, i.e. if } N \text{ and } Z \text{ are both odd} \\ -\Delta, & \text{for even-even nuclei, i.e. if } N \text{ and } Z \text{ are both even} \\ 0, & \text{for odd-even and even-odd nuclei, i.e. if } A \text{ is odd} \end{cases}, \tag{2.2}$$

where, classically, $\Delta = a_\mathrm{p}A^{-1/2}$ with a constant a_p. A more complex empirical expression for Δ was found to be more accurate especially for medium-heavy nuclei with $50 < Z < 82$ and $82 < N < 126$ [42].

For fixed A, Eq. (2.1) describes Z-dependent parabolic functions, so-called mass parabolas. The isotope closest to the minimum of the lowest mass parabola is stable. The other isotopes decay towards the stable isotope. If a neutron β^--decays into a proton, Z increases by one. If a proton β^+-decays into a neutron or if a proton captures an electron, Z decreases by one.

The presence of the pairing term for nuclei with even A, see Eq. (2.2), results in isotopes with odd and even Z being located on different mass parabolas. This is shown for $A = 76$ in Fig. 2.1a. In this case, ^{76}As has a higher mass than its direct neighbors, ^{76}Ge and ^{76}Se. As a consequence, ^{76}As undergoes both β^+ and β^- decay, and ^{76}Ge is stable with respect to regular β^- decay.

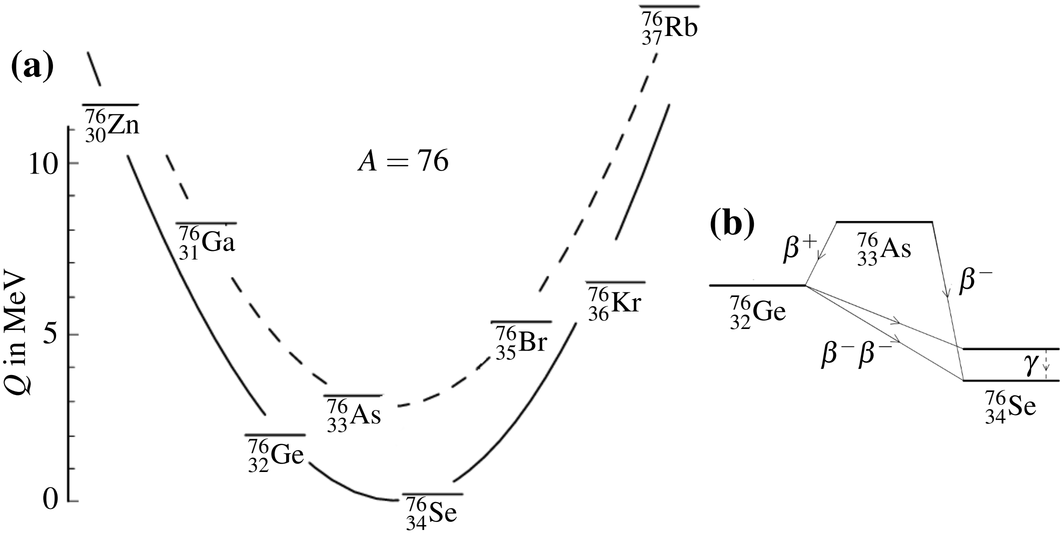

Figure 2.1: (a) Energy levels for isotopes with $A = 76$ and the two mass parabolas for odd (dashed) and even (solid) Z, adapted from [43], where Q is the energy excess compared to ^{76}Se. (b) Energy levels and decay modes of the isotopes near the minimum of the mass parabolas.

2.1.2 Discovery of the neutrino

During β^- decays, when neutrons decay to protons, electrons are emitted and charge is conserved. Assuming two-body decays and the conservation of energy and momentum, the electrons emitted in β^- decays of a given isotope would be mono-energetic, resulting in discrete energy spectra. In 1914, J. Chadwick observed that this was not the case and that the energy spectra of electrons were continuous [44].

In a "desperate remedy" to save the law of conservation of energy, W. Pauli proposed the existence of neutrinos in 1930 [45] — electrically neutral, spin–$1/2$ particles that would additionally be emitted in β decays, which we now refer to as neutrinos:

$$ {}^{A}_{Z}\mathrm{X} \xrightarrow{\beta^-} {}_{Z+1}^{\;\;A}\mathrm{Y} + e^- + \overline{\nu}_e \qquad\qquad {}^{A}_{Z}\mathrm{X} \xrightarrow{\beta^+} {}_{Z-1}^{\;\;A}\mathrm{Y} + e^+ + \nu_e \, , \tag{2.3} $$

where ν_e and $\overline{\nu}_e$ denote electron-neutrinos and -antineutrinos.

In 1956, F. Reines [46] and C.L. Cowan [47] were the first to observe $\overline{\nu}_e$ from a reactor through inverse β decay. In their experiment, the $\overline{\nu}_e$ interacted with protons in a water tank, converting them to neutrons under the emission of a positron. The events were identified through the observation of neutron capture and positron annihilation which result in the emission of a series of photons with characteristic energies within a few µs. In later experiments, two more generations of neutrinos were observed: the muon-neutrino ν_μ [48] and the tau-neutrino ν_τ [49].

2.1.3 Double-beta decay

Two-neutrino double-beta decay, $2\nu\beta\beta$, is a rare process which was first proposed by M. Goeppert-Mayer in 1935 [50]. It can be thought of as two simultaneous β decays, leading to the increase or decrease of Z by two:

$$^{A}_{Z}\mathrm{X} \xrightarrow{2\nu\beta^-\beta^-} {}^{\;\;A}_{Z+2}\mathrm{Y} + 2e^- + 2\overline{\nu}_e \qquad ^{A}_{Z}\mathrm{X} \xrightarrow{2\nu\beta^+\beta^+} {}^{\;\;A}_{Z-2}\mathrm{Y} + 2e^+ + 2\nu_e \tag{2.4}$$

The half-lives of $2\nu\beta\beta$ decays are several orders of magnitude longer than those of regular β decays. Thus, it is only experimentally observable if an isotope is stable with respect to regular β decay, i.e. when $M(A,Z\pm 2) < M(A,Z) < M(A,Z\pm 1)$. The decay energy, $Q_{\beta\beta} = M(A,Z) - M(A,Z\pm 2)$, is shared among the emitted leptons.

The first direct evidence of $2\nu\beta^-\beta^-$ in ^{82}Se was observed in a time-projection chamber measurement in 1987 [51], reporting a half-life of $(1.1^{+0.8}_{-0.3})\cdot 10^{20}$ yr. Up until today, $2\nu\beta^-\beta^-$ has been observed in eleven isotopes with half-lives ranging from 10^{18} to several 10^{21} yr [52], making it one of the rarest nuclear decay modes observed so far.

2.1.4 Neutrinoless double-beta decay

In the Dirac-Fermi theory [53], neutrinos and antineutrinos are different states, i.e. distinguishable particles. In 1937, E. Majorana proposed an alternative theory, in which neutrinos are their own antiparticles, so-called Majorana particles [54]. Applying Majorana's theory to double-beta decay, W.H. Furry predicted [55] the existence of neutrinoless double-beta decay, $0\nu\beta\beta$, where no (anti)neutrinos are emitted and where the decay energy $Q_{\beta\beta}$ is shared among the two electrons or positrons:

$$^{A}_{Z}\mathrm{X} \xrightarrow{0\nu\beta^-\beta^-} {}^{\;\;A}_{Z+2}\mathrm{Y} + 2e^- \qquad ^{A}_{Z}\mathrm{X} \xrightarrow{0\nu\beta^+\beta^+} {}^{\;\;A}_{Z-2}\mathrm{Y} + 2e^+ \,. \tag{2.5}$$

This lepton-number violating process has not yet been observed. Despite the existence of several mechanisms that would induce it, observing $0\nu\beta\beta$ would unambiguously prove that neutrinos are at least partially Majorana particles [56, 57] and provide support for leptogenesis, one possible explanation for the matter-antimatter-asymmetry observed in our universe [58].

2.2 Neutrinos in the Standard Model of Particle Physics

The Standard Model of Particle Physics, SM, was constructed to describe elementary particles and three of the four fundamental forces as known in the mid-1970s based on experimental observations.

In the SM, three generations of "active" left-handed neutrinos, i.e. ν_e, ν_μ and ν_τ, are implemented that, together with the corresponding charged leptons, form lepton doublets under the $SU(2)_L$ symmetry of the weak interaction. So far, all observations are consistent with only left-handed leptons and right-handed antileptons participating in weak interactions, providing strong evidence for maximal parity violation [59–61] and the $V-A$ nature [62, 63] of the weak interaction.

Measurements of the total decay width of the Z^0 boson determine the effective number of light-neutrino states with $m_\nu < m_{Z^0}/2$ as 2.9840 ± 0.0082 [64]. This is in good agreement with the three neutrino generations implemented in the SM. Additional neutrino states would need to be either heavy, i.e. $m_\nu > m_{Z^0}/2$, or sterile, i.e. neutrinos with no SM gauge interactions and singlets of the complete SM gauge group. As there was no experimental evidence for any such states, they were not implemented in the basic SM – it contains only left-handed Dirac neutrinos and no right-handed counterpart, resulting in neutrinos being massless at the Lagrangian level [65].

2.3 Neutrinos as currently observed

In quantum mechanics, neutrinos are described as quantum states with associated probabilities, which indicate potential outcomes of measurements.

Massive neutrinos with weak-interaction eigenstates (flavors), ν_α with $\alpha \in \{e, \mu, \tau\}$, different from neutrino-mass eigenstates, ν_i with $i \in \{1,2,3\}$, can oscillate, i.e. change flavor when propagating through space [66]. The relation between the neutrino weak eigenstates, ν_e, ν_μ and ν_τ, and the neutrino mass eigenstates, ν_1, ν_2 and ν_3, is described by the unitary Pontecorvo-Maki-Nakagawa-Sakata matrix, U_{PMNS} [66, 67]:

$$\begin{bmatrix} \nu_e \\ \nu_\mu \\ \nu_\tau \end{bmatrix} = \underbrace{\begin{bmatrix} U_{e1} & U_{e2} & U_{e3} \\ U_{\mu 1} & U_{\mu 2} & U_{\mu 3} \\ U_{\tau 1} & U_{\tau 2} & U_{\tau 3} \end{bmatrix}}_{= U_{\mathrm{PMNS}}} \begin{bmatrix} \nu_1 \\ \nu_2 \\ \nu_3 \end{bmatrix} . \tag{2.6}$$

This mixing matrix can be parameterized [65] as

$$U_{\mathrm{PMNS}} = \begin{bmatrix} 1 & 0 & 0 \\ 0 & c_{23} & s_{23} \\ 0 & -s_{23} & c_{23} \end{bmatrix} \begin{bmatrix} c_{13} & 0 & s_{13}e^{-i\delta_{\mathrm{CP}}} \\ 0 & 1 & 0 \\ -s_{13}e^{i\delta_{\mathrm{CP}}} & 0 & c_{13} \end{bmatrix} \begin{bmatrix} c_{12} & s_{12} & 0 \\ -s_{12} & c_{12} & 0 \\ 0 & 0 & 1 \end{bmatrix} \begin{bmatrix} 1 & 0 & 0 \\ 0 & \mathrm{e}^{i\eta_1} & 0 \\ 0 & 0 & \mathrm{e}^{i\eta_2} \end{bmatrix} , \tag{2.7}$$

with $s_{ij} = \sin(\theta_{ij})$ and $c_{ij} = \cos(\theta_{ij})$, where θ_{12}, θ_{23} and θ_{13} are three mixing angles, and a phase-angle, δ_{CP}, which is attributed to charge-parity violations. If neutrinos are Majorana particles, two additional Majorana phases, η_1 and η_2, are present in U_{PMNS}. For Dirac neutrinos, η_1 and η_2 can be absorbed into the neutrino states.

The observation of oscillations between all neutrino flavors [68, 69] proves that there are (at least) three non-degenerate neutrino-mass eigenstates, ν_1, ν_2 and ν_3, with masses, m_1, m_2 and m_3, and non-vanishing θ_{ij}. The observed oscillation probabilities are used to determine the squared mass differences, $\Delta m_{ij}^2 = m_i^2 - m_j^2$, and show that at least two neutrino masses are non-zero [65]. However, the mass generation mechanisms, the absolute neutrino masses and even the mass ordering are still unknown. From matter effects in the Sun, it is known that $\Delta m_{21}^2 > 0$, i.e. that $m_1 < m_2$ [70]. An updated global fit based on neutrino oscillation data from 2020 prefers the normal mass ordering, i.e. $m_1 < m_2 < m_3$, over the inverted mass ordering, i.e. $m_3 < m_1 < m_2$, with a statistical significance of 2.5σ [71].

There are different experimental approaches to measure the absolute neutrino masses.

Cosmological observations constrain the sum of all three known neutrino masses, $\sum m_i$. Massive neutrinos would influence the cosmic microwave background and the large-scale structure of the universe [72]. Currently, the most constraining limit on the sum of the neutrino masses assuming the ΛCDM model is $\sum m_i < 0.09\,\mathrm{eV}$ at 95% C.L. [73].

Massive neutrinos also influence the energy spectrum of the electrons emitted in β decay, as some of the energy, $Q_\beta = M(A,Z) - M(A,Z\pm 1)$, is converted to neutrino-mass energy, $\langle m_{\nu_e}\rangle$. Direct kinematic searches, investigating the spectrum of the electrons emitted in regular β decay close to the endpoint at Q_β are sensitive to the incoherent sum over the mass eigenvalues, $\langle m_{\nu_e}\rangle = \sqrt{\sum |U_{ei} m_i|^2}$. The current best limit of $\langle m_{\nu_e}\rangle < 0.8\,\mathrm{eV}$ at 90% C.L. was reported by the KATRIN collaboration in 2022 [74].

A third process to study the nature and masses of neutrinos is $0\nu\beta\beta$ [75].

2.4 Theory extensions for neutrinoless double-beta decay

2.4.1 Exchange of light Majorana neutrinos

As $0\nu\beta\beta$ does not conserve lepton number, it needs to be mediated by some physics process beyond the SM. One minimal and, perhaps, the most natural extension would be the exchange of a virtual light Majorana neutrino, ν_M, through charged-current weak interactions, see Fig. 2.2.

W.H. Furry originally assumed $0\nu\beta\beta$ to have a higher transition probability than $2\nu\beta\beta$ due to the larger phase space for the emitted electrons [55]. However, the maximal parity violation described as a $V-A$ weak interaction requires the neutrino helicity to be flipped.

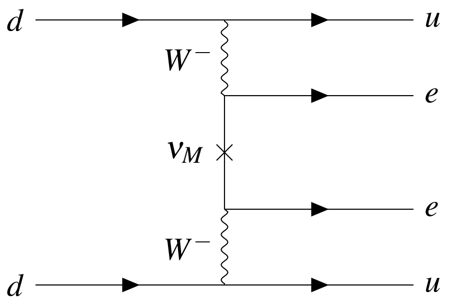

Figure 2.2: Feynman diagram depicting $0\nu\beta\beta$ mediated by the exchange of a virtual light Majorana neutrino, ν_M [56].

The helicity flip, enabled by a mass term of the neutrino in the Lagrangian, results in the suppression of $0\nu\beta\beta$ by the square of the effective Majorana mass,

$$\langle m_{\beta\beta}\rangle = \left|\sum_{i=1}^{3} U_{ei}^2\, m_i\right| = \left|m_1|U_{e1}|^2 + m_2|U_{e2}|^2\exp(2i\eta_1) + m_3|U_{e3}|^2\exp(2i\eta_2)\right| \;, \quad (2.8)$$

which is the coherent sum over the neutrino mass eigenvalues and depends on the absolute neutrino masses, m_1, m_2 and m_3, the values of U_{e1}, U_{e2} and U_{e3} and the Majorana phases η_1 and η_2, in Eq. (2.7).

While the values for U_{e1}, U_{e2}, U_{e3}, Δm^2_{21} and $|\Delta m^2_{31}|$ are known from neutrino oscillation experiments [76], there are no constraints on the Majorana phases, η_1 and η_2. For both normal and inverted mass ordering, the lowest mass, $m_{\min}$, can be used to calculate the other two masses. A probability distribution for $\langle m_{\beta\beta}\rangle$ can be composed by uniformly sampling values for η_1 and η_2 [77, 78].

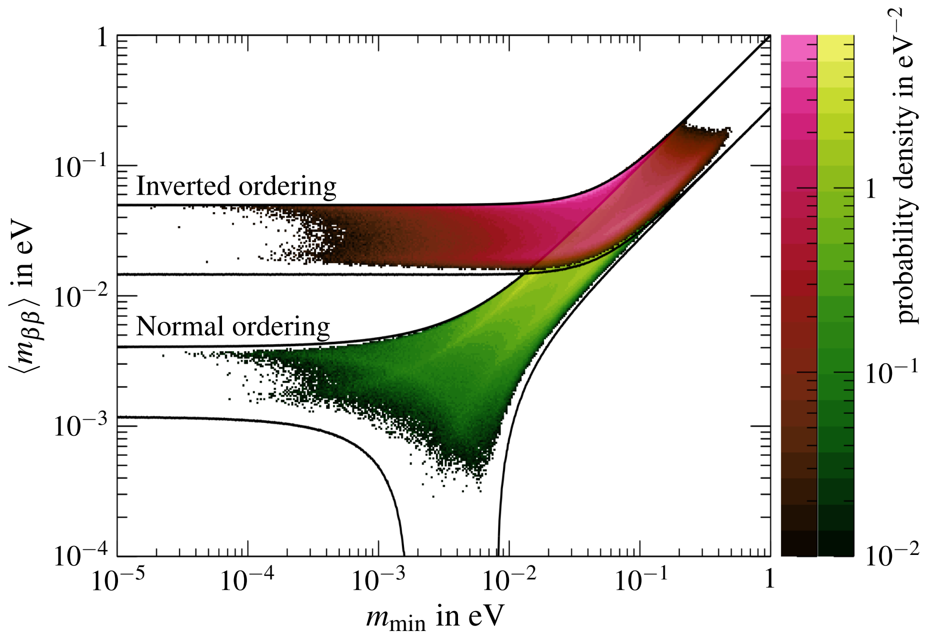

Figure 2.3: Marginalized posterior distributions for $\langle m_{\beta\beta} \rangle$ in dependence of the lightest neutrino mass, m_{min}, for the normal and the inverted mass ordering, adapted from [77]. The solid lines depict the allowed parameter space given by the 3σ intervals of the neutrino oscillation parameters [76]. The probability densities are normalized to the logarithms of $\langle m_{\beta\beta} \rangle$ and m_{min}.

Figure 2.3 shows the probability density of the neutrino mass parameters $\langle m_{\beta\beta} \rangle$ and m_{min} as published by Agostini *et al.* in 2017 [77] using logarithmic priors on mass observables and uniform priors on angles and phases*. The 90% central interval for $\langle m_{\beta\beta} \rangle$ is $20 - 119\,\text{meV}$ for the inverted ordering, and $3 - 104\,\text{meV}$ for the normal ordering. For the inverted ordering, $\langle m_{\beta\beta} \rangle$ is always larger than $(18.4 \pm 1.3)\,\text{meV}$ [80]. For normal ordering, $\langle m_{\beta\beta} \rangle$ could, in principle, be zero. This would, however, require fine-tuning of η_1 and η_2.

If mediated by only the exchange of a light Majorana neutrino, the half-life of $0\nu\beta\beta$, $T_{1/2}^{0\nu\beta\beta}$, is [81]

$$(T_{1/2}^{0\nu\beta\beta})^{-1} = G^{0\nu\beta\beta} g_A^4 \left| \mathcal{M}^{0\nu\beta\beta} \right|^2 \frac{\langle m_{\beta\beta} \rangle^2}{m_e^2} \,, \tag{2.9}$$

where $G^{0\nu\beta\beta}$ is the phase-space factor, $g_A \simeq -1.276$ [82] is the weak axial vector coupling constant, $\mathcal{M}^{0\nu\beta\beta}$ is the nuclear matrix element and m_e is the electron rest mass. The value for $G^{0\nu\beta\beta}$ depends on the atomic number Z of the isotope, scales with $Q_{\beta\beta}^5$, can be calculated very precisely and is of the order of $10^{-15}\,\text{yr}^{-1}$ [81]. Reported values for $\mathcal{M}^{0\nu\beta\beta}$ vary by a factor of up to three, depending on the nuclear model used for the computation [83].

Measuring (or setting lower limits on) $T_{1/2}^{0\nu\beta\beta}$ allows determining (or setting an upper limit on) $\langle m_{\beta\beta} \rangle$. Assuming the Majorana nature of neutrinos and no other processes involved, the effective Majorana neutrino mass $\langle m_{\beta\beta} \rangle$ can be extracted from $T_{1/2}^{0\nu\beta\beta}$. In this case, experiments sensitive to $T_{1/2}^{0\nu\beta\beta}$ of the order of $10^{28}\,\text{yr}$ are able to fully probe the mass parameter space for the inverted ordering.

---

*Note that the posterior probabilities depend strongly on the choice of prior on m_{min} [79].

2.4.2 Alternative processes mediating neutrinoless double-beta decay

While the exchange of light Majorana neutrinos in left-handed charged-current weak interactions is a very popular process that could mediate $0\nu\beta\beta$, it might not be the only one. Figure 2.4 shows alternative mechanisms mediating $0\nu\beta\beta$ through other lepton-number-violating extensions of the SM, e.g. via the exchange of

- heavy Majorana neutrinos or doubly-charged Higgs in left-right symmetric models which allow for small right-handed currents in the weak interactions [84],
- neutralinos or gluinos in R-parity-violating minimal supersymmetric models [85, 86],
- scalar or vector leptoquarks in combination with Majorana neutrinos [87].

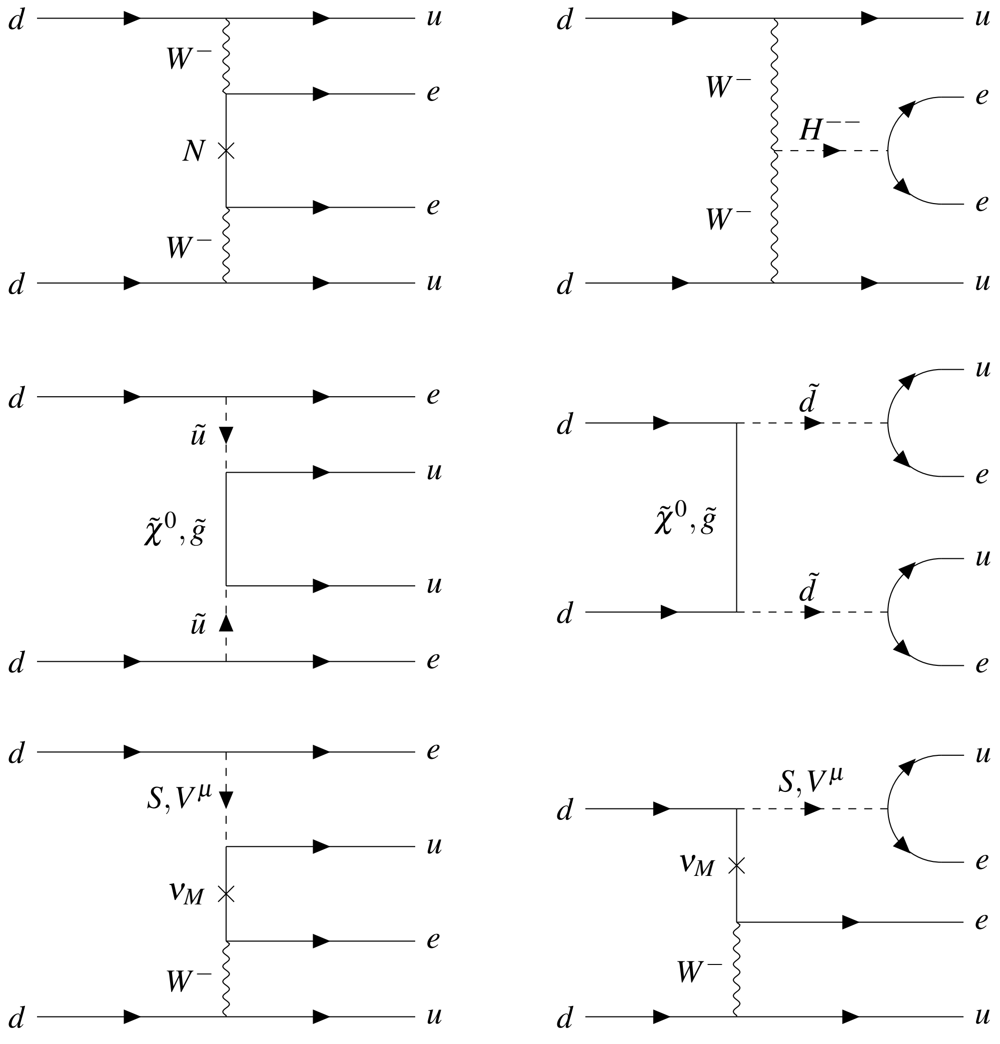

Figure 2.4: Feynman diagrams depicting possible $0\nu\beta\beta$ mechanisms mediated (top) by a heavy Majorana neutrino, N, or a doubly-charged Higgs boson, H^{--}, in left-right symmetric models [84], (middle) by neutralinos, $\tilde{\chi}^0$, or gluinos, $\tilde{g}$, in R-parity-violating minimal supersymmetric models involving the supersymmetric partners of the u and d quarks, $\tilde{u}$ and $\tilde{d}$, [86] or (bottom) by a Majorana neutrino, ν_M, together with a scalar or vector leptoquark, S or V^μ [87].

It is challenging to experimentally distinguish between these different mechanisms. If the theoretical model allows for right-handed currents in the weak interaction, measurements on the angular correlations between the emitted electrons might give an insight into the underlying physics of $0\nu\beta\beta$ [88].

It should also be noted that these alternative processes will result in additional Majorana mass terms in the Lagrangian. This leads to further contributions to $T_{1/2}^{0\nu\beta\beta}$ in Eq. (2.9), i.e. $\langle m_{\beta\beta}\rangle^2 \rightarrow \langle m_{\beta\beta}\rangle^2 + \langle M_{\beta\beta}\rangle^2$, where $\langle M_{\beta\beta}\rangle^2$ is an effective Majorana mass resulting from physics beyond light Majorana neutrino exchange [89]. If $0\nu\beta\beta$ is not only mediated by light Majorana neutrino exchange, $\langle M_{\beta\beta}\rangle^2$ might be the dominant contribution to $T_{1/2}^{0\nu\beta\beta}$ and $\langle m_{\beta\beta}\rangle$ could turn out to be as small as $< 10^{-24}$ eV [90].

In conclusion, $0\nu\beta\beta$ only allows for the measurement of $\langle m_{\beta\beta}\rangle$. Absolute neutrino masses can only be determined if neutrinos are 100% Majorana particles and if no other lepton-violating processes apart from light Majorana neutrino exchange cause $0\nu\beta\beta$.

2.5 Experimental searches for neutrinoless double-beta decay

2.5.1 Experimental signature

All isotopes undergoing $2\nu\beta\beta$ are candidates for $0\nu\beta\beta$. Experimentally, these two decay modes can be distinguished by measuring the sum of the kinetic energies of the two emitted electrons, $E_{\beta\beta}$. In $2\nu\beta\beta$, a part of the decay energy $Q_{\beta\beta}$ is carried away by the neutrinos and remains undetected. Thus, in analogy to regular β decay, the spectrum of $E_{\beta\beta}$ is continuous with $E_{\beta\beta} < Q_{\beta\beta}$. In $0\nu\beta\beta$, the decay energy is basically fully transferred to the electrons[*], i.e. $E_{\beta\beta} \approx Q_{\beta\beta}$, resulting in a discrete peak at $Q_{\beta\beta}$. An example spectrum of $E_{\beta\beta}$ is shown in Fig. 2.5.

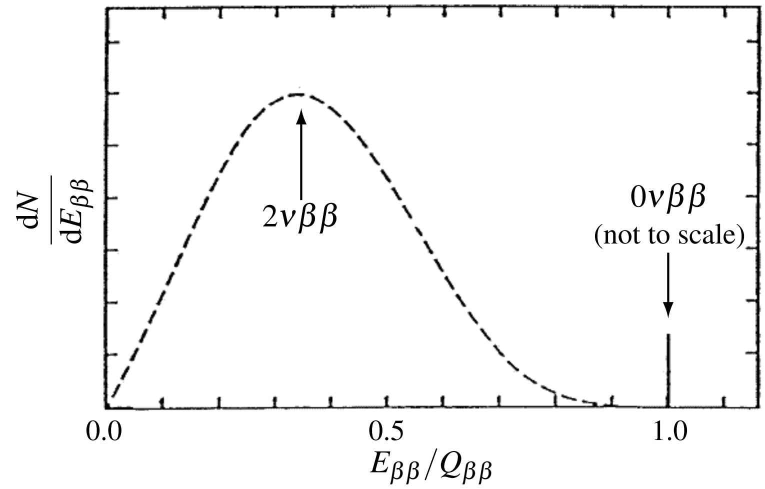

Figure 2.5: Spectrum of the sum of the kinetic energy, $E_{\beta\beta}$, of the two electrons emitted in $2\nu\beta\beta$ (dashed) and in $0\nu\beta\beta$ (solid), adapted from [91]. The $0\nu\beta\beta$ peak, if existent, is expected to be several orders of magnitude smaller and broadened by the finite energy resolution of the experimental setup.

---

[*] As the electrons are much lighter than the daughter nucleus, the recoil energy is negligible.

2.5.2 Event statistics and sensitivity

If existent, $0\nu\beta\beta$ is a very rare process and the probability distribution for the number of events has to be evaluated with Poisson statistics. The expected number of observed $0\nu\beta\beta$ events, $N_{\mathrm{obs}}^{0\nu\beta\beta}$, in the region of interest, ROI, around $Q_{\beta\beta}$ is [75]

$$N_{\mathrm{obs}}^{0\nu\beta\beta} = \varepsilon N_0 \left(1 - \exp\left(-\frac{\ln(2)\,t}{T_{1/2}^{0\nu\beta\beta}}\right)\right) \overset{t \ll T_{1/2}^{0\nu\beta\beta}}{\approx} \varepsilon N_0 \frac{\ln(2)\,t}{T_{1/2}^{0\nu\beta\beta}} = \ln(2)\frac{N_A}{W}\left(\frac{a\varepsilon Mt}{T_{1/2}^{0\nu\beta\beta}}\right) , \tag{2.10}$$

where ε is the efficiency to detect a $0\nu\beta\beta$ event in the ROI, t is the measurement time and N_0 is the number of $0\nu\beta\beta$ candidate nuclei. The latter is commonly rewritten as $N_0 = MaN_A/W$, where M is the source mass, a is the abundance of the $0\nu\beta\beta$ isotope in the source, N_A is Avogadro's constant and W is the molar mass of the source. The source mass multiplied by the measurement time, Mt, is often referred to as exposure.

As $T_{1/2}^{0\nu\beta\beta}$ is expected to be of the order of 10^{28} yr or beyond, $N_{\mathrm{obs}}^{0\nu\beta\beta}$ will be small. For example, for ^{76}Ge ($W = 75.92\,\mathrm{g\ mol}^{-1}$ [92]) and $T_{1/2}^{0\nu\beta\beta} = 10^{28}$ yr, an exposure of 10 t yr (e.g. 1 t of detector mass and 10 yr measurement time) leads to an expectation of only $N_{\mathrm{obs}}^{0\nu\beta\beta} \approx 5.5$, assuming 100% abundance and 100% detection efficiency.

It is crucial that a possible $0\nu\beta\beta$ peak in the spectrum is not hidden by background or mistaken for background. The background is typically quantified using the so-called background index, B, which describes the expected number of background events, $N_{\mathrm{obs}}^{\mathrm{bkg}}$, in a given energy window per unit of exposure:

$$N_{\mathrm{obs}}^{\mathrm{bkg}} = B\,\Delta E\,Mt , \tag{2.11}$$

where ΔE describes the width of the ROI.

In the absence of background events, the probability, $p_\emptyset$, of not observing any event in the ROI for the expectation $N_{\mathrm{obs}}^{0\nu\beta\beta}$ is given by Poisson statistics as $p_\emptyset = \exp(-N_{\mathrm{obs}}^{0\nu\beta\beta})$. Demanding $p_\emptyset$ to be lower than a given probability, e.g. 90%, results in a maximum value of $N_{\mathrm{obs}}^{0\nu\beta\beta}$ that could be missed. Using Eq. (2.10), this provides a lower bound on $T_{1/2}^{0\nu\beta\beta}$ proportional to $a\varepsilon Mt$.

In the presence of background events, the required number of $0\nu\beta\beta$ events has to be higher than possible random fluctuations expected from the background to set a limit or to claim a discovery. The 3σ discovery sensitivity of an experiment, $S^{0\nu\beta\beta}$, defined as the value for $T_{1/2}^{0\nu\beta\beta}$, for which a 50% chance to measure a signal with a significance of at least 3σ is expected [93], can be determined from heuristic counting analysis [77]. For $N_{\mathrm{obs}}^{\mathrm{bkg}} < 0.0027$, the measurement is quasi-background free and a single count in the ROI is sufficient to claim a 3σ discovery. Thus, $S^{0\nu\beta\beta} \propto a\varepsilon Mt$ only until the experiment exceeds the background-free threshold. Above that, the sensitivity approaches an asymptotic $S^{0\nu\beta\beta} \propto a\varepsilon\sqrt{Mt/B\Delta E}$ for high $N_{\mathrm{obs}}^{\mathrm{bkg}} \gtrsim 20$.

In order to have high $S^{0\nu\beta\beta}$, experiments searching for $0\nu\beta\beta$ should have high detection efficiencies, large source masses, long measurement times, an excellent energy resolution and preferably be background-free or at least have a low background index.

2.5.3 Detector concepts

From the 35 possible $0\nu\beta^-\beta^-$ candidates, 28 have been studied experimentally [94]. So far, no significant evidence for $0\nu\beta\beta$ has been observed. The various experiments have reported lower bounds on $T_{1/2}^{0\nu\beta\beta}$ for different isotopes of up to $2.3 \cdot 10^{26}\,\mathrm{yr}$, see Tab. 2.1. The corresponding ranges in $\langle m_{\beta\beta} \rangle$ reflect the ranges of the matrix elements published, see Eq. (2.9).

Table 2.1: Current best limits on the $0\nu\beta\beta$ half-life, $T_{1/2}^{0\nu\beta\beta}$, and on the effective neutrino Majorana mass, $\langle m_{\beta\beta} \rangle$, all at 90% confidence limit. Only limits with $T_{1/2}^{0\nu\beta\beta} > 10^{24}\,\mathrm{yr}$ are included.

Isotope	Experiment	Limit $T_{1/2}^{0\nu\beta\beta}$	Limit $\langle m_{\beta\beta} \rangle$	Ref.
^{76}Ge	GERDA	$> 1.8 \cdot 10^{26}\,\mathrm{yr}$	$< 79 - 180\,\mathrm{meV}$	[95]
^{76}Ge	MAJORANA	$> 8.3 \cdot 10^{25}\,\mathrm{yr}$	$< 113 - 269\,\mathrm{meV}$	[96]
^{82}Se	CUPID-0	$> 4.6 \cdot 10^{24}\,\mathrm{yr}$	$< 263 - 545\,\mathrm{meV}$	[97]
^{100}Mo	CUPID-Mo	$> 1.8 \cdot 10^{24}\,\mathrm{yr}$	$< 280 - 490\,\mathrm{meV}$	[98]
^{130}Te	CUORE	$> 2.2 \cdot 10^{25}\,\mathrm{yr}$	$< 90 - 305\,\mathrm{meV}$	[99]
^{136}Xe	EXO-200	$> 3.5 \cdot 10^{25}\,\mathrm{yr}$	$< 93 - 286\,\mathrm{meV}$	[100]
^{136}Xe	KamLAND-ZEN	$> 2.3 \cdot 10^{26}\,\mathrm{yr}$	$< 36 - 156\,\mathrm{meV}$	[101]

The experiments setting the strongest limits on $T_{1/2}^{0\nu\beta\beta}$, see Tab. 2.1, are based on combining the source and the detector, by either using the source as detector or embedding the source isotope into the detector material. The three main mechanisms to measure the electron energies are scintillation, ionization and emission of phonons [102].

In monolithic liquid detectors, hundreds of tons of liquid scintillator doped with $0\nu\beta\beta$ candidate isotopes, e.g. ^{136}Xe in KamLAND-ZEN [101] or ^{130}Te in SNO+ [103], are deployed. The signal electrons as well as other particles depositing energy will result in the emission of scintillation light which is measured using photomultiplier tubes. From this, the energy and the location of the event can be reconstructed. By selecting events in the center, the detector can self-shield against external background events. While these detectors can be scaled up easily to high exposures, the energy resolution at $Q_{\beta\beta}$ is of the order of hundreds of keV. Thus, the continuous $2\nu\beta\beta$ spectrum overlaps with the $0\nu\beta\beta$ peak, resulting in an unavoidable background in the ROI from $2\nu\beta\beta$ events.

In time-projection chambers holding liquids or gases, energy deposits in the detector medium lead to both scintillation and ionization signals. Ideally, the medium is chosen to only consist of the $0\nu\beta\beta$ candidate isotope, e.g. ^{136}Xe in EXO-200 [100]. Here, the energy and position inside the volume can be reconstructed from the difference in arrival time between the scintillation and ionization signals, which allows to detect external background events close to the surface. These time-projection chambers have reached energy resolutions of $30\,\mathrm{keV}$ at $Q_{\beta\beta}$, resulting in smaller $2\nu\beta\beta$ background in the ROI compared to monolithic liquid detectors.

In cryogenic calorimeters or bolometers, energy deposits in cryogenically cooled crystals result in the emission of phonons that induce heat which is registered using highly sensitive temperature sensors. In CUORE [99], 988 TeO_2 crystals with masses of $\sim 750\,g$ each and a natural abundance of 34% ^{130}Te were operated with an energy resolution of 7.8 keV at $Q_{\beta\beta}$. CUORE was limited by surface backgrounds from alpha decays. Upgrading CUORE by using scintillating bolometers, e.g. ZnSe with ^{82}Se in CUPID-0 [97] or Li_2MoO_4 with ^{100}Mo in CUPID-Mo [98], allows for particle identification which further reduces the background index and yields higher $S^{0\nu\beta\beta}$.

In germanium detectors enriched in ^{76}Ge, energy deposits are registered solely through the ionization of atoms in the crystal and subsequent charge collection on the electrodes of the detector. Detailed information on their working principles is presented in section 3.3. Experiments using germanium detectors to search for $0\nu\beta\beta$, i.e. GERDA [95] and MAJORANA [96], have reported the lowest background index in the ROI of any $0\nu\beta\beta$ experiment so far of $(5.2^{+1.6}_{-1.3}) \cdot 10^{-4}$ counts/(keV kg yr) [95], and excellent energy resolutions of 2.52 keV at $Q_{\beta\beta}$ [96]. Those achievements create a quasi-background-free environment for a search for $0\nu\beta\beta$ at $Q_{\beta\beta} = 2039.061\,\text{keV}$ [104].

One alternative concept searching for $0\nu\beta\beta$ is based on tracking calorimeters, as e.g. in NEMO-3 [105] or SuperNEMO [106]. Here, the source isotope is deployed in thin foils allowing the emitted electrons to escape from the foil. The foils are surrounded by a set of tracking chambers and calorimeters to reconstruct the tracks and energies of the electrons, respectively. Due to the required thinness of the foils, these experiments will not reach high exposures but would offer valuable insights into the kinematics of the emitted electrons in $2\nu\beta\beta$ and possibly $0\nu\beta\beta$. The former will provide a better understanding of the nuclear physics of the decaying isotope. The latter would allow to probe the different mechanisms mediating $0\nu\beta\beta$, see section 2.4.2.

In order to probe $T_{1/2}^{0\nu\beta\beta}$ of 10^{28} yr and beyond, i.e. the range relevant in case of the inverted ordering for light neutrino masses, three ton-scale experiments are planned.

- CUPID [107] (based on CUPID-Mo), using Li_2MoO_4 scintillating bolometers,
- nEXO [108] (based on EXO-200), using a ^{136}Xe time projection chamber,
- LEGEND [12] (based on GERDA and MAJORANA), using germanium detectors.

In the final part of this chapter, the LEGEND experiment is presented to demonstrate the effort required to build a ton-scale experiment searching for $0\nu\beta\beta$.

2.5.4 The LEGEND experiment

The LEGEND collaboration aims to build a ton-scale ^{76}Ge-based experiment searching for $0\nu\beta\beta$with the goal of probing $T_{1/2}^{0\nu\beta\beta} > 10^{28}$ yr [12]. The experimental program is divided into two stages: LEGEND-200 and LEGEND-1000, which will deploy 200 kg and 1000 kg of germanium detectors to reach exposures of 1 t yr and 10 t yr, respectively.

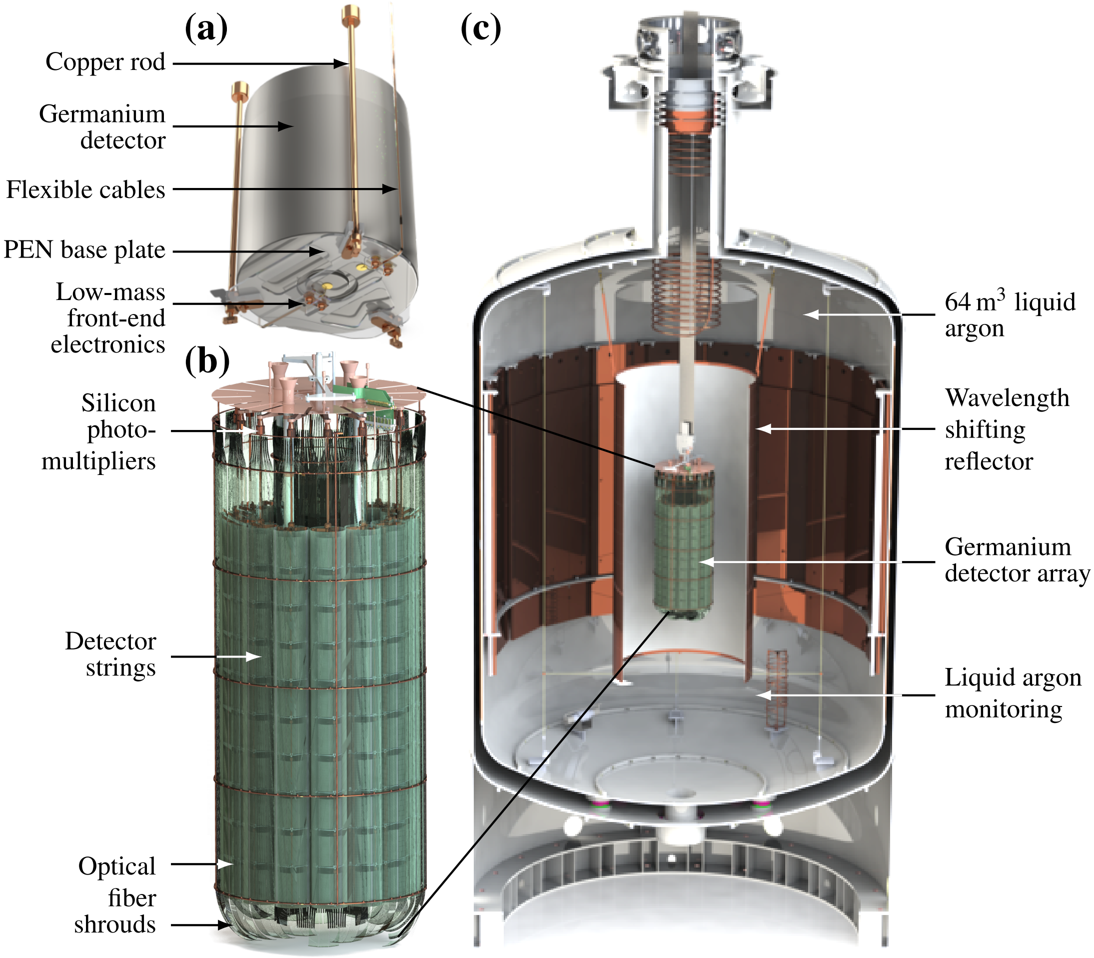

Figure 2.6: Artistic view of (a) a typical LEGEND detector with electronics, held by a PEN base plate and copper rods, (b) the LEGEND-200 detector array surrounded by optical fiber shrouds and (c) the LEGEND-200 liquid-argon cryostat. The LEGEND-200 water tank is not shown. Image courtesy of Patrick Krause.

For LEGEND-200, approximately 200 kg of ^{76}Ge-enriched germanium detectors were to be deployed in the existing infrastructure of GERDA Phase II [109]. The LEGEND-200 detectors have different geometries and masses, ranging from 500 g to more than 3 kg. The detectors are biased and read out using low-mass front-end electronics, placed onto base plates made of polyethylene naphthalate, PEN. They are held by rods machined underground out of electroformed copper, see Fig. 2.6a. These detector units are arranged into vertical strings which are combined to form a circular array. The detector array is enclosed in optical fiber shrouds covered with tetraphenyl butadiene, TPB, see Fig. 2.6b. The array is submerged in a cryostat filled with 64 m^3 of liquid argon and has walls covered by a wavelength-shifting reflector, see Fig. 2.6c. The liquid-argon cryostat is surrounded by a tank filled with 590 m^3 ultra-pure water, which is equipped with photomultiplier tubes on the tank walls. The LEGEND-200 experiment is located in Hall A of the INFN Gran Sasso National Laboratory, LNGS. At the time of writing, the LEGEND-200 detector array consisted of 142 kg of germanium detectors grouped in 10 strings and had started data taking.

In order to increase the sensitivity on $T_{1/2}^{0\nu\beta\beta}$ with respect to GERDA, LEGEND-200 aims to lower the background index by a factor of ≈ 3 to $2 \cdot 10^{-4}$ counts/(keV kg yr). The background reduction strategy of LEGEND-200 is based on the GERDA [95] experience: shielding against external background, reducing the sources of internal background and identifying the remaining background events.

Background from cosmic and atmospheric radiation is reduced by the 1400 m rock overburden that translates to 3500 m water equivalent. This reduces the flux of muons in the experiment down to $1.25\,\mathrm{m}^{-2}\,\mathrm{h}^{-1}$ [109]. The water in the outer tank shields against external neutrons, the liquid argon against external gammas.

In order to reduce the radioactivity in the vicinity of the detectors, the amount of material to hold or operate the detectors is minimized. All the materials in the vicinity of the detectors were carefully screened to avoid radioactive contaminations and stored mainly underground to reduce the impact of cosmic activation.

The remaining unavoidable background events are reduced using active veto systems. The water tank can detect muons through the detection of Cherenkov radiation. The liquid argon and the PEN base plates are scintillating in response to gamma events. The scintillation light is shifted to blue through the TPB and guided to the silicon photomultipliers through optical fibers. As $0\nu\beta\beta$ results in a single-detector event with an energy of $Q_{\beta\beta}$, any event with coincident triggers in the water tank, the liquid-argon tank or multiple detectors is classified as a background event and rejected. In addition, analyzing the detector signals, i.e. the pulse shapes, provides further classification of events into $0\nu\beta\beta$ candidates or background [30, 31, 110].

The background within GERDA [111] was dominated by alphas and gammas originating from contaminations with isotopes from the ^{238}U and the ^{232}Th decay chains. Also significant were background events originating from cosmogenically activated ^{42}K in the liquid argon. All of this was addressed in LEGEND-200 by improving the choice of materials in the vicinity of the detectors, e.g. by using optically active PEN base plates, underground-electroformed copper and low-mass front-end electronics. In addition, pulse shape analysis techniques need to be improved to more efficiently recognize unavoidable background events.

In LEGEND-1000, 1000 kg of germanium detectors are to be deployed in a new infrastructure at a site yet to be selected. The background index will need to be further reduced to $< 10^{-5}$ counts/(keV kg yr) in order to create a background-free ROI. LEGEND-1000 will build on the experience of LEGEND-200 to improve all parts of the experimental design, e.g. using underground liquid argon to reduce the amount of ^{42}K, enclosing the detectors in PEN to avoid surface contaminations from radioactive isotopes in the liquid argon and using improved germanium detectors.

The immense experimental effort will allow LEGEND to probe the inverted ordering for Majorana neutrino exchange and, thus, possibly provide answers to the open questions about the nature of neutrinos.

3 Germanium detectors

For all applications listed in chapter 1, germanium detectors are used to detect particle interactions by measuring the charge resulting from ionization in the germanium.

In this chapter, the different interaction processes between particles and germanium, relevant in the energy range between a few keV and a few MeV, as well as their event topologies are presented. Afterwards, a general introduction to the properties of germanium is given. Finally, the working principles and the fabrication of germanium detectors are discussed.

3.1 Interactions of relevant particles with germanium

3.1.1 Photons

Photons with an energy of a few keV or above are often called gammas. The detection of gammas in this energy range is especially important to identify nuclear decays. Gammas interact in germanium via photoelectric absorption, Compton scattering and pair production. Figure 3.1 shows the linear absorption coefficient for these processes as a function of the energy of the incident gamma, E_{in}.

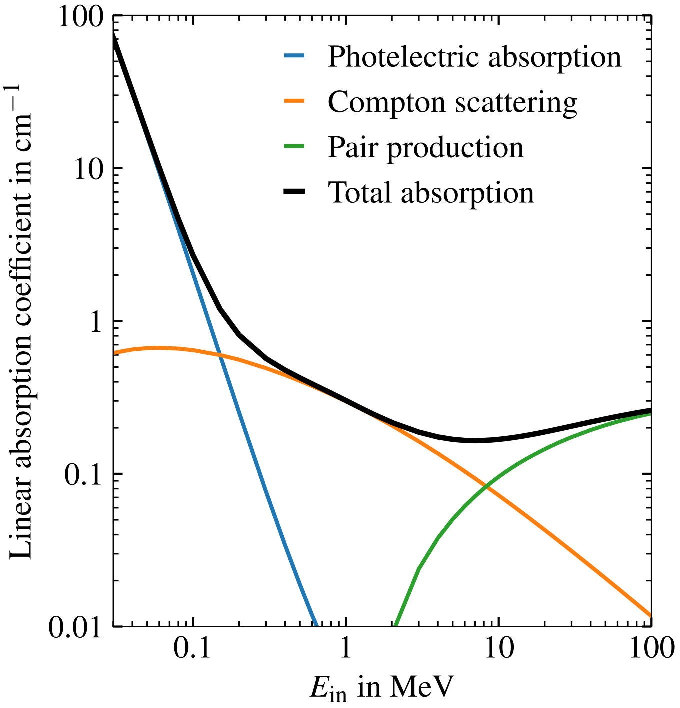

Figure 3.1: Linear absorption coefficient for different interaction processes of gammas in germanium as a function of the gamma energy, E_{in} [112].

3.1.1.1 Photoelectric absorption

For $E_{\text{in}} < 150\,\text{keV}$, the dominant process is photoelectric absorption. A free electron cannot absorb a gamma completely [29, p. 49] because energy and momentum cannot be simultaneously conserved. Therefore, photoelectric absorption requires the environment of an atom. During this process, the gamma transfers its full energy to one of the bound electrons, resulting in its ejection from the atom as a so-called photoelectron. Part of the energy is used to overcome the binding energy, E_B, and the rest of the energy is converted to the kinetic energy of the photoelectron, E_e, i.e.

$$E_e = E_{\text{in}} - E_B\ . \tag{3.1}$$

The interaction probability increases with smaller E_{in}, see Fig. 3.1.

In germanium, most of the gammas with $E_{\text{in}} > 11.1\,\text{keV}$ that undergo photoelectric absorption interact with electrons in the K shell [29, p. 49], where $E_B = 11.1\,\text{keV}$ [113]. Gammas with $E_{\text{in}} < 11.1\,\text{keV}$ interact in shells with smaller E_B, i.e. the L and the M shell. The vacancy created in the atom is subsequently filled by capturing a free electron from the surrounding or by rearranging the electron configuration within the atom, leading to the emission of characteristic X-rays or Auger electrons [29, p. 334], see Fig. 3.2. The range of these secondary particles emitted after photoelectric absorption is well below a millimeter, leading to reabsorption very close to the site of the primary interaction and resulting in very localized clusters of energy.

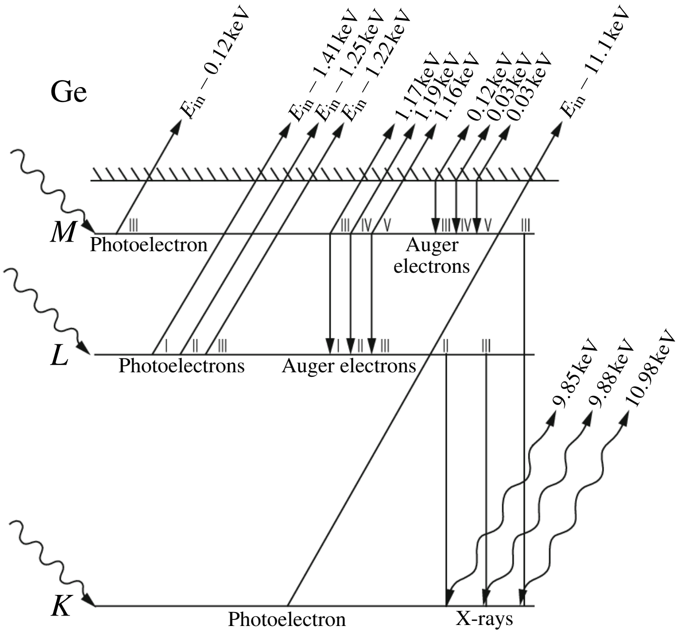

Figure 3.2: Sketch of the origin and energy of photoelectrons, Auger electrons and X-rays, based on [29, p. 334] with the values of the binding energies for germanium taken from [113].

3.1.1.2 Compton scattering

Gammas with $150\,\text{keV} \leq E_{\text{in}} \leq 8\,\text{MeV}$ predominantly interact in germanium via Compton scattering. The incident gamma scatters off a bound electron, transferring only part of its energy, E_{dep}, to the electron, see Fig. 3.3a. The gamma is deflected by the Compton angle, θ, with respect to its initial direction, where

$$\cos(\theta) = 1 - \frac{m_e c^2 E_{\text{dep}}}{E_{\text{in}}\left(E_{\text{in}} - E_{\text{dep}}\right)} \,. \tag{3.2}$$

The value of θ can be between 0° and 180° and its distribution depends on E_{in}. The differential cross-section for Compton scattering, $\mathrm{d}\sigma/\mathrm{d}\Omega$, is given by the Klein-Nishina formula [114]. For unpolarized incident gammas, it is [29, p. 51],

$$\frac{\mathrm{d}\sigma}{\mathrm{d}\Omega} = Zr_0^2 \left(\frac{1}{1+\alpha(1-\cos\theta)}\right)^2 \left(\frac{1+\cos^2\theta}{2}\right) \left(1 + \frac{\alpha^2(1-\cos\theta)^2}{(1+\cos^2\theta)[1+\alpha(1-\cos\theta)]}\right) , \tag{3.3}$$

where $\mathrm{d}\Omega = \sin\theta\,\mathrm{d}\theta\,\mathrm{d}\phi$ is the differential solid angle, $r_0 = 2.818\cdot 10^{-15}\,\text{m}$ is the classical electron radius and $\alpha = E_{\text{in}}/m_e c^2$.

For unpolarized gammas, the dependence of the solid angle on ϕ can be integrated out and $\mathrm{d}\Omega = 2\pi\sin(\theta)\,\mathrm{d}\theta$. The θ-distribution for Compton scattering becomes

$$\frac{\mathrm{d}\sigma}{\mathrm{d}\theta} = \frac{\mathrm{d}\sigma}{\mathrm{d}\Omega}\frac{\mathrm{d}\Omega}{\mathrm{d}\theta} = 2\pi\sin(\theta)\,\frac{\mathrm{d}\sigma}{\mathrm{d}\Omega} \,. \tag{3.4}$$

Figure 3.3b shows the polar distributions of Compton angles for different E_{in}.

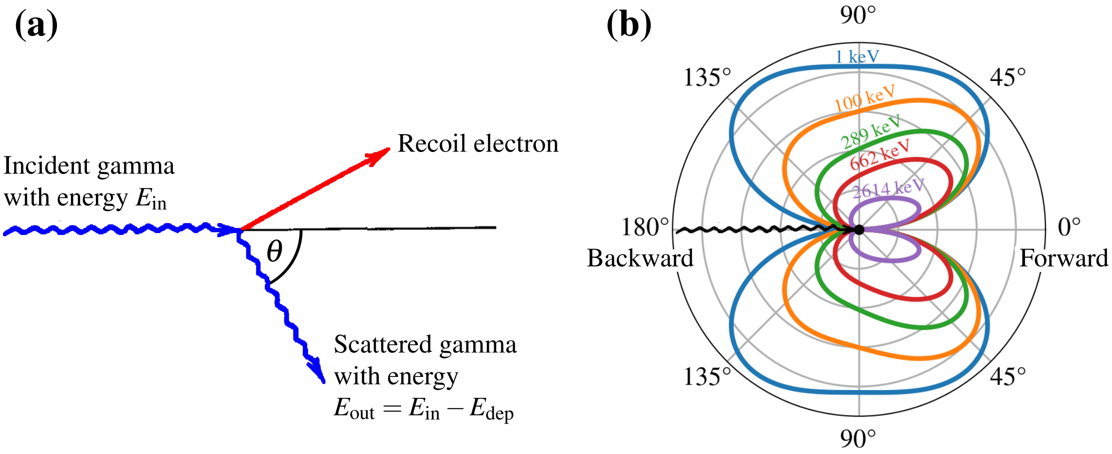

Figure 3.3: (a) Sketch of a gamma Compton scattering off an electron by the Compton angle, θ, adapted from [29, p. 51]. (b) θ-distribution of Compton scattered gammas as derived from $\mathrm{d}\sigma/\mathrm{d}\theta$ in Eq. (3.4) for different incident energies, E_{in}, for a gamma incident at $\theta = 180°$.

For E_{in} up to 1 keV, the most preferred θ values are 51.9° (forward-scattering) and 128.1° (backward-scattering), both with almost equal probability. With increasing E_{in}, the probability of backward-scattering rapidly decreases and forward-scattering is more likely. In general, the most preferred value for θ decreases with increasing E_{in}, e.g. to 38.4° for 289 keV, to 30.9° at 662 keV and to 18.7° for 2614 keV.

3.1.1.3 Pair production

The dominant interaction process for gammas with $E_{\text{in}} > 8\,\text{MeV}$ with germanium is pair production, i.e. the creation of an electron-positron pair. For this, the incident energy must exceed twice the rest mass of the electron, i.e. $E_{\text{in}} \geq 2m_ec^2 = 1022\,\text{keV}$. To conserve energy and momentum, pair production requires the exchange of a virtual photon with a nucleus in the target material which then experiences a small recoil. The positron subsequently annihilates with an electron in the material. If the positron was at rest, two back-to-back gammas with 511 keV energy each are emitted. If a 511 keV gamma interacts in germanium, it predominantly does so via Compton scattering.

3.1.2 Heavy charged particles

All charged particles but the electron count as heavy charged particles. A charged particle passing through a target material continuously loses energy through Coulomb interactions, predominantly through collisions with orbital electrons. While the charged particle continuously decelerates, electrons in the target material are either excited to higher-energy states within their atoms or the target atoms become ionized. Less than about 1/500 of the energy of the incident particle is transferred in a single collision [29, p. 30]. Typically, several hundreds of collisions are needed to noticeably decelerate or stop a particle.

The linear stopping power, $\langle -\mathrm{d}E/\mathrm{d}x \rangle$, acting on charged particles is defined as the average energy loss, $-\mathrm{d}E$, per unit path length, $\mathrm{d}x$. For heavy charged particles with charge ze, where e is the elementary charge, and velocity $\beta = v/c$, the linear stopping power through ionization (in units of MeV/cm) is described by the Bethe-Bloch formula [115]:

$$\left\langle -\frac{\mathrm{d}E}{\mathrm{d}x} \right\rangle = \frac{1}{2}\rho_A K z^2 \frac{Z}{A}\frac{1}{\beta^2}\left(\ln\frac{2m_ec^2\beta^2\gamma^2W_{\text{max}}}{I_{\text{exc}}^2} - 2\beta^2 - \delta(\beta\gamma)\right) , \qquad (3.5)$$

where ρ_A is the mass density of the target material, $K = 0.307\,\text{MeV}\,\text{cm}^2\,\text{g}^{-1}$, W_{max} is the maximum energy transfer in a single collision, I_{exc} is the mean excitation potential, $\gamma = 1/\sqrt{1-\beta^2}$ and δ is a density correction term [116]. This formula is a good approximation for all heavy charged particles with $0.1 < \beta\gamma < 1000$, which pass through intermediate-Z materials. Equation (3.5) provides an estimate of the penetration depth of heavy charged particles. For example, alpha particles with energies around 5 MeV penetrate around 20 µm into germanium before being stopped.

3.1.3 Electrons

For electrons, the Bethe-Bloch formula shown in Eq. (3.5) does not hold [115] because, in quantum mechanics, neither the incoming nor the electron off which it scatters can be identified with the outgoing electron. Energy transfers between electrons are described by the Møller cross-section [117], which gives the linear stopping power [115]:

$$\left\langle -\frac{\mathrm{d}E}{\mathrm{d}x} \right\rangle = \frac{1}{2}\rho_A K \frac{Z}{A}\frac{1}{\beta^2}\left(\ln\frac{m_e c^2 \beta^2 \gamma^2 (m_e c^2(\gamma-1)/2)}{I_{\mathrm{exc}}^2} + (1-\beta^2) - \right. \\ \left. \frac{2\gamma-1}{\gamma^2}\ln(2) + \frac{1}{8}\left(\frac{\gamma-1}{\gamma}\right)^2 - \delta(\beta\gamma) \right) . \tag{3.6}$$

3.1.4 Bremsstrahlung

All charged particles can get deflected by nuclei, resulting in the emission of radiation, so-called bremsstrahlung. This process is most relevant for electrons as it is suppressed by the mass of the charged particle. The emission of bremsstrahlung becomes the dominant energy-loss mechanism for electrons with energies above the so-called critical energy, which is 18.16 MeV in germanium [118].

The average bremsstrahlung energy is low, and it is reabsorbed in the vicinity of the original interaction site [29, p. 44]. However, bremsstrahlung cannot be neglected for events with electrons in the MeV range. In the absence of hard bremsstrahlung, electrons with energies of a few MeV are expected to deposit their energy within a millimeter. Once an electron is reduced to the critical energy $E < 18.16\,\mathrm{MeV}$, it predominantly loses its energy via ionization as described by Eq. (3.6).

3.1.5 Event topologies

In searches for $0\nu\beta\beta$ in ^{76}Ge, a peak in the combined energy spectrum of the two emitted electrons is expected at $Q_{\beta\beta} = 2039.061\,\mathrm{keV}$ [104], see Fig. 2.5. However, it is also possible that the energy deposited by any other particle falls into the ROI around $Q_{\beta\beta}$. Such events might be mistaken for signal events and become background.

The different interaction processes of gammas and of charged particles with germanium lead to differences in the event topologies, i.e. how the deposited energy is distributed. Information obtained on the event topology can be used to distinguish signal-like events from background-like events [110]. Events can, for example, be classified into single-site or multi-site events, reflecting whether the energy was deposited at a single site or at multiple well-separated sites in the detector.

In $0\nu\beta\beta$ and $2\nu\beta\beta$, the two electrons deposit 90% of their energy through ionization in a volume with a radius of approximately 1 mm around their origin [110], resulting in single-site events if no hard bremsstrahlung occurs. Background events with energies in the ROI around $Q_{\beta\beta}$ resulting from incident gammas with energies of a few MeV are most likely multi-site events. A selection of event topologies for gammas with energies of a few MeV is shown in Fig. 3.4.

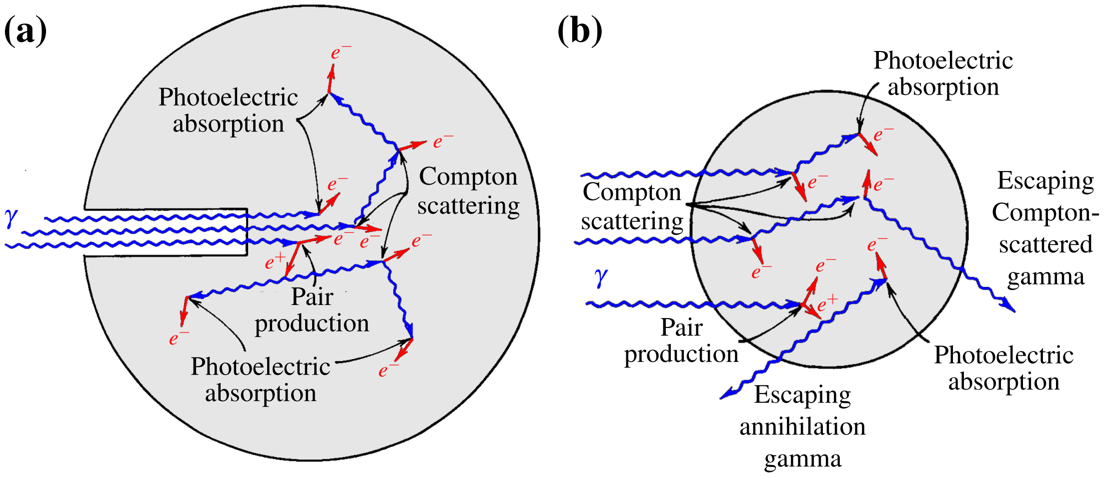

Figure 3.4: Possible gamma-event topologies in (a) an extremely large detector and (b) an intermediate-size detector, adapted from [29, p. 314–316]. Gammas, γ, are shown in blue, electrons, e^-, and positrons, e^+, in red. The possibility that MeV electrons and positrons can emit bremsstrahlung is not depicted here.

If the gamma is photoelectrically absorbed, its energy is fully transferred to a photoelectron which, in the absence of hard bremsstrahlung, results in a single-site event with $E_{\text{dep}} = E_{\text{in}}$, see Fig. 3.4a. These events could mimic $0\nu\beta\beta$ events if $E_{\text{in}} \approx Q_{\beta\beta}$ or if the photoelectron emits bremsstrahlung with an energy of $E_{\text{in}} - Q_{\beta\beta}$ that escapes from the detector. Note that the probability of photoelectric absorption strongly decreases with increasing energy. At $Q_{\beta\beta}$, Compton scattering is more than two orders of magnitude more likely than photoelectric absorption, see Fig. 3.1.

If the gamma Compton scatters once and escapes from the detector, the event is a single-site event with $E_{\text{dep}} < E_{\text{in}}$. If the scattered gamma does not escape immediately but additionally deposits all or part of its energy in the detector, the event is a multi-site event with $E_{\text{dep}} \leq E_{\text{in}}$. Both of these cases can lead to background events in the ROI around $Q_{\beta\beta}$ if $E_{\text{in}} \geq Q_{\beta\beta}$. However, the probability that a high-energy gamma deposits $E_{\text{dep}} \approx Q_{\beta\beta}$ via a single Compton scatter and creates a single-site event is extremely low due to the Klein-Nishina distribution, see Eq. (3.3). For example, the most probable Compton-scattering angle for a 2614.533 keV gamma emitted from ^{208}Tl decay [119] is $\theta = 18.7^\circ$, resulting in an energy deposit of only $E_{\text{dep}} = 556\,\text{keV}$. Only in 0.29% of the cases, E_{dep} falls within $Q_{\beta\beta} \pm 2.5\,\text{keV}$. In addition, the scattered gamma is highly likely to interact at least once more before possibly escaping the detector, resulting in a multi-site event.

If the gamma interacts via pair production, the electron and positron deposit their energy predominantly through ionization close to their point of creation. If both 511 keV gammas escape from the detector and no hard bremsstrahlung was emitted, this results in a single-site event with $E_{\text{dep}} = E_{\text{in}} - 2m_ec^2$. If the annihilation gammas interact with the detector, this results in a multi-site event with $E_{\text{dep}} \leq E_{\text{in}}$.

3.2 Germanium as solid-state detector material

3.2.1 Crystal structure, band structure and band gap

Germanium is a group-IV element with four valence electrons in hybrid sp^3 orbitals. Pure germanium crystallizes in the diamond structure, a face-centered cubic lattice structure with a two-atom base, see Fig. 3.5. The four valence electrons form covalent bonds with valence electrons from neighboring germanium atoms.

The high symmetry of this crystal structure results in a high symmetry of its energy potential, $V_e(\vec{r})$. Assuming a perfect, infinitely large crystal, $V_e(\vec{r})$ has a translation symmetry by any lattice vector, $\vec{L}$, i.e. $V_e(\vec{r}+\vec{L}) = V_e(\vec{r})$. In addition, it has a rotational symmetry along the main crystallographic axes.

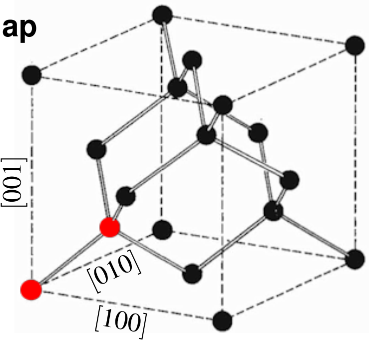

Figure 3.5: Diamond structure of the germanium crystal lattice. The two-atom base is shown in red. Axes are labeled with Miller indices [120, p. 9].

The dynamics of the electrons in the crystal can be described by solving Schrödinger's equation [121],

$$\left(-\frac{\hbar^2}{2m_e}\vec{\nabla}^2 + V_e(\vec{r})\right)\psi_e(\vec{r}) = E_e\psi_e(\vec{r}), \tag{3.7}$$

where $\hbar = h/2\pi$ is the reduced Planck constant, $\vec{\nabla}$ is the nabla operator, E_e is the total energy of the electron and $\psi_e(\vec{r})$ is the electron wave function. The probability of finding an electron at a position, $\vec{r}$, is given by $|\psi_e(\vec{r})|^2$.

For free electrons, i.e. $V_e(\vec{r}) = 0$, the solution of Eq. (3.7) for $\psi_e(\vec{r})$ are planar waves, i.e. $\psi_e(\vec{r}) = \psi_0 \exp(i\vec{k}\cdot\vec{r})$, and the corresponding electron energy is

$$E_e(\vec{k}) = \frac{\hbar^2 k^2}{2m_e}\,, \tag{3.8}$$

where $k = |\vec{k}|$ is the absolute value of the electron wave vector, $\vec{k}$, and ψ_0 is a normalization factor. In general, the relation between E_e and $\vec{k}$ is known as the de-Broglie dispersion relation. The wave vector can be associated with the classical momentum of the electron, $\vec{p}_e$, via $\vec{p}_e = \hbar\vec{k}$. The dispersion relation for free electrons in Eq. (3.8) takes the well-known form of the kinetic energy in classical mechanics, $E_e = p_e^2/2m_e$.

In the presence of a non-vanishing $V_e(\vec{r})$, solving Eq. (3.7) does not necessarily result in a planar wave solution for $\psi_e(\vec{r})$ and a parabolic dispersion relation.

For bound electrons in a perfect crystal, the periodicity of $V_e(\vec{r})$ results in a periodicity of $\psi_e(\vec{r})$. The electron wave function in such crystals can be described using Bloch functions, $\psi_e(\vec{r}) = u(\vec{r})\exp(i\vec{k}\cdot\vec{r})$, which are periodically modulated planar waves [122]. The modulation function, $u(\vec{r})$, accounts for the crystal symmetry, e.g. $u(\vec{r}+\vec{L}) = u(\vec{r})$. As a consequence, $\psi_e(\vec{r})$ and, thus, $E_e(\vec{k})$ are periodic* in $\vec{k}$, i.e. $E_e(\vec{k}) = E_e(\vec{k}+\vec{G})$, with $\vec{G}\cdot\vec{L}$ being an integer multiple of 2π.

---

* $\psi_e(\vec{r}) = \psi_e(\vec{r}+\vec{L}) = u(\vec{r}+\vec{L})\exp(i\vec{k}\cdot(\vec{r}+\vec{L})) = u(\vec{r})\exp(i\vec{k}\cdot\vec{r})\exp(i\vec{k}\cdot\vec{L}) = \psi_e(\vec{r})\exp(i\vec{k}\cdot\vec{L})$

The periodic dispersion relation in crystals is often referred to as the band structure. The calculation of the band structure can be restricted to the primitive unit cell of the reciprocal lattice, i.e. the first Brillouin zone [123]. It is defined as the set of $\vec{k}$-vectors that is closer to $\vec{0}$ than to any non-zero $\vec{G}$. In Fig. 3.6a, the first Brillouin zone of a face-centered cubic lattice, the coordinate system and points and directions of high symmetry, expressed through Miller indices, are shown.

The band structure of germanium can theoretically be derived from pseudopotentials [124] and is shown in Fig. 3.6b. In contrast to free electrons, a single $\vec{k}$ state can have multiple energy values assigned. In addition, the band structure shows a range of energies without corresponding states, the so-called band gap. The size of the band gap, E_g, in germanium is 0.746 eV at 0 K and 0.665 eV at 300 K [29, p. 357].

The states below and above the band gap are referred to as valence and conduction band, respectively. Electrons in the valence band are bound to the atoms and do not contribute to an electric current. In contrast, electrons in the conduction band are not bound and can contribute to an electric current. In the absence of any excitation, all states in the valence band and none of the states in the conduction band are occupied. The excitation of electrons from the valence to the conduction band creates vacancies in the valence band, so-called holes. Holes act as positive charge carriers with energies $E_h = -E_e$ and also contribute to the conductivity. Thus, the overall conductivity is determined by the sum of electrons in the conduction band and holes in the valence band.

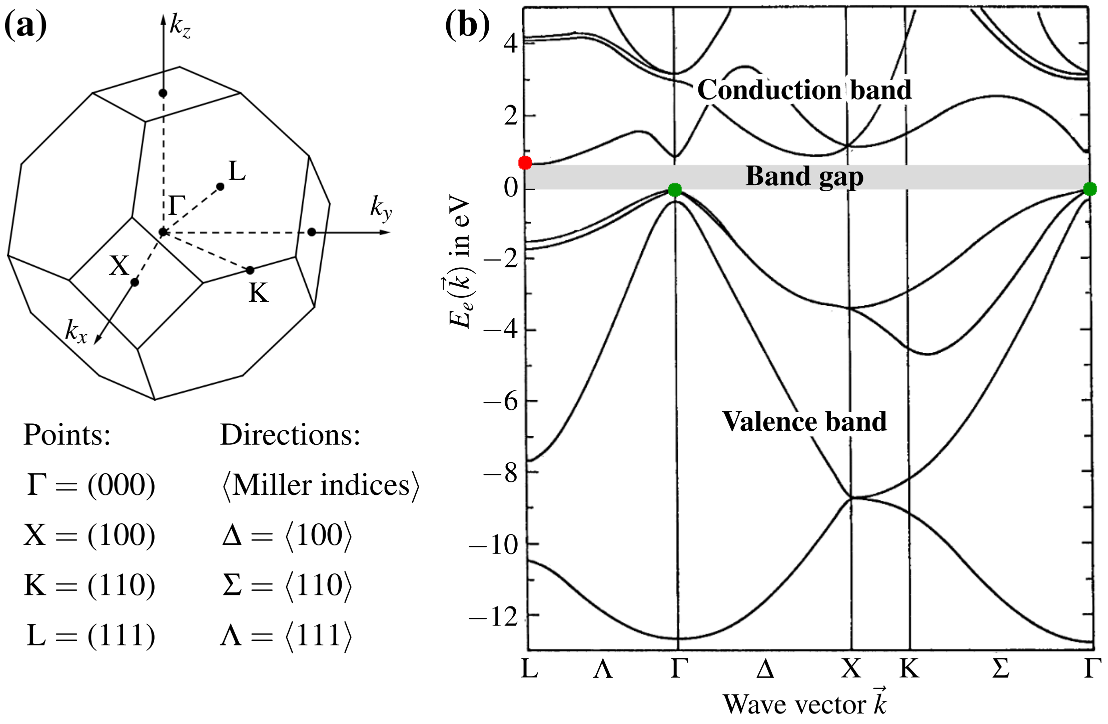

Figure 3.6: (a) First Brillouin zone of a face-centered cubic crystal with high symmetry points, Γ, X, K, L, and their Miller indices, taken from [123]. (b) Theoretically derived band structure of germanium along the directions of high symmetry, adapted from [124]. The minimum of the conduction band is shown as a red point, the maximum of the conduction band as a green point.

In germanium, the maximum of the valence band is located at the Γ-point at $\vec{k} = 0$, whereas the minimum of the conduction band is found at the L-points at $\vec{k} \neq 0$. There are eight L-points laying exactly at the boundary of the first Brillouin zone, resulting in a four-fold space degeneracy of the minima of the conduction band [125]. Near the maximum of the valence band and the minimum of the conduction band, the band structure is nearly parabolic as expected for free electrons. However, the curvatures of the parabolas differ from the expectation for m_e in Eq. (3.8). Thus, electrons and holes populating these states can be described as free particles with effective masses, m_e^* and m_h^*, given by the curvatures of the band structure at the L- and Γ-point:

$$m_e^* = \hbar^2 \left(\left. \frac{\mathrm{d}^2 E_e}{\mathrm{d}k^2} \right|_{\mathrm{L}} \right)^{-1} \qquad \text{and} \qquad m_h^* = \hbar^2 \left(\left. \frac{\mathrm{d}^2 E_h}{\mathrm{d}k^2} \right|_{\Gamma} \right)^{-1} . \tag{3.9}$$

The effective masses also depend on the direction of the propagation of the charge carriers. Along the $\langle 111 \rangle$-direction, the curvature around the minimum of the conduction band at the L-point is smaller than perpendicular to $\langle 111 \rangle$. This results in different effective electron masses at the L-point, along and perpendicular to the $\langle 111 \rangle$-direction of $m_{e,L}^* = (1.64 \pm 0.03) m_e$ and $m_{e,T}^* = (0.0819 \pm 0.0003) m_e$, respectively [126]. The valence band maximum is reached by two bands with different curvatures, see Fig. 3.6b, giving rise to light and heavy holes with $m_{lh}^* = 0.044\, m_e$ and $m_{hh}^* = 0.28\, m_e$ [127].

3.2.2 Crystal defects, impurities and doping

In reality, germanium crystals are not perfect but have crystal defects and impurities. Crystal defects can be missing or additional atoms, as well as line and surface defects. These lead to deviations in the crystal periodicity and, hence, from the ideal band structure shown in Fig. 3.6b. Impurities are atoms of other elements that replace or occupy space between the germanium atoms in the crystal lattice. They are called electrically active if they influence the electric properties of the germanium crystal. The intentional introduction of impurities into a germanium crystal, so-called doping, creates additional states in the band gap that can lead to an excess of holes in the valence band (p-type doping) or of electrons in the conduction band (n-type doping).

In p-type germanium, germanium atoms are replaced by atoms with fewer valence electrons, so-called acceptors, which are usually group-III elements. The absence of valence electrons leads to unsaturated covalent bonds that create empty states in the band gap with energies very close to the valence band maximum. By thermal excitation of electrons from the valence band, these acceptor atoms become negatively ionized and holes are created in the valence band.

In n-type germanium, germanium atoms are replaced by atoms with more valence electrons, so-called donors, which are usually group-V elements. Here, the additional electrons populate energy states in the band gap very close to the conduction band. Thermal excitation of these electrons leads to the positive ionization of the donor atoms and an increase of electrons in the conduction band.

A doped germanium crystal is more conductive if the impurities are ionized through thermal excitation but still remains electrically neutral as a whole.

3.2.3 Electric potential, electric field and depletion

When p-type and n-type materials are connected, a so-called p-n-junction is created, see Fig. 3.7. As the hole concentration is much higher in the p-type region, the holes diffuse towards the n-type region and recombine with electrons there, leaving negatively charged impurities behind. Likewise, electrons diffusing from the n-type to the p-type region leave positively charged impurities behind. These ionized impurities create an electric field, $\vec{\mathcal{E}}(\vec{r})$, which counteracts the diffusion. According to Gauss's law,

$$\vec{\nabla}(\varepsilon_r(\vec{r})\,\vec{\mathcal{E}}(\vec{r})) = \frac{\rho(\vec{r})}{\varepsilon_0} \tag{3.10}$$

$$\vec{\nabla}(\varepsilon_r(\vec{r})\vec{\nabla}\phi(\vec{r})) = -\frac{\rho(\vec{r})}{\varepsilon_0} \tag{3.11}$$

where $\rho(\vec{r})$ is the space charge density, $\phi(\vec{r})$ is the electric potential, $\vec{\mathcal{E}}(\vec{r}) = -\vec{\nabla}\phi(\vec{r})$, $\varepsilon_0 = 8.854 \cdot 10^{-12}\,\mathrm{F/m}$ is the vacuum permittivity and $\varepsilon_r(\vec{r})$ is the relative permittivity. In pure germanium, $\varepsilon_r(\vec{r}) = 16$ [29, p. 357].

The electric field causes the drift of the electrons and holes which counteract their diffusion. The electric field strength increases until the diffusion currents and the drift currents reach an equilibrium. When the equilibrium is reached, a layer with almost no free charge carriers has formed at the p-n-junction, the so-called depletion layer, see Fig. 3.7. Due to charge conservation, the charges in the p-type and in the n-type regions have the same magnitude. If the impurity concentration in the p-type material is higher than that in the n-type material, the depletion layer extends deeper into the n-type region, see Fig. 3.7. The electric potential difference between both ends of the depletion layer is called the contact potential, $V_C \approx E_g/e$, where e is the elementary charge.

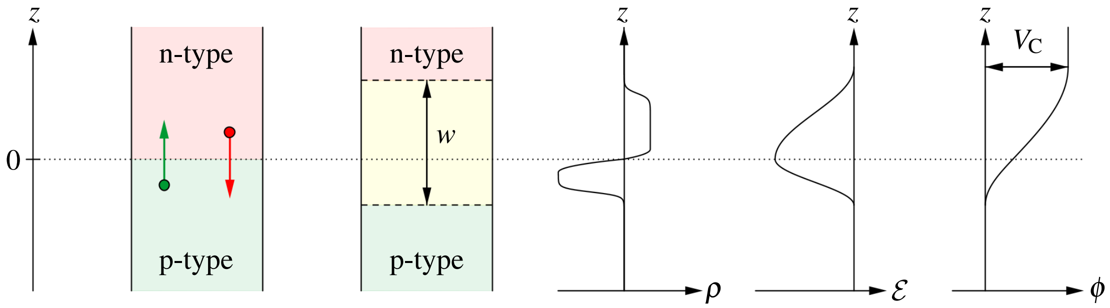

Figure 3.7: Schematic of a p-n-junction along the spatial coordinate z, with a depletion layer of width w and the corresponding density of fixed space charges ρ, electric field strength $\mathcal{E}$ and electric potential ϕ, taken from [128]. The contact potential is denoted as V_C. Electrons are shown in red, holes in green and the depleted volume in yellow.

3.3 Working principle of germanium detectors

3.3.1 Charge carrier statistics

In all of the interactions described in section 3.1, the energy deposited in the germanium crystal leads to the creation of electron-hole pairs. The average energy required to produce one electron-hole pair at 77 K of $E_{eh} = 2.95\,\mathrm{eV}$ [129] is larger than E_g because most of the energy is absorbed by the crystal through the creation of phonons.

The number of electron-hole pairs, N_{eh}, created from an energy deposit, E_dep, is subject to statistical fluctuations. The mean value, $\langle N_{eh}\rangle$, and the standard deviation, σ_{eh}, of the number of electron-hole pairs are

$$\langle N_{eh}\rangle = \frac{E_\mathrm{dep}}{E_{eh}} \qquad \sigma_{eh} = \sqrt{\frac{F E_\mathrm{dep}}{E_{eh}}}\,. \tag{3.12}$$

The Fano factor, F, accounts for the observation that due to the influence of the crystal the electron-hole creation is not a purely statistical process and that the variance is reduced compared to what would be expected for Poisson statistics. The small Fano factor of $F = 0.129 \pm 0.003$ in germanium [130] results in small statistical fluctuations and an excellent energy resolution.

3.3.2 Charge separation and active volume

If the electron-hole pairs recombine, the energy deposit and, hence, the particle interaction cannot be detected. In order to detect and reconstruct deposited energy, the electrons and holes need to be quickly separated and subsequently collected.

In principle, the depletion layer of an unbiased p-n-junction can be operated as a detector. The electric field in the depletion layer allows for the separation of the electrons and holes towards the n-type and p-type region, respectively, where they can then be collected. However, this would not be very suitable for efficient detection because the depletion layer, which is the active volume of the detector, would be small.

To increase the width of the depleted volume and the electric field strength, the p-n-junction is operated in reverse-bias mode by applying a positive potential to the n-type region or a negative potential to the p-type region. When the bias voltage is increased, the electric field in the depleted volume is first weakened. The charge carriers resume diffusing, increasing the width of the depleted volume until reaching equilibrium.

The operation in reversed-bias mode requires electric contacts with well-defined potentials on the surface of the detector. A germanium detector is fabricated using an n-type or p-type germanium crystal that forms the so-called bulk. The contacts are typically created by heavily doping the surface to form n^+-type and p^+-type layers with impurity concentrations orders of magnitude higher than the concentration in the bulk.

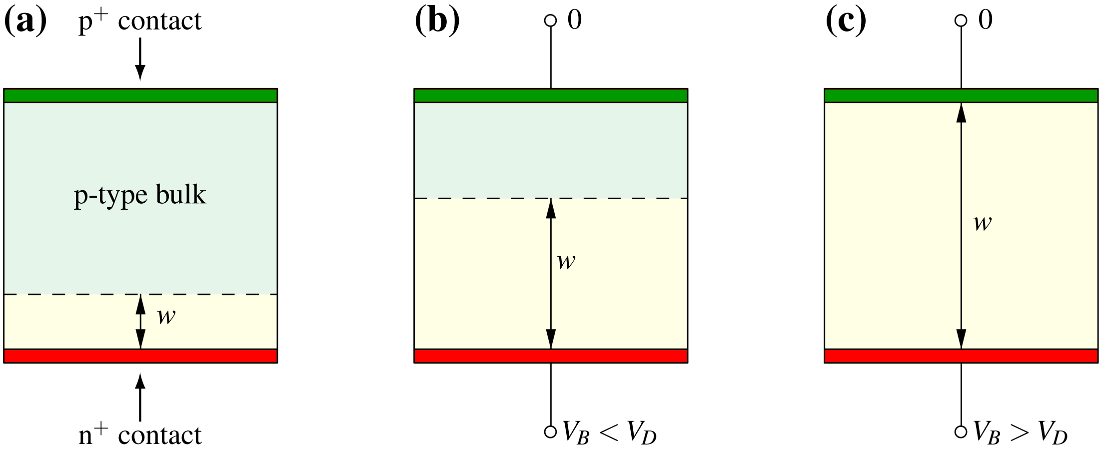

Figure 3.8: p-type detector with p$^+$ and n$^+$ contacts in planar geometry (a) unbiased, (b) with a positive potential V_B below and (c) above the full-depletion voltage V_D applied to the n$^+$ contact, adapted from [128]. The depleted volume is shown in yellow, the undepleted p-type bulk is shown in light green, and the p$^+$ and n$^+$ contacts are shown in green and red, respectively.

By heavily doping the surface, the depleted volume extends almost exclusively into the bulk of the detector when a reversed-bias voltage is applied, see Fig. 3.8. For a planar detector, the depletion width, w, is given by [29, p. 375]

$$w \approx \sqrt{\frac{2\varepsilon_0\varepsilon_r V_B}{eN_I}}\ , \tag{3.13}$$

where V_B is the bias voltage and N_I is the density of ionized impurities in the bulk. The derivation of Eq. (3.13) and the formula for a cylindrical geometry can be found in Appendix A on page 185. In high-purity germanium, N_I is typically as low as $10^{10}\,\mathrm{cm}^{-3}$, resulting in active volumes with dimensions of up to 10 cm.

In reversed-bias mode, $\phi(\vec{r})$ is defined by the space charge density from the ionized impurities $\rho(\vec{r})$ and the bias voltages, $V_{B,i}$, applied to the contacts, S_i:

$$\vec{\nabla}(\varepsilon_r(\vec{r})\vec{\nabla}\phi(\vec{r})) = -\frac{\rho(\vec{r})}{\varepsilon_0} \qquad \phi(\vec{r})|_{S_i} = V_{B,i}\ . \tag{3.14}$$

Here, $\phi(\vec{r})$ can be written as a sum of two components, i.e. $\phi(\vec{r}) = \phi_V(\vec{r}) + \phi_\rho(\vec{r})$ with

$$\vec{\nabla}(\varepsilon_r(\vec{r})\vec{\nabla}\phi_V(\vec{r})) = 0 \qquad \phi_V(\vec{r})|_{S_i} = V_{B,i} \tag{3.15}$$

$$\vec{\nabla}(\varepsilon_r(\vec{r})\vec{\nabla}\phi_\rho(\vec{r})) = -\frac{\rho(\vec{r})}{\varepsilon_0} \qquad \phi_\rho(\vec{r})|_{S_i} = 0\ , \tag{3.16}$$

where $\phi_V(\vec{r})$ satisfies the boundary conditions due to the applied $V_{B,i}$ to the contacts S_i and $\phi_\rho(\vec{r})$ accounts for the charge density from the ionized impurities. The electric field follows from

$$\vec{\mathcal{E}}(\vec{r}) = -\vec{\nabla}\phi(\vec{r})\ . \tag{3.17}$$

In the depleted volume, $\vec{\mathcal{E}}$ leads to the separation and to the collection of electrons and holes on the detector contacts. If $\vec{\mathcal{E}}$ is small or zero, the electron-hole pairs get trapped or do not move at all, leading to incomplete charge collection. It is, thus, desirable to operate germanium detectors such that volumes with low or vanishing $\vec{\mathcal{E}}$ are avoided.

The voltage at which the bulk of the detector is fully depleted is called the full-depletion voltage, V_D. Operating a germanium detector at $V > V_D$ maximizes the active volume and ensures fast and full charge collection, resulting in good detection efficiency.

For $V < V_D$, a part of the detector volume remains undepleted. In the undepleted volume, the electric field vanishes. If energy is deposited there, the electron-hole pairs recombine and the energy deposit cannot be registered. The size and the geometry of the undepleted volume are determined by the density of ionized impurities in the depleted volume and the bias voltage, see Eq. (3.13). Note that the density of non-ionized impurities in the undepleted volume does not influence the size and geometry of the active volume. Thus, measuring the evolution of the active volume of an undepleted detector provides an estimate for the density of its electrically active impurities.

3.4 Signal generation in germanium detectors

3.4.1 Schockley-Ramo theorem

The electrons and holes create an additional electric potential in the detector. As the electric contacts are conductive and kept at fixed potentials, this is balanced out by the induced mirror charges on the surface of the contacts. The output signal of a germanium detector is given by the induced charges on the contacts which should not be mistaken for the charges drifting through the bulk of the detector.

Electrons induce negative charges while holes induce positive charges on the contacts. When the electron-hole pairs are created, the contributions from the electrons and holes cancel and no net charge is induced on any of the contacts. As the charge carriers subsequently move, the contributions do not cancel anymore, resulting in observable net induced charges on the contacts.

The charges induced on the contacts can be calculated using the Schockley-Ramo theorem [131, 132] which is based on the concept of weighting potentials. The weighting potential, $\mathcal{W}_i(\vec{r})$, describes how much charge is induced on the contact, S_i, by a unit charge located at a position, $\vec{r}$, where $i \in \{1,\dots,N\}$ and N is the number of contacts.

If a charge has reached a contact S_j, it will see the full charge, i.e. $\mathcal{W}_j(\vec{r})|_{S_j} = 1$. At that time, no charge is induced on all contacts S_k with $k \neq j$, i.e. $\mathcal{W}_k(\vec{r})|_{S_j} = 0$.

A formula for $\mathcal{W}_j(\vec{r})$ can be derived from Eq. (3.11), effectively setting $\rho(\vec{r}) = 0$ and the boundary conditions to be one on S_j and zero on all other contacts [133], i.e.

$$\vec{\nabla}(\varepsilon_r(\vec{r})\vec{\nabla}\mathcal{W}_j(\vec{r})) = 0 \qquad \mathcal{W}_j(\vec{r})|_{S_k} = \delta_{jk} = \begin{cases} 1, & \text{if } j = k \\ 0, & \text{if } j \neq k \end{cases} \quad . \tag{3.18}$$

Note that all $\mathcal{W}_i(\vec{r})$ are only defined by the contact geometry of the detector and are independent of any space charges. The net induced charges on S_i, Q_i, are given by evaluating $\mathcal{W}_i(\vec{r})$ at the positions $\vec{r}_p$ of all point-like particles, p, that carry a charge q_p:

$$Q_i = \sum_p q_p \mathcal{W}_i(\vec{r}_p) \ . \tag{3.19}$$

The sum in Eq. (3.19) can be split into the contributions from the electrons and holes. As the positions of the electrons and holes, $\vec{r}_e(t)$ and $\vec{r}_h(t)$, evolve with time, t, during their drift through the detector volume, the net induced charge also evolves with time:

$$Q_i(t) = -e \sum_{\text{electrons}} \mathcal{W}_i(\vec{r}_e(t)) + e \sum_{\text{holes}} \mathcal{W}_i(\vec{r}_h(t)) \ . \tag{3.20}$$

The time evolution of the net induced charge, $Q_i(t)$, is called charge pulse. The length of a pulse is given by the time from the creation of electron-hole pairs until the full collection of all charge carriers. The shape of a pulse depends on the drift paths of the charge carriers and the geometry of $\mathcal{W}_i(\vec{r})$, which is defined by the detector geometry. Note that while the fixed space charges resulting from ionized impurities do not influence $\mathcal{W}_i(\vec{r})$, they can significantly influence the electric field and, thus, the drift of the charges and impact the shape and lengths of the charge pulses.

3.4.2 Segmentation

The simplest detector contact geometry comprises a p-type crystal equipped with one n$^+$-type contact collecting the electrons and one p$^+$-type contact collecting the holes.

In more complex contact geometries, the surfaces are segmented into smaller contacts which are read out individually. If there are multiple n$^+$ contacts, the electrons will, depending on the locations of the energy deposits, be collected in one or more segments. The segments which collect electrons provide charge pulses ending at a non-zero height, reflecting the energy deposited in this segment. In contrast, non-collecting segments will show pulses that return back to their initial value after the charge drift has ended, so-called mirror pulses. If the p$^+$ contact remains unsegmented, it will collect all holes and its final pulse height will be proportional to N_{eh} and, thus, to the total energy deposited in the detector, see Eq. (3.12).

Segmented detectors increase the number of independent charge pulses per event. Analyzing pulse shapes from segmented detectors allows for the extraction of more information on the topology of a given event than analyzing only the pulse shapes from the central p$^+$ contact.

3.4.3 Capacitances

There are capacitances between all contacts of the detector. As a consequence, a change of potential, $\mathrm{d}V_k$, applied to a contact S_k results in a change in charge, $\mathrm{d}Q_j$, on another contact S_j. The capacitance between S_j and S_k, c_{jk}, is

$$c_{jk} = \frac{\mathrm{d}Q_j}{\mathrm{d}V_k} \ . \tag{3.21}$$

The capacitance c_{jk} can be calculated from the overlap of the gradients of the weighting potentials $\mathcal{W}_j(\vec{r})$ and $\mathcal{W}_k(\vec{r})$, integrated over the closed system volume, V_W [134]:

$$c_{jk} = \varepsilon_0 \iiint\limits_{V_\mathrm{W}} d^3r \, \vec{\nabla}\mathcal{W}_j(\vec{r}) \cdot \varepsilon_r(\vec{r}) \cdot \vec{\nabla}\mathcal{W}_k(\vec{r}) \ . \tag{3.22}$$

For $j \neq k$, the values for c_{jk} are negative.

The capacitances depend on the level of depletion of the detector. For a fully-depleted detector, c_{jk} is solely given by the geometry of the surface contacts S_j and S_k and does not depend on how much larger than V_D the applied bias voltage V_B is. If V_B is below V_D, the presence of undepleted volumes leads to additional conductive volumes in the bulk of the detector. Contacts connected to the undepleted volumes effectively extend further into the bulk. This reduces the distance between the contacts, resulting in steeper $\vec{\nabla}\mathcal{W}_j(\vec{r})$ and $\vec{\nabla}\mathcal{W}_k(\vec{r})$ and, thus, higher absolute values for c_{jk}.

As the extent of the depleted volume is given by the impurity density, see section 3.3.2, measuring the detector capacitance as a function of V_B below full depletion provides valuable insight into the impurity density distribution in the bulk of the detector.

3.4.4 Cross-talk

The capacitances between contacts result in intrinsic cross-talk, i.e. the induction of a signal in one contact from another contact. In addition, capacitances between the read-out cables result in electronic cross-talk. Thus, the measured charge pulses are not completely independent from each other. For segmented detectors, cross-talk has been observed [135] to have (at least) a linear and a differential component and to significantly influence the observed pulse shapes.

Linear cross-talk describes the fact that a pulse shape observed for a given segment consists to a small fraction of a linear combination of the pulse shapes from the other contacts. As one consequence, mirror pulses that would normally return to their baseline after the charge collection will show a shift of the baseline after the pulse from contributions of collecting segments.

Differential cross-talk describes an additional form of cross-talk where a fraction of the derivative of a pulse shape is seen by neighboring contacts. Differential cross-talk is significant when the pulses from the involved contacts rise with different speeds [136] and does not affect the final pulse height.

3.4.5 Energy resolution

One of the main advantages of using germanium detectors is their excellent energy resolution. The energy resolution defines how well the detector can reconstruct the energy of an event. The three terms that dominate the energy resolution are statistical fluctuations in the number of created electron-hole pairs, incomplete charge collection and electronic noise [29, p. 416]. The terms are independent and added in quadrature.

Statistical fluctuations in the number of created electron-hole pairs are small but cannot be avoided and depend on the deposited energy, see Eq. (3.12). Incomplete charge collection can be mitigated by avoiding germanium detector operation with too low average electric fields to prevent the recombination of electrons and holes before being collected. In general, the energy resolution is better for higher V_B. If the detector is operated below the full-depletion voltage, its energy resolution usually degrades.

Electronic noise can be reduced by operating detectors with capacitances of a few pF or below with low-noise readout electronics. However, this term usually dominates.

3.5 High-purity germanium detector fabrication

In order to fabricate large-volume germanium detectors, high-purity germanium with impurity densities of the order of $10^{10}\,\mathrm{cm}^{-3}$ or below is needed. However, the impurity concentration in raw germanium is typically of the order of $10^{13-14}\,\mathrm{cm}^{-3}$ [137]. In this section, the steps needed to purify raw germanium to detector-grade germanium and to fabricate high-purity germanium detectors are described.

3.5.1 Germanium purification: Zone refinement

A widely used process to purify germanium is zone refinement [138]. It is based on locally melting a part of a germanium metal rod, creating solid-liquid interfaces which cause unwanted impurities to segregate, i.e. to accumulate in the liquid phase, and to move the impurities to one end of the rod.

The segregation behavior of impurities in germanium is quantified by their segregation coefficients, k_S, which describe the ratio between the impurity concentrations in the solid phase and in the liquid phase of germanium in equilibrium [140]. In germanium, most acceptors (aluminum, gallium, indium) and donators (phosphorus, arsenic, antimony) have segregation coefficients $k_S \lesssim 0.1$ [140], which means that they preferably accumulate in molten germanium. In contrast, boron has $k_S > 5$ [141] and, thus, a strong preference for accumulating in crystalline germanium.

The zone refinement method is depicted in Fig. 3.9. The raw germanium rod is first placed into a container. Then, one or more circular heaters locally melt the germanium and are moved along the rod. Impurities with $k_S < 1$ accumulate in the molten zone. In contrast, boron segregates quickly out of the molten zone into the recrystallized zone. By moving the heater toward one end of the rod, the molten zone and the accumulated impurities with $k_S < 1$ are guided toward one side of the rod.

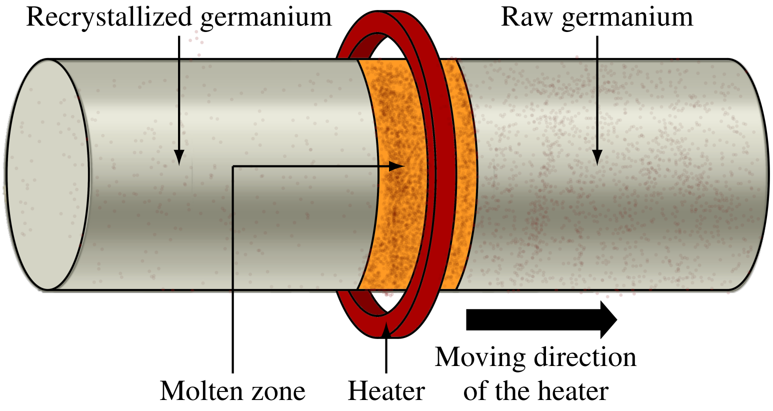

Figure 3.9: Schematic of the zone refinement method, adapted from [139].

After several repetitions of this process, boron has slightly accumulated in one end of the rod, whereas all other impurities with $k_S < 1$ are mostly concentrated in the other part of the rod [142]. If the center part reaches the desired purity, the outer parts are cut off and the center part is used to produce high-purity germanium crystals.

3.5.2 Crystal growth: Czochralski method

High-purity germanium detectors are based on single crystals. Large-volume single crystals are usually grown using the Czochralski method [143], see Fig. 3.10. The purified germanium is first molten. Then, a small seed crystal is inserted at the center of the molten bath. The crystal is grown by slowly rotating and pulling the seed crystal out. Crystal growth parameters like temperature gradients, pulling rates and rotation speeds, as well as tempering procedures have to be controlled and optimized in order to grow large-volume single crystals with reasonably small differences in impurities and the required density of long-range defects.

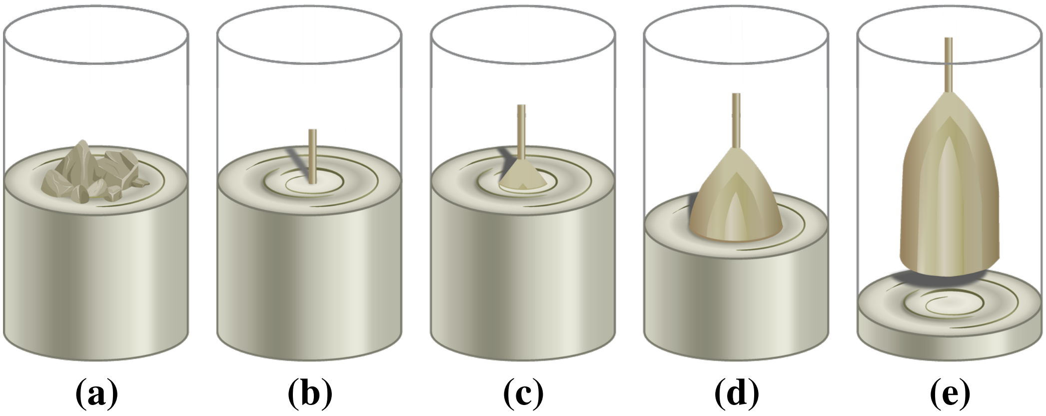

Figure 3.10: Schematic of the steps of growing a germanium single-crystal using the Czochralski method, taken from [144]: (a) melting purified germanium material, (b) introducing a seed crystal, (c) starting the crystal growth by slowly rotating the seed crystal, (d) pulling the crystal out of the melt and (e) tempering it.

The electrical properties of the crystal can be manipulated by doping the germanium melt. Depending on the concentration of electrically active impurities in the melt and the temperature gradients, p-type or n-type germanium crystals can be grown.

The impurity density distribution is in general not completely uniform throughout the crystal. Boron is expected to accumulate at the top whereas all other impurities with $k_S < 1$ are expected to concentrate at the lower end of the crystal, resulting in an impurity gradient between the top and the bottom of the crystal. In addition, the crystal-melt interface surface is not perfectly flat. When viewed from the melt, it is concave at the beginning and slightly convex at the end of the growing process [145]. As a consequence, impurities are more likely to concentrate in the center of the crystal. Depending on the strength of the offset, this results in a radially decreasing impurity density.

One special impurity that might unintentionally appear in germanium is copper [146]. Copper has a very low $k_S < 10^{-5}$ and a high diffusion coefficient at low temperatures. As k_S is very small, copper contaminations during the crystal growth are expected to originate from the gas phase. It has also been seen that the copper distribution strongly depends on the time-dependent temperature at which the crystal was grown [146]. Copper contaminations also result in radial impurity gradients, so-called coring.

3.5.3 Contact fabrication and passivation

To fabricate a high-purity germanium detector, a detector-grade slice is cut out from a large-volume single crystal. Depending on the desired detector properties, the geometry is further optimized, e.g. by drilling boreholes or grooves or by tapering or rounding sharp edges. Then, contacts are added onto the crystal surface.

Holes are collected on p^+ contacts which are normally created using boron implantation [147]. The resulting contacts have thicknesses of a few hundred nm. These contacts can easily be segmented using lithography.

Electrons are collected on n^+ contacts which are usually made by lithium diffusion [148] with thicknesses of around 1 mm. To create segmented lithium-drifted contacts, the segments need to be spaced at least 1 mm apart or mechanically separated by cutting grooves between the segments. In addition, the diffusion temperatures needed for fabricating lithium-diffused contacts of 160°C or above will add copper contaminations to the germanium crystal [149]. Recent studies have explored the possibilities to replace lithium-diffused n^+ contacts with thin-layer contacts made from amorphous germanium [150] or pulsed-laser diffused antimony [151].

Surfaces without a contact can be covered by passivation layers made from silicon monoxide, silicon dioxide, germanium oxide or amorphous germanium, with thicknesses of the order of 10 nm to 2 µm. The passivation protects the crystal from pollution and corrosion. It has to have a high and homogeneous surface resistivity to prevent high surface currents and localized charge-ups. Passivated surfaces can influence the electric field and the charge-carrier drift in germanium and have a significant impact on the pulse shapes for energy deposits close to the surface.

4 Charge-carrier drift in germanium

Electrons and holes drift whenever an electric field $\vec{\mathcal{E}}$ is present. The electron- and hole-drift velocities, $\vec{v}_e$ and $\vec{v}_h$, are given by the electron and hole mobilities, μ_e and μ_h:

$$\vec{v}_e = \mu_e \vec{\mathcal{E}} \qquad\qquad \vec{v}_h = \mu_h \vec{\mathcal{E}} \ . \tag{4.1}$$

In addition to the physics introduced in chapter 3, a model that accurately describes μ_e and μ_h in germanium is needed to simulate events in germanium detectors. In this chapter, the models used to describe charge-carrier drift in germanium are summarized.

4.1 Time-of-flight measurements

Originally, values for $\vec{v}_e$ and $\vec{v}_h$ were obtained from time-of-flight measurements [152] conducted in planar single-crystal samples with thicknesses of several hundred µm. Electron-hole pairs were created very close to one of the surfaces of the sample. Depending on which side of the crystal was irradiated, either the electrons or the holes drifted through the bulk of the sample and reached the other side of the sample after the so-called transit time. The electric field strength, $\mathcal{E} = |\vec{\mathcal{E}}|$, was modified by applying different reverse-bias voltages V_B. For each $\mathcal{E}$, the drift velocity was determined by dividing the thickness of the sample by the transit time.

In the analyses of the time-of-flight measurements, a constant electric field of $\mathcal{E} = V_B/d$ was assumed, where d is the thickness of the sample. This assumption neglects the linear gradient in the electric field resulting from ionized impurities, resulting in deviations of up to $\Delta\mathcal{E} = eN_I d/2\varepsilon_0\varepsilon_r$ from the assumed electric field. Typical values of $N_I \approx 10^{10}\,\mathrm{cm}^{-3}$ and $d = 500\,\mu\mathrm{m}$ [152] result in $\Delta\mathcal{E} = 28.3\,\mathrm{V/cm}$.

4.2 Longitudinal anisotropy

The time-of-flight measurements revealed a strong dependence of μ_e and μ_h on $\vec{\mathcal{E}}$ [153]. For electric fields parallel to one of the three main crystal axes, $\langle 100\rangle$, $\langle 110\rangle$ and $\langle 111\rangle$, $\vec{v}_e$ and $\vec{v}_h$ are parallel to the electric field, i.e. the drift is longitudinal. The longitudinal drift velocities, $v_{L,e}$ and $v_{L,h}$, are different along the different axes. This is also known as longitudinal anisotropy. The longitudinal anisotropy causes drifts that are not parallel to the electric field lines between the crystal axes. This is known as transverse anisotropy.

For all axes, $v_{L,e/h}$ increase linearly with $\mathcal{E}$ before approaching saturation drift velocities for $\mathcal{E} \gtrsim 1000\,\mathrm{V/cm}$. A first parameterization for the saturation behavior of $v_{L,e/h}$ was proposed in 1971 by D.M. Caughey and R.E. Thomas for silicon [154] and later expanded by adding a negative term by L. Mihailescu *et al.* [155]:

$$v_{L,e/h}(\mathcal{E}) = \frac{\mu_0 \mathcal{E}}{(1 + (\mathcal{E}/\mathcal{E}_0)^{\beta})^{1/\beta}} - \mu_n \mathcal{E} \ . \tag{4.2}$$

The parameters μ_0, $\beta > 0$, $\mathcal{E}_0$ and $\mu_n \ll \mu_0$ are different for electrons and holes and for the different crystal axes. They are also known to be temperature-dependent [156].

Table 4.1: Literature values for the drift velocity parameters in Eq. (4.2) for electrons and holes along the $\langle 100\rangle$ and $\langle 111\rangle$ axes in germanium at $T_0 = 78\,\mathrm{K}$ [135].

Charge carrier	Axis	μ_0 in $\frac{\mathrm{cm}^2}{\mathrm{Vs}}$	$\mathcal{E}_0$ in $\frac{\mathrm{V}}{\mathrm{cm}}$	β	μ_n in $\frac{\mathrm{cm}^2}{\mathrm{Vs}}$
Electrons	$\langle 100\rangle$	38609	511	0.805	-171
	$\langle 111\rangle$	38536	538	0.641	510
Holes	$\langle 100\rangle$	61824	185	0.942	
	$\langle 111\rangle$	61215	182	0.662	

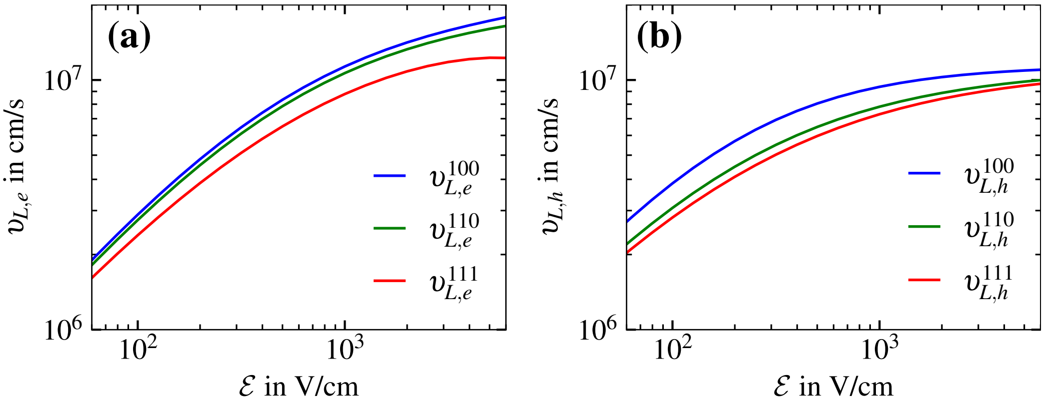

Figure 4.1: Longitudinal (a) electron- and (b) hole-drift velocity as a function of $\mathcal{E}$ along the $\langle 100\rangle$, $\langle 110\rangle$ and $\langle 111\rangle$ axes at $T_0 = 78\,\mathrm{K}$. $v_{L,e/h}^{100}$ and $v_{L,e/h}^{111}$ were calculated using Eq. (4.2) and the values in Tab. 4.1, $v_{L,e/h}^{110}$ using the charge drift models introduced in section 4.4.

The values for μ_0, β, $\mathcal{E}_0$ and μ_n for electrons and holes along the $\langle 100\rangle$ and $\langle 111\rangle$ axes in germanium were extracted by fits to experimental data measured at a reference temperature of $T_0 = 78\,\mathrm{K}$ [135], see Tab. 4.1 and Fig. 4.1.

For $\mathcal{E} \ll \mathcal{E}_0$, the term $(\mathcal{E}/\mathcal{E}_0)^\beta$ in Eq. (4.2) is negligible, resulting in $v_{L,e/h} \approx \mu_0\mathcal{E}$. Thus, μ_0 describes the mobility in this linear region, i.e. for low electric field strengths. The values for μ_0 depend only slightly on the axes, see Tab. 4.1. This predicts an almost isotropic drift for $\mathcal{E} \ll \mathcal{E}_0$, i.e. $v_{L,e/h}^{100} \approx v_{L,e/h}^{110} \approx v_{L,e/h}^{111}$, for both electrons and holes.

For $\mathcal{E} \gg \mathcal{E}_0$, $(\mathcal{E}/\mathcal{E}_0)^\beta$ becomes the dominant term in the denominator of Eq. (4.2), resulting in a constant saturation velocity for holes, i.e. $v_{L,h} \approx v_{\mathrm{sat},h} = \mu_0\mathcal{E}_0$. As for μ_0, the values for $\mathcal{E}_0$ in Tab. 4.1 are similar for the different axes, implying similar $v_{\mathrm{sat},h}$. For electrons, $v_{\mathrm{sat},e}$ shows a slight $\mathcal{E}$-dependence, i.e. $v_{L,e} \approx v_{\mathrm{sat},e} = \mu_0\mathcal{E}_0 - \mu_n\mathcal{E}$. This results from electrons being transferred from the conduction band minima at the L-points to higher-energetic conduction band minima, e.g at the Γ-point, see Fig. 3.6, where they acquire a different m_e^* and, hence, a different $\vec{v}_e$ than at the L-points [153]. The parameter μ_n accounts for this so-called Gunn effect.

The parameter $\mathcal{E}_0$ describes the electric field strength at which the transition between the linear region and the saturated region sets in. The transition region around $\mathcal{E} \approx \mathcal{E}_0$ is mostly influenced by β. Smaller values for β result in longer transition regions. The parameter β differs significantly for the $\langle 100\rangle$ and the $\langle 111\rangle$ axes, see Tab. 4.1, resulting in anisotropic charge-carrier drift for $\mathcal{E} \gtrsim \mathcal{E}_0$, i.e. in $v_{L,e/h}^{100} > v_{L,e/h}^{110} > v_{L,e/h}^{111}$ [157].

4.3 Scattering processes

In vacuum, a homogeneous electric field continuously accelerates electrons and their drift velocity increases with time. In a solid, electrons and holes repeatedly scatter, losing part of their energy and changing their direction. As a consequence, $|\vec{v}_e|$ and $|\vec{v}_h|$ reach finite, $\vec{\mathcal{E}}$-dependent values as result from μ_e and μ_h in Eq. (4.1).

The anisotropy of $\vec{v}_e$ and $\vec{v}_h$ is due to the anisotropy in μ_e and μ_h. It results from different effective masses, m^*, of the charge carriers depending on the direction of their movement [158, 159]. In addition, the various scattering processes, which limit the linear charge-carrier mobility μ_0 for both electrons and holes, have different functional dependencies on m^*. Furthermore, the values for μ_0 strongly depend on the densities of ionized and neutral impurities in the crystal, N_I and N_N, and the temperature T.

The resistivity of germanium can be expressed as the sum of the resistivity of a pure and perfect crystal and the resistivity resulting from imperfections, e.g. from impurities and lattice defects [160]. As μ_0 is inversely proportional to the resistivity, it is related to the individual mobilities, μ_P, due to different scattering processes, P, as

$$\frac{1}{\mu_0} = \sum_P \frac{1}{\mu_P} \tag{4.3}$$

The temperature dependence of the charge-carrier mobilities is dominated by the process with the smallest μ_P. In high-purity germanium, this process is the scattering off acoustic phonons, i.e. the interaction with the thermal motion of the crystal lattice. It is modeled as [161]

$$\mu_\mathrm{A} = \frac{\sqrt{8\pi} e \hbar^4 \langle C_L \rangle}{3E_\mathrm{ac}^2 (m^*)^{5/2} (k_B T)^{3/2}} \propto (m^*)^{-5/2} T^{-3/2} , \tag{4.4}$$

where $k_B = 1.381 \cdot 10^{-23}$ J/K is the Boltzmann constant, $\langle C_L \rangle$ is the average longitudinal elastic constant of the crystal and E_ac is the acoustic deformation-potential constant.

Charge carriers can also scatter off ionized impurities [162], for which

$$\mu_\mathrm{I} = \frac{64\sqrt{\pi}\varepsilon_0^2 \varepsilon_r^2 (2k_B T)^{3/2}}{N_\mathrm{I}\, e^3 (m^*)^{1/2} \ln\left(1 + \left(12\pi\varepsilon_0\varepsilon_r k_B T e^{-2} N_\mathrm{I}^{-1/3}\right)^2\right)} \propto (m^*)^{-1/2} N_\mathrm{I}^{-1} T^{3/2} . \tag{4.5}$$

This contribution is only relevant in depleted volumes of the detector where N_I is sufficiently high. In high-purity germanium, the influence of μ_I on μ_0 is expected to be negligible because $N_\mathrm{I} \lesssim 10^{10}\,\mathrm{cm}^{-3}$. For $T = 78\,\mathrm{K}$, μ_I is of the order of $10^{10}\,\mathrm{cm}^2$/Vs, which is orders of magnitude higher than the measured values for μ_0 listed in Tab. 4.1.

Finally, μ_0 can be reduced by scattering off neutral impurities [163]. In that case,

$$\mu_\mathrm{N} = \frac{e^3 m^*}{20\kappa N_\mathrm{N} \hbar^3} = \frac{e^3 m^*}{80\pi\varepsilon_0\varepsilon_r N_\mathrm{N} \hbar^3} \propto (m^*)\, N_\mathrm{N}^{-1} , \tag{4.6}$$

where $\kappa = 4\pi\varepsilon_0\varepsilon_r$. This contribution was originally assumed to be temperature independent [163]. A later publication proposed a T-dependence of $\mu_N \propto T^{1/2}$ [164].

Neutral impurities are contaminations introduced during the crystal and detector fabrication. The value for N_N in high-purity germanium detectors is unknown. According to Eq. (4.6), scattering off neutral impurities is relevant if $N_N \gtrsim 10^{15}\,\text{cm}^{-3}$, where $\mu_N \lesssim 10^5\,\text{cm}^2/\text{Vs}$. The electrically active impurities are actually neutral impurities in undepleted volumes but are not significant as $10^{10}\,\text{cm}^{-3} \ll 10^{15}\,\text{cm}^{-3}$.

In 1981, E.E. Haller *et al.* published measured values for N_N for different elements in high-purity germanium [165]. It was seen that these values depend on the conditions, under which the high-purity germanium crystals were grown. If the crystal was grown in a hydrogen atmosphere, the hydrogen concentration was of the order of $10^{14}\,\text{cm}^{-3}$. For crystals grown in a nitrogen atmosphere, a concentration of oxygen of more than $4 \cdot 10^{14}\,\text{cm}^{-3}$ was observed. In addition, silicon impurities were measured to be of the order of $10^{14}\,\text{cm}^{-3}$. If grown from a melt in a graphite-coated quartz crucible, the carbon concentration in the germanium crystal was of the order of $2 \cdot 10^{14}\,\text{cm}^{-3}$ [166]. Currently, the standard procedure is to grow crystals in a hydrogen atmosphere from carbon or carbon-coated crucibles. The companies do not provide details and the concentration of neutral impurities is not known.

If $N_N \ll 10^{15}\,\text{cm}^{-3}$, the influence of μ_N on μ_0 can be neglected and μ_0 is dominated by μ_A, resulting in $\mu_0 \propto (m^*)^{-5/2} T^{-3/2}$. The measured temperature dependence of μ_0 in the range from 130 K and 300 K was reported to be $\mu_0 \propto T^{-1.68}$ for electrons and $\mu_0 \propto T^{-2.40}$ for holes [167–170]. In recent measurements at lower temperatures and higher electric field strengths, the temperature dependence was significantly less pronounced than the expected $T^{-3/2}$ proportionality [35, 36].

4.4 General charge-drift models

So far, only longitudinal drifts along the main crystal axes have been discussed. Established values for the drift parameters exist only for the $\langle 100 \rangle$ and $\langle 111 \rangle$ axes, see Tab. 4.1. For drifts between the crystal axes, the electron or hole drift velocity is not necessarily parallel to the electric field vector. This transverse anisotropy cannot be predicted using just the parameterization of the longitudinal drift velocity in Eq. (4.2).

A good model for the charge-carrier drift in germanium not only has to accurately predict the charge-drift velocity parallel to the crystal axes but also the transverse anisotropy for arbitrary orientations of the electric field. For this, general expressions for $\vec{\upsilon}_e$ and $\vec{\upsilon}_h$, motivated by the band structure and predicting the measured values for the longitudinal drift velocities $\upsilon^{100}_{L,e/h}$ and $\upsilon^{111}_{L,e/h}$ given by Eq. (4.2), are needed.

4.4.1 Hole drift model

Holes in germanium populate states around the valence band maximum at the Γ-point. At thermal equilibrium, the hole population consists of 96% heavy holes and 4% light holes [171]. Therefore, most hole-drift models only consider the contributions of heavy holes. In the absence of an electric field, the heavy holes are symmetrically distributed around the Γ-point and the mean wave vector of the holes, $\vec{k}_0$, is zero. This symmetry is broken in the presence of an electric field, resulting in a non-zero $\vec{k}_0 \parallel \vec{\mathcal{E}}$.

In general, the $\vec{k}$-distribution of heavy holes around $\vec{k}_0$ can be approximated by a drifted Maxwellian distribution [172],

$$f(\vec{k},\vec{k}_0) = a \cdot \exp\left(-\frac{\hbar^2(\vec{k}-\vec{k}_0)^2}{2m^*_{hh}k_BT_{hh}}\right) , \tag{4.7}$$

where m^*_{hh} and T_{hh} are the effective mass and the temperature of the heavy holes.

The overall hole-drift velocity for a given electric field, $\vec{\upsilon}_h(\vec{\mathcal{E}})$, results from averaging the velocity contributions, $\vec{\upsilon}_k(\vec{k})$, over all $\vec{k}$-states:

$$\vec{\upsilon}_h(\vec{\mathcal{E}}) = \frac{\hbar}{a\pi^{3/2}\sqrt{2m^*_{hh}k_BT_{hh}}} \int\limits_{\mathbb{R}^3} \mathrm{d}^3k \;\; \vec{\upsilon}_k(\vec{k})\, f(\vec{k},\vec{k}_0(\vec{\mathcal{E}})) \; . \tag{4.8}$$

The associated hole-drift velocity $\vec{\upsilon}_k(\vec{k})$ for a given $\vec{k}$-state depends on the band structure of the heavy holes $E_h(\vec{k})$. In spherical coordinates, $\vec{k} = \vec{k}(k,\theta,\varphi)$, it is

$$\vec{\upsilon}_k(\vec{k}) = \frac{1}{\hbar}\vec{\nabla}_k E_h(\vec{k})|_{\vec{k}} \quad \text{with} \quad E_h(\vec{k}) = A\,\frac{\hbar^2k^2}{2m_e}\,(1-q(\theta,\varphi)) \tag{4.9}$$

$$\text{and} \quad q(\theta,\varphi) = \sqrt{B^2 + \frac{C^2}{4}\,(\sin(\theta)^4\sin(2\varphi)^2 + \sin(2\theta)^2)}\;; \tag{4.10}$$

$$\begin{aligned}\vec{\nabla}_k E_h(\vec{k}) = \frac{\partial E_h}{\partial k}\vec{e}_k + \frac{1}{k}\frac{\partial E_h}{\partial \theta}\vec{e}_\theta + \frac{1}{k\sin(\theta)}\frac{\partial E_h}{\partial \varphi}\vec{e}_\varphi = \frac{A\hbar^2k}{m_e}\,(1-q(\theta,\varphi))\,\vec{e}_k - \\ \frac{C^2A\hbar^2k}{8m_eq(\theta,\varphi)}\left[\left(2\sin(\theta)^3\cos(\theta)\sin(2\varphi)^2 + \sin(4\theta)\right)\vec{e}_\theta + \sin(\theta)^3\sin(4\varphi)\,\vec{e}_\varphi\right] ,\end{aligned} \tag{4.11}$$

where $A = 13.35$, $B = 0.6367$ and $C = 0.9820$ are measured germanium-specific parameters [171] and $\vec{e}_k$, $\vec{e}_\theta$, $\vec{e}_\varphi$ are the unit vectors in the local spherical coordinate system. The function $q(\theta,\varphi)$ describes the slightly warped structure of $E_h(\vec{k})$ [173], resulting in smaller drift velocities along the $\langle 111\rangle$ axis compared to all other directions.

For a given electric field expressed in spherical coordinates, $\vec{\mathcal{E}} = \vec{\mathcal{E}}(\mathcal{E},\theta_0,\varphi_0)$, the mean wave vector is aligned with $\vec{\mathcal{E}}$, i.e. $\vec{k}_0 = \vec{k}_0(k_0,\theta_0,\varphi_0)$ where $k_0 = |\vec{k}_0|$ depends on $\mathcal{E}$.[*] The hole-drift velocity $\vec{\upsilon}_h$ can be calculated for any $\vec{k}_0$ by numerically integrating the right side of Eq. (4.8). Details can be found elsewhere [171]. Choosing θ_0 and φ_0 to be aligned with the $\langle 100\rangle$, $\langle 110\rangle$ or $\langle 111\rangle$ axes allows to determine the longitudinal hole-drift velocities, $\upsilon^{100}_{L,h}(k_0)$, $\upsilon^{110}_{L,h}(k_0)$ and $\upsilon^{111}_{L,h}(k_0)$, as functions of k_0.

The results for $\vec{\upsilon}_h$ for arbitrary θ_0 and φ_0 can be approximated well as inspired by Eq. (4.11) [171]. For the x-axis, i.e. $\theta_0 = \frac{\pi}{2}$ and $\varphi_0 = 0$, aligned with the $\langle 100\rangle$ axis of the crystal, the radial, polar and azimuth components of $\vec{\upsilon}_h$, i.e. υ^r_h, υ^θ_h and υ^φ_h, are expressed as functions of k_0, θ_0 and φ_0:

$$\upsilon^r_h = \upsilon^{100}_{L,h}(k_0)\;[1-\Lambda(k_0)(\sin(\theta_0)^4\sin(2\varphi_0)^2 + \sin(2\theta_0)^2]\;, \tag{4.12}$$

$$\upsilon^\theta_h = \upsilon^{100}_{L,h}(k_0)\;\Omega(k_0)\;[2\sin(\theta_0)^3\cos(\theta_0)\sin(2\varphi_0)^2 + \sin(4\theta_0)]\;, \tag{4.13}$$

$$\upsilon^\varphi_h = \upsilon^{100}_{L,h}(k_0)\;\Omega(k_0)\;\sin(\theta_0)^3\sin(4\varphi_0)\;. \tag{4.14}$$

---

[*] The exact expression for $k_0(\mathcal{E})$ is not required for this hole drift model. However, for values of $\mathcal{E}$ relevant for germanium detectors: $0 \le \hbar k_0/\sqrt{2m^*_{hh}k_BT_{hh}} \le 3$ [171].

Here, k_0 still needs to be replaced by a physical observable, e.g. $\upsilon_{\text{rel}}(\mathcal{E}) = \upsilon_{L,h}^{111}(\mathcal{E})/\upsilon_{L,h}^{100}(\mathcal{E})$. The functions $\Lambda(k_0)$ and $\Omega(k_0)$ denote the relative difference in radial velocity and the relative tangential velocity, respectively.

The longitudinal and the transverse anisotropy arise through $\Lambda(k_0)$ and $\Omega(k_0)$:

$$\Lambda(k_0) = \frac{\upsilon_{L,h}^{100}(k_0) - \upsilon_{L,h}^{110}(k_0)}{\upsilon_{L,h}^{100}(k_0)} \quad \text{and} \quad \Omega(k_0) = \frac{\upsilon_h^{\varphi}(\theta = \frac{\pi}{2}, \varphi = \frac{\pi}{8})(k_0)}{\upsilon_{L,h}^{100}(k_0)} \,, \tag{4.15}$$

where $\upsilon_h^{\varphi}(\theta = \frac{\pi}{2}, \varphi = \frac{\pi}{8})$ is the hole-drift velocity transverse to the axis that bisects the $\langle 100 \rangle$ and $\langle 110 \rangle$ axes, which can also be determined through Eq. (4.8).

The computation of Λ and Ω is time-consuming as it involves several numerical integrations. Therefore, analytical approximations of Λ and Ω have to be used. Unlike in the publication from Bruyneel *et al.* [171], the analytical expressions for Λ and Ω in this thesis are not functions of k_0 but directly depend on the physical observable $\upsilon_{\text{rel}}(\mathcal{E}) = \upsilon_{L,h}^{111}(\mathcal{E})/\upsilon_{L,h}^{100}(\mathcal{E})$. Thus, k_0 does not appear in the final expression for $\vec{\upsilon}_h(\vec{\mathcal{E}})$ and only $\upsilon_{L,h}^{100}(\mathcal{E})$ and $\upsilon_{L,h}^{111}(\mathcal{E})$ enter the calculation. Evaluating Eq. (4.12) along the $\langle 111 \rangle$ axis, i.e. $\theta_0 = \operatorname{asin}(\sqrt{2/3})$ and $\varphi_0 = \pi/4$, results in

$$\upsilon_{L,h}^{111} = \upsilon_{L,h}^{100}\left[1 - \frac{4}{3}\Lambda(k_0)\right] \quad \Rightarrow \quad \Lambda(\upsilon_{\text{rel}}) = \frac{3}{4}(1 - \upsilon_{\text{rel}}) \,, \tag{4.16}$$

which is independent of the germanium-specific parameters A, B and C in Eq. (4.10). In particular, the isotropic case, i.e. $\upsilon_{L,h}^{100} = \upsilon_{L,h}^{111} \Leftrightarrow \upsilon_{\text{rel}} = 1$ results in $\Lambda(\upsilon_{\text{rel}} = 1) = 0$. Substituting this into Eq. (4.12) predicts $\upsilon_{L,h}^{r} = \upsilon_{L,h}^{100}$, i.e. an isotropic drift independent of the crystal axes.

Combining Eqs. (4.15) and (4.16) defines a relation between $\upsilon_{L,h}^{100}$, $\upsilon_{L,h}^{110}$ and $\upsilon_{L,h}^{111}$, i.e. $\upsilon_{L,h}^{110} = \frac{1}{4}\upsilon_{L,h}^{100} + \frac{3}{4}\upsilon_{L,h}^{111}$, which allows calculating $\upsilon_{L,h}^{110}$ from $\upsilon_{L,h}^{100}$ and $\upsilon_{L,h}^{111}$, see Fig. 4.1b.

The expression for $\Omega(\upsilon_{\text{rel}})$ is determined by calculating $\Omega(k_0)$ and $\upsilon_{\text{rel}}(k_0)$ for a set of k_0 in the region of interest, $0 \leq \hbar k_0/\sqrt{2m_{hh}^{*}k_B T_{hh}} \leq 3$ [171], using Eqs. (4.8) and (4.15) and fitting a fourth-order polynomial to the result, see Fig. 4.2. The fourth-order polynomial was constructed in orders of $(1 - \upsilon_{\text{rel}})$ and with no constant term to ensure $\Omega(\upsilon_{\text{rel}} = 1) = 0$, i.e. no anisotropy in the isotropic case $\upsilon_{L,h}^{100} = \upsilon_{L,h}^{111} \Leftrightarrow \upsilon_{\text{rel}} = 1$:

$$\begin{aligned}\Omega(\upsilon_{\text{rel}}) = &- 0.29711 \cdot (1 - \upsilon_{\text{rel}}) \; - 1.12082 \cdot (1 - \upsilon_{\text{rel}})^2 \\ &+ 3.83929 \cdot (1 - \upsilon_{\text{rel}})^3 - 4.80825 \cdot (1 - \upsilon_{\text{rel}})^4 \,.\end{aligned} \tag{4.17}$$

Thus, $\vec{\upsilon}_h(\vec{\mathcal{E}})$ is calculated independently of k_0 for arbitrarily oriented $\vec{\mathcal{E}}$ based on just $\upsilon_{L,h}^{111}(\mathcal{E})$ and $\upsilon_{L,h}^{100}(\mathcal{E})$ given by the parameterization in Eq. (4.2) and the values listed in Tab. 4.1. The ratio between the two provides $\upsilon_{\text{rel}}(\mathcal{E}) = \upsilon_{L,h}^{111}(\mathcal{E})/\upsilon_{L,h}^{100}(\mathcal{E})$ which is used to calculate $\Lambda(\upsilon_{\text{rel}})$ and $\Omega(\upsilon_{\text{rel}})$ for a given $\vec{\mathcal{E}}$ using Eqs. (4.16) and (4.17):

$$\vec{\upsilon}_h(\vec{\mathcal{E}}) = \begin{cases} \upsilon_h^{r}(\vec{\mathcal{E}}) = \upsilon_{L,h}^{100}(\mathcal{E}) \; [1 - \Lambda(\upsilon_{\text{rel}})(\sin(\theta_0)^4 \sin(2\varphi_0)^2 + \sin(2\theta_0)^2] \\ \upsilon_h^{\theta}(\vec{\mathcal{E}}) = \upsilon_{L,h}^{100}(\mathcal{E}) \; \Omega(\upsilon_{\text{rel}}) \; [2\sin(\theta_0)^3 \cos(\theta_0) \sin(2\varphi_0)^2 + \sin(4\theta_0)] \\ \upsilon_h^{\varphi}(\vec{\mathcal{E}}) = \upsilon_{L,h}^{100}(\mathcal{E}) \; \Omega(\upsilon_{\text{rel}}) \; \sin(\theta_0)^3 \sin(4\varphi_0) \end{cases} . \tag{4.18}$$

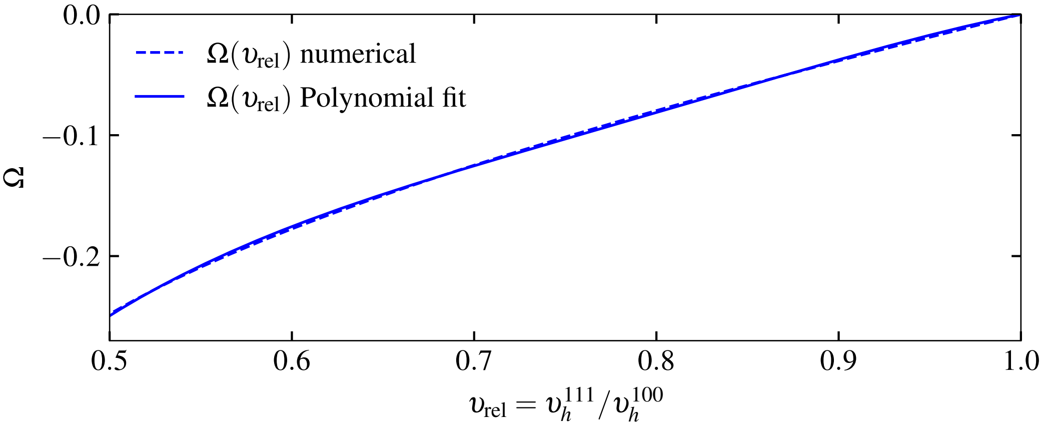

Figure 4.2: Numerically calculated values for $\Omega(\upsilon_{\mathrm{rel}})$ in germanium and a corresponding fit of a fourth-order polynomial, see Eq. (4.17). The values for Ω and υ_{rel} were calculated using Eqs. (4.8) and (4.15) for $0 \leq \hbar k_0/\sqrt{2m^*_{hh}k_B T_{hh}} \leq 3$ [171] in steps of 0.01 and are connected by a dashed line. The fit is shown as a solid line.

4.4.2 Electron-drift model

The electron-drift model in germanium [155] is more complex than the hole-drift model. Electrons do not populate a single conduction band minimum but four degenerate minima at the L-points. In each of these so-called valleys, the effective electron mass takes a value between $m^*_{e,T} = 0.0819\, m_e$ and $m^*_{e,L} = 1.64\, m_e$ [126], depending on the orientation of the electric field. The electron population of the valleys also depends on $\vec{\mathcal{E}}$. All of this needs to be taken into account when deriving a general expression for $\vec{\upsilon}_e(\vec{\mathcal{E}})$ based on the longitudinal electron-drift velocities, $\upsilon^{100}_{L,e}(\mathcal{E})$ and $\upsilon^{111}_{L,e}(\mathcal{E})$.

4.4.2.1 Effective electron masses

The dispersion relation, $E_j(\vec{k})$, for each conduction band minimum, $j \in \{1,2,3,4\}$ can be approximated using a parabolic function in $\vec{k}$,

$$E_j(\vec{k}) = \frac{\hbar^2}{2}\vec{k}^\dagger \gamma_j \vec{k}\,, \tag{4.19}$$

where γ_j is the inverse effective mass matrix of the j-th valley. In the local coordinate system of a valley, $x'y'z'$, with the y'-axis pointing parallel to the $\langle 111\rangle$ axis, see Fig. 4.3, the inverse effective mass matrix, γ_0, is

$$\gamma_0 = \begin{bmatrix} (m^*_{e,T})^{-1} & 0 & 0 \\ 0 & (m^*_{e,L})^{-1} & 0 \\ 0 & 0 & (m^*_{e,T})^{-1} \end{bmatrix},$$

which has the transverse and longitudinal inverse effective electron masses on the diagonals and accounts for the curvature of the band structure.

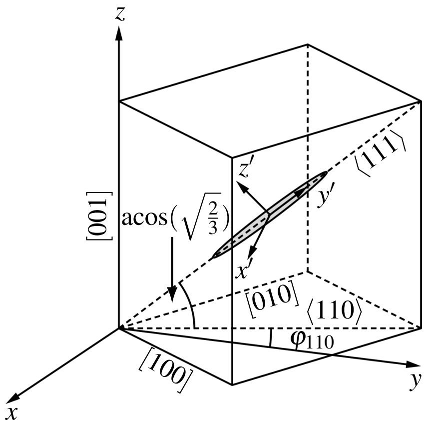

Figure 4.3: Relation between the local coordinates $x'y'z'$ in the conduction band minimum and the crystal coordinate system xyz. The y'-axis is aligned with the $\langle 111\rangle$ axis.

In the global coordinate system, xyz, the inverse effective mass matrix, γ_j, for the j-th conduction band minimum can be derived from γ_0 by applying two rotations, see Fig. 4.3: one rotation by $\mathrm{acos}(\sqrt{2/3})$ around the x'-axis aligning the y'-axis with the $\langle 110\rangle$ axis, and one further rotation around the z-axis aligning the y'-axis with the y-axis,

$$\gamma_j = R_j^{-1}\gamma_0 R_j \qquad \text{with} \qquad R_j = R_{x'}(\mathrm{acos}(\sqrt{2/3}))\, R_z(\varphi_{110} + j\pi/2)\ , \tag{4.20}$$

where φ_{110} is the angle between the $\langle 110\rangle$ and the y-axis. The differences between the four γ_j are the rotations by multiples of $\pi/2$ around the z-axis.

Equation (4.19) implies that, for a given $\vec{k}$, the inverse effective electron mass, $(m^*_{e,j})^{-1}$, in the j-th minimum is the projection of γ_j along $\vec{k}$, see section 3.2.1. If $\vec{k}$ is aligned with the electric field, i.e. $\vec{k} \parallel \vec{\mathcal{E}}_N$, where $\vec{\mathcal{E}}_N = \vec{\mathcal{E}}/\mathcal{E}$ is the normalized electric field vector, then $(m^*_{e,j})^{-1} = \vec{\mathcal{E}}_N^\dagger \gamma_j \vec{\mathcal{E}}_N$.

Table 4.2: Expressions for $(m^*_{e,j})^{-1} = \vec{\mathcal{E}}_N^\dagger \gamma_j \vec{\mathcal{E}}_N$ for electric fields $\vec{\mathcal{E}}$ parallel to the $\langle 100\rangle$, $\langle 110\rangle$ and $\langle 111\rangle$ axes for the four conduction band minima j.

	$\vec{\mathcal{E}} \parallel \langle 100\rangle$	$\vec{\mathcal{E}} \parallel \langle 110\rangle$	$\vec{\mathcal{E}} \parallel \langle 111\rangle$
$j=1$	$\frac{2}{3}(m^*_{e,T})^{-1} + \frac{1}{3}(m^*_{e,L})^{-1}$	$\frac{1}{3}(m^*_{e,T})^{-1} + \frac{2}{3}(m^*_{e,L})^{-1}$	$(m^*_{e,L})^{-1}$
$j=2$	$\frac{2}{3}(m^*_{e,T})^{-1} + \frac{1}{3}(m^*_{e,L})^{-1}$	$(m^*_{e,T})^{-1}$	$\frac{8}{9}(m^*_{e,T})^{-1} + \frac{1}{9}(m^*_{e,L})^{-1}$
$j=3$	$\frac{2}{3}(m^*_{e,T})^{-1} + \frac{1}{3}(m^*_{e,L})^{-1}$	$\frac{1}{3}(m^*_{e,T})^{-1} + \frac{2}{3}(m^*_{e,L})^{-1}$	$\frac{8}{9}(m^*_{e,T})^{-1} + \frac{1}{9}(m^*_{e,L})^{-1}$
$j=4$	$\frac{2}{3}(m^*_{e,T})^{-1} + \frac{1}{3}(m^*_{e,L})^{-1}$	$(m^*_{e,T})^{-1}$	$\frac{8}{9}(m^*_{e,T})^{-1} + \frac{1}{9}(m^*_{e,L})^{-1}$

The expressions for $\vec{\mathcal{E}}_N^\dagger \gamma_j \vec{\mathcal{E}}_N$ for $\vec{\mathcal{E}}$ parallel to the main crystal axes are listed in Tab. 4.2. For $\vec{\mathcal{E}} \parallel \langle 100\rangle$, the effective electron mass is identical for all conduction band minima. For $\vec{\mathcal{E}} \parallel \langle 110\rangle$, the electrons in two of the valleys acquire the lowest possible effective mass of $m^*_{e,T}$. In the other two valleys, effective electron masses are slightly higher. For $\vec{\mathcal{E}} \parallel \langle 111\rangle$, the electrons in one valley acquire the highest possible effective mass of $m^*_{e,L}$. In the other three valleys, the effective electron masses is significantly lower.

For arbitrarily oriented $\vec{\mathcal{E}}$ between the main crystal axes, the expressions for $\vec{\mathcal{E}}_N^\dagger \gamma_j \vec{\mathcal{E}}_N$ for the four conduction band minima are typically different from each other.

4.4.2.2 Population of the conduction band minima

The population of electrons in the j-th valley also depends on $\vec{\mathcal{E}}_N^\dagger \gamma_j \vec{\mathcal{E}}_N$ [174]. If the expressions for $\vec{\mathcal{E}}_N^\dagger \gamma_j \vec{\mathcal{E}}_N$ are not identical for the four valleys, the electrons will redistribute, resulting in an unequal population of the four valleys. In this case, the population of the conduction band minima is changed by the external electric field.

If no electric field is applied, the four valleys are equally populated. If an electric field parallel to the $\langle 100\rangle$ axis is applied, all valleys remain equally populated and no redistribution of the electrons is expected. For electric fields along the $\langle 110\rangle$ or $\langle 111\rangle$ axes, the electrons accumulate in the valleys where $m^*_{e,j}$ is higher, i.e. where $\vec{\mathcal{E}}_N^\dagger \gamma_j \vec{\mathcal{E}}_N = \frac{1}{3}(m^*_{e,T})^{-1} + \frac{2}{3}(m^*_{e,L})^{-1}$ for $\langle 110\rangle$ and $\vec{\mathcal{E}}_N^\dagger \gamma_j \vec{\mathcal{E}}_N = (m^*_{e,L})^{-1}$ for $\langle 111\rangle$.

A first parameterization for the fraction of electrons, $\frac{n_j}{n}$, populating the j-th valley was given by H.G Reik and H. Risken in 1962 [159], assuming a Maxwellian energy distribution of the electrons and redistribution of the electrons in the valleys through isotropic scattering of the electrons off phonons:

$$\frac{n_j}{n} = \frac{(\vec{\mathcal{E}}_N^\dagger \gamma_j \vec{\mathcal{E}}_N)^{-1/2}}{\sum\limits_{i=1}^{4} (\vec{\mathcal{E}}_N^\dagger \gamma_i \vec{\mathcal{E}}_N)^{-1/2}} , \tag{4.21}$$

L. Mihailescu *et al.* modified the expression for $\frac{n_j}{n}$ to account for the electric-field dependence of the electron redistribution by introducing an empirical function $\mathcal{R}(\mathcal{E})$ that scales the deviation from an equal distribution [155]:

$$\frac{n_j}{n} = \mathcal{R}(\mathcal{E}) \left(\frac{(\vec{\mathcal{E}}_N^\dagger \gamma_j \vec{\mathcal{E}}_N)^{-1/2}}{\sum\limits_{i=1}^{4} (\vec{\mathcal{E}}_N^\dagger \gamma_i \vec{\mathcal{E}}_N)^{-1/2}} - \frac{1}{4} \right) + \frac{1}{4} . \tag{4.22}$$

The function $\mathcal{R}(\mathcal{E})$ is determined from measurements with $\vec{\mathcal{E}} \parallel \langle 111 \rangle$, where a redistribution of the electrons between the valleys is expected. The expression in Eq. (4.22) is assumed to hold for all orientations of $\vec{\mathcal{E}}$.

4.4.2.3 Electron-drift velocity

A general expression for $\vec{\upsilon}_e(\vec{\mathcal{E}})$ was proposed by H.G. Reik and H. Risken in 1962 [159] which was further developed by L. Mihailescu *et al.* [155]:

$$\vec{\upsilon}_e(\vec{\mathcal{E}}) = \mathcal{A}(\mathcal{E}) \cdot \sum_{j=1}^{4} \frac{n_j}{n} \frac{\gamma_j \vec{\mathcal{E}}_N}{\sqrt{\vec{\mathcal{E}}_N^\dagger \gamma_j \vec{\mathcal{E}}_N}} , \tag{4.23}$$

The expression consists of a term $\mathcal{A}(\mathcal{E})$ which depends only on the magnitude of the electric field $\mathcal{E}$ and a term that depends only on the orientation of the electric field $\vec{\mathcal{E}}_N$. The function $\mathcal{A}(\mathcal{E})$ captures the saturation behavior of $\vec{\upsilon}_e(\vec{\mathcal{E}})$ for $\mathcal{E} \gg \mathcal{E}_0$, see section 4.2. The second term results in longitudinal and transverse anisotropies which arise from effective-mass anisotropies and the redistribution of electrons between the valleys for differently oriented $\vec{\mathcal{E}}$.

The function $\mathcal{A}(\mathcal{E})$ is determined from measurements of $\upsilon_{L,e}^{100}(\mathcal{E})$. For $\vec{\mathcal{E}} \parallel \langle 100 \rangle$, the expressions for $\vec{\mathcal{E}}_N^\dagger \gamma_j \vec{\mathcal{E}}_N$ are independent of j, see Tab. 4.2. The valleys are equally populated, i.e. $\frac{n_j}{n} = \frac{1}{4}$, and contribute equally to $\vec{\upsilon}_e$. Substituting this into Eq. (4.23) yields

$$\vec{\upsilon}_e(\vec{\mathcal{E}}) = \mathcal{A}(\mathcal{E}) \sqrt{\tfrac{2}{3}(m_{e,T}^*)^{-1} + \tfrac{1}{3}(m_{e,L}^*)^{-1}}\, \vec{\mathcal{E}}_N \overset{!}{=} \upsilon_{L,e}^{100}(\mathcal{E})\, \vec{\mathcal{E}}_N \tag{4.24}$$

$$\Rightarrow \mathcal{A}(\mathcal{E}) = \frac{\upsilon_{L,e}^{100}(\mathcal{E})}{\sqrt{\tfrac{2}{3}(m_{e,T}^*)^{-1} + \tfrac{1}{3}(m_{e,L}^*)^{-1}}} \tag{4.25}$$

$$\Rightarrow \vec{\upsilon}_e(\vec{\mathcal{E}}) = \upsilon_{L,e}^{100}(\mathcal{E}) \sum_{j=1}^{4} \frac{n_j}{n} \frac{1}{\sqrt{\tfrac{2}{3}(m_{e,T}^*)^{-1} + \tfrac{1}{3}(m_{e,L}^*)^{-1}}} \frac{\gamma_j \vec{\mathcal{E}}_N}{\sqrt{\vec{\mathcal{E}}_N^\dagger \gamma_j \vec{\mathcal{E}}_N}} . \tag{4.26}$$

The function $\mathcal{R}(\mathcal{E})$ in Eq. (4.22) is determined from $\upsilon_{L,e}^{111}(\mathcal{E})$. For $\vec{\mathcal{E}} \parallel \langle 111 \rangle$, one of the valleys, i.e. $j = 1$, is aligned with the electric field, resulting in $\vec{\mathcal{E}}_N^\dagger \gamma_1 \vec{\mathcal{E}}_N = (m_{e,L}^*)^{-1}$ and $\vec{\mathcal{E}}_N^\dagger \gamma_j \vec{\mathcal{E}}_N = \frac{8}{9}(m_{e,T}^*)^{-1} + \frac{1}{9}(m_{e,L}^*)^{-1}$ for $j \in \{2,3,4\}$. As a consequence, the electrons are redistributed with $\frac{n_1}{n} \neq \frac{n_2}{n} = \frac{n_3}{n} = \frac{n_4}{n}$. Substituting this into Eq. (4.26) yields

$$\upsilon_{L,e}^{111}(\mathcal{E}) = \upsilon_{L,e}^{100}(\mathcal{E})\, \frac{\frac{n_1}{n}\sqrt{(m_{e,L}^*)^{-1}} + \left(1 - \frac{n_1}{n}\right)\sqrt{\frac{8}{9}(m_{e,T}^*)^{-1} + \frac{1}{9}(m_{e,L}^*)^{-1}}}{\sqrt{\frac{2}{3}(m_{e,T}^*)^{-1} + \frac{1}{3}(m_{e,L}^*)^{-1}}}$$

$$\Rightarrow \frac{n_1}{n} = \frac{\sqrt{\frac{2}{3}(m_{e,T}^*)^{-1} + \frac{1}{3}(m_{e,L}^*)^{-1}}\, \frac{\upsilon_{L,e}^{111}(\mathcal{E})}{\upsilon_{L,e}^{100}(\mathcal{E})} - \sqrt{\frac{8}{9}(m_{e,T}^*)^{-1} + \frac{1}{9}(m_{e,L}^*)^{-1}}}{\sqrt{(m_{e,L}^*)^{-1}} - \sqrt{\frac{8}{9}(m_{e,T}^*)^{-1} + \frac{1}{9}(m_{e,L}^*)^{-1}}} \; . \quad (4.27)$$

This means that the electron population of the valley $j = 1$ is defined by $m_{e,T}^*$, $m_{e,L}^*$, $\upsilon_{L,e}^{100}(\mathcal{E})$ and $\upsilon_{L,e}^{111}(\mathcal{E})$. Inserting this in Eq. (4.22) for $\vec{\mathcal{E}} \parallel \langle 111 \rangle$ provides an analytic expression for $\mathcal{R}(\mathcal{E})$ of

$$\mathcal{R}(\mathcal{E}) = \frac{\sqrt{(m_{e,L}^*)^{-1}} + \frac{1}{3}\sqrt{\frac{8}{9}(m_{e,T}^*)^{-1} + \frac{1}{9}(m_{e,L}^*)^{-1}}}{(\sqrt{(m_{e,L}^*)^{-1}} - \sqrt{\frac{8}{9}(m_{e,T}^*)^{-1} + \frac{1}{9}(m_{e,L}^*)^{-1}})^2} \times \quad (4.28)$$

$$\left(-4\sqrt{\frac{2}{3}(m_{e,T}^*)^{-1} + \frac{1}{3}(m_{e,L}^*)^{-1}}\, \frac{\upsilon_{L,e}^{111}(\mathcal{E})}{\upsilon_{L,e}^{100}(\mathcal{E})} + \sqrt{(m_{e,L}^*)^{-1}} + 3\sqrt{\frac{8}{9}(m_{e,T}^*)^{-1} + \frac{1}{9}(m_{e,L}^*)^{-1}} \right)$$

With $m_{e,T}^* = 0.0819\, m_e$ and $m_{e,L}^* = 1.64\, m_e$ [126], Eqs. (4.25) and (4.28) become

$$\mathcal{A}(\mathcal{E}) = \frac{\upsilon_{L,e}^{100}(\mathcal{E})}{2.888} \quad \text{and} \quad \mathcal{R}(\mathcal{E}) = -3.414\, \frac{\upsilon_{L,e}^{111}(\mathcal{E})}{\upsilon_{L,e}^{100}(\mathcal{E})} + 3.161 \; . \quad (4.29)$$

The electron-drift model presented here allows to predict $\vec{\upsilon}_e(\vec{\mathcal{E}})$ for arbitrarily oriented $\vec{\mathcal{E}}$ taking only $\upsilon_{L,e}^{100}(\mathcal{E})$ and $\upsilon_{L,e}^{111}(\mathcal{E})$ given by Eq. (4.2) and the values listed in Tab. 4.1 as input. From $\upsilon_{L,e}^{100}(\mathcal{E})$ and $\upsilon_{L,e}^{111}(\mathcal{E})$, $\mathcal{A}(\mathcal{E})$ and $\mathcal{R}(\mathcal{E})$ are determined, see Eq. (4.29), which define the saturation of $\vec{\upsilon}_e$ at high electric fields and the longitudinal and transverse anisotropy, respectively. Then, for a given $\vec{\mathcal{E}}$, the expressions for $\vec{\mathcal{E}}_N^\dagger \gamma_j \vec{\mathcal{E}}_N$ are determined and $\frac{n_j}{n}$ are calculated using Eq. (4.22). The final electron-drift velocity $\vec{\upsilon}_e(\vec{\mathcal{E}})$ is determined using Eq. (4.23). For $\vec{\mathcal{E}} \parallel \langle 110 \rangle$, Eq. (4.23) yields a relation of $\upsilon_{L,e}^{110} = 0.7858\, \upsilon_{L,e}^{100} + 0.2002\, \upsilon_{L,e}^{111}$, which was used for Fig. 4.1a.

By construction, this electron-drift model never predicts the perfectly isotropic case, for which $\upsilon_{L,e}^{100} = \upsilon_{L,e}^{110} = \upsilon_{L,e}^{111}$. Even for equally populated valleys, i.e. $\frac{n_j}{n} = \frac{1}{4}$, the different expressions for $\vec{\mathcal{E}}_N^\dagger \gamma_j \vec{\mathcal{E}}_N$ for differently oriented $\vec{\mathcal{E}}$ already result in a longitudinal anisotropy of $\upsilon_{L,e}^{110}/\upsilon_{L,e}^{100} \approx 0.971$ and $\upsilon_{L,e}^{111}/\upsilon_{L,e}^{100} \approx 0.926$.

4.4.2.4 Modifications to the electron-drift model

The terms $\gamma_j\vec{\mathcal{E}}_N/\sqrt{\vec{\mathcal{E}}_N^\dagger\gamma_j\vec{\mathcal{E}}_N}$ in Eq. (4.23) describe the projection of $\gamma_j \propto (m_e^*)^{-1}$ along the normalized electric field $\vec{\mathcal{E}}_N$ and scale with $(m_e^*)^{-1/2}$. The resulting dependence of $\upsilon_e \propto (m_e^*)^{-1/2}$ implies that the ionized impurities are the predominant scattering centers, see Eq. (4.5). Recent measurements of the temperature dependence of the electron-drift anisotropy in germanium challenge this assumption [36].

In high-purity germanium, the density of ionized impurities is typically as low as $10^{10}\,\mathrm{cm}^{-3}$. Therefore, it is reasonable to assume that the dominant process is the scattering off acoustic phonons and that $\upsilon_e \propto (m_e^*)^{-5/2}$, see Eq. (4.4). The latter can be incorporated in the electron-drift model by modifying Eqs. (4.22) and (4.23) to

$$\vec{\upsilon}_e(\vec{\mathcal{E}}) = \mathcal{A}(\mathcal{E}) \cdot \sum_{j=1}^{4} \frac{n_j}{n} (\vec{\mathcal{E}}_N^\dagger\gamma_j\vec{\mathcal{E}}_N)^{3/2}\,\gamma_j\vec{\mathcal{E}}_N\ , \tag{4.30}$$

$$\frac{n_j}{n} = \mathcal{R}(\mathcal{E}) \left(\frac{(\vec{\mathcal{E}}_N^\dagger\gamma_j\vec{\mathcal{E}}_N)^{-5/2}}{\sum\limits_{i=1}^{4} (\vec{\mathcal{E}}_N^\dagger\gamma_i\vec{\mathcal{E}}_N)^{-5/2}} - \frac{1}{4} \right) + \frac{1}{4}\ . \tag{4.31}$$

The expressions for $\mathcal{A}(\mathcal{E})$ and $\mathcal{R}(\mathcal{E})$ for the modified electron-drift model are

$$\mathcal{A}(\mathcal{E}) = \frac{\upsilon_{L,e}^{100}(\mathcal{E})}{\sqrt{\tfrac{2}{3}(m_{e,T}^*)^{-1} + \tfrac{1}{3}(m_{e,L}^*)^{-1}}^{\,5}}\ , \tag{4.32}$$

$$\begin{aligned}\mathcal{R}(\mathcal{E}) = {} & \frac{\sqrt{(m_{e,L}^*)^{-1}}^{\,5} + \frac{1}{3}\sqrt{\tfrac{8}{9}(m_{e,T}^*)^{-1} + \tfrac{1}{9}(m_{e,L}^*)^{-1}}^{\,5}}{\left(\sqrt{(m_{e,L}^*)^{-1}}^{\,5} - \sqrt{\tfrac{8}{9}(m_{e,T}^*)^{-1} + \tfrac{1}{9}(m_{e,L}^*)^{-1}}^{\,5}\right)^2} \times \qquad (4.33)\\ & \left(-4\sqrt{\tfrac{2}{3}(m_{e,T}^*)^{-1} + \tfrac{1}{3}(m_{e,L}^*)^{-1}}^{\,5}\, \frac{\upsilon_{L,e}^{111}(\mathcal{E})}{\upsilon_{L,e}^{100}(\mathcal{E})} + \sqrt{(m_{e,L}^*)^{-1}}^{\,5} + 3\sqrt{\tfrac{8}{9}(m_{e,T}^*)^{-1} + \tfrac{1}{9}(m_{e,L}^*)^{-1}}^{\,5} \right)\ ,\end{aligned}$$

With $m_{e,T}^* = 0.0819\,m_e$ and $m_{e,L}^* = 1.64\,m_e$ [126], Eqs. (4.32) and (4.33) become

$$\mathcal{A}(\mathcal{E}) = \frac{\upsilon_{L,e}^{100}(\mathcal{E})}{201.066} \quad \text{and} \quad \mathcal{R}(\mathcal{E}) = -0.683\,\frac{\upsilon_{L,e}^{111}(\mathcal{E})}{\upsilon_{L,e}^{100}(\mathcal{E})} + 1.004\ . \tag{4.34}$$

The modified electron-drift model yields a relation of $\upsilon_{L,e}^{110} = 0.3860\,\upsilon_{L,e}^{100} + 0.6901\,\upsilon_{L,e}^{111}$, i.e. the electron-drift anisotropy between the $\langle 100\rangle$ and $\langle 110\rangle$ directions is larger compared to the unmodified electron-drift model. This has also been observed in the past [36].

By construction, the default and the modified electron-drift model both predict the longitudinal drift velocities along the $\langle 100\rangle$ and the $\langle 111\rangle$ axis provided as input. However, the expressions for $\mathcal{A}(\mathcal{E})$ and $\mathcal{R}(\mathcal{E})$ in Eqs. (4.29) and (4.34) define different transverse anisotropies, resulting in different behaviors along the $\langle 110\rangle$ axis and between the axes.

4.5 Charge-cloud effects

So far, electrons and holes have been described as charge carriers that independently drift in clusters as a response to an external electric field. Charge-cloud effects inside these clusters, i.e. diffusion and Coulomb self-repulsion, additionally influence the trajectories of the charge carriers and, hence, the pulse shapes [175].

Diffusion describes the random motion of charge carriers. Their average velocity depends on the temperature of the material and results in a particle flux from regions with high concentration to regions with low concentration. Coulomb self-repulsion describes the effect that same-sign charge carriers within a cluster repel each other.

The dynamics of charge-carrier clusters, diffusion plus Coulumb self-repulsion, are well described by the continuity equation:

$$\frac{\partial}{\partial t} n_{e/h}(\vec{r},t) + \vec{\nabla}\vec{j}_{e/h}(\vec{r},t) = s_{e/h}(\vec{r},t) \ , \tag{4.35}$$

where $n_{e/h}(\vec{r},t)$ is the number density and $\vec{j}_{e/h}(\vec{r},t)$ is the flux of electrons and holes, respectively. The term $s_{e/h}(\vec{r},t)$ is the generation ($s_{e/h} > 0$) or annihilation ($s_{e/h} < 0$) of charge carriers per unit volume and unit time. For electrons and holes, $\vec{j}_{e/h}$ is the sum of the diffusion flux, $\vec{j}^{\,\text{diff}}_{e/h}$, and the drift flux, $\vec{j}^{\,\text{drift}}_{e/h}$, with

$$\vec{j}^{\,\text{diff}}_{e/h}(\vec{r},t) = -D_{e/h}(\vec{r})\,\vec{\nabla} n_{e/h}(\vec{r},t) \quad \text{and} \quad \vec{j}^{\,\text{drift}}_{e/h}(\vec{r},t) = n_{e/h}(\vec{r},t)\,\mu_{e/h}(\vec{r})\,\vec{\mathcal{E}}(\vec{r}) \ , \tag{4.36}$$

where $D_{e/h}$ is the electron or hole diffusion coefficient, which can be estimated from the mobility $\mu_{e/h}$ using the Einstein-Smoluchowski relation [29, p. 356]:

$$D_{e/h}(\vec{r}) = \frac{k_B T}{e} \mu_{e/h}(\vec{r}) \ . \tag{4.37}$$

Substituting Eq. (4.36) into Eq. (4.35) and setting $s_{e/h}(\vec{r},t) = 0$ results in a differential equation for the charge-carrier concentration of

$$\frac{\partial}{\partial t} n_{e/h}(\vec{r},t) + \vec{\nabla}(-D_{e/h}(\vec{r})\vec{\nabla} n_{e/h}(\vec{r},t) + n_{e/h}(\vec{r},t)\mu_{e/h}(\vec{r})\vec{\mathcal{E}}(\vec{r})) = 0 \ . \tag{4.38}$$

In the rest frame of the charge cluster, the distribution of the charge carriers can be approximated as a sphere with charge

$$Q(r,t) = \pm e \iiint\limits_V \mathrm{d}^3 r \, n_{e/h}(r,t) = \pm e \int_0^r \mathrm{d}r \, 4\pi r^2 \, n_{e/h}(r,t) \ , \tag{4.39}$$

using "+" for holes and "−" for electrons. The electric field created by the charge cluster is

$$\vec{\mathcal{E}}(\vec{r},t) = \frac{Q(\vec{r},t)}{4\pi\varepsilon_0\varepsilon_r(\vec{r}) r^2} \vec{e}_r \ . \tag{4.40}$$

In the absence of an external electric field and in a spherical coordinate system with the origin in the center of the charge cluster, the evolution of a spherical charge cloud, $Q(r,t)$, can be described by a second-order differential equation [176]:

$$-\frac{1}{D_{e/h}(\vec{r})}\frac{\partial Q}{\partial t}+\underbrace{\frac{\partial^2 Q}{\partial r^2}-\frac{2}{r}\frac{\partial Q}{\partial r}}_{\text{Diffusion}}\underbrace{-Q\frac{\partial Q}{\partial r}\frac{e}{k_BT}\frac{1}{4\pi\varepsilon_0\varepsilon_r r^2}}_{\text{Coulomb self-repulsion}}=0\,. \tag{4.41}$$

The detailed derivation of Eq. (4.41) can be found in Appendix B on page 187.

4.5.1 Diffusion

An analytical formula for the diffusion-driven evolution of the size of the charge cluster is obtained from Eq. (4.41), neglecting the term that describes the Coulomb self-repulsion. and assuming a constant $\mu_{e/h}(\vec{r})$, i.e. a constant $D_{e/h}(\vec{r})$, see Eq. (4.37):

$$\frac{\partial Q}{\partial t}=D_{e/h}\left(\frac{\partial^2 Q}{\partial r^2}-\frac{2}{r}\frac{\partial Q}{\partial r}\right)\quad\Rightarrow\quad Q(r,t)=A(t_0)\sqrt{\frac{t}{t_0}}\exp\left(-\frac{r^2}{4D_{e/h}t}\right) \tag{4.42}$$

$$n_{e/h}(r,t)=\frac{N_{e/h}}{(4\pi D_{e/h}t)^{3/2}}\exp\left(-\frac{r^2}{4D_{e/h}t}\right)\,, \tag{4.43}$$

where $N_{e/h}$ is the number of charge carriers in the cluster. The density is normally distributed and the sphere expands in time with a radial standard-deviation of $\sigma_{e/h}=\sqrt{6D_{e/h}t}$ in three dimensions. The charge cluster evolution is given only by the material properties of the detector and does not depend on the deposited energy.

4.5.2 Coulomb self-repulsion

The contribution of Coulomb self-repulsion to the size evolution of the charge cluster is calculated using Eq. (4.41), neglecting effects from diffusion:

$$\frac{\partial Q}{\partial t}+Q\frac{\partial Q}{\partial r}\frac{\mu_{e/h}}{4\pi\varepsilon_0\varepsilon_r r^2}=0\quad\Rightarrow\quad Q(r,t)=\frac{4\pi\varepsilon_0\varepsilon_r r^3}{3\mu_{e/h}t}\,. \tag{4.44}$$

As the total charge is expected to be constant, i.e. $Q(r,t)=Q$, Eq. (4.44) describes a sphere with with radius r which monotonously expands with time t as

$$r=\sqrt[3]{\frac{3\mu_{e/h}Qt}{4\pi\varepsilon_0\varepsilon_r}}\,, \tag{4.45}$$

and has a radially constant charge-carrier density which decreases over time,

$$n(r,t)=\frac{\varepsilon_0\varepsilon_r}{e\mu_{e/h}t}\,. \tag{4.46}$$

In contrast to the case of diffusion, the evolution of the charge cluster driven by Coulomb self-repulsion also depends on the charge in the cluster and, hence, on the number of created electron-hole pairs. Therefore, the effect of Coulomb self-repulsion increases for larger energy deposits.

4.5.3 Initial charge-cloud size

So far, the initial size of the charge cloud has been neglected. When gammas interact with germanium, the recoil electron produced during photoelectric absorption, Compton scattering or pair production travels a certain range while dissipating its energy through the creation of electron-hole pairs. Higher energy depositions lead to higher-energetic recoil electrons, which lead to electron-hole pairs being created over a wider range. Values for the initial size of the charge cloud can be estimated either from Monte Carlo simulations, e.g. using GEANT4 [177], or from tabulated values of the range of electrons in matter.

There are several ways to classify the range of electrons in germanium [178]:

- The continuous-slowing-down approximation, CSDA, range is a measure of the average path length of an electron until thermalizing. It is calculated by integrating the inverse of the total linear stopping power with respect to the electron energy [179]. For electrons with an initial energy of E_0, the CSDA range, R_{CSDA}, is
$$R_{\mathrm{CSDA}} = \int_0^{E_0} \left\langle -\frac{\mathrm{d}E}{\mathrm{d}x} \right\rangle^{-1} \mathrm{d}E \; . \tag{4.47}$$
- The practical range, R_p, is a measure of straight-line penetration length [180]. The recoil electron does typically not move along a straight line but is deflected multiple times through Coulomb scattering, especially at low electron energies. The practical range is shorter than the CDSA range and defines a distance after which 90 to 95% of the incident electrons have stopped [180]. For germanium, R_p fits within 10% to
$$R_p = \alpha E \left(1 - \beta/(1+\gamma E)\right) \, , \tag{4.48}$$
with $\alpha = 0.83\,\mu\mathrm{m/keV}$, $\beta = 0.9841$ and $\gamma = 0.0030/\mathrm{keV}$ [181].

In Tab. 4.3, values of the CSDA and the practical range of electrons in germanium are listed for selected electron energies. The values of the CSDA range are around twice as large as the values of the practical range.

The initial charge-cloud volume can be approximated as a sphere with a diameter of R_p. This approximation overestimates the effects of the initial charge-cloud size [181]. However, it describes the charge-cloud dynamics more realistically than assuming a point-like energy deposition and neglecting the range of the recoil electrons.

Table 4.3: Electron ranges in germanium for selected energies E_0 of the incident electrons. The values of the CSDA range R_{CSDA} were taken from literature [179]. The values of the practical range R_p were calculated using Eq. (4.48).

E_0 in keV	R_{CSDA} in µm	R_p in µm
300	248	120
662	740	368
1020	1262	641

5 Detector simulation using SolidStateDetectors.jl

Within the framework of this thesis, substantial work was put into improving existing charge drift models and implementing models for charge cloud dynamics into the open-source julia simulation software package SolidStateDetectors.jl [37], SSD.

SSD has been developed by the LEGEND group at the Max Planck Institute for Physics in Munich. It provides a framework to simulate three-dimensional solid-state detector geometries including their environments to calculate electric fields and to generate pulse shapes. The modular structure of the package facilitates fast modifications of the source code, e.g. the implementation of custom impurity density profiles or charge drift models.

SSD comprises two parts: the field calculation for a given detector configuration and the pulse-shape simulation for a given event, see Fig. 5.1.

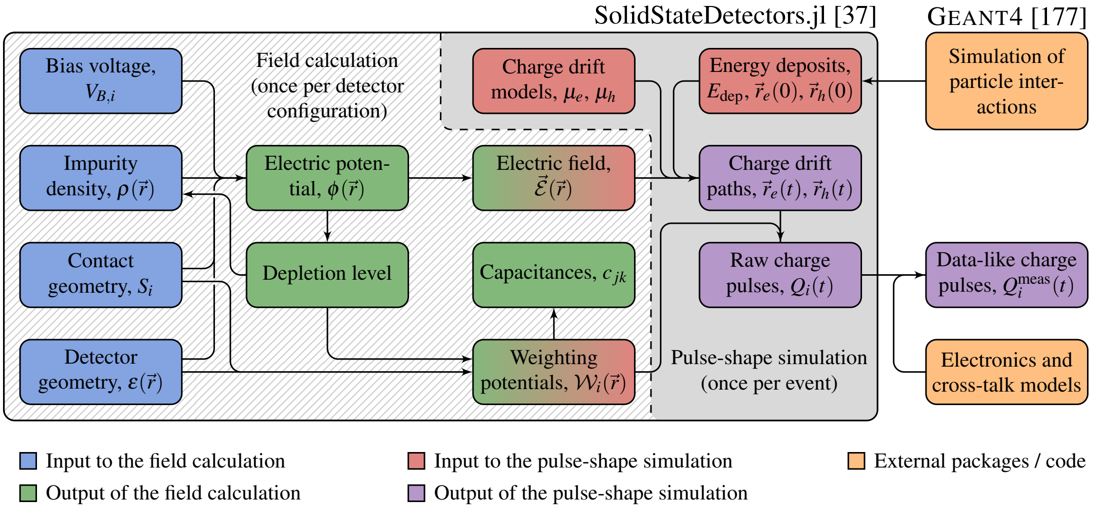

Figure 5.1: Flowchart of SSD, consisting of the field calculation (hatched) and the pulse-shape simulation (solid).

The electric potential $\phi(\vec{r})$ is calculated from the impurity density, the applied potentials to the contacts as well as the detector and contact geometries. If the detector is operated below the full-depletion voltage, local extrema will appear in $\phi(\vec{r})$ that can be attributed to undepleted volumes. If set by the user, the density of ionized impurities is set to zero in the undepleted volume and the electric potential is recalculated. The electric field is determined by differentiating the electric potential. The weighting potentials are calculated for each contact based on the geometry and the depletion level of the detector. The capacitance matrix can be calculated from the weighting potentials.

The electric field and the weighting potentials are inputs to the pulse-shape simulation. The distribution of energy deposits, e.g. simulated using the simulation toolkit GEANT4 [177], and models describing the electron and hole drift in the detector are needed for the simulation of pulse shapes. The pulses obtained from pulse-shape simulations using SSD depict the raw charge pulses expected from the equations listed in sections 3.4 and 4. Effects from the limited bandwidth of the read-out electronics or from cross-talk need to be accounted for using external code to obtain data-like pulses.

In the this chapter, the different steps of the field calculation and the pulse-shape simulation as well as their implementation in SSD are presented.

5.1 Constructive solid geometry

Solid-state detectors can have complex geometries. Therefore, SSD provides a simple way to easily define general geometries.

Geometries in SSD are defined via constructive solid geometry [182]. A small set of basic volume primitives are implemented, i.e. tubes, cones, spheres, boxes, tori and polygonal prisms. These volume primitives can be combined to form more complex geometries using boolean operators, i.e. unions, differences and intersections as shown in Fig. 5.2, as well as translations and rotations. Constructive solid geometry provides the possibility to define a wide range of complex geometries, especially everything needed to describe germanium detectors.

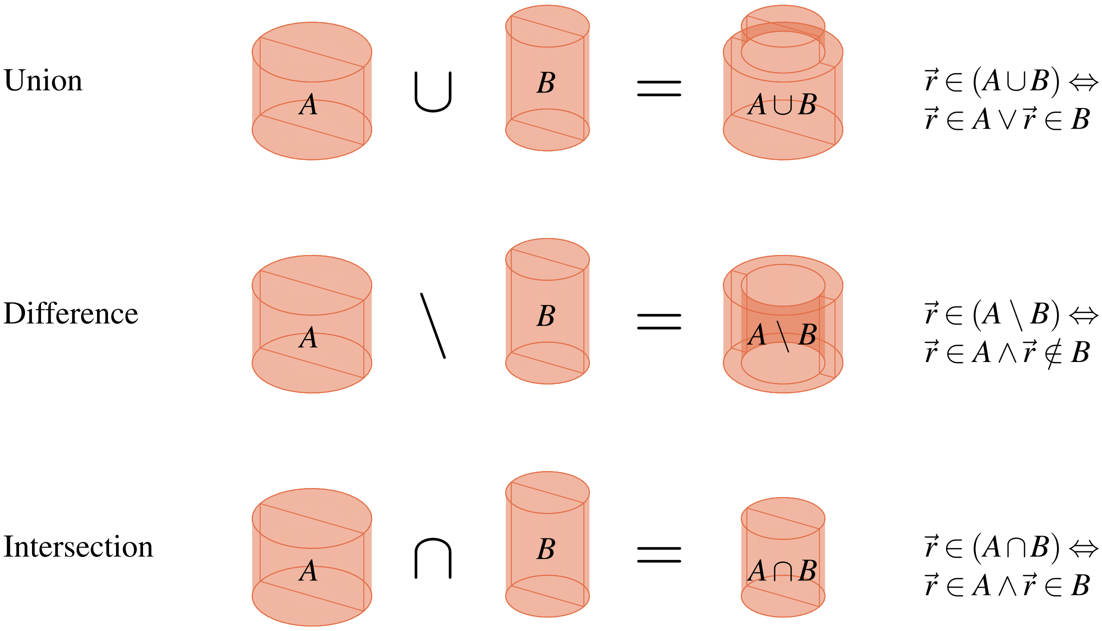

Figure 5.2: Boolean operators, union ($\cup$), difference ($\setminus$) and intersection ($\cap$), used to combine volumes using constructive solid geometry, as well as their mathematical definitions. Example geometries using differently shaped tubes are shown for demonstration purposes.

SSD provides a number of example detector geometries. One of them is an inverted coaxial point-contact, ICPC, detector [183] which is the baseline detector geometry for the LEGEND-1000 experiment [12]. Figures 5.4 and 5.4 show how constructive solid geometry is used to define the detector and contact geometry of an ICPC detector in SSD. The corresponding configuration file is listed in Appendix C on page 188.

The mother volume of the semiconductor is a full tube. The ICPC detector is tapered at the top outer corner and has a borehole that penetrates from the top. These two features are implemented by subtracting a hollow cone for the tapering and a small-radius tube for the borehole, see Fig. 5.3.

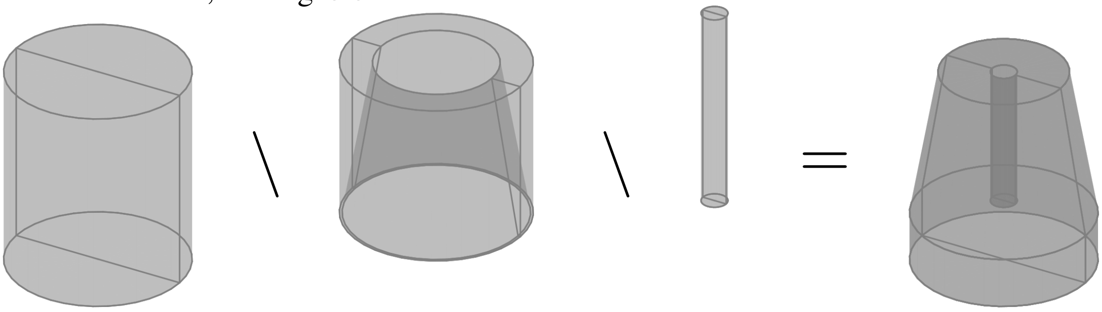

Figure 5.3: Definition of the geometry of the bulk of an ICPC detector as implemented in SSD using constructive solid geometry.

The ICPC detector has two contacts: one small point contact at the bottom of the detector, and one contact that covers the large outer surface including the top, the inner borehole and part of the bottom, see Fig. 5.4. The small point contact is defined simply as a tube. The outer contact is defined as a union of six primitives, one for each part of the surface that it covers.

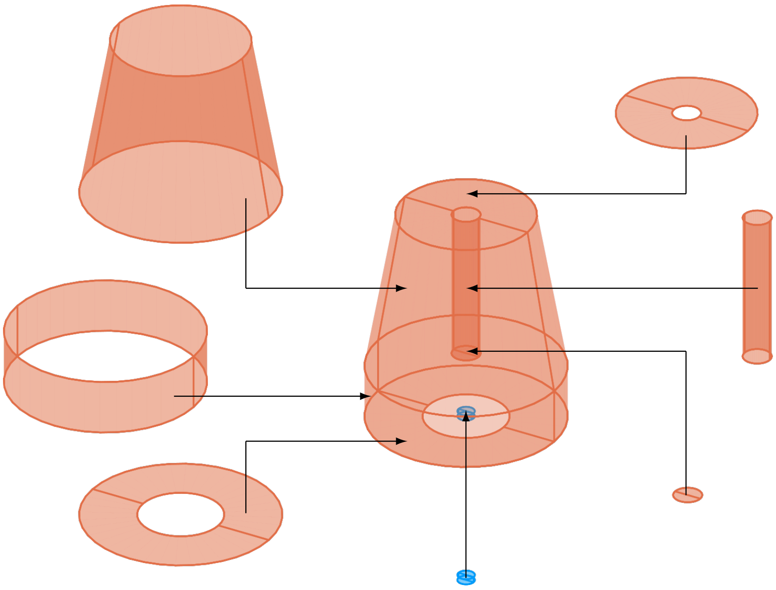

Figure 5.4: Composition of the contacts of the ICPC detector implemented in SSD from their primitive parts. The outer contact is defined as a union of six primitive parts. The point contact is shown in blue, the outer contact and parts thereof are shown in orange.

5.2 Calculation of the electric potential

The electric potential is numerically computed from Gauss's law, see Eq. (3.14), which is a time-independent equation which has to be solved only once at the beginning of a detector field calculation. For this, the simulation "world" is mapped on a grid in either Cartesian coordinates, x, y and z, or cylindrical coordinates, r, φ and z.

In cylindrical coordinates, each axis is divided into a finite number of ticks, i.e. r_i with $i \in \{1, \ldots, N_r\}$, φ_j with $j \in \{1, \ldots, N_\varphi\}$ and z_k with $k \in \{1, \ldots, N_z\}$. The combinations of these ticks, $\vec{r}_{i,j,k} = (r_i, \varphi_j, z_k)$, are a set of $N_p = N_r \cdot N_\varphi \cdot N_z$ points that form the grid.

Each grid point is assigned a small volume element, see Fig. 5.5. This so-called voxel is defined as the set of all points, (r, φ, z) where each of the coordinates are closest to the tick of the grid point, i.e. r is closest to r_i, φ is closest to φ_j and z is closest to z_k. The resulting voxel is a sector of a tube, see Fig. 5.5a. The boundaries of the voxel are given by the midpoints, see Fig. 5.5b, where

$$r_{mp,i} = \frac{1}{2} \cdot (r_i + r_{i+1}) \ , \quad \varphi_{mp,j} = \frac{1}{2} \cdot (\varphi_j + \varphi_{j+1}) \quad \text{and} \quad z_{mp,k} = \frac{1}{2} \cdot (z_k + z_{k+1}) \ .$$

Points in the voxel assigned to $\vec{r}_{i,j,k}$ fulfill $r_{mp,i-1} < r \leq r_{mp,i}$, $\varphi_{mp,j-1} < \varphi \leq \varphi_{mp,j}$ and $z_{mp,k-1} < z \leq z_{mp,k}$.

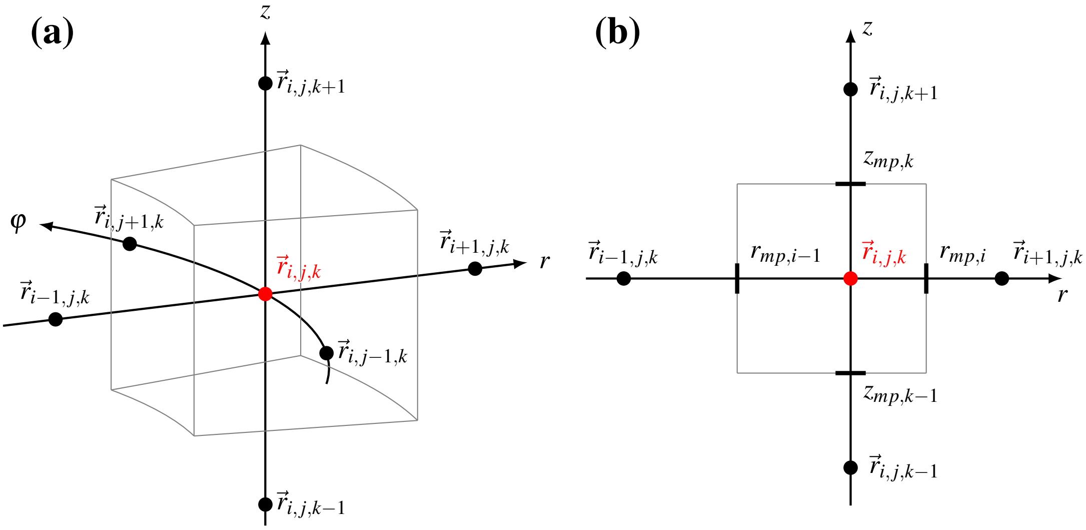

Figure 5.5: Sketch of (a) a voxel around the grid point $\vec{r}_{i,j,k}$ and (b) the two-dimensional cut in r and z at φ_j, with the midpoints defining the voxel boundaries, adapted from [184].

Dividing the world into voxels allows for the determination of the electric potential for the corresponding individual grid point, $\phi_{i,j,k} = \phi(\vec{r}_{i,j,k})$. In the voxel belonging to the grid point $\vec{r}_{i,j,k}$, Eq. (3.14) can be rewritten in integral form, i.e.

$$\iiint\limits_{V_{i,j,k}} \mathrm{d}^3 r \, \vec{\nabla} \left(\varepsilon(\vec{r}) \vec{\nabla} \phi(\vec{r}) \right) = - \iiint\limits_{V_{i,j,k}} \mathrm{d}^3 r \, \frac{\rho(\vec{r})}{\varepsilon_0} \ , \tag{5.1}$$

where $V_{i,j,k}$ is the volume of the voxel.

The term on the right side becomes

$$-\iiint\limits_{V_{i,j,k}} \mathrm{d}^3 r \, \frac{\rho(\vec{r})}{\varepsilon_0} \approx -\frac{\rho^{w}_{i,j,k}}{\varepsilon_0} \iiint\limits_{V_{i,j,k}} \mathrm{d}^3 r = -\frac{\rho^{w}_{i,j,k}}{\varepsilon_0} V_{i,j,k} =: Q^{\mathrm{eff}}_{i,j,k} \,, \tag{5.2}$$

where $\rho^{w}_{i,j,k}$ is the geometrically weighted space charge density obtained by averaging over the values at the eight corners of the voxel. The effective charge, $Q^{\mathrm{eff}}_{i,j,k}$, is defined as the charge, $\rho^{w}_{i,j,k} V_{i,j,k}$, contained in the volume of the voxel divided by $-\varepsilon_0$.

The left side of Eq. (5.1) can be rewritten [184] using the divergence theorem:

$$\begin{aligned} Q^{\mathrm{eff}}_{i,j,k} = \iiint\limits_{V_{i,j,k}} \mathrm{d}^3 r \, \vec{\nabla} \Big(\varepsilon(\vec{r}) \vec{\nabla} \phi(\vec{r}) \Big) &= \oiint\limits_{\partial V_{i,j,k}} \mathrm{d}\vec{S} \, \varepsilon_r(\vec{r}) \vec{\nabla} \phi(\vec{r}) = \iint\limits_{r^+} + \iint\limits_{r^-} + \iint\limits_{\varphi^+} + \iint\limits_{\varphi^-} + \iint\limits_{z^+} + \iint\limits_{z^-} \\ &\approx \frac{\phi_{i+1,j,k} - \phi_{i,j,k}}{r_{i+1} - r_i} \, \varepsilon^{w,r^+}_{i,j,k} \, A^{r^+}_{i,j,k} - \frac{\phi_{i,j,k} - \phi_{i-1,j,k}}{r_i - r_{i-1}} \, \varepsilon^{w,r^-}_{i,j,k} \, A^{r^-}_{i,j,k} \\ &+ \frac{\phi_{i,j+1,k} - \phi_{i,j,k}}{r_i(\varphi_{j+1} - \varphi_j)} \, \varepsilon^{w,\varphi^+}_{i,j,k} \, A^{\varphi^+}_{i,j,k} - \frac{\phi_{i,j,k} - \phi_{i,j-1,k}}{r_i(\varphi_j - \varphi_{j-1})} \, \varepsilon^{w,\varphi^-}_{i,j,k} \, A^{\varphi^-}_{i,j,k} \\ &+ \frac{\phi_{i,j,k+1} - \phi_{i,j,k}}{z_{k+1} - z_k} \, \varepsilon^{w,z^+}_{i,j,k} \, A^{z^+}_{i,j,k} - \frac{\phi_{i,j,k} - \phi_{i,j,k-1}}{z_k - z_{k-1}} \, \varepsilon^{w,z^-}_{i,j,k} \, A^{z^-}_{i,j,k} \,. \end{aligned} \tag{5.3}$$

Each term in the final approximation in Eq. (5.3) corresponds to the flux through one of the six surfaces, $S \subset \partial V_{i,j,k}$, in positive and negative directions for all three dimensions, i.e. $S \in \{r^+, r^-, \varphi^+, \varphi^-, z^+, z^-\}$, and depends on three quantities: the forward difference of $\vec{\nabla}\phi(\vec{r})$ perpendicular to the surface, the geometrically weighted mean of $\varepsilon_r(\vec{r})$, $\varepsilon^{w,S}_{i,j,k}$, evaluated at the four corners of the surface, and the area $A^{S}_{i,j,k}$ of the surface.

Rearranging Eq. (5.3) provides a formula to calculate $\phi_{i,j,k}$ from the values of its direct neighbors.

$$\begin{aligned} \phi_{i,j,k} = a^{0}_{i,j,k} \, (Q^{\mathrm{eff}}_{i,j,k} &+ a^{r^+}_{i,j,k} \phi_{i+1,j,k} + a^{r^-}_{i,j,k} \phi_{i-1,j,k} + a^{\varphi^+}_{i,j,k} \phi_{i,j+1,k} \\ &+ a^{\varphi^-}_{i,j,k} \phi_{i,j-1,k} + a^{z^+}_{i,j,k} \phi_{i,j,k+1} + a^{z^-}_{i,j,k} \phi_{i,j,k-1}) \,. \end{aligned} \tag{5.4}$$

The coefficients $a^{0}_{i,j,k}$ and $a^{S}_{i,j,k}$ depend on $\varepsilon_r(\vec{r})$ and the grid geometry, see Eq. (5.3). The values $Q^{\mathrm{eff}}_{i,j,k}$ are given by $\rho(\vec{r})$ and the geometry of the grid, see Eq. (5.2). Therefore, for fixed $\varepsilon(\vec{r})$ and $\rho(\vec{r})$ and a given grid, $Q^{\mathrm{eff}}_{i,j,k}$, $a^{0}_{i,j,k}$ and all $a^{S}_{i,j,k}$ are constant.

Some grid points are located in or on contacts, S_ν. In this case, the corresponding electric potential value is fixed to the potential, $V_{B,\nu}$, applied to this contact, i.e.

$$\phi_{i,j,k} = V_{B,\nu} \qquad \text{if } \vec{r}_{i,j,k} \in S_\nu \,. \tag{5.5}$$

The linear equations for the non-fixed potential values of individual grid points can be mapped into a matrix equation changing to linear indexing, i.e. $(i, j, k) \rightarrow 1, \dots, N_p$:

$$\underbrace{\begin{bmatrix} \phi_1 \\ \phi_2 \\ \vdots \\ \phi_{N_p} \end{bmatrix}}_{\vec{\phi} \in \mathbb{R}^{N_p}} = \underbrace{\begin{bmatrix} a_{1,1} & a_{1,2} & \dots & a_{1,N_p} \\ a_{2,1} & a_{2,2} & \dots & a_{2,N_p} \\ \vdots & \vdots & \ddots & \vdots \\ a_{N_p,1} & a_{N_p,2} & \dots & a_{N_p,N_p} \end{bmatrix}}_{A \in \mathbb{R}^{N_p \times N_p}} \cdot \underbrace{\begin{bmatrix} \phi_1 \\ \phi_2 \\ \vdots \\ \phi_{N_p} \end{bmatrix}}_{\vec{\phi} \in \mathbb{R}^{N_p}} + \underbrace{\begin{bmatrix} a_1^0 Q_1^{\text{eff}} \\ a_2^0 Q_2^{\text{eff}} \\ \vdots \\ a_{N_p}^0 Q_{N_p}^{\text{eff}} \end{bmatrix}}_{\vec{b} \in \mathbb{R}^{N_p}} \tag{5.6}$$

The electric potential is numerically calculated by finding $\vec{\phi}$ that fulfills Eq. (5.6). This is realized by starting with an initial state, $\vec{\phi}^0$, and solving Eq. (5.6) iteratively using the Gauss-Seidel method, i.e.

$$\vec{\phi}^{t+1} = A \cdot \vec{\phi}^{t} + \vec{b} \tag{5.7}$$

with the iteration index $t \in \{0, 1, 2, \dots, N_t - 1\}$, where N_t is the number of iterations.

The initial state $\vec{\phi}^0$ is chosen such that the values of the electric potential on grid points on contacts and grounded parts are set to their fixed potential, and all other potential values are set to zero. This is shown for the example ICPC detector in Fig. 5.6a on an initial grid with $24 \times 1 \times 20 = 480$ grid points. The values of $\vec{\phi}$ are iteratively updated using Eq. (5.7) until reaching convergence, i.e. $|\phi_i^{t+1} - \phi_i^t| < \phi_{\text{threshold}}$ for all $i \in \{1, \dots, N_p\}$, or exceeding the maximally allowed number of iteratios. The electric potential calculation for the example ICPC detector using the default $\phi_{\text{threshold}} = 10^{-7}\,V_B$ converges after 426 iterations and the resulting $\vec{\phi}$ is shown in Fig. 5.6b.

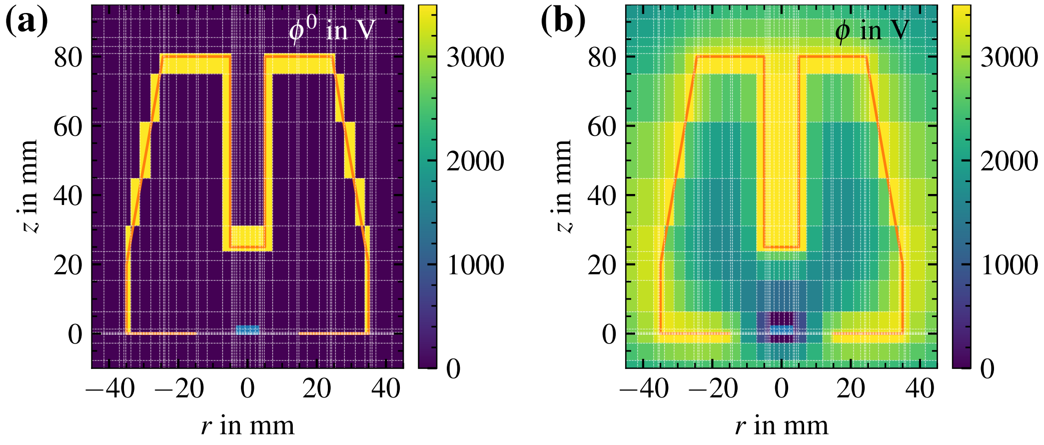

Figure 5.6: (a) Initial state, $\vec{\phi}_0$, and (b) final state, $\vec{\phi}$, after 426 iterations for the example ICPC detector in SSD shown in the r-z-plane at $\varphi = 0°$. The contacts of the detector are shown in the same color as in Fig. 5.4.

The potential value at a grid point with even $i+j+k$ only depends on the potential values of grid points with odd $i+j+k$ and vice versa, see Eq. (5.4). Thus, the grid can be divided into two subgrids with red (odd $i+j+k$) and black (even $i+j+k$) grid points, see Fig. 5.5. Then, Eq. (5.7) becomes

$$\vec{\phi}_R^{t+1} = A_R \vec{\phi}_B^{t} + \vec{b}_R \qquad \text{and} \qquad \vec{\phi}_B^{t+1} = A_B \vec{\phi}_R^{t+1} + \vec{b}_B \tag{5.8}$$

where the subscripts R and B denote red and black grid points, respectively. The red-black division results in lower dimensional matrices $A_R, A_B \in \mathbb{R}^{N_p/2 \times N_p/2}$ and faster convergence because the updated values for $\vec{\phi}_R^{t+1}$ enter the determination of $\vec{\phi}_B^{t+1}$ [184].

Faster convergence is also obtained in SSD by extending the basic Gauss-Seidel method in Eq. (5.7) to the so-called successive over-relaxation, SOR, method [185], i.e.

$$\vec{\phi}^{t'} = A\vec{\phi}^{t} + \vec{b} \qquad \Rightarrow \qquad \vec{\phi}^{t+1} = \vec{\phi}^{t} + \omega_{\text{SOR}}(\vec{\phi}^{t'} - \vec{\phi}^{t}) \tag{5.9}$$

where ω_{SOR} is the SOR-constants which is chosen from $0 < \omega_{\text{SOR}} < 2$. The SOR method with $1 < \omega_{\text{SOR}} < 2$ usually converges faster than the Gauss-Seidel method ($\omega_{\text{SOR}} = 1$). The default values for ω_{SOR} in SSD are between 1.4 and 1.85.

Technically, the iteration steps are optimized to ensure fast and efficient execution. Each iteration step only comprises additions and multiplications, which can be executed in parallel on modern CPUs. SSD also supports GPU-accelerated programming which speeds up the electric potential calculation significantly for large N_p.

SSD performs the potential calculation on an adaptive grid. At the beginning, the grid is very coarse and consists of a few points in each dimension. Therefore, convergence is reached quickly. After convergence, the grid is refined, i.e. additional grid points are added in regions where $|\phi_{i,j,k} - \phi_{i+1,j,k}| > \phi_r$ where ϕ_r is a user-defined refinement threshold. This is done for all three indices i, j and k separately. The grid refinement ensures additional precision in regions with high field gradients or small structures. For the initial values $\vec{\phi}^0$ of the next iteration, the old grid points are kept at their values and the newly added grid points are assigned values as determined from a linear interpolation between the neighboring grid points. Then, $\vec{\phi}$ is updated until convergence. The number of refinements and the refinement limits can be provided by the user.

In Figure 5.7, $\vec{\phi}$ as numerically calculated with SSD is shown for different numbers of refinements. As the ICPC detector is rotationally symmetric, a 2D calculation is sufficient. The effect of the grid spacing becomes less pronounced with an increasing number of refinements and the result for $\vec{\phi}$ becomes smoother.

In order to test the numerical calculation of $\vec{\phi}$ in SSD, several test cases with known analytical solutions [37] are run by SSD as test cases every time the source code is modified. Two of them are listed in Appendix A on page 185.

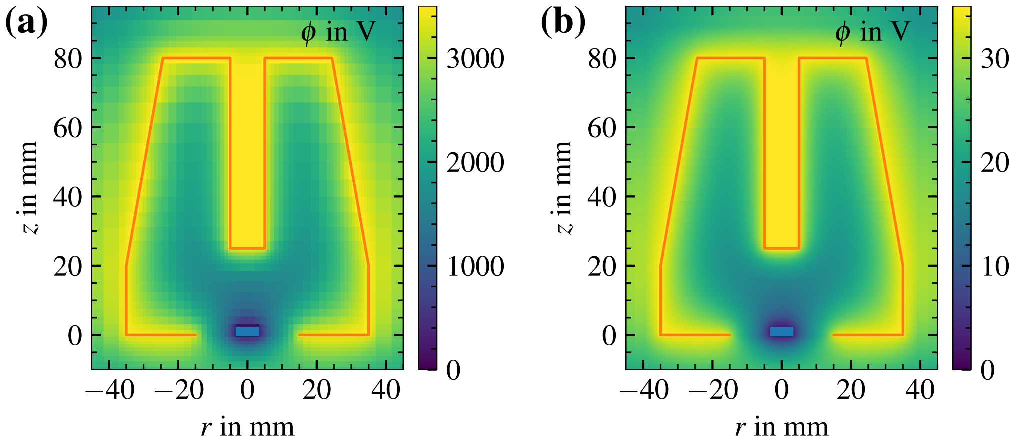

Figure 5.7: Electric potential as calculated with SSD for the example ICPC detector (a) after two refinements with a final grid with $38 \times 1 \times 44 = 1672$ grid points and (b) after four refinements with a final grid with $150 \times 1 \times 210 = 31\,500$ grid points.

5.3 Depletion handling

For a fully-depleted detector, all electrically active impurities are ionized and the charge density is given as $\rho(\vec{r}) = \pm e N_I(\vec{r})$ with "+" for an n-type and "−" for a p-type bulk. For a partially depleted detector, $\phi(\vec{r})$ would have local extrema in the bulk, e.g. a local minimum for a p-type bulk, if all impurities were ionized. In reality, this local minimum would not form because it would attract free holes which would recombine with the ionized impurities and neutralize them, resulting in undepleted volumes with a net charge density of $\rho(\vec{r}) = 0$. Prior to the potential calculation, it is not known which volumes of the detector are depleted ($\rho(\vec{r}) = \pm e N_I(\vec{r})$) and which ones are not ($\rho(\vec{r}) = 0$) and the exact form of $\rho(\vec{r})$, i.e. the depletion level, is unclear.

SSD can determine the depletion level of a detector using so-called depletion handling: In the initial state $\vec{\phi}^0$, all impurities are assumed to be ionized. After updating $\vec{\phi}$ using Eq. (5.9), SSD checks for each $\vec{r}_{i,j,k}$ if the new value $\phi_{i,j,k}$ is a local extremum with respect to its six nearest neighbors, i.e. if $\phi_{i,j,k} > \phi_{i,j,k}^{\max} = \max\{\phi_{i\pm1,j,k}, \phi_{i,j\pm1,k}, \phi_{i,j,k\pm1}\}$ for an n-type bulk or if $\phi_{i,j,k} < \phi_{i,j,k}^{\min} = \min\{\phi_{i\pm1,j,k}, \phi_{i,j\pm1,k}, \phi_{i,j,k\pm1}\}$ for a p-type bulk. If this is the case, this grid point is considered to belong to an undepleted volume of the detector, which means that the impurities are partially or not at all ionized. SSD accounts for this by scaling $Q_{i,j,k}^{\text{eff}}$ in Eq. (5.4) by a factor $0 \leq f_{i,j,k} < 1$ such that $\phi_{i,j,k}$ becomes $\phi_{i,j,k}^{\max}$or $\phi_{i,j,k}^{\min}$, respectively. This scale factor $f_{i,j,k}$ is 0 for grid points in undepleted volumes (0% ionized), 1 for grid points in depleted volumes (100% ionized) and $0 < f_{i,j,k} < 1$ for grid points at the boundary between depleted and undepleted volumes.

Figure 5.8 shows the calculated depletion level of the ICPC detector for bias voltages of 600 V and 1200 V applied to the mantle contact. The ICPC detector is simulated with a p-type impurity density profile that increases linearly from $1.0 \cdot 10^{10}\,\text{cm}^{-3}$ at the bottom to $1.8 \cdot 10^{10}\,\text{cm}^{-3}$ at the top of the detector with no r-dependence. Equation (3.13) provides a rough estimate for the depletion width of 10.3 mm at 600 V and 14.6 mm at 1200 V. This agrees well with the calculated depletion levels shown in Fig. 5.8.

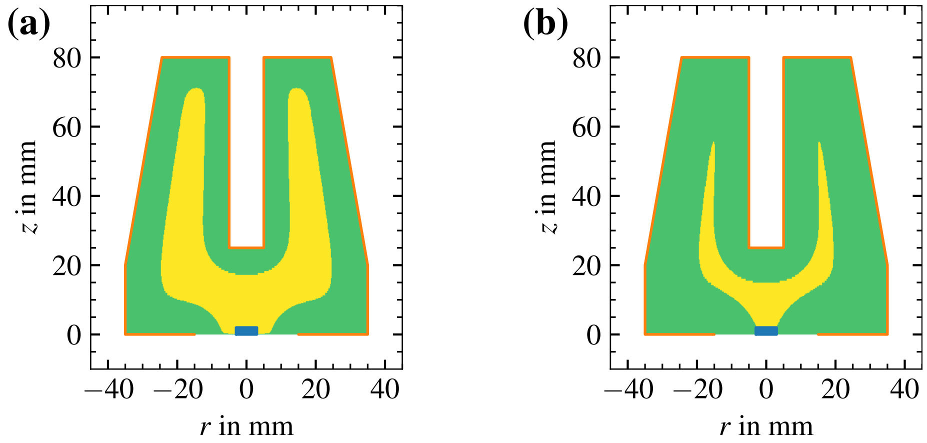

Figure 5.8: Depletion levels of the example ICPC detector as determined by SSD for bias voltages of (a) 600 V and (b) 1200 V applied to the mantle contact. The depleted volumes are shown in green, the undepleted volumes are shown in yellow.

5.4 Calculation of the electric field

The electric field is calculated from the electric potential based on $\vec{\mathcal{E}}(\vec{r}) = -\vec{\nabla}\phi(\vec{r})$, where $\vec{\nabla}\phi(\vec{r})$ is approximated using finite differences. For each grid point $\vec{r}_{i,j,k}$, the electric field, $\vec{\mathcal{E}}_{i,j,k}$, is determined for each dimension by averaging the finite difference in the positive and in the negative direction, i.e.

$$\vec{\mathcal{E}}_{i,j,k} = \mathcal{E}^r_{i,j,k}\vec{e}_r + \mathcal{E}^\varphi_{i,j,k}\vec{e}_\varphi + \mathcal{E}^z_{i,j,k}\vec{e}_z \,,$$

where $\vec{e}_r$, $\vec{e}_\varphi$ and $\vec{e}_z$ are the unit vectors in r-, φ- and z-direction, respectively, and

$$\mathcal{E}^r_{i,j,k} = -\frac{1}{2}\left(\frac{\phi_{i+1,j,k}-\phi_{i,j,k}}{r_{i+1}-r_i} + \frac{\phi_{i,j,k}-\phi_{i-1,j,k}}{r_i - r_{i-1}}\right),$$

$$\mathcal{E}^\varphi_{i,j,k} = -\frac{1}{2}\left(\frac{\phi_{i,j+1,k}-\phi_{i,j,k}}{r_i(\varphi_{j+1}-\varphi_j)} + \frac{\phi_{i,j,k}-\phi_{i,j-1,k}}{r_i(\varphi_j - \varphi_{j-1})}\right),$$

$$\mathcal{E}^z_{i,j,k} = -\frac{1}{2}\left(\frac{\phi_{i,j,k+1}-\phi_{i,j,k}}{z_{k+1}-z_k} + \frac{\phi_{i,j,k}-\phi_{i,j,k-1}}{z_k - z_{k-1}}\right).$$

The electric field of the example ICPC detector is shown in Fig. 5.9. The electric field is strongest close to the surface of the detector and weakest in the parts of the bulk that are the furthest away from the surface and in the bottom corners.

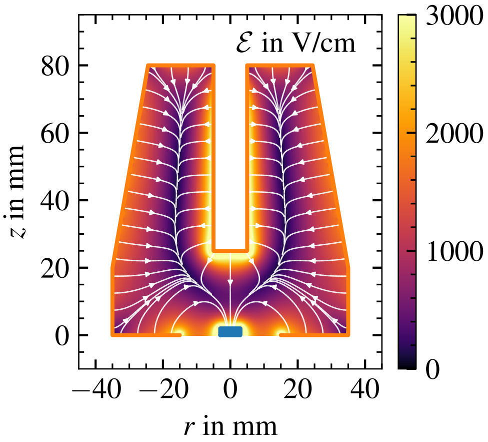

Figure 5.9: Electric field in the example ICPC detector as determined by SSD, together with electric field lines shown in white. For clarity, the electric field is shown only for points inside the detector.

5.5 Calculation of the weighting potentials

The SOR algorithm is also used to calculate the weighting potentials for all contacts of the detector. As there is no $\rho(\vec{r})$ term present in Eq. (3.18), all $Q^{\mathrm{eff}}_{i,j,k}$ and, therefore, $\vec{b}$ in Eq. (5.6) are zero. The weighting potentials for the two contacts of the fully-depleted example ICPC detector are shown in Fig. 5.10.

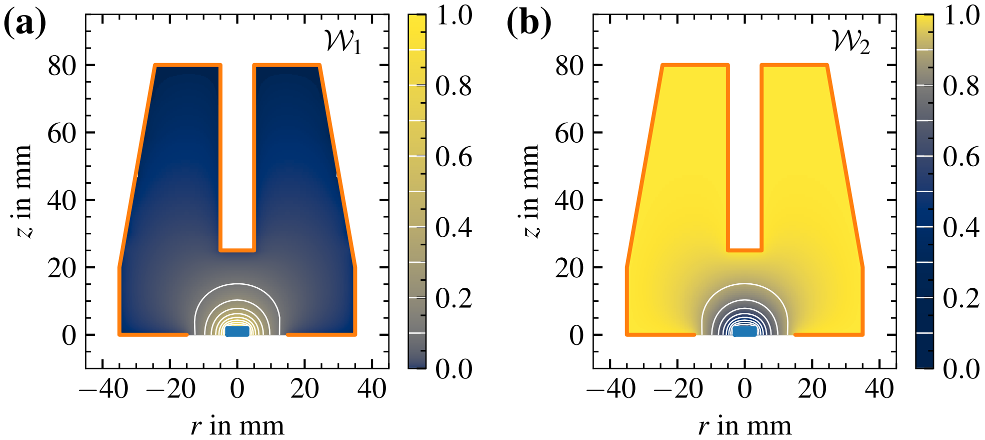

Figure 5.10: Weighting potentials for (a) the point contact, $\mathcal{W}_1$, and (b) the mantle contact, $\mathcal{W}_2$, of the fully-depleted ICPC detector for a bias voltage of 3500 V applied to the mantle contact as calculated with SSD. The gradients of the color bar are chosen as (a) logarithmic and (b) exponential. Equipotential lines are shown for every 10% level.

The impurity density does not directly enter the calculation of the weighting potentials. However, for partially depleted detectors, undepleted volumes determined as described in section 5.3 have to be considered in the calculation of the static weighting potentials. Undepleted volumes are expected to be conductive, i.e. the weighting potentials should be constant within each of the connected undepleted volumes. In SSD, this is effectively achieved by scaling $\varepsilon_r(\vec{r})$ in the undepleted volumes up by several orders of magnitude, e.g. by 10^5, before calculating the weighting potentials. Large values for $\varepsilon_r(\vec{r})$ are compensated by almost vanishing $\vec{\nabla}\mathcal{W}_i(\vec{r})$, see Eq. (3.18), automatically resulting in nearly constant $\mathcal{W}_i(\vec{r})$ in the undepleted volumes.

In Fig. 5.11, the weighting potentials for the example ICPC detector are shown for a bias voltage of 600 V applied to the mantle contact. The undepleted volume, shown in Fig. 5.8a, is directly connected to the point contact, where $\mathcal{W}_1(\vec{r}) = 1$ and $\mathcal{W}_2(\vec{r}) = 0$. Therefore, these weighting potential values extend way further into the bulk than for the fully-depleted ICPC detector, see Fig. 5.10.

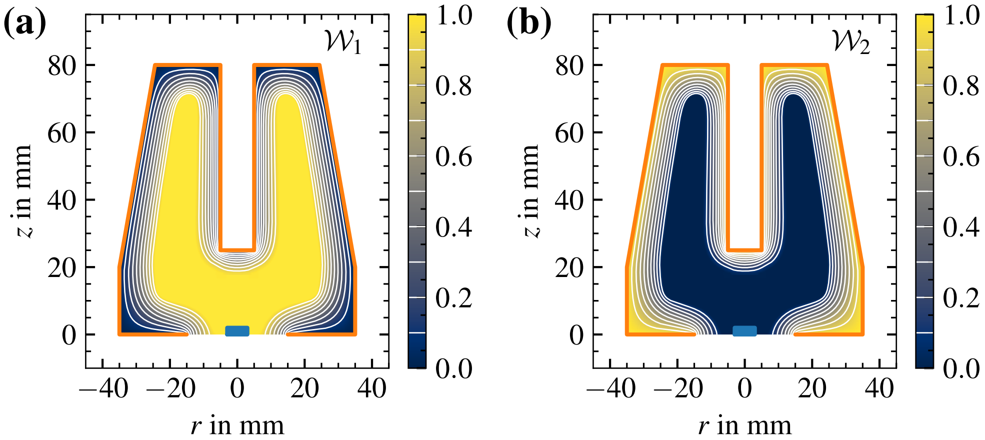

Figure 5.11: Weighting potentials for (a) the point contact, $\mathcal{W}_1$, and (b) the mantle contact, $\mathcal{W}_2$, of the partially depleted ICPC detector for a bias voltage of 600 V applied to the mantle contact as calculated with SSD. Equipotential lines are shown for every 10% level.

5.6 Capacitances

The capacitance, c_{jk}, between two contacts, S_j and S_k, can be calculated from the weighting potentials, see section 3.4.3. The weighting potentials $\mathcal{W}_j$ and $\mathcal{W}_k$ are determined independently of each other, possibly on different grids, depending on the detector geometry and the grid refinement. Therefore, both weighting potentials have to be mapped onto the same grid, e.g. by interpolating $\mathcal{W}_k$ onto the grid of $\mathcal{W}_j$. Then, the volume integral in Eq. (3.22) can be evaluated over all voxel volumes. The gradients of the weighting potentials are computed numerically using finite differences as shown for the electric field in section 5.4.

5.7 Charge drift simulation

The charge drift simulation in SSD is based on the electric field obtained from the field calculation and on charge drift models, e.g. the ones presented in chapter 4. The simulation of electron and hole drift paths, $\vec{r}_e(t)$ and $\vec{r}_h(t)$, requires the user to pass energies and locations of energy deposits to SSD. This can either be done manually by the user or by reading in output files from computational tool-kits which simulate the passage of particles through matter, e.g. GEANT4 [177]. The deposited energy, E_dep, defines the expected number of electron-hole pairs, see Eq. (3.12). The charges expected in the electron and hole clouds are $-q_e = q_h = e\langle N_{eh}\rangle = e\,E_\text{dep}/E_{eh}$.

The subsequent drift of the electron and hole clouds is described in this section. For simplicity, the event is assumed to consist of only one energy deposit. However, the following description also applies to events with multiple energy deposits.

5.7.1 Basic charge drift simulation

In the basic charge drift simulation, the electron and hole clouds are each described as single point charges. For each step, the electric fields at $\vec{r}_e$ and $\vec{r}_h$ are linearly interpolated from the electric field values at the six closest grid points. Then, the drift velocities $\vec{\upsilon}_e$ and $\vec{\upsilon}_h$ are determined from the electric field, e.g. using drift models presented in sections 4.4.1 and 4.4.2. The drift step is calculated as the product of $\vec{\upsilon}_{e/h}$ and Δt, resulting in a new position of

$$\vec{r}_{e/h}(t+\Delta t) = \vec{r}_{e/h}(t) + \vec{\upsilon}_{e/h}(\vec{\mathcal{E}}(\vec{r}_{e/h}(t))) \,. \tag{5.10}$$

If the new position is still inside the bulk of the detector, the position is updated and the next step is initiated. Otherwise, the intersection between the surfaces of the detector and the line that connects $\vec{r}_{e/h}(t)$ and $\vec{r}_{e/h}(t+\Delta t)$ is determined. If the intersection is a contact, then the charge is moved into the contact and the drift for that point charge is completed. If the intersection is not contacted, then the drift step is projected parallel to the surface and scaled by a factor if wanted by the user. The latter can account for differently fast surface drifts compared to the drifts in the bulk.

The basic charge drift simulation procedure captures the dominant contribution to the charge drift given by the static electric field inside of the detector. However, it neglects effects arising from the substructure of the charge clouds, see section 4.5.

5.7.2 Charge drift simulations including charge cloud effects

Charge cloud effects, e.g. diffusion and Coulomb self-repulsion of the charge carriers, within one charge cloud cannot be modeled if the cloud is described as a single point charge. SSD offers the possibility to simulate a charge cloud using multiple point charges which can diffuse independently and repel from other charge carriers within the same charge cloud. The number of point charges is set by the user.

In SSD, two models for the initial distribution of the point charges within one charge cloud are implemented, see Fig. 5.12. Both start with a point charge at the position of the energy deposit. Around that center charge, additional point charges are placed on shells. If the number of point charges is $\lesssim 50$, point-like objects are placed on the vertices of platonic solids in each shell, see Fig. 5.12a. For higher numbers of point charges, each shell consists of point-like objects that are evenly distributed on spheres, see Fig. 5.12b. The number and the radius of the shells can be set by the user. If point charges are placed outside of the detector volume, they are moved inside along the direction towards the center charge.

The charge resulting from E_{dep} is distributed onto the individual point charges. SSD provides functions to distribute the charge equally onto all point charges or exponentially decreasing with distance to the center charge. Other charge distribution methods can easily be implemented by the user.

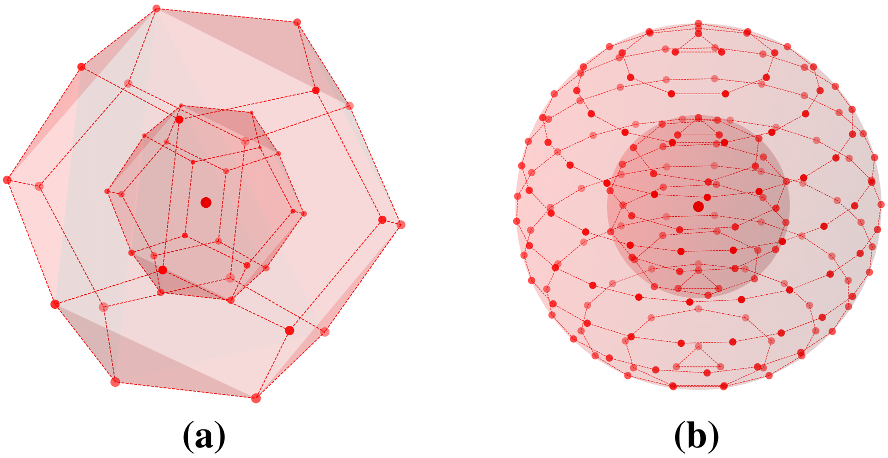

Figure 5.12: Example initial configurations of charge clouds consisting of a center charge and (a) 40 charges distributed on two shells, each of which consists of vertices of a dodecahedron, and (b) 200 charges evenly distributed on two spherical shells. Charges as shown as red points. Dashed lines are shown to guide the eye.

5.7.2.1 Diffusion

In SSD, diffusion is modeled using a random-walk algorithm [186]: For each time step and point charge, a diffusion step vector with fixed length $\sqrt{6D_{e/h}\Delta t}$ but random orientation is added onto the step vector resulting from the electric field. The default values in SSD for the diffusion coefficients in germanium are $D_e = 101\,\mathrm{cm}^2/\mathrm{s}$ and $D_h = 49\,\mathrm{cm}^2/\mathrm{s}$. The user can also pass custom values for $D_{e/h}$ to SSD.

Figure 5.13 shows the result of a diffusion simulation, where charge clouds consisting of 50 electrons and holes were diffusing in the absence of an external electric field for 1000 ns in time steps of $\Delta t = 1\,\mathrm{ns}$ using the default values for $D_{e/h}$. As $D_e > D_h$, the electron cloud expands faster than the hole cloud, see Figs. 5.13a and 5.13b. The size evolution of the electron and the hole charge cloud shown in Fig. 5.13c agrees very well with the analytical expression for the root mean square of $\sqrt{6D_{e/h}t}$ expected in three dimensions, see section 4.5.1.

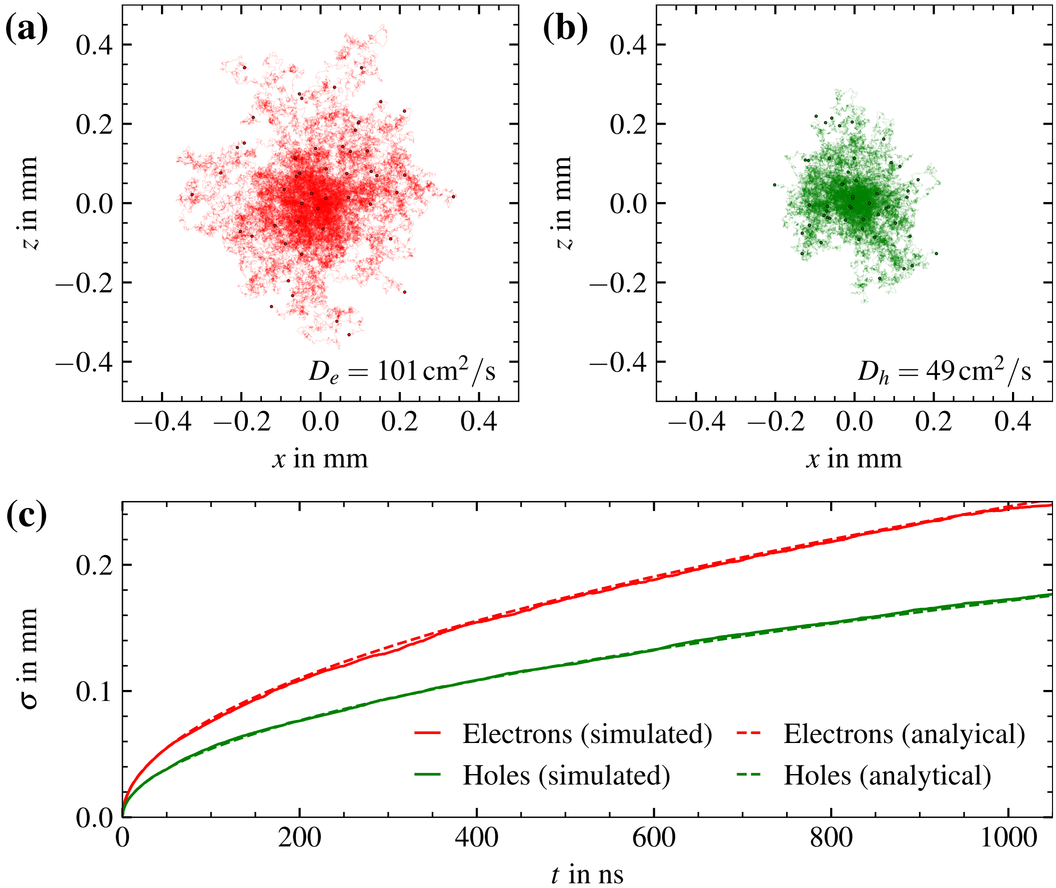

Figure 5.13: Two-dimensional projection of the distribution of (a) 50 electrons and (b) 50 holes starting at the origin of the coordinate system and diffusing for 1000 ns as simulated with SSD. (c) Size evolution of diffusing charge clouds consisting of 1000 point charges as a function of time, t. The size, σ, was calculated from the simulated drift paths as the root mean squared distance of all electrons/holes to the center of the charge cloud. The analytical expectations $\sigma_{e/h} = \sqrt{6D_{e/h}t}$ are shown as dashed lines for comparison. All simulations were performed with $\Delta t = 1\,\mathrm{ns}$ and the default values $D_e = 101\,\mathrm{cm}^2/\mathrm{s}$ and $D_h = 49\,\mathrm{cm}^2/\mathrm{s}$.

5.7.2.2 Coulomb self-repulsion

The implementation of the Coulomb self-repulsion in SSD is very straightforward. In each step, the distance between each pair of point charges is determined. Each point charge, P, at position, $\vec{r}_P$, with charge q_P creates an additional electric field,

$$\vec{\mathcal{E}}(\vec{r}) = \frac{q_P}{4\pi\varepsilon_0\varepsilon_r(\vec{r})|\vec{r}-\vec{r}_P|^2} \cdot \frac{\vec{r}-\vec{r}_P}{|\vec{r}-\vec{r}_P|} \, . \tag{5.11}$$

This electric field is added onto the static electric field. Then, the drift velocity vector is determined and the charges are drifted as explained is section 5.7.1.

Figure 5.14 depicts the effects of Coulomb self-repulsion onto charge clouds consisting of 500 point charges each with a charge corresponding to 500 eV. For $\mathcal{E} < \mathcal{E}_0$, the charge-carrier mobilities are $\mu_e \approx 38570\,\text{cm}^2/\text{Vs}$ and $\mu_h \approx 61500\,\text{cm}^2/\text{Vs}$, see Tab. 4.1. Thus, the hole cloud expands faster than the electron cloud, see Figs. 5.14a and 5.14b. The analytical expression for the root mean square of $\sqrt{3/5}\sqrt[3]{3\mu_{e/h}Qt/4\pi\varepsilon_0\varepsilon_r}$ is very well reproduced by the charge drift simulation, see Fig. 5.14c.

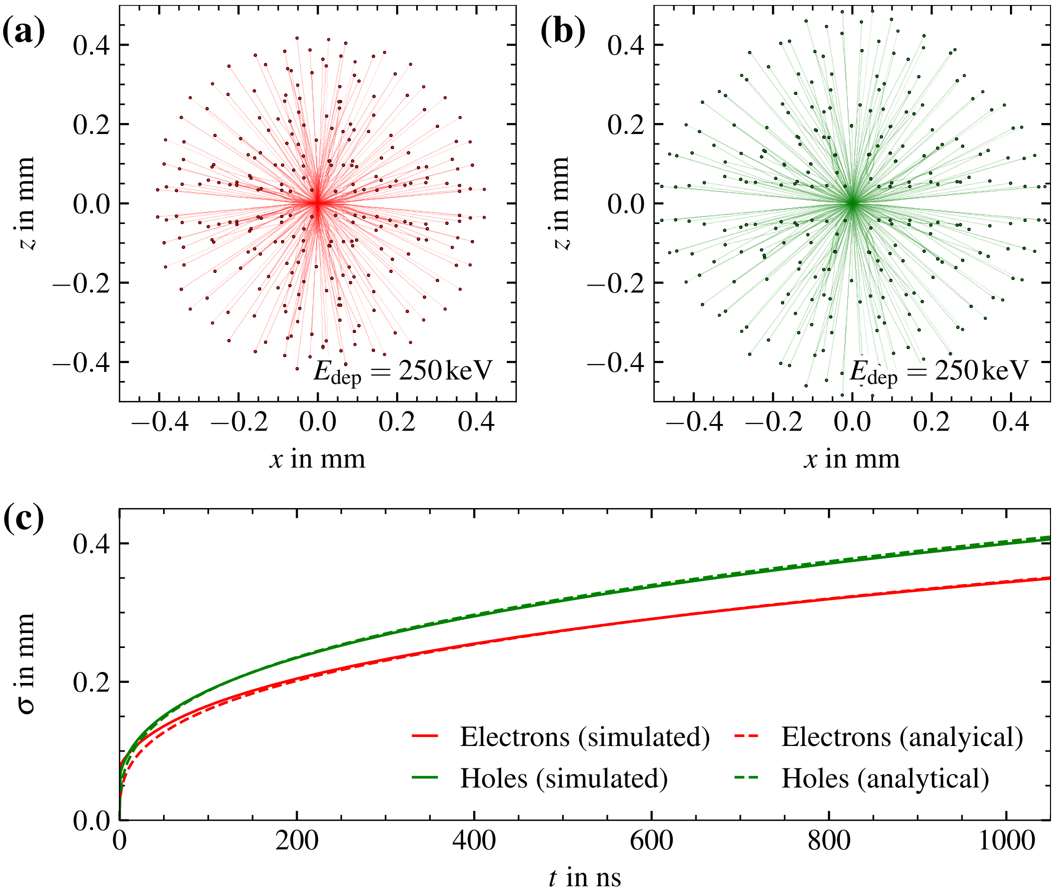

Figure 5.14: Two-dimensional projection of the distribution of (a) 500 electrons and (b) 500 holes starting on a sphere with radius 1 µm around the origin and self-repelling for 1000 ns as simulated with SSD. (c) Size evolution of these charge clouds as a function of time, t. The analytical expectations $\sigma_{e/h} = \sqrt{3/5}\sqrt[3]{3\mu_{e/h}Qt/4\pi\varepsilon_0\varepsilon_r}$ are shown as dashed lines for comparison. All simulations were performed with $\Delta t = 1\,\text{ns}$ and $E_\text{dep} = 250\,\text{keV}$. The energy is equally distributed onto all 500 point charges.

5.7.2.3 Initial charge-cloud size

In interactions of gammas with germanium, the initial size of the electron and hole clouds depend on the energy of the recoil electron, see section 4.5.3. The initial charge-cloud size defines an initial condition for the solution of the continuity equation.

For a spherical charge cloud with initial size, σ_0, the root mean square of the expanding cloud due to diffusion, $\sigma_{e/h}^{\text{diff}}$, and due to Coulomb self-repulsion, $\sigma_{e/h}^{\text{SR}}$, are

$$\sigma_{e/h}^{\text{diff}} = \sqrt{6D_{e/h}t + \sigma_0^2} \tag{5.12}$$

$$\sigma_{e/h}^{\text{SR}} = \sqrt[3]{\sqrt{27/125}\cdot 3\mu_{e/h}Qt/4\pi\varepsilon_0\varepsilon_r + \sigma_0^3}\,. \tag{5.13}$$

Figure 5.15 depicts the size evolution of the electron and hole clouds for energy deposits, E_{dep}, of 300 keV, 662 keV and 1020 keV. The initial charge clouds are modeled as 2000 point charges, evenly distributed on a spherical shell with a diameter equal to the practical range of electrons at the respective energy [181], see Tab. 4.3.

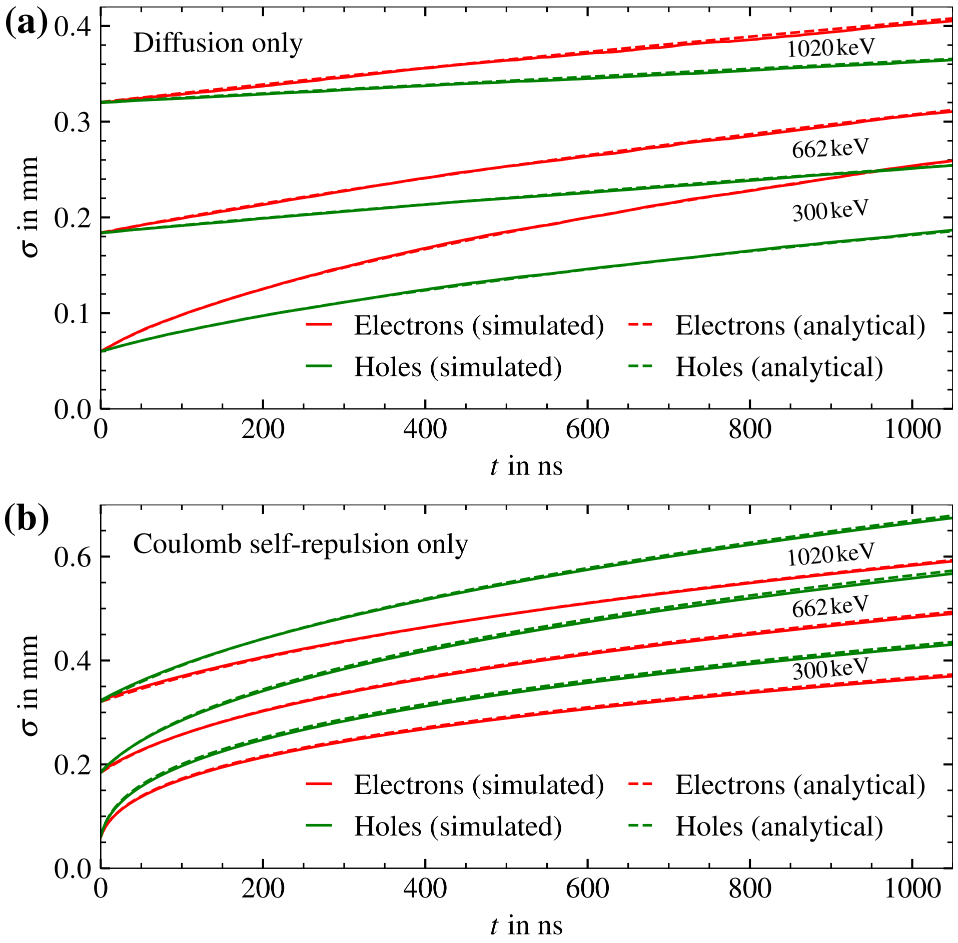

Figure 5.15: Simulated size evolution of spherical charge clouds as a function of time, t, resulting from (a) diffusion only and (b) Coulomb self-repulsion only, resulting from SSD simulations (solid) and the analytical expressions in Eqs. (5.12) and (5.13) (dashed). The diameters of the initial charge clouds are set to the practical range for the annotated energies, see Tab. 4.3.

Fig. 5.15a depicts the charge-cloud expansion due to diffusion. For $E_\mathrm{dep} = 300\,\mathrm{keV}$, the charge-cloud size increases by a factor of 4 for electrons and a factor of 3 for holes after diffusing for 1000 ns. The relative increase after diffusion for 1000 ns is 67% for electrons 42% for holes for $E_\mathrm{dep} = 662\,\mathrm{keV}$, and 26% for electrons and 12% for holes for $E_\mathrm{dep} = 1020\,\mathrm{keV}$. The relative importance of diffusion effects decreases with E_dep due to the expansion rate not depending on E_dep but exclusively on the diffusion coefficients $D_{e/h}$.

The size evolution of the charge clouds due to Coulomb self-repulsion is shown in Fig. 5.15b. In this case, E_dep does not only affect the initial size of the charge clouds but also the expansion rate via the charge Q contained within the clouds, see Eq. (5.13). For $E_\mathrm{dep} = 300\,\mathrm{keV}$, the electron and hole clouds expand to approximately 7 and 6 times their initial size after 1000 ns, respectively. For $E_\mathrm{dep} = 1020\,\mathrm{keV}$, the electron cloud is more than twice and the hole cloud is slightly less than twice the initial size due to Coulomb self-repulsion after 1000 ns. While the relative increase in charge-cloud size decreases with E_dep, the absolute increase in charge-cloud size is 350 µm for electrons and 300 µm for holes.

5.8 Pulse-shape simulation

The charge pulses induced on the contacts are computed from the drift paths of the charges and the weighting potentials of the contacts using the Schockley-Ramo theorem, see section 3.4. For each point-like object, P, with charge q_P and drift path, $\vec{r}_P(t)$, the induced charge on the contact S_i is given by

$$Q_i(t) = \sum_P q_P \mathcal{W}_i(\vec{r}_P(t)) \,, \tag{5.14}$$

where $\mathcal{W}_i(\vec{r}_P(t))$ is linearly interpolated from the values at the closest grid points.

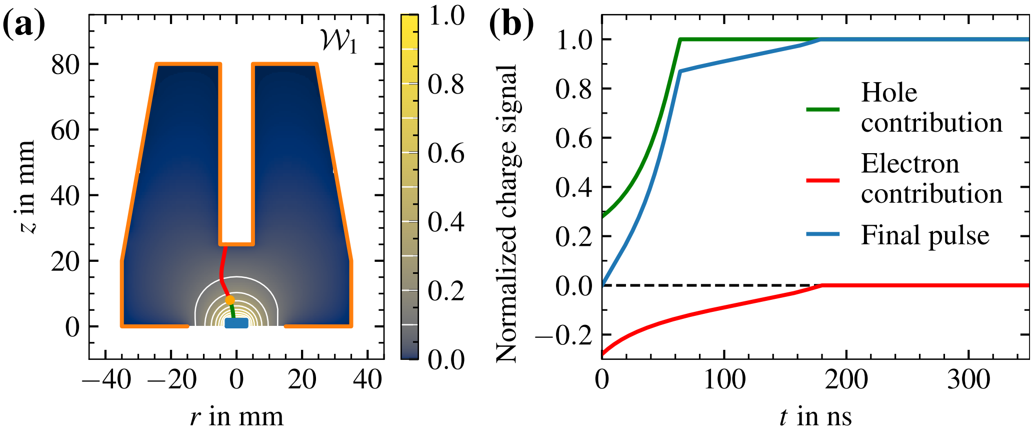

Figure 5.16: (a) Electron and hole drift paths as simulated with SSD for a point-like energy deposit at $r = -2\,\mathrm{mm}$ and $z = 8\,\mathrm{mm}$ in the example ICPC detector, together with the weighting potential $\mathcal{W}_1(\vec{r})$ of the point contact in logarithmic color scale. The location of the energy deposit is shown as an orange dot, the electron drift path as a red line and the hole drift path as a green line. (b) Induced charges by the electrons (red) and holes (green), as well as the final charge pulse (blue) on the point contact, normalized to its amplitude.

Figure 5.16a depicts the results from the basic charge drift simulation of a single-site event in the example ICPC detector. The energy is deposited close to the point contact, where $\mathcal{W}_1(\vec{r}_{\text{dep}}) \approx 0.3$. Therefore, the electron cloud induces a negative charge of $0.3q_e$ and the hole cloud induces a positive charge of $0.3q_h$ on the point contact. As $q_h = -q_e$, both contributions cancel and the net induced charge on the point contact at the time of the electron-hole pair creation is zero, see Fig. 5.16b. As the mantle contact is at a positive potential, it attracts the electrons, which drift into a region where $\mathcal{W}_1(\vec{r})$ becomes smaller. The holes drift towards the point contact where $\mathcal{W}_1(\vec{r})$ becomes larger. Thus, the hole contribution to the point-contact pulse shape increases and the electron contribution decreases with time, see Fig. 5.16b.

Kinks are observed in the simulated pulse shapes shown in Fig. 5.16b when the holes or the electrons are collected on the contacts. The hole drift towards the point contact results in a steep slope of the pulse compared to the still ongoing electron drift after the holes are collected after around 60 ns. This is because the gradient of $\mathcal{W}_1(\vec{r})$ is steeper close to the point contact than close to the mantle contact. For the ICPC detector geometry, kinks preceded by steep slopes are attributed to hole collections and kinks with preceding moderate slopes are attributed to electron collections.

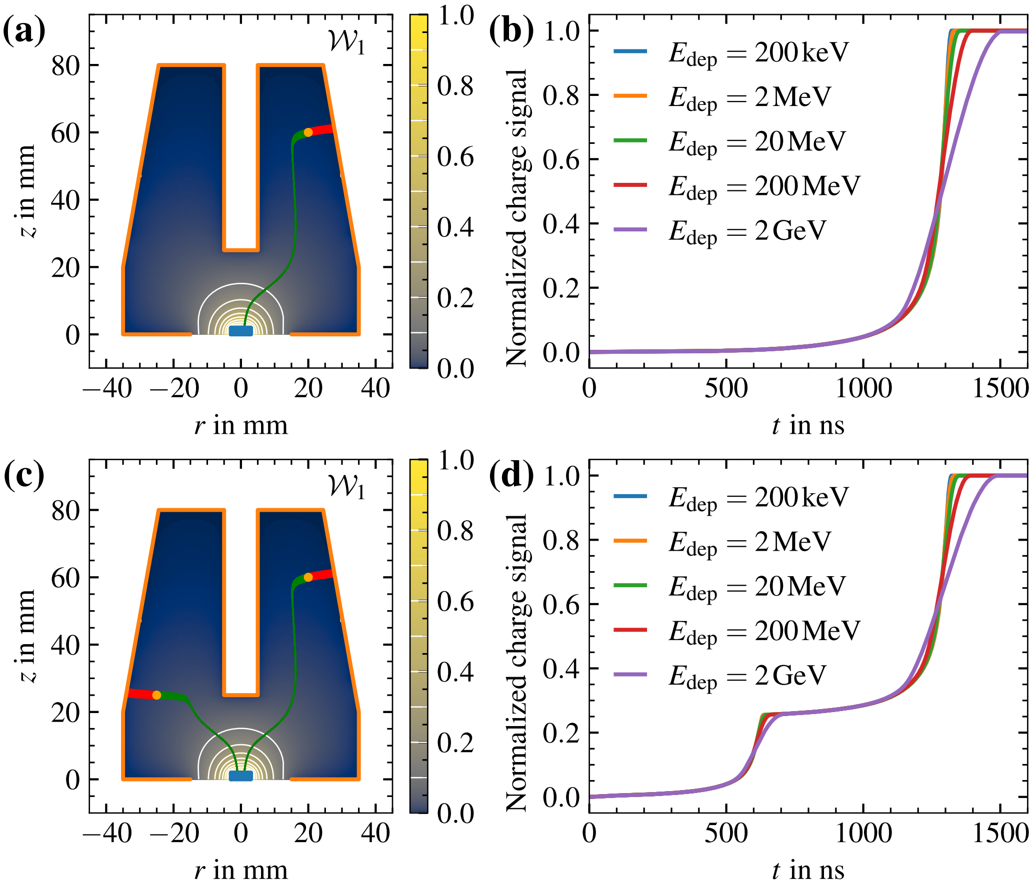

Figure 5.17: Electron and hole drift paths as simulated with SSD (a) for a single-site event and (b) for a multi-site event in the example ICPC detector. The electron and hole charge clouds each consist of 250 point charges. The locations of the energy deposits are shown as orange dots, the electron drift paths as red lines and the hole drift paths as green lines. (b, d) Resulting normalized charge signals on the point contact for different E_{dep} as given in the legend.

In Figs. 5.17a and 5.17c, events with energy deposits far away from the point contact, where $\mathcal{W}_1(\vec{r}_{\text{dep}}) < 0.01$, are depicted. Each energy deposit was simulated as a charge cloud consisting of 250 electrons and 250 holes, allowing for diffusion and Coulomb self-repulsion of the charge carriers within the charge clouds.

In Fig. 5.17b, the core pulse shapes for single-site events with different E_{dep} in the ICPC detector are shown. The electron contribution is below the percent level, i.e. the pulse shapes are almost exclusively given by the hole contribution. At first, the holes drift in regions with low $\vec{\mathcal{E}}(\vec{r})$ and small $\mathcal{W}_1(\vec{r})$, resulting in an almost flat beginning of the pulse. Shortly before the holes reach the point contact, they pass through a region where $\vec{\mathcal{E}}(\vec{r})$ and $\mathcal{W}_1(\vec{r})$ are strong, resulting in a very steep rise of the core pulse. The kink observed at $t = 1300\,\text{ns}$ for $E_{\text{dep}} = 200\,\text{keV}$, preceded by the sharp rise, implies that the holes are collected 1300 ns after they were created.

Figure 5.17d depicts the pulse shape for a multi-site event in the ICPC detector. It features two kinks preceded by sharp rises at around 650 ns and 1300 ns. These can be associated with the two times at which the respective hole cloud reaches the point contact: 650 ns for the closer, and 1300 ns for the more distant cloud.

Figure 5.17 also demonstrates the effects of diffusion and Couloumb self-repulsion on the charge-drift and the shape of the pulse. The effects of diffusion on the pulse shape are expected to depend only on the diffusion coefficients $D_{e/h}$ but not on the deposited energy E_{dep}. In contrast, the effects of Coulomb self-repulsion on the pulse shapes increase with E_{dep}. This is because the electric field created by a charge cloud itself scales with $\mathcal{E} \propto \sqrt{Q} \propto \sqrt{E_{\text{dep}}}$. The more the charge cloud expands, the earlier the first holes and the later the last holes reach the point contact. Therefore, the rise begins earlier and ends later with increasing E_{dep}, see Figs. 5.17b and 5.17d.

The duration of the hole collection, t_{coll}, is the time between the first and the last hole reaching the point contact. If the hole charge cloud is modeled as a single point charge, t_{coll} becomes zero by definition. The charge cloud in the single-site event shown in Fig. 5.17a was modeled consisting of 250 point charges evenly distributed on a spherical shell with a diameter of the practical range at a given energy, see Eq. (4.48). Allowing for an independent drift of the individual point charges and including diffusion in the simulation already results in $t_{\text{coll}} = 14\,\text{ns}$. The effect of Coulomb self-repulsion on t_{coll} depends on E_{dep} and is shown in Fig. 5.18. From 0 to 2.5 MeV, Coulomb self-repulsion results in an increase of t_{coll} to 82 ns.

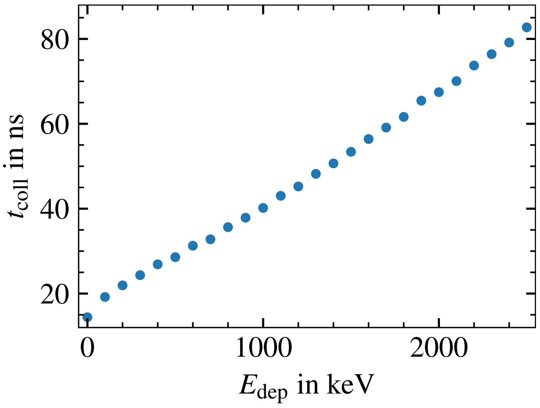

Figure 5.18: Duration of the hole collection, t_{coll}, as a function of deposited energy, E_{dep}, for the single-site event at $r = 20\,\text{mm}$ and $z = 60\,\text{mm}$ shown in Fig. 5.17a. The electron and hole clouds each consist of 250 point charges. Diffusion and self-repulsion are added to the simulation. The point at $E_{\text{dep}} = 0\,\text{keV}$ corresponds to diffusion only.

5.9 Post-processing of simulated pulses

5.9.1 Influence of the read-out electronics on the pulse shapes

The simulated charge pulses, $Q_i(t)$, for events with E_{dep} of up to a few MeV tend to have pronounced edges and kinks which occur on time scales of a few ns, see Figs. 5.17b and 5.17d. These features are smoothed out in measurements due to the limited bandwidth of the read-out electronics. In order to simulate data-like pulses, $Q_i^{\text{meas}}(t)$, the effects of the electronics on the pulses have to be properly modeled and applied to the simulation output.

The effects of the read-out electronics on charge pulses can be expressed via the so-called response function, $\zeta(t)$. It describes what would be measured by the read-out electronics for a Dirac δ-like pulse as input and is typically determined experimentally when characterizing the read-out electronics.

Mathematically, the influence of the read-out electronics is described as the convolution of the simulated $Q_i(t)$ with the response function, $\zeta_i(t)$, of the read-out of contact i, plus random noise, $n(t)$:

$$Q_i^{\text{meas}}(t) = (\zeta_i * Q_i)(t) + n(t) \ . \qquad (5.15)$$

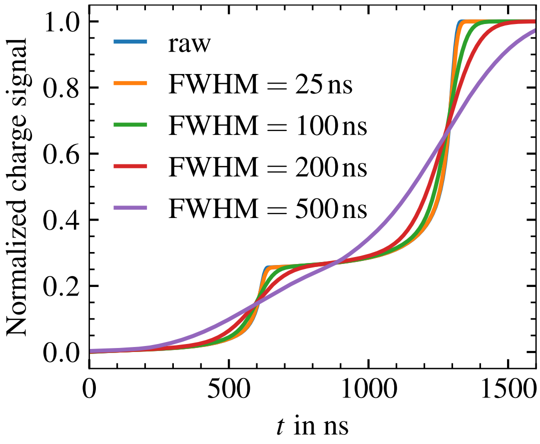

Figure 5.19: Simulated charge pulse from the multi-site event with $E_{\text{dep}} = 2\,\text{MeV}$ shown in Fig. 5.17d, convolved with Gaussian response functions with FWHM as given in the legend.

To demonstrate the effect of the response function on the final pulse shapes, Gaussian response functions with different full widths at half maximum, FWHM, were convolved with the example pulse with $E_{\text{dep}} = 2\,\text{MeV}$ from Fig. 5.17d. The results are shown in Fig. 5.19.

The electronics to read out pulses from germanium detectors typically have bandwidths of 10 to 15 MHz, corresponding to a FWHM between 20 and 40 ns. For the response function with a FWHM of 25 ns, the pulse shape looks almost identical to the raw pulse obtained from the SSD simulation. The only observable differences are the smoothed-out kinks directly after the sharp rises of the pulse.

The smoothing of the kinks becomes more pronounced with increasing FWHM. The time difference between the charge collection time at 1300 ns and the pulse reaching its final amplitude is approximately the FWHM of the response function. The fast rises can only be resolved if the FWHM of the response function is comparable to the time scale within which the fast rise is expected. For the example pulse shown in Fig. 5.19, a response function with a FWHM of 500 ns almost completely smooths out the double-kink structure, hiding characteristic features of the pulse relevant for pulse shape analysis.

5.9.2 Cross-talk models

The number of pulses obtained per event corresponds to the number of read-out contacts of the detector, N. These N pulses are not only subject to the limited bandwidth of the read-out electronics but also to possible cross-talk effects, see section 3.4.4.

The relation between the simulation output, $Q_i(t)$, and the pulses after applying cross-talk, $Q_i^C(t)$, can be modeled via two cross-talk matrices, C^L and C^D:

$$\underbrace{\begin{bmatrix} Q_1^C(t) \\ \vdots \\ Q_N^C(t) \end{bmatrix}}_{=\vec{Q}^C(t)} = \underbrace{\begin{bmatrix} C_{1,1}^L & \cdots & C_{1,N}^L \\ \vdots & \ddots & \vdots \\ C_{N,1}^L & \cdots & C_{N,N}^L \end{bmatrix}}_{=C^L} \underbrace{\begin{bmatrix} Q_1(t) \\ \vdots \\ Q_N(t) \end{bmatrix}}_{=\vec{Q}(t)} + \underbrace{\begin{bmatrix} C_{1,1}^D & \cdots & C_{1,N}^D \\ \vdots & \ddots & \vdots \\ C_{N,1}^D & \cdots & C_{N,N}^D \end{bmatrix}}_{=C^D} \underbrace{\begin{bmatrix} \frac{\mathrm{d}}{\mathrm{d}t} Q_1(t) \\ \vdots \\ \frac{\mathrm{d}}{\mathrm{d}t} Q_N(t) \end{bmatrix}}_{=\frac{\mathrm{d}}{\mathrm{d}t}\vec{Q}(t)} . \tag{5.16}$$

The non-diagonal matrix elements, $C_{j,k}^L$ and $C_{j,k}^D$, describe the linear and differential cross-talk on contact S_j originating from contact S_k. The diagonal elements of the linear cross-talk matrix, $C_{j,j}^L$, describe the amplification of the pulse $Q_j(t)$ given by the read-out of the contact S_j. The diagonal elements of the differential cross-talk matrix, $C_{j,j}^D$, are zero as the concept of cross-talk of a contact onto itself would imply a self-amplification which is non-physical here.

The models for the limited bandwidth of the read-out electronics and for cross-talk can also be combined. If ζ_j is the response function of contact S_j, then

$$Q_j^C(t) = \zeta_j * \left(\sum_{k=1}^{N} C_{i,k}^L Q_k + \sum_{k=1}^{N} C_{i,k}^D \frac{\mathrm{d}}{\mathrm{d}t} (\zeta_k * Q_k) \right)(t) , \tag{5.17}$$

where the response functions are applied to the pulses entering the differential cross-talk and the final set of pulses.

6 The segmented Broad Energy germanium detector

The charge-drift models and mobility parameters used in SSD are tested against data to examine their validity. This is done by simulating existing detectors and comparing the output of the simulation to data. For this thesis, a p-type segmented Broad Energy germanium, segBEGe, detector was chosen as test detector.

6.1 Detector geometry and specifications

The p-type segBEGe detector is a research detector designed at the Max Planck Institute for Physics in Munich and produced by Mirion Technologies, formerly Canberra France. The geometry of the p-type segBEGe detector is depicted in Fig. 6.1 and its specifications are listed in Tab. 6.1. Its geometry resembles that of regular unsegmented p-type BEGe detectors as used in the LEGEND experiment but its segmentation allows for more detailed studies.

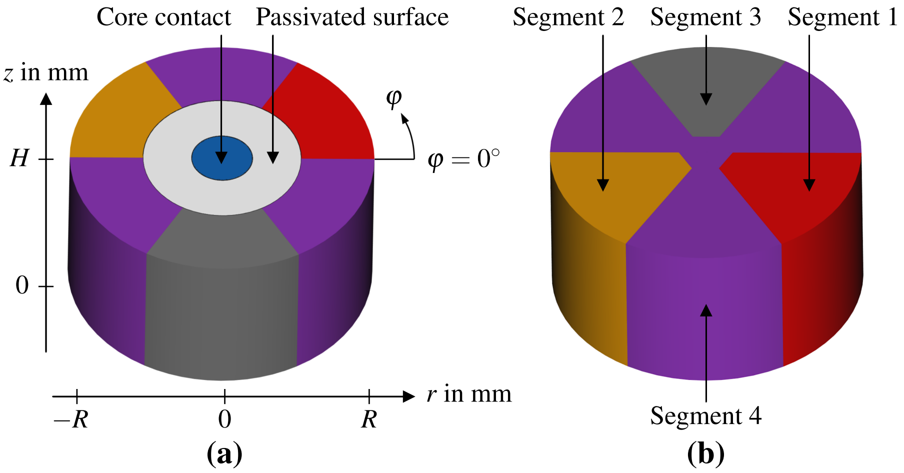

Figure 6.1: Schematic of the segBEGe detector geometry: (a) top view and (b) bottom view. In (a), the cylindrical coordinate system to describe positions in the segBEGe detector is shown.

The p-type segBEGe detector has a diameter of 74.5 mm and a height of 39.5 mm. It features a 15 mm-diameter p^+ point contact, i.e. the core contact, on the top surface and a four-fold segmented n^+ contact on the mantle surface of the detector. The core contact is surrounded by a passivated area with a diameter of 39 mm, see Fig. 6.1a. Segments 1, 2 and 3 each extend over an arc of 60° and cover the outer 30 mm on the bottom surface. Segment 4 covers the remaining regions and has a closed bottom end-plate, see Fig. 6.1b.

Table 6.1: Specifications of the p-type segBEGe detector as provided by Mirion Technologies [187].

Core contact material	p^+ boron
Segment contact material	n^+ lithium
Diameter $2R$	74.5 mm
Height H	39.5 mm
Core contact diameter	15.0 mm
Passivation outer diameter	39.0 mm
Net impurity density (top)	$6.5 \cdot 10^9\,\mathrm{cm}^{-3}$
Net impurity density (bottom)	$5.8 \cdot 10^9\,\mathrm{cm}^{-3}$
Recommended V_B at core	−3000 V

The core contact of the p-type segBEGe detector was fabricated using boron implantation. Thus, the core contact is expected to extend only up to 500 nm into the bulk. The segment contacts were fabricated using lithium diffusion. Therefore, they are expected to penetrate up to 1 mm into the bulk of the detector [187, 188]. To ensure that the segments do not overlap, the segments are more than 1 mm apart. The segment contacts are coated with a thin film of aluminum to provide easy contacting and to achieve better field stability.

The manufacturer recommends applying a bias voltage of $-3000\,\mathrm{V}$ to the core contact in order to fully deplete the detector. The segment contacts are kept at ground. The full-depletion voltage was measured to be $V_D = -1275\,\mathrm{V}$.The manufacturer also provided values for the net impurity density at the top and at the bottom of the detector determined from Hall measurements, see Tab. 6.1. According to these values, impurity density increases by 12.1% from the bottom to the top.

In this thesis, positions in the p-type segBEGe detector are described using the cylindrical coordinates, r, φ and z, shown in Fig. 6.1a. The center of the detector in the horizontal plane is defined as $r = 0\,\mathrm{mm}$. The polar angle has its origin $\varphi = 0^\circ$ at the boundary between the segments 1 and 4 which is closer to segment 3 and increases counterclockwise, looking from the top. The bottom of the detector corresponds to $z = 0\,\mathrm{mm}$. The color scheme used in Fig. 6.1 for the contacts is used throughout this thesis. Whenever subscripts are used for variables, the subscript 0 refers to the core, while the subscripts 1, 2, 3 and 4 refer to the segment with the respective number.

6.2 Detector cryostat K2 and data-acquisition system

The p-type segBEGe detector is installed inside the cryostat K2 depicted in Fig. 6.2. The cryostat facilitates the operation in a vacuum environment and at stable temperatures, allowing for the investigation of the temperature dependence of pulse shapes.

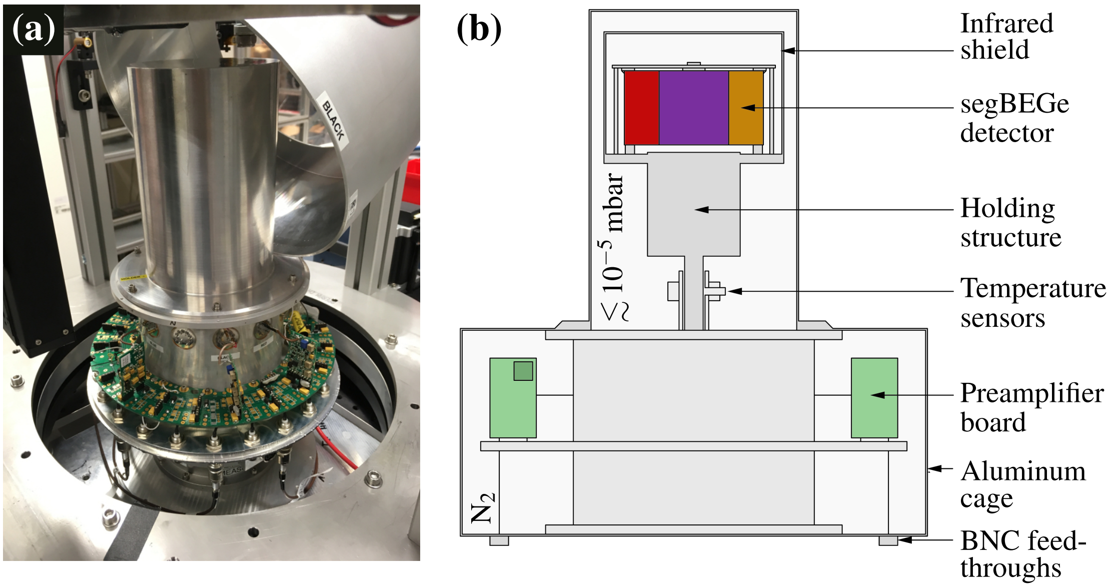

Figure 6.2: (a) Photo and (b) schematic cross-section of the top part of the detector cryostat K2.

The detector is embedded in a holding structure which keeps the detector at a stable position inside the cryostat, see Fig. 6.2b. The bottom part of this holding structure is connected to a copper cold finger which thermally connects the detector to the electric cooling system which is externally supported by water cooling. The cooling system constantly reads out the temperature via a temperature sensor installed at the tip of the cold finger and keeps the temperature stable to $\pm 0.5\,\mathrm{K}$ through a feedback loop. In addition, the temperature can also be read out by a set of three temperature sensors which are attached to the bottom of the detector holding structure, see Fig. 6.2b.

The volume surrounding the detector is pumped to a vacuum of $\lesssim 10^{-5}$ mbar. In addition, molecular sieves installed inside the cryostat absorb extraneous gases. This prevents contaminations on the surface of the detector resulting from cold trapping or from attracting small charged particles which can lead to surface leakage currents and increased electronic noise.

For each event, the p-type segBEGe detector produces one charge pulse for each of the five contacts, see section 3.4. Charge-sensitive read-outs [189] are used to convert these charge pulses to voltage pulses which are then further processed by the data acquisition system, DAQ. The charge-sensitive preamplifier system used for the p-type segBEGe detector is depicted in Fig. 6.3.

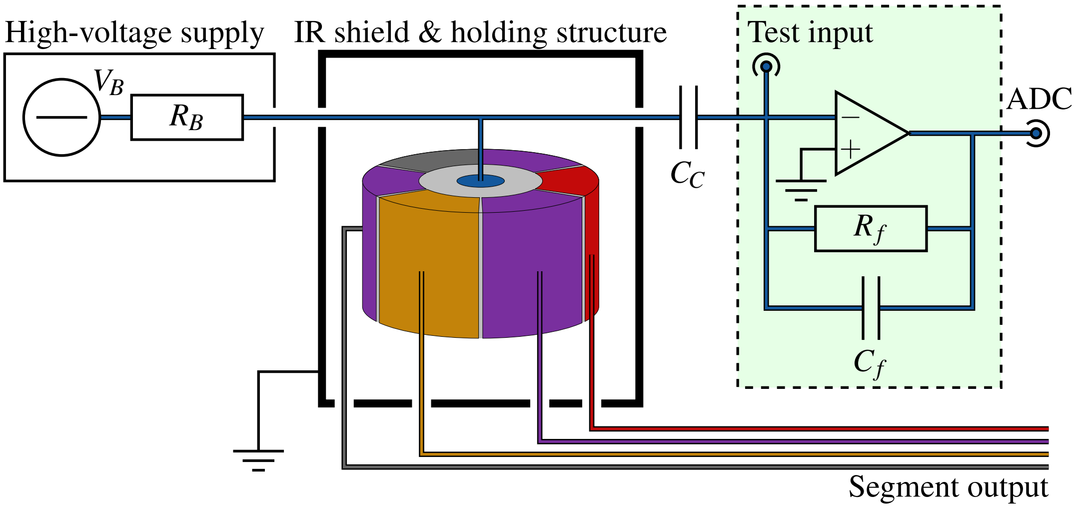

Figure 6.3: Schematic of the data acquisition system of the p-type segBEGe detector. The simplified RC feedback charge-sensitive preamplifier circuit used for the core output is highlighted in green. The bias voltage V_B is applied through a bias resistor R_B and decoupled from the core preamplifier system by the coupling capacitor, C_C. The segments are kept at ground through their preamplifiers. The preamplifier systems reading out the segments are not shown.

In charge-sensitive amplifiers, the charges from the detector are collected on the feedback capacitor, C_f. The output voltage is proportional to the integrated charge on C_f. If the detector contact collects charge carriers, charge accumulates on C_f. To reset the output voltage to the initial baseline value, a resistor, R_f, is included in the feedback loop. This ensures the exponential discharge of the feedback capacitor with a characteristic 1/e decay time, $\tau = R_f C_f$, which is around 50 µs for all contact read-outs.

Each contact of the p-type segBEGe detector is connected to its own PSC823C preamplifier [190]. The complete preamplifier boards for processing the segment outputs are placed in a ring around the cryostat below the vacuum cap housing the detector, see Fig. 6.2. The preamplifier ring is covered by an aluminum cage to screen against electromagnetic radiation and flushed with gaseous nitrogen to prevent corrosion damage.

For the core contact, C_f and R_f as well as a part of the preamplifier are installed very close to the core contact in the cold part of K2. This prevents electronic noise resulting from the capacitance of a long cable, improving the energy resolution of the core contact. The coaxial wire connected to the core contact is used both to apply the bias voltage, V_B, through a bias resistor, R_B, and to the read out the pulses. The constant offset in the electric potential of V_B is filtered out by inserting a coupling capacitor, C_C, of 1.2 nF between the core contact and the core preamplifier, see Fig. 6.3. The remaining preamplifier read-out electronics for the core are placed at room temperature in the preamplifier ring together with the segment amplifiers.

The amplified voltage pulses are accessed from the outside through cable feed-throughs at the bottom of the preamplifier ring and passed to a 16-channel analog-to-digital converter, ADC, STRUCK SIS3316-250-14 [191]. Pulses from events exceeding a predefined threshold in the core are recorded with a sampling frequency of 250 MHz, i.e. a sampling time of 4 ns. The voltage values for every sample are converted to 14 bit integer numbers between 0 and 16383 which are referred to as ADC units. In addition to the trigger threshold, the gain and time interval in which the pulses are recorded can be set. As the segments collect electrons, all segment pulses were inverted by the STRUCK ADC to store them with positive pulse amplitudes.

6.3 Simulation results with manufacturer specifications

The detector specifications and the geometry of the structures inside the K2 cryostat are needed as input to calculate the electric field and to simulate pulse shapes for the p-type segBEGe detector.

For the K2 setup, it is sufficient to simulate the detector together with its holding structure and the grounded infrared shield, see Fig. 6.4. These metallic parts shield the detector from electric potentials further away. Including these parts in the simulation changes the electric potential in the bulk by only a few volts [192, p. 133].

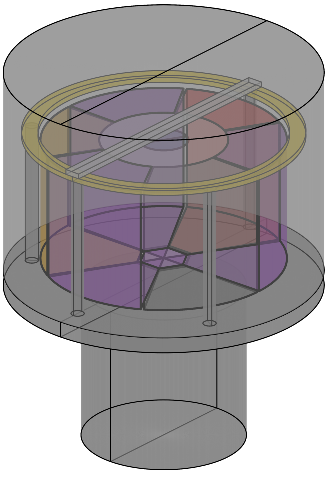

Figure 6.4: Geometry of the segBEGe detector, its holding structure and its infrared shield as defined in SSD.

As only two impurity density values at the top and at the bottom of the detector were provided by the manufacturer, a linear z-dependence but no r- and φ-dependence of the impurity density profile are initially assumed. The values are scaled to 89% to match the measured full-depletion voltage of $V_D = -1275\,\mathrm{V}$. The thickness of the segment contacts is assumed to be 0.75 mm. These assumptions will be tested in comparison to data later in this thesis.

6.3.1 Electric potential and electric field

The electric potential and the electric field inside the p-type segBEGe detector result from the bias voltage applied to the core contact and from the space charge density resulting from the ionized impurities in the detector bulk, see section 3.3.2. The contributions to $\phi(\vec{r})$ and $\vec{\mathcal{E}}(\vec{r})$ are shown in Fig. 6.5.

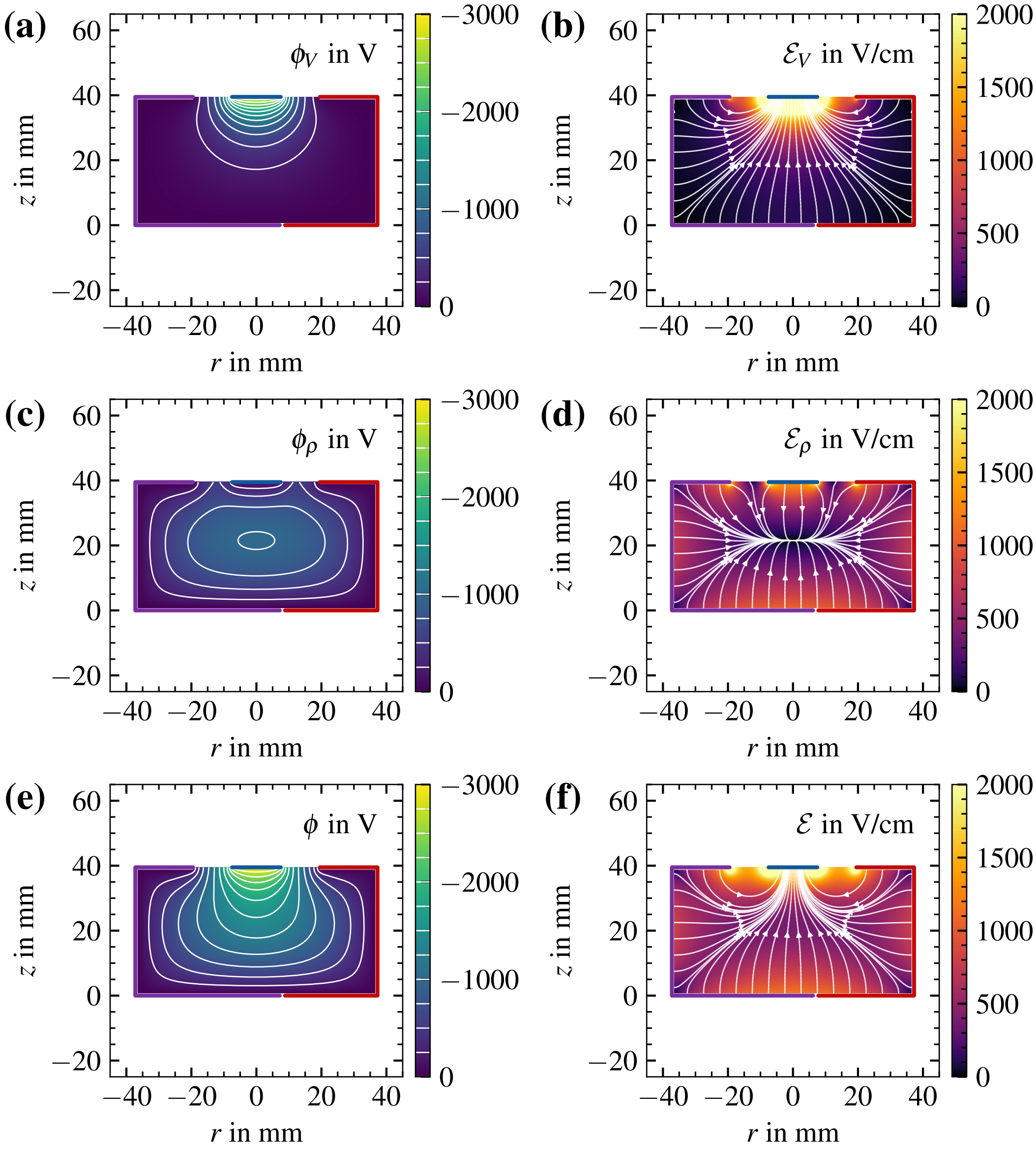

Figure 6.5: Electric potential and electric field in the p-type segBEGe detector in the r-z-plane at $\varphi = 30°$ as calculated with SSD using the impurity density values listed in Tab. 6.1 scaled to 89%, assuming only a linear z-gradient. In (a) and (b), ϕ_V and $\mathcal{E}_V$ only result from the bias voltage of $-3000\,\mathrm{V}$ applied to the core contact. In (c) and (d), ϕ_ρ and $\mathcal{E}_\rho$ only result from the ionized impurities in the detector bulk. In (e) and (f), the ϕ and $\mathcal{E}$ resulting from the sum of both contributions are depicted. The electric potential is shown with equipotential lines for every 250 V level. The electric field is shown together with electric field lines.

In Figs. 6.5a and 6.5b, the electric potential, $\phi_V(\vec{r})$, and field, $\vec{\mathcal{E}}_V(\vec{r})$, arising from the bias voltage applied to the core contact, see Eq. (3.15), are shown. The electric field $\vec{\mathcal{E}}_V(\vec{r})$ predominantly points towards the core contact and is strong close to the core contact and very weak at the mantle and the bottom of the detector. If $\vec{\mathcal{E}}_V(\vec{r})$ was the only contribution to the total electric field, the charge-collection times for events from the bottom of the detector would exceed the lifetimes of the charge carriers, resulting in inefficient charge collection.

The ionized impurities inside the depleted detector lead to an additional contribution to the electric potential and electric field, see Eq. (3.16), shown in Figs. 6.5c and 6.5d. The slight increase of the impurity density towards higher z results in the peak value of $\phi_\rho(\vec{r})$ of $-1017\,\mathrm{V}$ being reached slightly above the center of the detector bulk. Accordingly, $\vec{\mathcal{E}}_\rho(\vec{r})$ points towards the center of the detector and is strongest close to the detector surface and weakest in the middle of the detector. In the volume underneath the core contact, $\vec{\mathcal{E}}_\rho(\vec{r})$ points in the opposite direction as $\vec{\mathcal{E}}_V(\vec{r})$.

The overall electric potential, $\phi(\vec{r})$, and field, $\vec{\mathcal{E}}(\vec{r})$, are shown in Figs. 6.5e and 6.5f. The electric field underneath the core contact is dominated by $\vec{\mathcal{E}}_V(\vec{r})$ and in the rest of the detector by $\vec{\mathcal{E}}_\rho(\vec{r})$. The bias voltage, V_B, needs to be high enough such that $\vec{\mathcal{E}}_V(\vec{r})$ fully compensates $\vec{\mathcal{E}}_\rho(\vec{r})$, which points away from the core contact. This requirement defines the full-depletion voltage, which was determined as $V_D = -1275\,\mathrm{V}$ from measurements of energy-peak positions and detector capacitances at different V_B. The detector efficiently collects charge carriers on the core contact for V_B above V_D. If charge carriers are created close to the detector surface, $\vec{\mathcal{E}}_\rho(\vec{r})$ pulls the holes to the center of the detector where they are accelerated upwards towards the point contact by $\vec{\mathcal{E}}_V(\vec{r})$.

6.3.2 Performance of the point contact

The weighting potential of the core contact, $\mathcal{W}_0(\vec{r})$, and $\phi_V(\vec{r})$ differ only by a scaling factor, V_B. As shown in Fig. 6.6, $\mathcal{W}_0(\vec{r})$ increases rapidly close to the core contact and is very weak in the rest of the detector. The structure of $\mathcal{W}_0(\vec{r})$ leads to the characteristic core pulse shapes from BEGe detectors, see Fig. 6.7.

In Fig. 6.7a, the charge drift paths resulting from a single-site event in the outer part of the detector are depicted. The electrons are quickly collected on the mantle surface and do not contribute noticeably to the core charge pulse as $\mathcal{W}_0(\vec{r}_e)$ is very weak along their path. The holes drift towards the center of the detector before moving upwards towards the core contact. During the early hole drift, $\mathcal{W}_0(\vec{r}_h)$ increases slowly, leading to a slow rise of the core pulse. Below the core contact, $\mathcal{W}_0(\vec{r}_h)$ has a high gradient, resulting in a steep rise at the end of the core charge pulse.

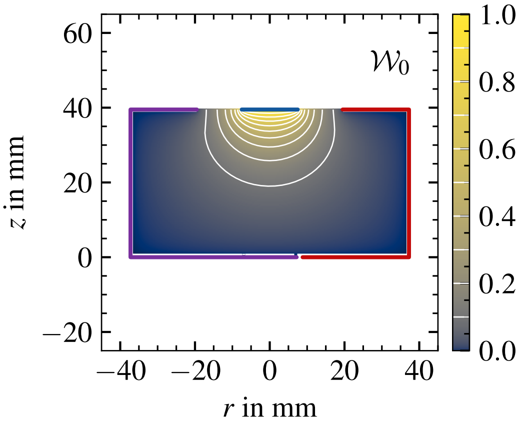

Figure 6.6: Weighting potential, $\mathcal{W}_0$, of the core contact of the p-type segBEGe detector in the r-z-plane at $\varphi = 30°$ as calculated with SSD, with equipotential lines for every 10% level.

The derivative of the charge signal is the current signal. For a single-site event, the current initially has an almost constant value and features a peak shortly before the holes reach the core contact, see Fig. 6.7b. The characteristic shape of the current pulse with a slow beginning and a steep end, as expected from single-site events, is observed multiple times in a multi-site event if the holes from each energy deposition reach the core contact at different times, see Fig. 6.7d. Hence, pulse shape analysis allows to classify events as single-site or multi-site.

One way to discriminate pulse shapes is the A/E-method [31], used in the analysis of data from the BEGe detectors in the GERDA and LEGEND experiments. When normalized to the charge pulse amplitude, E_0, the maximum current amplitude, A_0, is typically smaller for multi-site events than for single-site events. Hence, a threshold for the ratio A_0/E_0 can be determined, above which events are classified as single-site. More complex techniques based on deep learning algorithms [193] currently under development require less tuning and might recognize background events more efficiently.

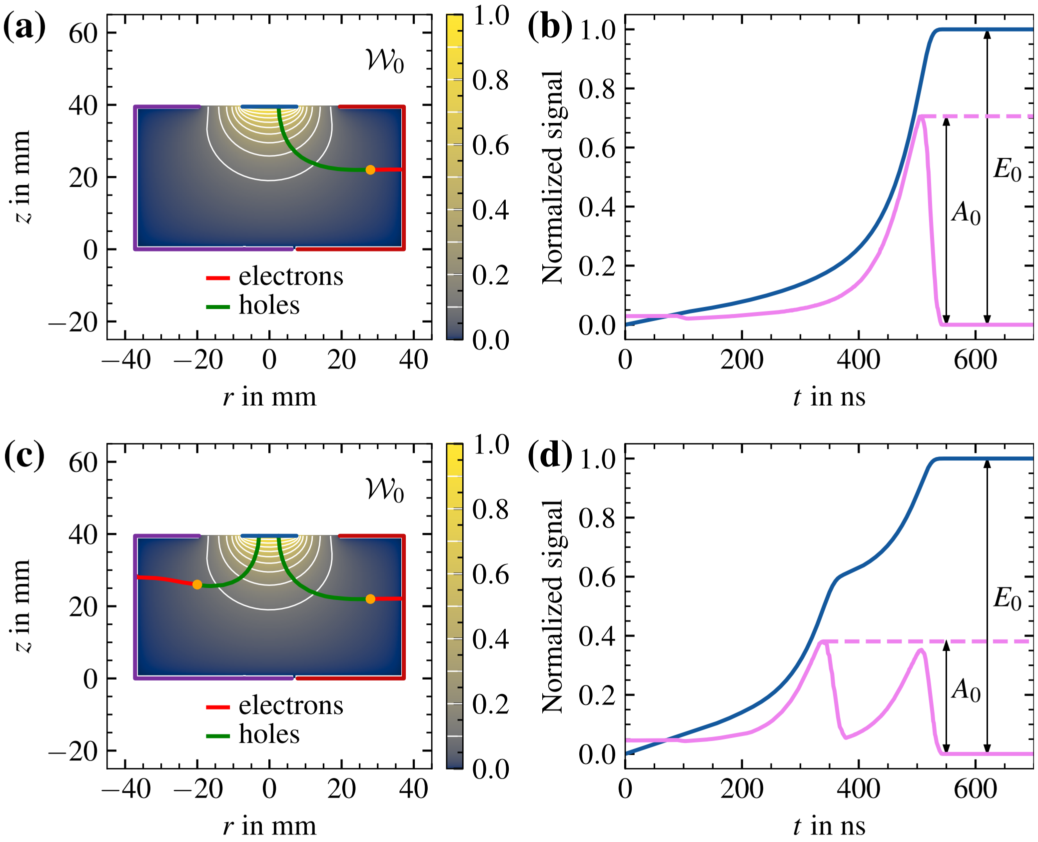

Figure 6.7: Drift paths from (a) a single-site event and (c) a multi-site event in the p-type segBEGe detector in the r-z-plane at $\varphi = 30°$ with corresponding pulse shapes in (b) and (d) as simulated with SSD. The electron and hole clouds each consist of 250 point charges. The charge signal shown in blue and the corresponding current signal shown in pink are both normalized to the amplitude of the core charge pulse, E_0.

6.3.3 Segmentation

The n^+ contact of the p-type segBEGe detector is divided into four segments, see Fig. 6.1. In Fig. 6.8, the weighting potentials in the r-z-plane at $\varphi = 30°$ of the four segments are shown. At $\varphi = 30°$, segments 1 and 4 cover part of the detector surface and, thus, $\mathcal{W}_1(\vec{r})$ and $\mathcal{W}_4(\vec{r})$ are large. In contrast, $\mathcal{W}_2(\vec{r})$ and $\mathcal{W}_3(\vec{r})$ are comparatively small with peak values of around 0.18. This means that a charge cloud at $\varphi = 30°$ will, during the drift, induce a maximum of 18% of its charge on segments 2 and 3.

The weighting potentials of segments 1, 2 and 3 increase steadily close to the respective contact. However, the large area of the segments prevents the formation of gradients in the bulk as steep as the one observed in $\mathcal{W}_0(\vec{r})$. The weighting potentials of the segments also increase steadily towards the core contact along the passivated area. Very steep gradients are seen at the boundaries of adjacent segments. Further away from the segment contacts, the weighting potentials are comparatively small. Thus, charges drifting far from the three small segment contacts will only be seen weakly. Resulting from the contact geometry of segment 4, $\mathcal{W}_4(\vec{r})$ extends wide into the detector bulk. Figure 6.8d shows that $\mathcal{W}_4(\vec{r})$ is still 0.5 in the center of the detector. Hence, charges drifting inside the detector will, during their drift, always induce a noticeable amount of charge on segment 4, even if the electron-hole pairs were created close to the contact of one of the smaller segments.

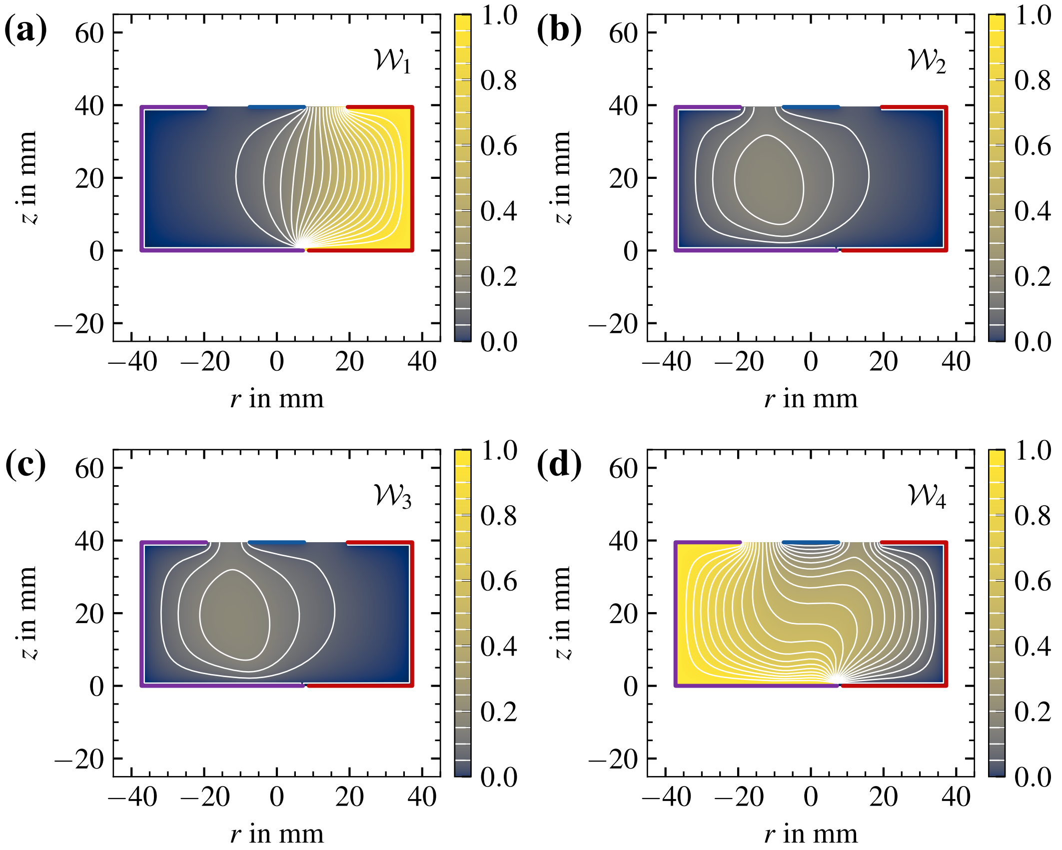

Figure 6.8: Weighting potentials of the four segments of the p-type segBEGe detector in the r-z-plane at $\varphi = 30°$ as calculated with SSD. Equipotential lines are shown for every 5% level.

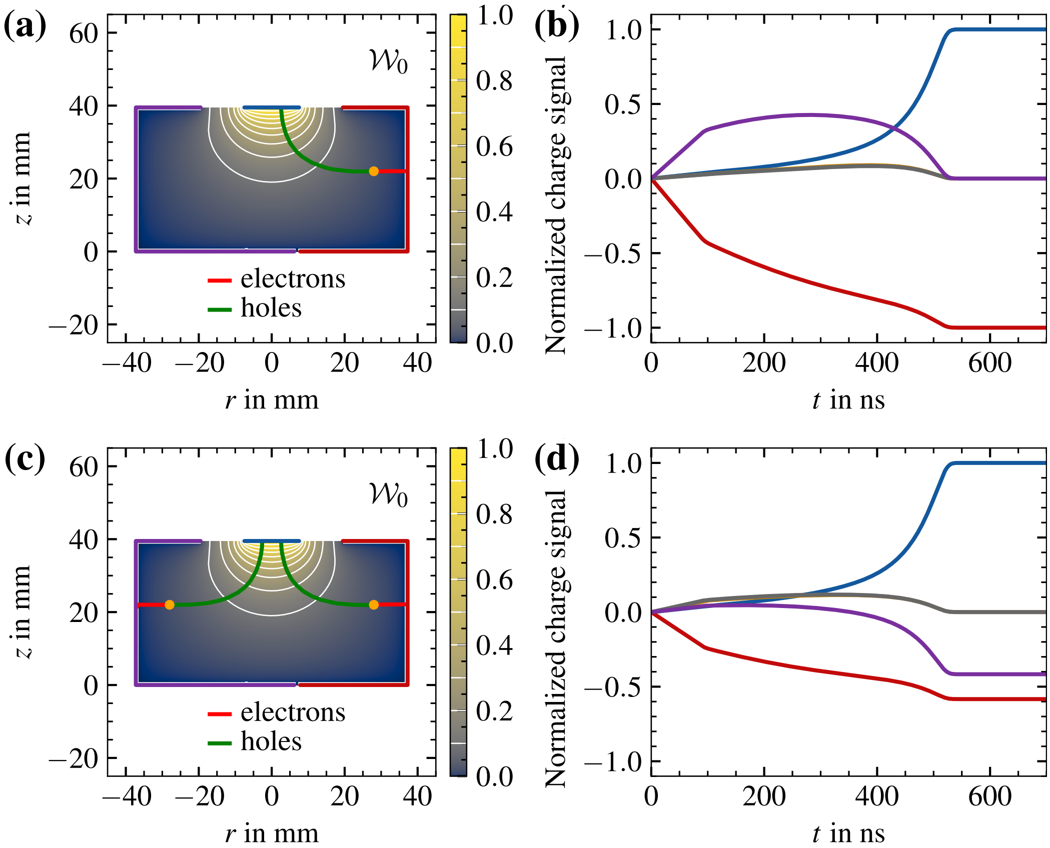

Figure 6.9: Drift paths from (a) a single-site event and (c) a multi-site event in the p-type segBEGe detector in the r-z-plane at $\varphi = 30°$. The electron and hole clouds each consist of 250 point charges. The corresponding charge pulses as simulated with SSD are shown in (b) and (d). The pulses are normalized to the amplitude of the core pulse and depicted in the color scheme introduced in Fig. 6.1.

The electrons are collected on the segment contact that is closest to their point of creation. In most single-site events, the electrons are collected on a single segment, see Fig. 6.9a. Thus, the pulse of the collecting segment S_i has the same amplitude, E_i, as the core pulse, i.e. $E_i = E_0$, see Fig. 6.9b. The other segments produce mirror pulses which return to their baseline value after all charges have been collected.

In multi-site events, the electrons are collected on different segments if the energy deposits are sufficiently separated, see Fig. 6.9c. In that case, the amplitudes of the charge pulses in all segments S_i will be lower than the amplitude of the core charge pulse, i.e. $E_i < E_0$, see Fig. 6.9d. Events with multiple collecting segments result from either multi-site events or from single-site events close to a segment boundary. Demanding all charge carriers to be collected on a single segment can be used to independently discriminate against multi-site events, especially those with similar r and z, but different φ.

6.3.4 Depletion behavior

The p-n-junction in the p-type segBEGe detector forms between the bulk and the segments. Thus, the detector is expected to deplete from the segments into the bulk.

The development of the depleted volume for the p-type segBEGe detector was simulated with SSD using the values for the impurity density ρ as provided by the manufacturer, see Tab. 6.1, scaled to 89%. The depleted volumes predicted by full 3D simulations and by faster 2D simulations neglecting the segmentation of the n^+ contact were seen to be identical for all relevant purposes. Therefore, these simulations were performed in 2D and only validated with 3D simulations before final conclusions were drawn. The simulation results are shown in Fig. 6.10 and discussed quantitatively in Appendix D on page 189.

For V_B below $-300\,\mathrm{V}$, the depleted volume penetrates with similar widths from the top, bottom and outer surface into the bulk of the detector, see Fig. 6.10a. The bottom interface between the depleted and the undepleted volumes is mainly flat. The outer interface is basically cylindrical.

At $V_B = -600\,\mathrm{V}$, the undepleted volume is significantly smaller, see Fig. 6.10b. The bottom interface is still mainly flat while the outer interface becomes bottle-shaped. The undepleted volume fully covers the core contact.

With increasing V_B, the undepleted volume becomes more drop-shaped, see Figs. 6.10c and 6.10d. At $V_B = -900\,\mathrm{V}$, a part of the core contact is in direct contact with depleted germanium. The undepleted volume becomes smaller and moves further up until completely disappearing at the full-depletion voltage.

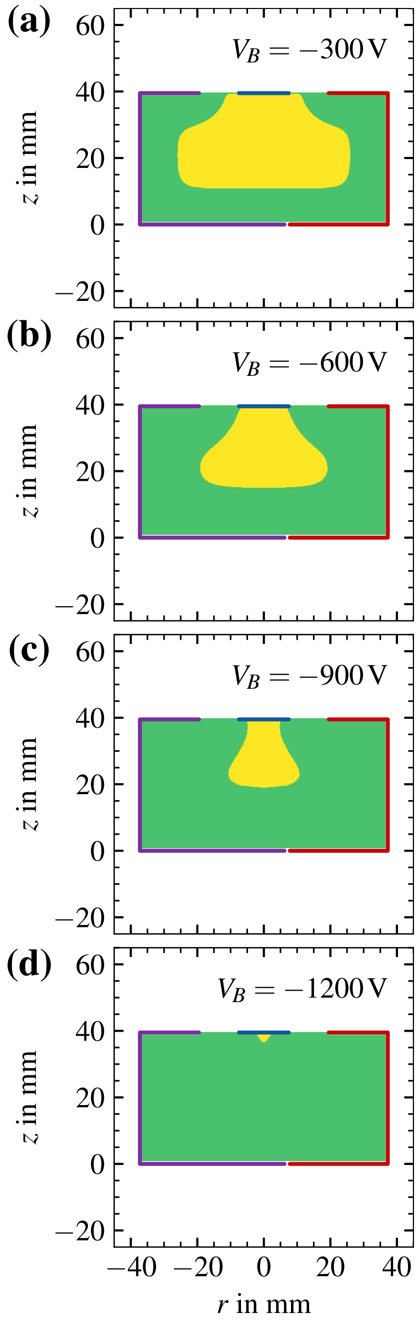

Figure 6.10: Depleted volumes of the p-type segBEGe detector as determined with SSD for different V_B using the ρ values listed in Tab. 6.1 scaled to 89%, assuming only a linear z-gradient. The depleted volumes are shown in green, the undepleted volumes are shown in yellow.

In large-volume detectors, the undepleted volume can disconnect from the contacts, resulting in an isolated undepleted volume in the bulk of the detector. This is known as pinch-off [11]. Based on the SSD simulations, the undepleted volume is always connected to the core contact and no pinch-off is expected for the p-type segBEGe detector.

6.3.5 Simulated CV curve

The capacitance matrix for the fully-depleted p-type segBEGe detector is obtained from the weighting potentials of the core contact and the four segments:

$$c = \begin{bmatrix} 5.54 & -0.89 & -0.89 & -0.89 & -2.78 \\ -0.89 & 35.18 & -0.58 & -0.58 & -32.99 \\ -0.89 & -0.58 & 35.18 & -0.58 & -32.99 \\ -0.89 & -0.58 & -0.58 & 35.18 & -32.99 \\ -2.78 & -32.99 & -32.99 & -32.99 & 101.38 \end{bmatrix} \text{pF} \,. \tag{6.1}$$

This capacitance matrix is defined by the geometry of the detector and the contacts and is not influenced by the impurity density profile in the bulk of the detector.

One characteristic of a germanium detector is its capacitance-voltage curve, CV-curve. It describes how the detector capacitance, C_d, evolves with V_B below the full-depletion voltage V_D. For the segBEGe detector, the detector capacitance, C_d, is defined as the capacitance between the core contact and all segments, i.e. the single n^+ contact obtained by connecting all segments together.

The detector capacitance can be calculated from the weighting potentials of the contacts. The depleted volumes shown in Fig. 6.10 enter the weighting potential calculation and, thus, influence C_d, see section 5.6. There were no noticeable differences between the results from full 3D simulations and faster 2D simulations.

The CV-curve for the p-type segBEGe detector as determined from 2D simulations using the impurity density values in Tab. 6.1 scaled to 89% is shown in Fig. 6.11. For $V_B = -120\,\text{V}$, C_d is 258.4 pF. With increasing V_B, C_d decreases monotonously until reaching its minimal value of 5.54 pF at $V_D = -1275\,\text{V}$. Above V_D, the weighting potential calculation is not affected by V_B, resulting in a constant C_d.

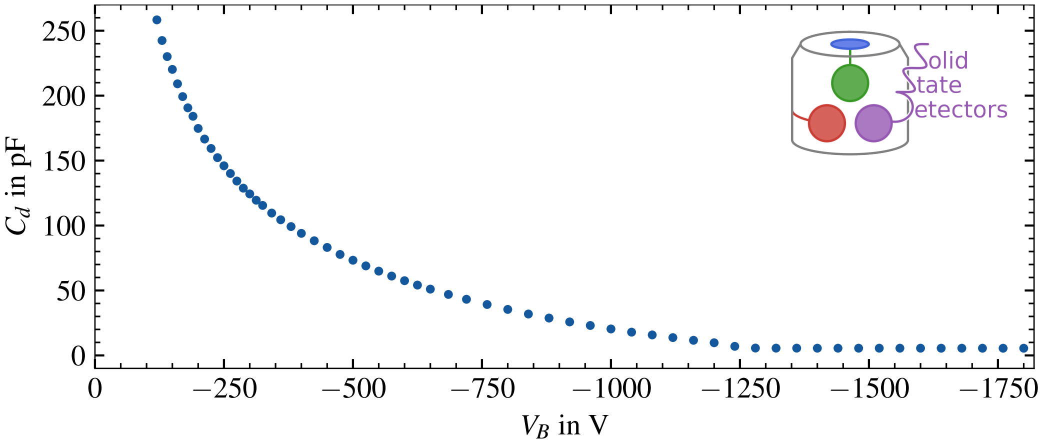

Figure 6.11: CV-curve for the p-type segBEGe detector as calculated with SSD using the impurity density values listed in Tab. 6.1 scaled to 89%, assuming only a linear z-gradient.

7 Pulse processing

The physical observables of germanium detectors are charge pulses. The charges collected on the contacts and, thus, the deposited energies can be determined from the amplitudes of the pulses. The shapes of the pulses provide information about the event topologies.

Unfortunately, the read-out electronics have a significant impact on the measured pulses. First of all, the finite bandwidth of the preamplifiers limits the capabilities to resolve fast changes in the pulse shapes. In addition, an exponential decay in the tail of the pulses is caused by from the RC feedback in the preamplifier circuit, see Fig. 6.3. Finally, measured pulse shapes are subject to noise and are recorded in uncalibrated ADC units that need to be converted to charge or energy units.

In this chapter, methods to correct for these electronics effects, to determine the pulse amplitudes and to calibrate these pulse amplitudes to true energies are presented.

7.1 Basic determination of pulse amplitudes

A basic procedure to determine the pulse amplitudes is explained using the output pulses resulting from injecting voltage pulses into the test input of each preamplifier circuit, see Fig. 6.3. Rectangular voltage pulses with peak-to-peak amplitudes of 150 mV were generated at a rate of 66.7 Hz. The rise times of these rectangular pulses were determined with an oscilloscope to be 2 ns.

For each preamplifier circuit, the output pulses were recorded for 5 min. Each output pulse was recorded over a time interval of 20 µs. An example output pulse is shown in Fig. 7.1. The amplitude of the pulse corresponds to the charge collected on the feedback capacitor of the preamplifier circuit. The charge values are stored as 14 bit unsigned integer numbers in uncalibrated ADC units.

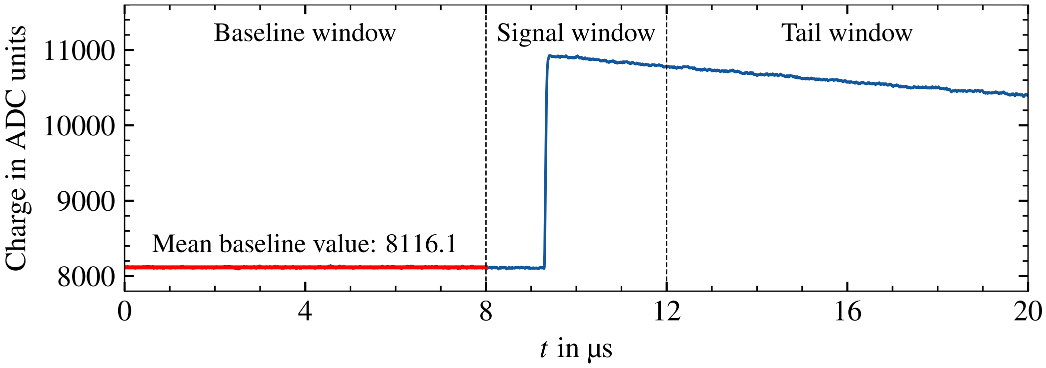

Figure 7.1: Example output pulse from the core preamplifier in response to a rectangular voltage pulse on the test input of the preamplifier. The dashed lines separate three parts of the pulse: the baseline window, the signal window and the tail window.

Pulses were divided into three parts: the baseline window, the signal window and the tail window. The baseline window covers the part of the pulse before the rise and is ideally flat. The signal window is set around the part of the pulse in which the rise is observed. The tail window covers the part of the pulse in which the pulse has reached its final amplitude and only the exponential decay from the preamplifier feedback is observed.

The baseline of the example pulse shown in Fig. 7.1 is flat. The mean value of the baseline corresponds to no charge collected on the feedback capacitor of the preamplifier system, i.e. $Q(t) = 0$. The mean baseline values are non-zero and different for the different preamplifier circuits. These offsets are corrected for by subtracting the mean baseline value as determined from the baseline window from the pulses on an event-by-event basis, see Fig. 7.2.

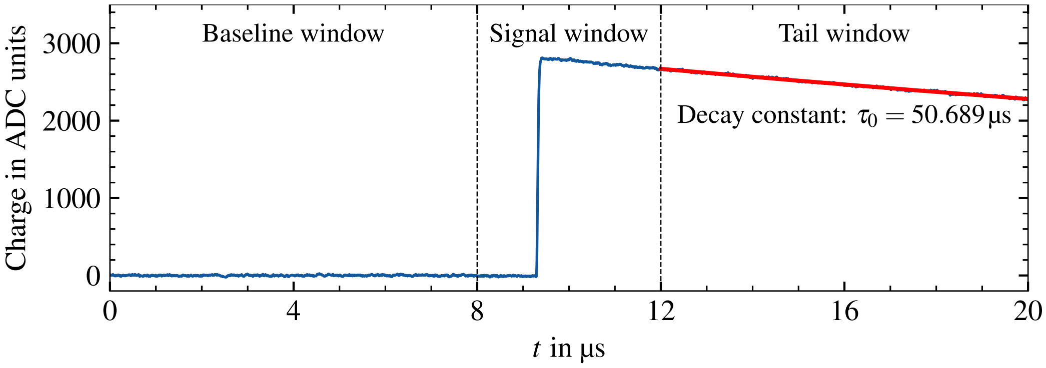

Figure 7.2: Baseline-corrected pulse from Fig. 7.1 with an exponential fit to the tail shown in red used to extract the decay time τ_0 of the core preamplifier circuit.

The exponential decay of the output signal is clearly visible in the tail window of the pulses, see Fig. 7.2. The output pulse has already decayed to around 80% of the initial pulse amplitude 10 µs after the end of the rise. To measure the pulse amplitude, the pulses need to be corrected for this decay.

For each contact read-out $i \in \{0,1,2,3,4\}$, the decay times τ_i are assumed to be constant for a given configuration. Their values are determined by fitting an exponential function to the tails of the baseline-corrected pulses. The fits are performed via linear regression to the logarithm of the pulse tail to ensure stable and fast computation. The decay time τ_i is then given by the inverse negative slope of the fit:

$$Q_i(t) = Q_i^{\max} \exp(-\frac{t}{\tau_i}) \qquad \Rightarrow \qquad \ln(Q_i(t)) = \ln(Q_i^{\max}) - \frac{t}{\tau_i} \,. \tag{7.1}$$

The fit results for the τ_i fluctuate on an event-by-event basis due to electronic noise. Their distributions are well described by Gaussian distributions, see Fig. 7.3a. The mean decay times, $\bar{\tau}_i$, and the full widths at half maximum, FWHM, determined by Gaussian fits are listed in Fig. 7.3b. The decay times are around 50 µs. The τ_0 distribution for the core is the narrowest, directly followed by the ones for τ_3 and τ_1. Higher noise levels in the read-out of segments 2 and 4 lead to broader distributions in τ_2 and τ_4.

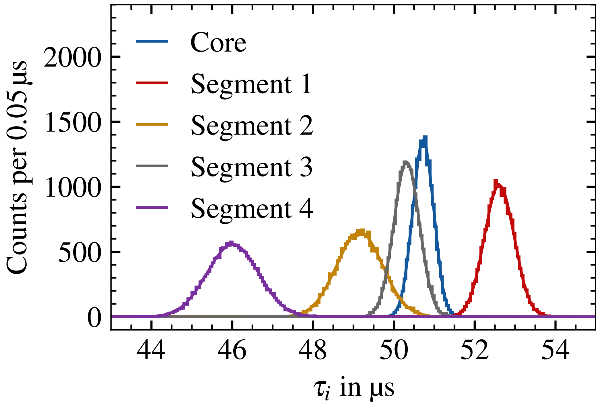

(a)

Channel	$\bar{\tau}_i$ in µs	FWHM in µs
Core	50.723	0.610
Seg. 1	52.608	0.870
Seg. 2	49.152	1.349
Seg. 3	50.316	0.746
Seg. 4	46.014	1.499

(b)

Figure 7.3: (a) Distribution of τ_i of the preamplifier output pulses from 5 min pulser measurements for the p-type segBEGe detector. (b) Mean decay times, $\bar{\tau}_i$, and full widths at half maximum, FWHM, as determined from Gaussian fits to the distributions.

The mean values for the decay times, $\bar{\tau}_i$, are used to filter out the exponential decay on a sample-by-sample basis throughout the whole length of the output pulses. The decay correction has no noticeable effect on the flat baseline but compensates for the exponential decay in the tail window, resulting in a flat tail. In Fig. 7.4, the decay-corrected pulse corresponding to Fig. 7.1 is shown.

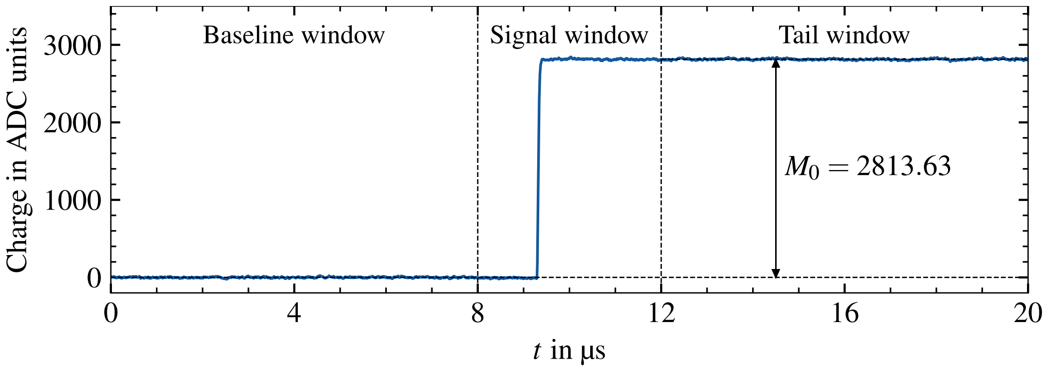

Figure 7.4: Decay-corrected pulse from Fig. 7.2 using $\bar{\tau}_0 = 50.723$ µs from Fig. 7.3, resulting in a flat tail of the pulse. The measured pulse amplitude, M_0, in ADC units is given by the difference between the mean value of the pulse in the tail window and in the baseline window.

After baseline and decay correction, the measured charge pulses ideally start with a flat baseline and end with a flat tail. The measured pulse amplitude, M_i, i.e. the difference between the average values in the tail window and the baseline window, are measures for the total charge collected on the feedback capacitor of the preamplifier circuit of the contact S_i. The shape of the corrected pulse in the signal window can be analyzed to extract information about the event topology.

7.2 Pile-up and improved determination of pulse amplitudes

For pulses starting on a flat baseline, the procedure described in section 7.1 provides a sufficient estimate of the pulse amplitudes M_i. However, it is possible that a pulse starts on the decaying tail of the previous pulse or is distorted by a rapidly following pulse. This is referred to as pile-up.

Pulses from pile-up events start with a negative slope in the baseline window or feature a sudden rise in the tail window. For pile-up events, the baseline and decay correction described in section 7.1 does not result in pulses with flat baselines and tails, see Fig. 7.5. As a consequence, the values for M_i are underestimated for pile-up in the baseline window and overestimated for pile-up in the tail window.

Pile-up can be rejected by discarding pulses with negative slopes above a given threshold. However, this reduces the statistics. Therefore, the pulse correction procedure and the determination of M_i were improved to also work for pile-up events.

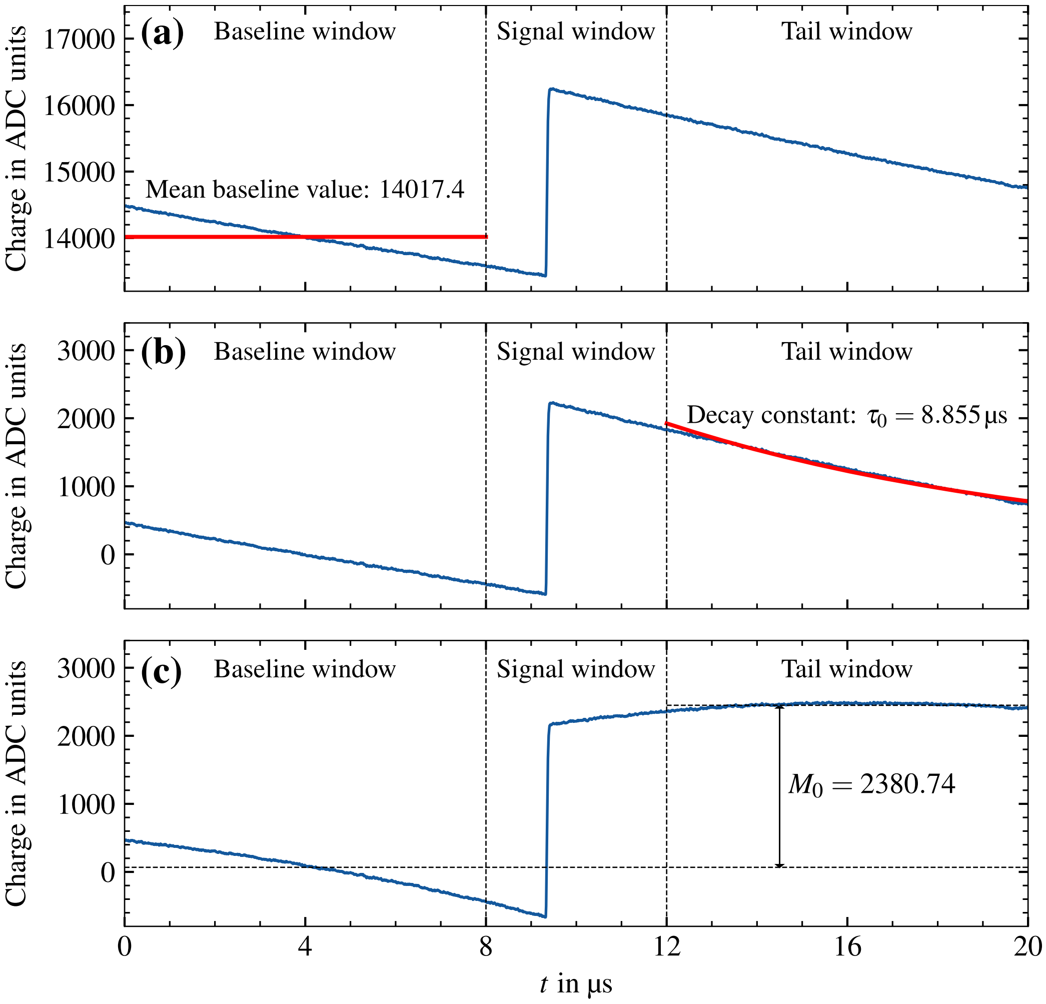

Figure 7.5: (a) Example pile-up pulse as measured by the core contact of the p-type segBEGe detector, (b) after subtracting the mean value in the baseline window and (c) after correcting with the exponential decay constant as determined from the tail window.

The mean baseline value for pile-up pulses is different from the zero-baseline value corresponding to $Q_i(t) = 0$. Therefore, the baseline correction was not performed by subtracting the mean baseline values from the pulses on an event-by-event basis, but by subtracting the same zero-baseline value from all pulses. This zero-baseline value was determined for each 5 min measurement separately. Assuming no significant baseline shifts, the zero-baseline value can be determined from the baseline mean spectrum for each contact.

Figure 7.6 shows the distribution of mean baseline values for pulses measured in the core contact of the p-type segBEGe detector from a 5 min measurement with no significant baseline shifts. The zero-baseline value is determined as the peak position of the Gaussian distribution fitted to the main peak that contains most of the events.

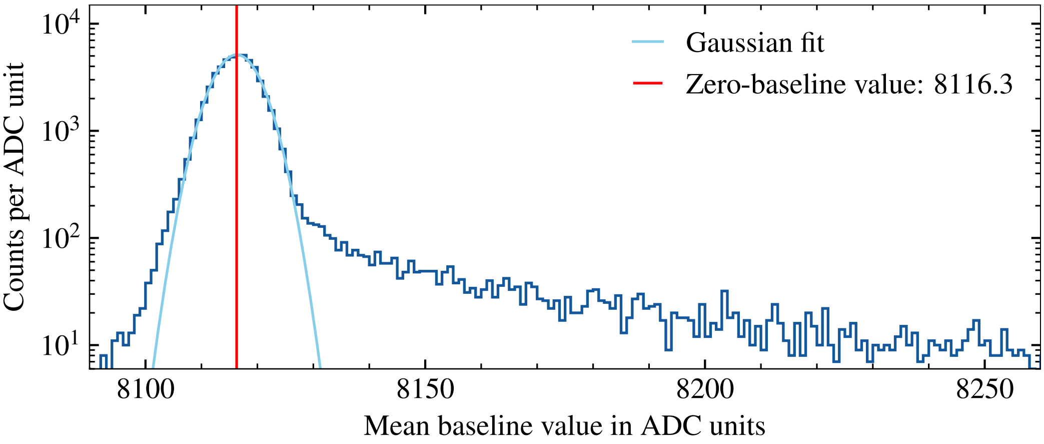

Figure 7.6: Example spectrum of the mean baseline values as determined for core pulses from the baseline window. The zero-baseline value can be determined as the mean of the Gaussian distribution fitted to the main peak.

In some measurements, the zero-baseline value was not constant within a 5 min measurement but subject to sudden changes. This is referred to as common ground. In these measurements, time-dependent zero-baseline values were determined and subtracted from the individual pulses.

The pulse correction for an example pile-up pulse is depicted in Fig. 7.7. Instead of subtracting the mean value in the baseline window, the zero-baseline value is subtracted. Then, the exponential decay is corrected for over the whole pulse length using the mean decay time of the core contact, $\bar{\tau}_0$. The corrected pulse features a flat baseline at a non-zero value and a flat tail, from which the measured pulse amplitude M_0 can be determined.

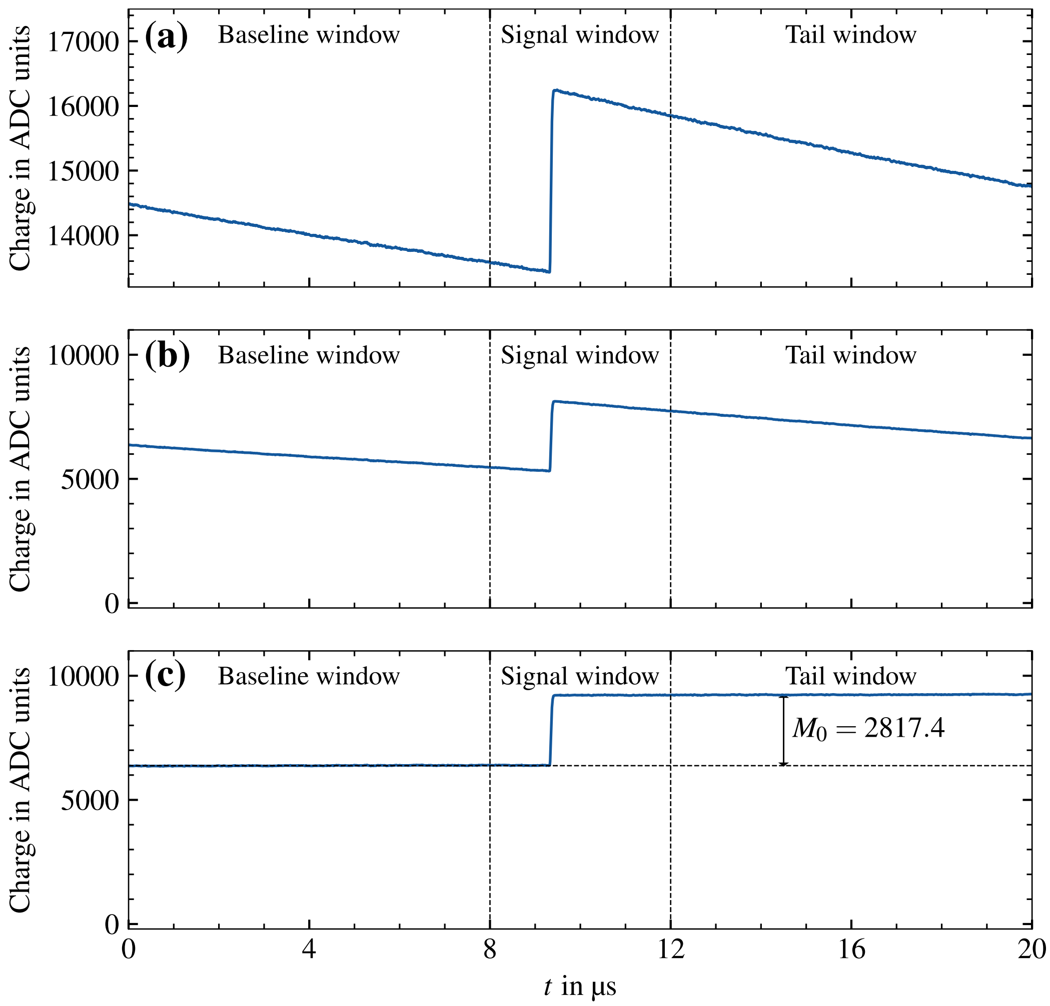

Figure 7.7: (a) Example pile-up pulse shown in Fig. 7.5a, (b) after subtracting the zero-baseline value of 8116.3, see Fig. 7.6, and (c) after correcting the exponential decay with $\bar{\tau}_0 = 50.723\,\mu\text{s}$.

7.3 Response functions

The preamplifier circuits do not only lead to an exponential decay of the pulses. They also have a limited capability to process high-frequency signals, i.e. their bandwidth is limited, such that abrupt changes in the charge signal are smoothed out.

The effect of the limited bandwidth on the measured pulses can be quantified by studying the output pulses from the pulser measurement. The output pulses expected in response to the rectangular input pulses are expected to occur every 15 ms and to have similar measured pulse amplitudes. For example, 18 171 measured output signals from the core were selected imposing a cut on the pulser frequency and the measured pulse amplitudes. The baseline- and decay-corrected pulses are shown in Fig. 7.8.

The output signals are very reproducible, implying that the influence of the read-out electronics on the measured pulse shapes is not subject to significant statistical fluctuations. The only differences between the individual pulses result from electronic noise.

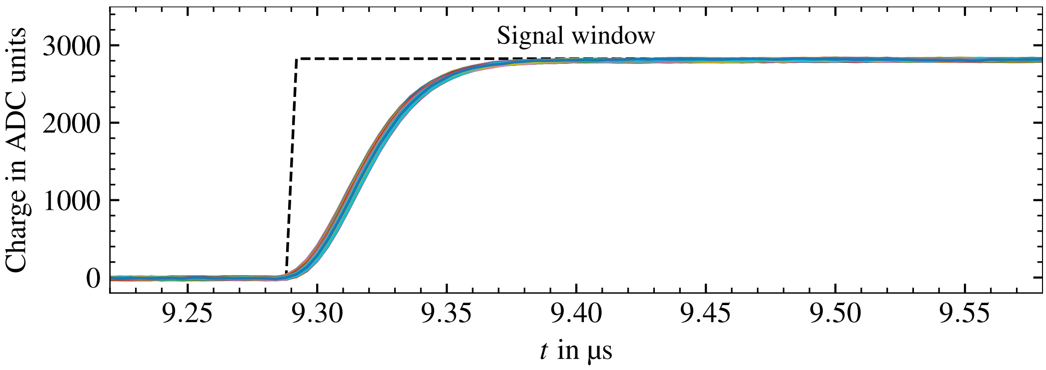

Figure 7.8: Baseline- and decay-corrected output pulses in response to rectangular voltage pulses on the test input of the core preamplifier. The pulses are time-aligned to reach their maximum slope at the same time. Shown as a dashed line is the input signal.

The 5-95% rise times of the output pulses, which are defined as the times in which the pulses rise from 5 to 95% of their final amplitude, are in average $(63.2 \pm 0.4)\,\mathrm{ns}$ and significantly longer than the 2 ns rise times of the input pulses. This illustrates that the limited bandwidth does not allow for the observation of extremely fast changes in the pulses which might be predicted by simulations for specific cases.

For each detector contact S_i, $i \in \{0,1,2,3,4\}$, the influence of the read-out electronics on the raw pulse shapes $Q_i(t)$ can be described by the respective response function $\zeta_i(t)$, see section 5.9.1. The narrower the response function, the higher the bandwidth of the preamplifier and the less influence on the pulse shapes is expected.

The rectangular input pulses rise faster than the 4 ns sampling time of the STRUCK ADC and follow approximately the course of a Heaviside step function, $H(t)$ [194]. The distributional derivative of the Heaviside step function is the Dirac-δ-distribution. Therefore, the expected output pulse in response to a step input pulse, i.e. $Q_i(t) \approx H(t)$, assuming a negligible noise level, i.e. $n(t) \approx 0$, is given by Eq. (5.15) as

$$Q_i^{\mathrm{meas}}(t) \approx (\zeta_i * H)(t) = \int_{-\infty}^{\infty} \mathrm{d}t' \zeta_i(t') H(t-t') \tag{7.2}$$

$$\Rightarrow \frac{\mathrm{d}}{\mathrm{d}t} Q_i^{\mathrm{meas}}(t) \approx \int_{-\infty}^{\infty} \mathrm{d}t'\ \zeta_i(t') \frac{\mathrm{d}}{\mathrm{d}t} H(t-t') = \int_{-\infty}^{\infty} \mathrm{d}t'\ \zeta_i(t')\, \delta(t-t') = \zeta_i(t)\ . \tag{7.3}$$

In other words: the response functions $\zeta_i(t)$ can be identified with the derivatives of the baseline- and decay-corrected output signals from the pulser measurement. For individual output pulses, the noise level is too large to determine $\zeta_i(t)$. However, the statistical fluctuations caused by electronic noise can be removed by creating superpulses from approximately 20 000 pulses for each read-out channel.

The response functions determined from the derivatives of the low-noise superpulses have to be normalized to unit area to preserve the pulse amplitude. The response functions for the core and segment preamplifier circuits of the p-type segBEGe detector are depicted in Fig. 7.9.

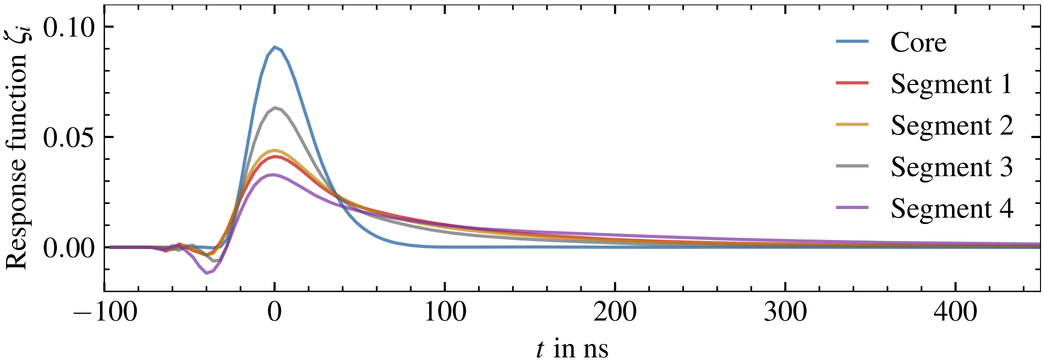

Figure 7.9: Response functions of the preamplifiers of the p-type segBEGe detector. The pulses are aligned to reach their maximum at $t = 0\,\text{ns}$ and normalized to unit area.

The core response function has a FWHM of 40.6 ns and is the narrowest of all response functions. This results from the fact that a part of the core preamplifier is installed inside the cold part of K2, which reduces the input capacitance to the preamplifier. Thus, the core pulse shapes are influenced the least by the read-out electronics.

The segment response functions show broader and more asymmetric shapes. They have a small negative dip at the beginning, followed by a comparatively fast rise and a slow end. Especially, the response function of segment 4 shows a long tail. This is due to the large capacitance of segment 4. This means that the pulse shapes of segment 4 are most affected by the bandwidth of the system.

7.4 Energy calibration

Figure 7.10 shows the spectra of measured pulse amplitudes for all contacts of the p-type segBEGe detector resulting from a 2 h measurement with an uncollimated ^{133}Ba source on top of the K2 cryostat. The peaks observed in the spectra can be associated with radioactive decays with known gamma energies [119]. The positions of the peaks in the uncalibrated spectra mostly depend on the amplification and the input ranges of the preamplifiers. While the position of the peaks are quite similar in the four segment spectra, the uncalibrated core spectrum peaks at larger ADC values.

In experiments, the true energies are not directly measurable but can be reconstructed from the measured pulse amplitudes. To first order, the measured pulse amplitudes can be calibrated to true energies by scaling them with raw calibration factors. This accounts for the different gains of the preamplifier circuits. These factors are determined by fitting the peaks observed in the spectrum to the known characteristic energies [119] of the associated radioactive decays. The values for the core and the four segment read-out chains are listed in Fig. 7.10. However, due to linear cross-talk between the detector contacts, simply scaling the measured pulse amplitudes by raw calibration factors does not lead to an accurate reconstruction of the true energies.

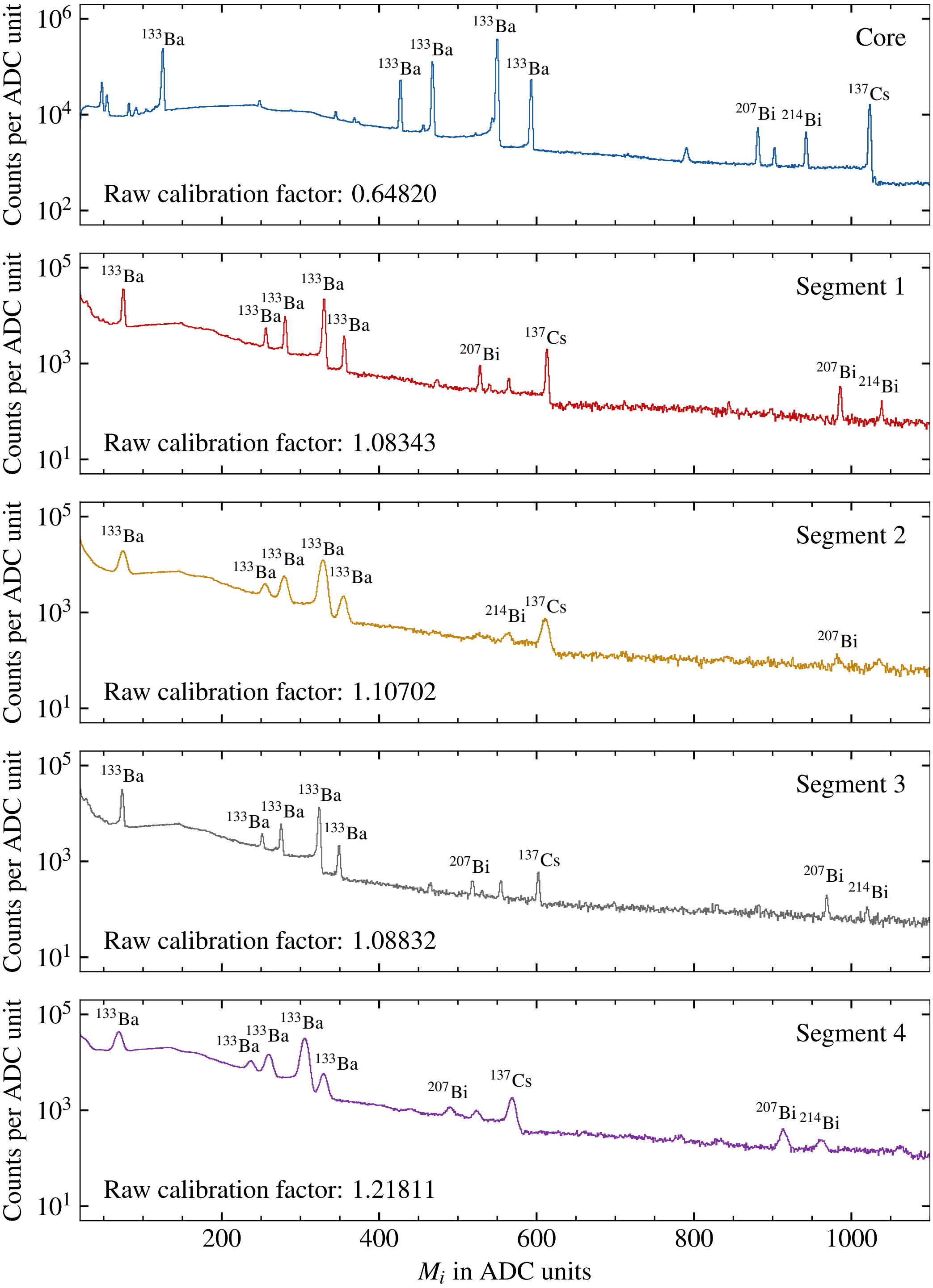

Figure 7.10: Uncalibrated energy spectra for all contacts of the p-type segBEGe detector, obtained from a 2 h measurement with an uncollimated ^{133}Ba source on top of the K2 cryostat. Labeled are the most dominant peaks associated with the decays of ^{133}Ba (80.997 keV, 276.398 keV, 302.853 keV, 356.017 keV, 383.851 keV), ^{137}Cs (661.660 keV), ^{207}Bi (569.702 keV, 1063.662 keV) and ^{214}Bi (609.312 keV, 1120.287 keV) [119].

7.4.1 Linear cross-talk

In the absence of linear cross-talk, the pulses from the core and the collecting segments have a non-zero amplitude and the mirror pulses from non-collecting segments return to their baseline. However, linear cross-talk and different preamplifier gains alter the amplitudes of the measured charge pulses, $Q_i^C(t)$, see section 5.9.2. As a consequence, mirror pulses do not necessarily return to the baseline. Their final amplitude depends on the magnitude of the linear cross-talk between the contacts.

The relationship between the measured pulse amplitudes, M_i, and the true energies, E_i, can be expressed through the linear cross-talk matrix, C^L, as

$$\underbrace{\begin{bmatrix} M_0 \\ M_1 \\ M_2 \\ M_3 \\ M_4 \end{bmatrix}}_{=\vec{M}} = \underbrace{\begin{bmatrix} C^L_{0,0} & C^L_{0,1} & C^L_{0,2} & C^L_{0,3} & C^L_{0,4} \\ C^L_{1,0} & C^L_{1,1} & C^L_{1,2} & C^L_{1,3} & C^L_{1,4} \\ C^L_{2,0} & C^L_{2,1} & C^L_{2,2} & C^L_{2,3} & C^L_{2,4} \\ C^L_{3,0} & C^L_{3,1} & C^L_{3,2} & C^L_{3,3} & C^L_{3,4} \\ C^L_{4,0} & C^L_{4,1} & C^L_{4,2} & C^L_{4,3} & C^L_{4,4} \end{bmatrix}}_{=C^L} \underbrace{\begin{bmatrix} E_0 \\ E_1 \\ E_2 \\ E_3 \\ E_4 \end{bmatrix}}_{=\vec{E}} . \tag{7.4}$$

If core contact of the p-type segBEGe detector collects all holes in an event, the true energy to be seen in the core contact is equal to the deposited energy, i.e. $E_0 = E_{\text{dep}}$. The electrons are not necessarily collected on a single segment. However, the sum of the true energies to be seen in the segments should be equal to E_{dep} and, therefore, to the true energy to be seen in the core contact, i.e. $\sum_{i=1}^{4} E_i = E_0$.

For single-segment events in segment i, i.e. when all electrons are collected in segment i, $E_i = E_0 = E_{\text{dep}}$ and $E_j = 0$ for $j \neq i$. According to Eq. (7.4), the measured pulse amplitude in the core contact is

$$M_0 = \sum_{j=0}^{4} C^L_{0,j} E_j = C^L_{0,0} E_0 + C^L_{0,i} E_i = (C^L_{0,0} + C^L_{0,i}) E_{\text{dep}} , \tag{7.5}$$

i.e. the measured pulse amplitude not only depends on the deposited energy E_{dep} but also on which segment collected the electrons. For the fully-depleted p-type segBEGe detector, $C^L_{0,i}$ is several orders of magnitude smaller than $C^L_{0,0}$ such that $M_0 \approx C^L_{0,0} E_0$.

For a single-segment event in segment i, the measured pulse amplitude M_i is given by

$$M_i = \sum_{j=0}^{4} C^L_{i,j} E_j = C^L_{i,0} E_0 + C^L_{i,i} E_i = (C^L_{i,0} + C^L_{i,i}) E_{\text{dep}} , \tag{7.6}$$

where $C^L_{i,0}$ denotes the core-to-segment cross-talk and $C^L_{i,i}$ denotes the amplification factor of segment i.

For events with full charge collection, where $E_0 = \sum_{i=1}^{4} E_i$, core-to-segment cross-talk always interferes with segment amplification and segment-to-segment cross-talk, i.e.

$$M_i = \sum_{j=0}^{4} C^L_{i,j} E_j = C^L_{i,0} E_0 + \sum_{j=1}^{4} C^L_{i,j} E_j = C^L_{i,0} \sum_{j=1}^{4} E_j + \sum_{j=1}^{4} C^L_{i,j} E_j = \sum_{j=1}^{4} (C^L_{i,0} + C^L_{i,j}) E_j \,. \tag{7.7}$$

As $C^L_{i,0}$ and $C^L_{i,j}$ always appear in a sum, C^L can be rewritten as

$$C = \begin{bmatrix} C_{0,0} & C_{0,1} & C_{0,2} & C_{0,3} & C_{0,4} \\ 0 & C_{1,1} & C_{1,2} & C_{1,3} & C_{1,4} \\ 0 & C_{2,1} & C_{2,2} & C_{2,3} & C_{2,4} \\ 0 & C_{3,1} & C_{3,2} & C_{3,3} & C_{3,4} \\ 0 & C_{4,1} & C_{4,2} & C_{4,3} & C_{4,4} \end{bmatrix} , \tag{7.8}$$

where $C_{0,i} = C^L_{0,i}$ and $C_{i,j} = C^L_{i,0} + C^L_{i,j}$ for $i, j \in \{1,2,3,4\}$ such that $\vec{M} = C\vec{E}$.

7.4.2 Determination of the linear cross-talk matrix

The top-left element of the linear cross-talk matrix C in Eq. (7.8), $C_{0,0}$, is set to the inverse of the raw core calibration factor, see Fig. 7.10. The remaining 20 elements of C are determined experimentally from single-segment events. For single-segment events in segment i, where $E_0 = E_i = E_{\text{dep}}$ and $E_j = 0$ for $j \neq i$, the measured pulse amplitudes are $M_0 = (C_{0,0} + C_{0,i}) E_{\text{dep}}$, $M_i = C_{i,i} E_{\text{dep}}$ and $M_j = C_{j,i} E_{\text{dep}}$ for $j \neq i$. Thus,

$$\left\langle \frac{M_0}{E_{\text{dep}}} \right\rangle_i = C_{0,0} + C_{0,i} \,, \quad \left\langle \frac{M_i}{M_0} \right\rangle_i = \frac{C_{i,i}}{C_{0,0} + C_{0,i}} \quad \text{and} \quad \left\langle \frac{M_j}{M_0} \right\rangle_i = \frac{C_{j,i}}{C_{0,0} + C_{0,i}} \,, \tag{7.9}$$

where $\langle x \rangle_i$ denotes the expectation value of any quantity x for single-segment events in segment i. The relations in Eq. (7.9) allow for the determination of the top-row, the diagonal and the off-diagonal elements of C, respectively. In order to determine the expectation values in Eq. (7.9), single-segment events in all four segments need to be selected first.

Single-segment events can be selected from the M_i/M_0 spectra. In Fig. 7.11, the M_i/M_0 spectra determined from the measured spectra shown in Fig. 7.10 are shown. The two peaks observed in each of the spectra correspond to events in which the segment i collected none, i.e. $M_i/M_0 \approx 0$ and $E_i/E_0 = 0$, or all of the electrons, i.e. $M_i/M_0 \approx 0.6$ and $E_i/E_0 = 1$. The region between the two peaks originates from multi-segment events. Single-segment events are selected for each of the four segments by fitting a Cauchy distribution to the peak at $M_i/M_0 \approx 0.6$ and keeping only the events with M_i/M_0 in the FWHM of the resulting fit function, see Fig. 7.11.

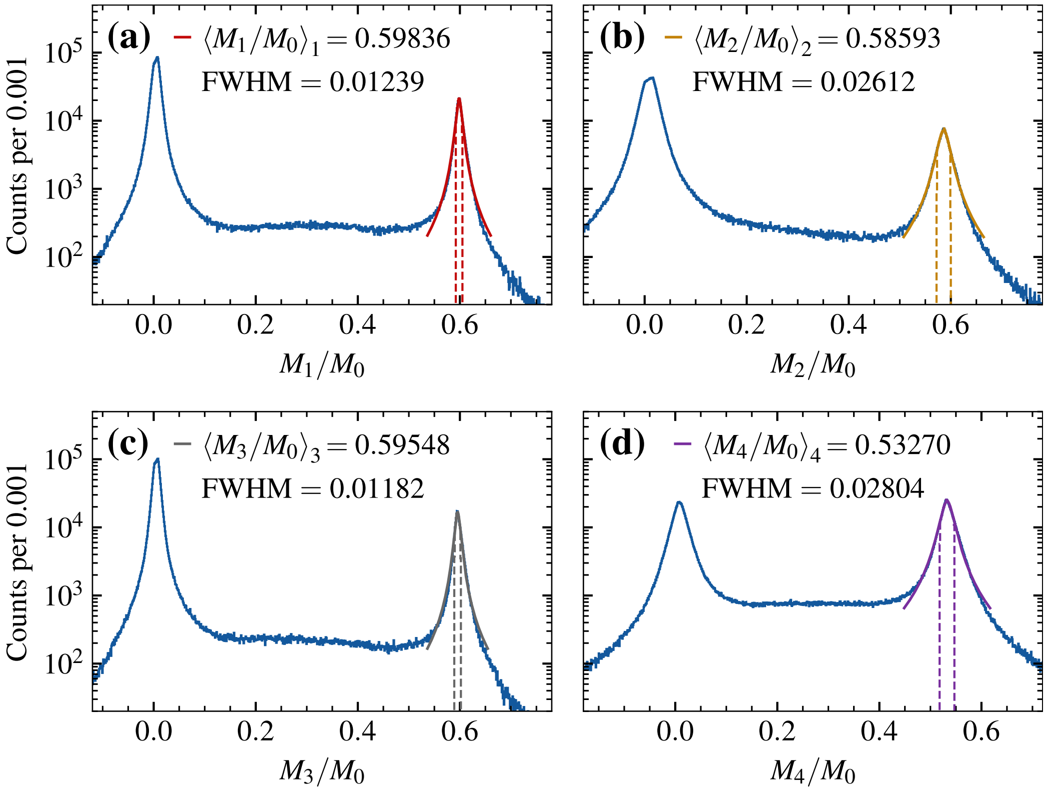

Figure 7.11: Ratios between the measured pulse amplitudes of the segment i, M_i, and the core, M_0, for the segment (a) 1, (b) 2, (c) 3 and (d) 4. Single-segment events can be selected by fitting a Cauchy distribution to the right peak at $M_i/M_0 \approx 0.6$ and keeping only the events in the FWHM shown with dashed lines. The mean values of M_i/M_0 for single-segment events in segment i, $\langle M_i/M_0\rangle_i$, and the FWHM as determined from the fits are listed in the legends.

The four top-row elements $C_{0,i}$ with $i \neq 0$ describe the segment-to-core cross-talk. For different segment-to-core cross-talk, the value of M_0 does not only depend on E_{dep} but also on which segment collected the electrons. This results in segment-specific core calibration factors, $\langle M_0/E_{\text{dep}}\rangle_i$, which can be determined by calibrating the core spectrum resulting from single-segment events in segment i. Their deviations from the mean core amplification factor $C_{0,0}$ are accounted for in $C_{0,i}$.

The four diagonal elements of C, $C_{i,i}$ with $i \in \{1,2,3,4\}$ describe the segment amplification factors. They are determined by multiplying $\langle M_i/M_0\rangle_i$ as determined from the Cauchy fits in Fig. 7.11 with the segment-specific core-calibration factors, i.e.

$$C_{i,i} = \left\langle \frac{M_i}{M_0} \right\rangle_i \cdot \left\langle \frac{M_0}{E_{\text{dep}}} \right\rangle_i . \tag{7.10}$$

The 12 off-diagonal elements $C_{j,i}$ with $j \neq i$ describe the segment-to-segment cross-talk. For single-segment events in segment i, the measured pulse amplitudes M_j in the non-collecting segments $j \neq i$ peak around 0. As for the core spectrum, the mean value of M_j/M_0 depends on which segment collected the electrons, see Fig. 7.12. By fitting Cauchy functions to the subpeaks resulting from selecting single-segment events in segment i, the values for $\langle M_j/M_0\rangle_i$ listed in Fig. 7.12 were determined.

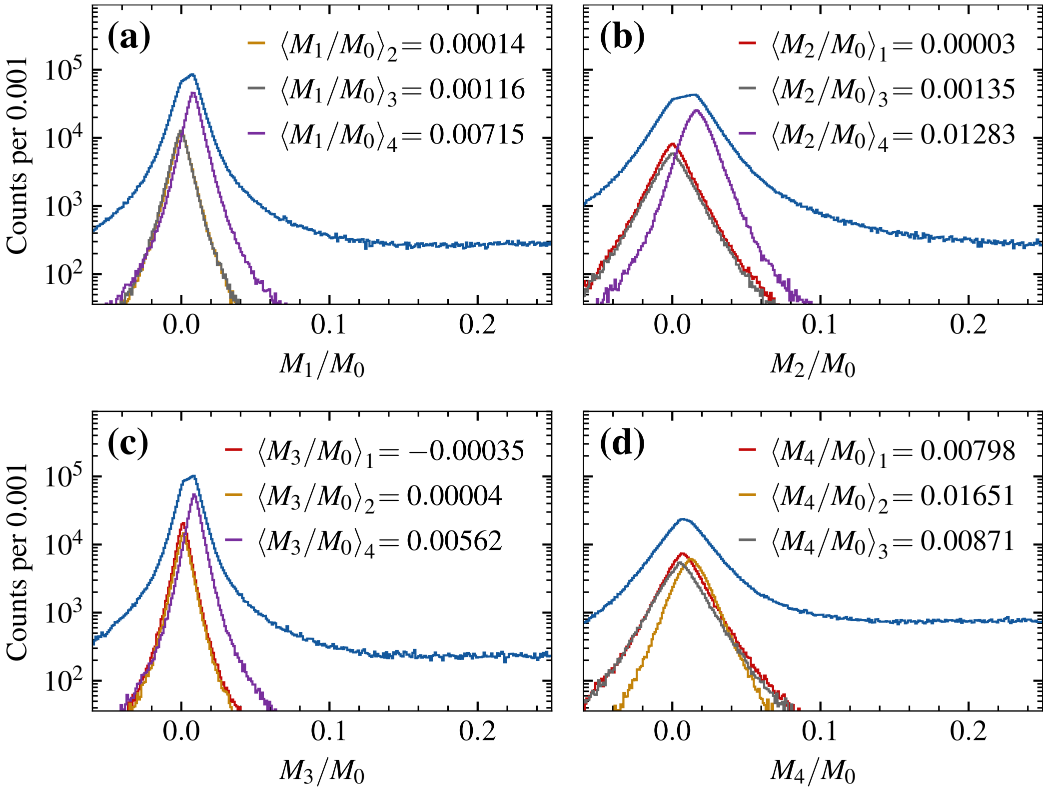

Figure 7.12: M_i/M_0 from Fig. 7.11, zoomed into the left peak around $M_i/M_0 \approx 0$, for all events (blue), as well as for single-segment events (in the color of the collecting segment, see Fig. 6.1). The values for $\langle M_i/M_0\rangle_j$ with $j \neq i$ as determined from Cauchy fits are given in the legend.

The 12 off-diagonal elements result from multiplying the values for $\langle M_j/M_0\rangle_i$ with the segment-specific core amplification factor, i.e.

$$C_{j,i} = \left\langle \frac{M_j}{M_0} \right\rangle_i \cdot \left\langle \frac{M_0}{E_{\text{dep}}} \right\rangle_i \tag{7.11}$$

Overall, the linear cross-talk matrix for the p-type segBEGe detector as determined from the measured spectra in Fig. 7.10 is

$$C = \begin{bmatrix} 1.54274 & 0.00009 & -0.00002 & 0.00054 & -0.00020 \\ 0 & 0.92316 & 0.00005 & -0.00054 & 0.01231 \\ 0 & 0.00022 & 0.90394 & 0.00006 & 0.02546 \\ 0 & 0.00179 & 0.00209 & 0.91898 & 0.01344 \\ 0 & 0.01103 & 0.01979 & 0.00867 & 0.82170 \end{bmatrix} . \tag{7.12}$$

The diagonal elements of C represent the raw calibration factors extracted from the uncalibrated spectra in Fig. 7.10. The segment-to-core cross-talk is at the sub-permille level. The segment-to-segment cross-talk is at the percent level if segment 4 is involved, and at the sub-percent level if segment 4 is not involved.

To correct for linear cross-talk and to calibrate the measured pulse amplitudes to true energies, the inverse of the linear cross-talk matrix, C^{-1}, is needed:

$$C^{-1} = \begin{bmatrix} 0.64820 & -0.00007 & -0.00002 & -0.00038 & 0.00017 \\ 0 & 1.08343 & 0.00029 & 0.00079 & -0.01625 \\ 0 & 0.00015 & 1.10702 & 0.00025 & -0.03431 \\ 0 & -0.00190 & -0.00212 & 1.08832 & -0.01771 \\ 0 & -0.01453 & -0.02664 & -0.01150 & 1.21822 \end{bmatrix} . \tag{7.13}$$

The true energies are obtained using $\vec{E} = C^{-1}\vec{M}$.

The calibrated energy spectra using the calibration matrix C^{-1} in Eq. (7.13) are shown in Fig. 7.13. The peaks associated with the decays of ^{133}Ba, ^{207}Bi, ^{214}Bi and ^{137}Cs are located at their respective energies for all contacts of the detector.

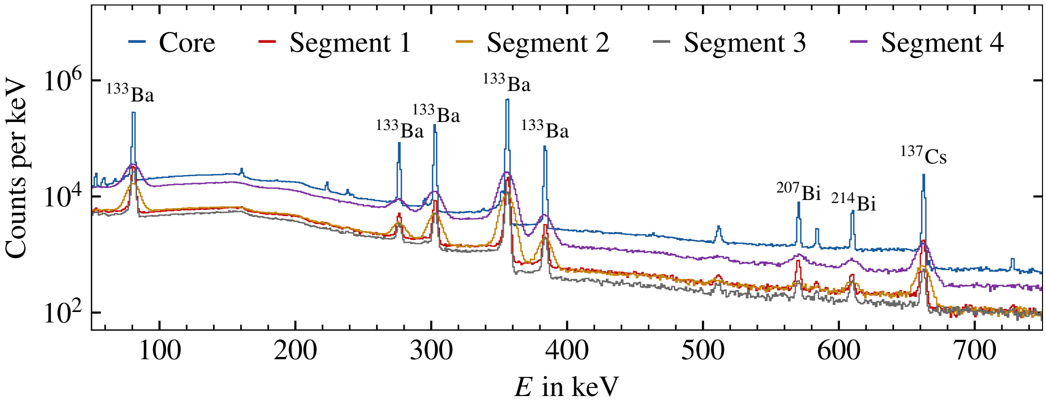

Figure 7.13: Calibrated energy spectra for $V_B = -3000\,\text{V}$, obtained by correcting for the linear cross-talk using the cross-talk matrix listed in Eq. (7.13).

7.4.3 Energy resolution

The energy resolution qualifies the ability to reliably reconstruct E_{dep}. Deviations of the measured energies from the true E_{dep} result from statistical fluctuations of the number of electron-hole pairs, incomplete charge collection and electronic noise, see section 3.4.5.

Characteristic gamma lines in the energy spectrum are typically observed as Gaussian-shaped peaks with certain widths representing the energy resolution, see Fig. 7.13. The relative energy resolution is defined as the ratio between the FWHM of a peak and its mean. The energy resolutions as determined from Gaussian fits to the gamma lines associated with ^{133}Ba and ^{137}Cs decays are listed in Tab. 7.1.

Table 7.1: Mean energy, FWHM and energy resolution for the p-type segBEGe detector, obtained from Gaussian fits to the ^{133}Ba and ^{137}Cs peaks in the calibrated energy spectra for $V_B = -3000\,\mathrm{V}$, see Fig. 7.13. The literature values for the decay energies are taken from [119].

Decay energy	Quantity	Core	Seg. 1	Seg. 2	Seg. 3	Seg. 4
^{133}Ba (80.997 keV)	E in keV	80.98	80.85	80.57	80.91	80.44
	FWHM in keV	1.40	3.26	9.95	3.27	11.11
	Resolution in %	1.73	4.03	12.35	4.05	13.81
^{133}Ba (276.398 keV)	E in keV	276.42	276.37	276.02	276.36	275.43
	FWHM in keV	1.45	3.35	10.46	3.61	11.53
	Resolution in %	0.52	1.21	3.79	1.31	4.19
^{133}Ba (302.853 keV)	E in keV	302.85	302.92	302.39	302.94	301.85
	FWHM in keV	1.46	3.27	10.90	3.26	12.64
	Resolution in %	0.48	1.08	3.60	1.08	4.19
^{133}Ba (356.017 keV)	E in keV	356.01	356.22	355.74	356.02	355.34
	FWHM in keV	1.49	3.27	9.73	3.22	10.88
	Resolution in %	0.42	0.92	2.73	0.90	3.06
^{133}Ba (383.851 keV)	E in keV	383.90	384.04	383.60	383.79	383.03
	FWHM in keV	1.52	3.34	10.55	3.43	12.79
	Resolution in %	0.39	0.87	2.75	0.89	3.34
^{137}Cs (661.660 keV)	E in keV	662.41	662.06	661.42	662.10	661.80
	FWHM in keV	1.71	3.19	10.09	3.10	10.57
	Resolution in %	0.26	0.48	1.53	0.47	1.60

The core contact has by far the best energy resolution of all the contacts. Thus, the core pulses are used to determine E_{dep}. The energy resolutions of segments 1 and 3 are similar to each other and around twice as large as the core energy resolution. Segments 2 and 4, which already showed the broadest distribution of τ_i and higher noise levels, have much worse resolutions. Segment 2 has shown some symptoms of a bad contact. Segment 4 is more than three times larger than the other segments and has the largest capacitance of more than 100 pF, see Eq. (6.1).

In general, the relative energy resolution decreases with increasing energy. This is due to the fact that the relative influence of statistical fluctuations of the number of electron-hole pairs decreases with E_{dep}.

7.5 Pulses from the undepleted detector

Core pulses from the fully-depleted p-type segBEGe detector typically feature a very fast rise before approaching their final amplitude, see section 6.3.2. Core pulses from the undepleted p-type segBEGe detector do not reach their final amplitude immediately but approach it exponentially with a characteristic time constant, τ_u, which depends on the depletion level of the detector.

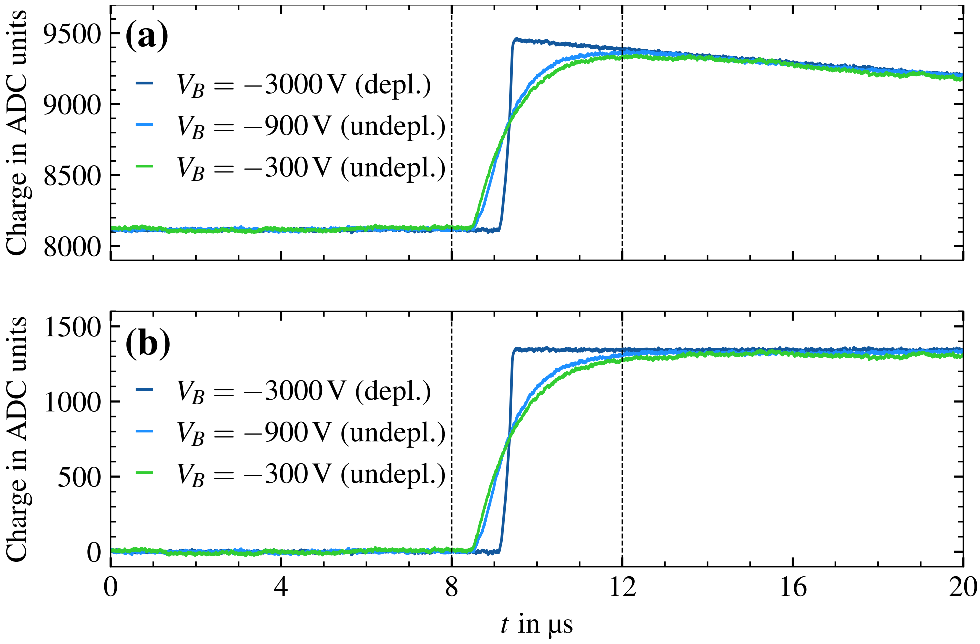

Figure 7.14: Typical pulses from the core contact of the depleted and the undepleted p-type segBEGe detector, (a) before and (b) after baseline- and decay-correction using $\bar{\tau}_0$ determined at $V_B = -3000\,\text{V}$.

Figure 7.14 depicts typical core pulses from the p-type segBEGe detector at different bias voltages. As the exponential decay of the pulses is a feature depending only on the read-out electronics, the values of $\bar{\tau}_i$ do not depend on the bias voltage applied to the detector. Therefore, the values for $\bar{\tau}_i$ determined at $V_B = -3000\,\text{V}$ were used to correct the pulses for the undepleted detector.

The corrected core pulses from the undepleted detector still feature a slight rise in the tail window, see Fig. 7.14b. Therefore, the mean value of the pulse in the tail window is not a good approximation for the final pulse amplitude. For undepleted detectors, the core pulse amplitude, M_0, is extracted by fitting an exponential function

$$Q_0(t) = M_0 \cdot (1 - \exp(-(t - t_0)/\tau_u)) \tag{7.14}$$

to the tail window of the core pulse.

The resulting core energy spectra for different V_B are shown in Fig. 7.15. The gamma lines associated with the decays of ^{133}Ba and ^{137}Cs are visible in all these spectra. However, the widths of the peaks increase and the peaks shift towards smaller ADC units with decreasing depletion level.

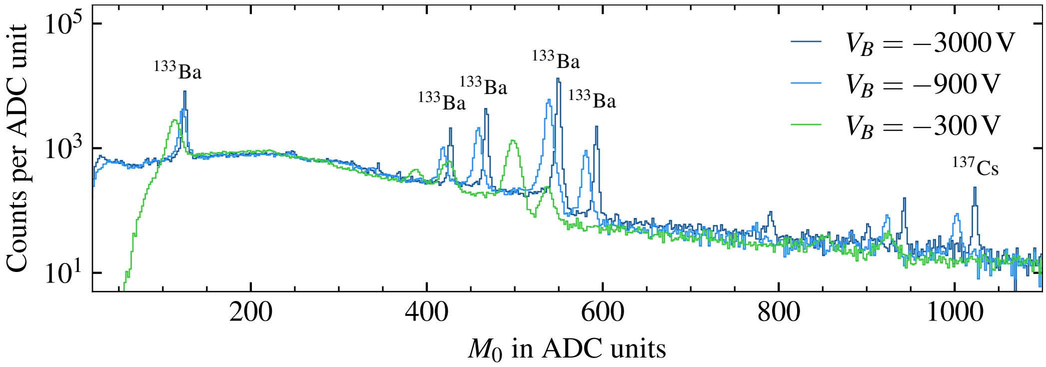

Figure 7.15: Uncalibrated energy spectrum for the core contact of the p-type segBEGe detector for different bias voltages V_B obtained from 20 min measurements with an uncollimated ^{133}Ba source on top of the K2 cryostat. Labeled are the peaks associated with the decays [119] of ^{133}Ba (80.997 keV, 276.398 keV, 302.853 keV, 356.017 keV, 383.851 keV) and ^{137}Cs (661.660 keV).

The measured pulse amplitudes determined from the undepleted detector can be calibrated using the procedure described in section 7.4. The resulting calibration matrix for the measurement at $V_B = -300\,\mathrm{V}$ is

$$C = \begin{bmatrix} 1.39563 & 0.00611 & 0.00498 & 0.00294 & -0.00422 \\ 0 & 0.91826 & 0.00188 & 0.00180 & 0.01111 \\ 0 & -0.00076 & 0.91395 & -0.00086 & 0.01645 \\ 0 & 0.00470 & 0.00511 & 0.89817 & 0.01427 \\ 0 & -0.01621 & -0.00702 & -0.01574 & 0.81048 \end{bmatrix} \tag{7.15}$$

$$C^{-1} = \begin{bmatrix} 0.71652 & -0.00469 & -0.00385 & -0.00227 & 0.00391 \\ 0 & 1.08876 & -0.00234 & -0.00245 & -0.01484 \\ 0 & 0.00051 & 1.09398 & 0.00066 & -0.02223 \\ 0 & -0.00604 & -0.00636 & 1.11304 & -0.01938 \\ 0 & 0.02166 & 0.00930 & 0.02157 & 1.23297 \end{bmatrix} . \tag{7.16}$$

The raw core calibration factor $C^{-1}_{0,0}$ at $V_B = -300\,\mathrm{V}$ is more than 10% higher than for $V_B = -3000\,\mathrm{V}$, see Eq. (7.13). In addition, the values for $C^{-1}_{0,i}$ corresponding to segment-to-core cross-talk differ more than for $V_B = -3000\,\mathrm{V}$.

The calibrated energy spectrum for $V_B = -300\,\mathrm{V}$ is shown in Fig. 7.16. The energy resolutions determined at the ^{133}Ba and ^{137}Cs peaks are listed in Tab. 7.2. The peaks in the core energy spectrum are around seven times wider compared to the peaks at $V_B = -3000\,\mathrm{V}$, see Fig. 7.13. In contrast, the FWHMs of the peaks in the energy spectra of the segments increase by only around 50%. For $V_B = -300\,\mathrm{V}$, the energy resolutions of segments 1 and 3 are around twice as good as the ones for the core and segments 2 and 4. Thus, for single-segment events in segment 1 and 3, E_{dep} can be reconstructed around twice as accurately from the segments than from the core. In general, the detector works quite well when not fully depleted, although the active volume is reduced compared to the fully-depleted case.

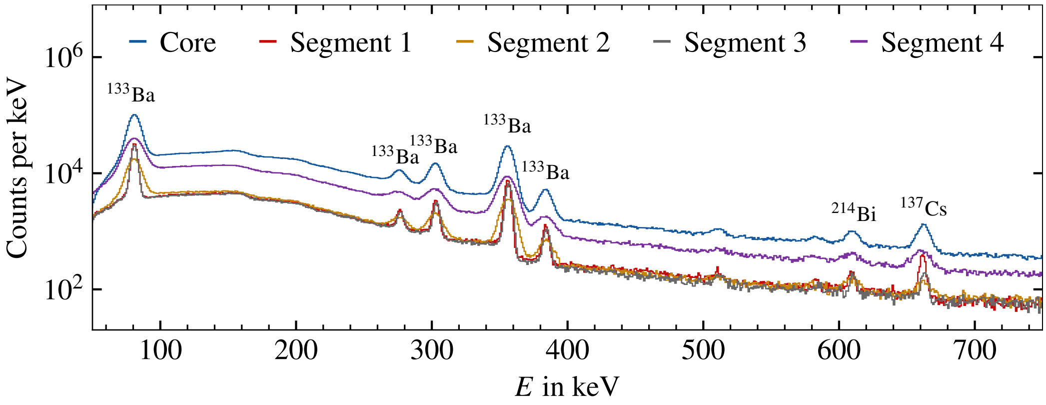

Figure 7.16: Calibrated energy spectrum for $V_B = -300\,\text{V}$ obtained by correcting for the linear cross-talk using the cross-talk matrix listed in Eq. (7.16).

Table 7.2: Mean energy, FWHM and energy resolution for the p-type segBEGe detector, obtained from Gaussian fits to the ^{133}Ba and ^{137}Cs peaks in the calibrated energy spectra for $V_B = -300\,\text{V}$, see Fig. 7.16. The literature values for the decay energies were taken from [119].

Decay energy	Quantity	Core	Seg. 1	Seg. 2	Seg. 3	Seg. 4
^{133}Ba (80.997 keV)	E in keV	80.95	80.94	80.73	80.91	80.97
	FWHM in keV	9.82	4.84	11.00	5.12	13.46
	Resolution in %	12.13	5.99	13.63	6.33	16.62
^{133}Ba (276.398 keV)	E in keV	275.80	276.32	275.45	276.88	274.31
	FWHM in keV	10.53	5.03	14.15	5.66	15.21
	Resolution in %	3.82	1.82	5.14	2.04	5.54
^{133}Ba (302.853 keV)	E in keV	302.12	302.79	301.92	303.51	301.20
	FWHM in keV	11.88	5.07	13.76	5.33	17.76
	Resolution in %	3.93	1.67	4.56	1.76	5.90
^{133}Ba (356.017 keV)	E in keV	355.67	355.93	355.84	356.74	355.18
	FWHM in keV	9.67	4.74	10.77	5.08	13.11
	Resolution in %	2.72	1.33	3.03	1.42	3.69
^{133}Ba (383.851 keV)	E in keV	383.36	383.79	383.57	384.61	381.95
	FWHM in keV	11.17	4.79	12.50	5.31	19.20
	Resolution in %	2.91	1.25	3.26	1.38	5.03
^{137}Cs (661.660 keV)	E in keV	662.01	661.54	661.97	663.12	660.07
	FWHM in keV	9.77	4.76	10.76	5.25	14.27
	Resolution in %	1.48	0.72	1.63	0.79	2.16

8 Determination of the impurity density profile from capacitance measurements

The extraction of charge drift mobility values from measured charge pulses requires the electric field in the detector to be known. In point-contact detectors, the electric field in most parts of the detector is defined by the impurity density profile in the bulk of the detector, whose exact nature is not provided by the detector manufacturer.

The impurity density profile defines the depletion behavior of the detector and can, thus, be determined from the capacitance measurements below the depletion voltage [34, 195–197]. In this chapter, the measurement of a capacitance-voltage curve, CV-curve, of the p-type segBEGe detector and the results for the impurity density profile and the electric field in the bulk of the detector are presented.

8.1 Experimental setup

One way to measure the CV-curve of a detector with two contacts is to apply voltage step pulses with known amplitude to one contact and to measure the increase of charge on the other contact. The schematic of the experimental setup to measure a CV-curve of the p-type segBEGe detector is shown in Fig. 8.1. All segments were connected together to form a single n^+ contact. The bias voltage V_B was applied to the core contact and the n^+ contact was kept at ground over a termination resistor R_2.

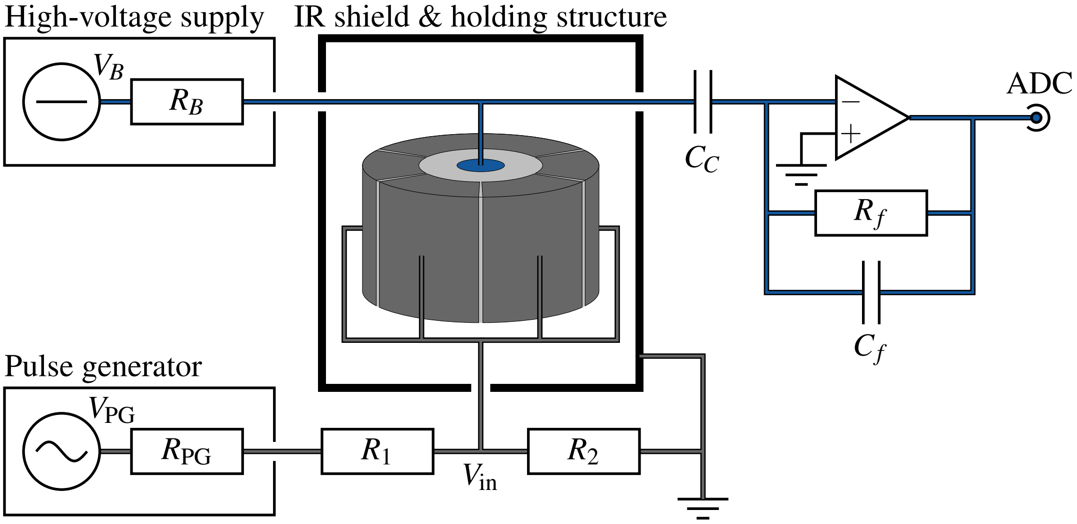

Figure 8.1: Schematic of the setup to measure a CV-curve of the p-type segBEGe detector in K2. The read-out electronics of the core were not modified with respect to Fig. 6.3.

A pulse generator was used to inject voltage pulses into the n^+ contact at a frequency of 200 Hz. A voltage divider consisting of the two resistors, $R_1 = (6170 \pm 70)\,\Omega$ and $R_2 = (51.1 \pm 0.7)\,\Omega$, and the internal resistor of the pulse generator, $R_{PG} = 50\,\Omega$, was used to reduce the peak-to-peak amplitude of these pulses of $V_{PG} = 200\,\text{mV}$ to

$$V_{in} = V_{PG}\,\frac{R_2}{R_{PG} + R_1 + R_2} = (1.630 \pm 0.028)\,\text{mV}\ . \tag{8.1}$$

This measurement will be referred to as pulser measurement.

8.2 Determination of the CV-curve

The detector capacitance, C_d, is defined as the capacitance of the depleted volume. It is connected in series to the coupling capacitor, C_C, resulting in a total capacitance, C_{tot}, of

$$\frac{1}{C_{\text{tot}}} = \frac{1}{C_d} + \frac{1}{C_C} \quad \Rightarrow \quad C_{\text{tot}} = \frac{C_d \cdot C_C}{C_d + C_C} , \tag{8.2}$$

The fully-depleted detector is well described by C_d, see Fig. 8.2a. In the partially depleted detector, the depleted and the undepleted volume must be modeled differently [198], see Fig. 8.2b. The depleted volume is well modeled by C_d which is higher than the full-depletion capacitance. In the undepleted volume, the concentration of free holes is higher than in the depleted volume. This results in a finite resistance, R_u, of the undepleted volume in addition to its capacitance C_u.

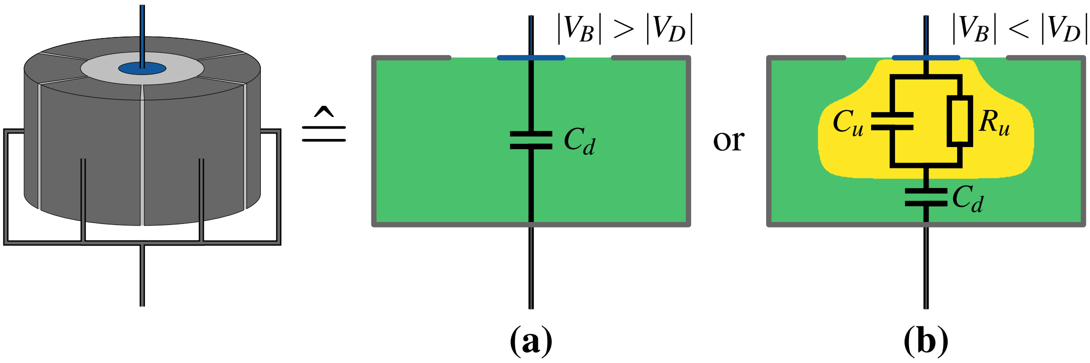

Figure 8.2: Schematic of the electronic circuits describing the p-type segBEGe detector with connected segments as in Fig. 8.1 for a (a) fully-depleted and (b) partially-depleted detector. The depleted volume is shown in green, the undepleted volume is shown in yellow.

The voltage V_{in} applied to the n$^+$ contact leads to charges being collected on the feedback capacitor, C_f, of the charge-sensitive preamplifier. In the fully-depleted detector, the charge pulses from pulser events quickly reach their final amplitude of $Q_{\text{out}} = -V_{\text{in}} C_{\text{tot}}$. In the partially depleted detector, the undepleted volume leads to a slow-down of the charge collection. Based on the formula derived for a setup without a coupling capacitor [195], pulses from pulser events are expected to take the form

$$Q(t) = \underbrace{-V_{\text{in}}\, C_{\text{tot}}}_{= Q_{\text{out}}} \cdot \left(1 - \frac{C_{\text{tot}}}{C_u + C_{\text{tot}}} \exp\left(-\frac{t}{R_u(C_u + C_{\text{tot}})}\right)\right) , \tag{8.3}$$

where C_{tot} is again defined as C_d and C_C connected in series, see Eq. (8.2). Thus, the output pulses for a partially depleted detector exponentially approach their final amplitudes $Q_{\text{out}} = -V_{\text{in}} C_{\text{tot}}$ with a time constant of $\tau_u = R_u(C_u + C_{\text{tot}})$, which depends on the geometry of the undepleted volume.

The values of C_{tot} are determined from Q_{out} for different V_B applied to the point contact of the segBEGe detector. The CV-curve is corrected for $C_C = 1.2\,\text{nF}$ using Eq. (8.2).

8.2.1 Charge calibration

At a pulse generation frequency of 200 Hz, 120 000 pulser events were recorded for each 10 min measurement. The spectra of the uncalibrated measured pulse amplitudes from the core contact, determined as explained in chapter 7, are shown in Fig. 8.3 for a selection of bias voltages V_B. Each spectrum features a dominant peak associated with pulser events. Smaller peaks resulting from physical events, e.g. from ^{208}Tl decays, are also present as the detector DAQ was not time-coupled to the pulse generator.

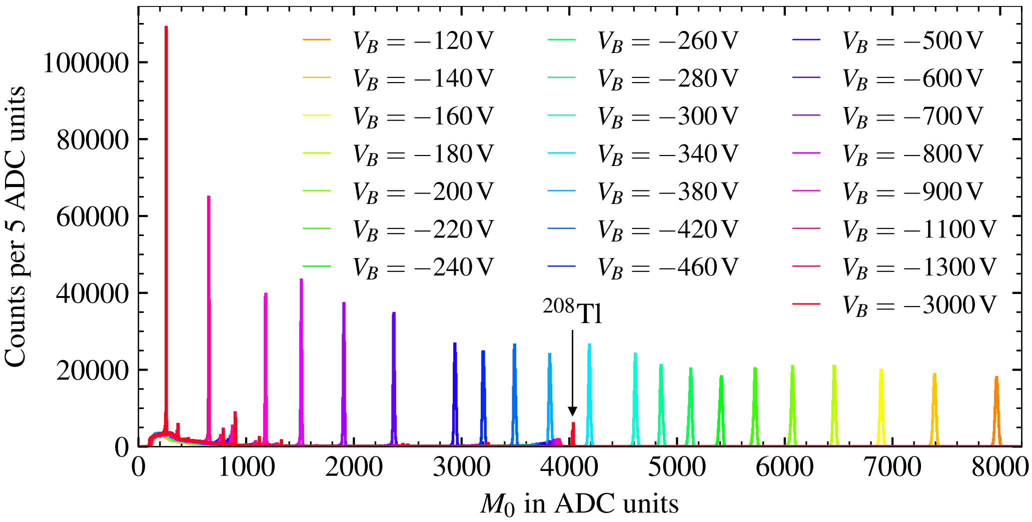

Figure 8.3: Uncalibrated core energy spectra from 10 min pulser measurements for a selection of bias voltages V_B as given in the legend. The peak at around 4030.2 ADC units corresponds to 2614.533 keV gammas associated with the decay of ^{208}Tl [119].

The ADC values for M_0 have to be calibrated to the corresponding charge Q_{out}. For the capacitance measurement, the segment contacts are connected and, therefore, there is no segment-specific cross-talk onto the core contact. This allows for a precise calibration of M_0 by simply multiplying M_0 with a core calibration factor.

The core calibration factor is determined from the peaks resulting from energy deposits in the detector, e.g. the 2614.533 keV peak from ^{208}Tl decays [119], see Fig. 8.3. The energies are converted to charges based on the ionization energy of germanium of $E_{eh} = 2.95\,\text{eV}$ [129]. For example, an energy deposit of 2614.533 keV corresponds to a charge of 0.142 pC. From the measurement at $V_B = -3000\,\text{V}$, the core calibration factor is $3.527 \cdot 10^{-17}\,\text{C / ADC unit}$ or 0.6487 keV / ADC unit. The latter agrees with the raw core calibration factor for standard operation, where the segments are not connected, see Fig. 7.10.

The overall core calibration factor increases with decreasing depletion level, see section 7.5. However, this is due to higher cross-talk between the core and the segments resulting from higher capacitances at lower depletion levels. The conversion from M_0 to Q_{out} is assumed to be independent of the depletion level of the detector. Therefore, the core calibration factor determined at $V_B = -3000\,\text{V}$ was applied for all pulser measurements.

8.2.2 Pulser event selection

The amplitudes measured from individual pulses were subject to fluctuations due to electronic noise. Therefore, averaged superpulses were determined to mitigate the influence of electronic noise. Pulser events were selected by applying three cuts:

- **Amplitude cut**

  The dominant peaks in the M_0 spectra in Fig. 8.3 were classified as pulser event candidates. Events in the highest peak in the M_0 spectrum were selected by finding the bin with the most counts and keeping events in surrounding bins with M_0 values of $\pm^{1.2}_{1.0}\%$. This asymmetric interval was always wider than the FWHM of the peak.

- **Frequency cut**

  Most of the events selected by the amplitude cut are pulser events. However, some pulses from physics events also pass the amplitude cut and need to be identified and discarded. For this, the time stamps of the events are used.

  Pulser events occur every 5 ms. Figure 8.4a shows the distribution of the time difference between two consecutive pulses that passed the amplitude cut. The main peak is observed at 5 ms. Smaller peaks at multiples of 5 ms correspond to cases where the amplitude cut removed pulser events between two non-consecutive pulser events. Events with time differences deviating more than 100 ns from multiples of 5 ms, see Fig. 8.4b, were discarded. As the time window of 100 ns is significantly shorter than the pulse lengths of 20 µs, this frequency cut discards all non-pulser events.

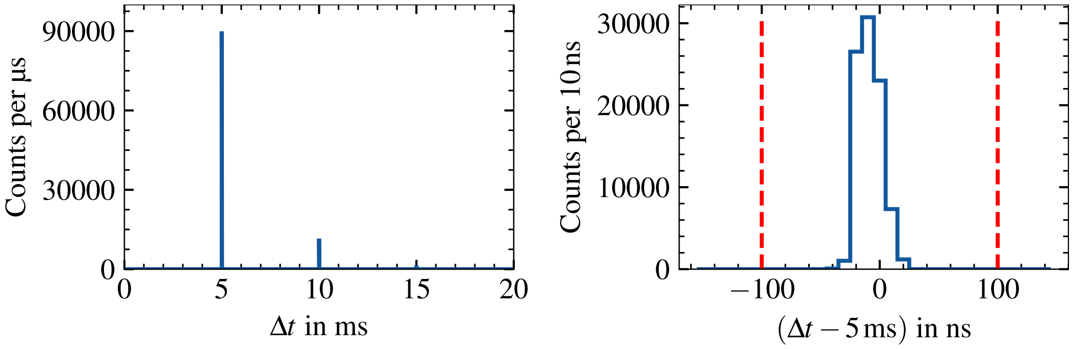

Figure 8.4: (a) Time difference Δt between pulses passing the amplitude cut from the 10 min pulser measurement at $V_B = -3000\,\text{V}$, (b) zoomed into the peak at $\Delta t = 5\,\text{ms}$.

- **Similarity cut**

  All events selected by the amplitude and the frequency cuts are pulser events. However, pile-up can led to additional rises in the pulses if energy was deposited during the baseline or the tail window, see Figs. 8.5a and 8.5b. To discard pile-up events, an additional cut was imposed on the similarity between the pulses.

  Two pulses are considered to be similar if they agree within their noise levels. All pulses were time-aligned to reach 50% of their final amplitude at the same time and a preliminary superpulse was determined, see Figs. 8.5a and 8.5b. Events with pulses that deviate by $\chi^2/\text{ndf} \geq 7$ from this preliminary superpulse were discarded. This similarity cut efficiently discarded remaining outliers.

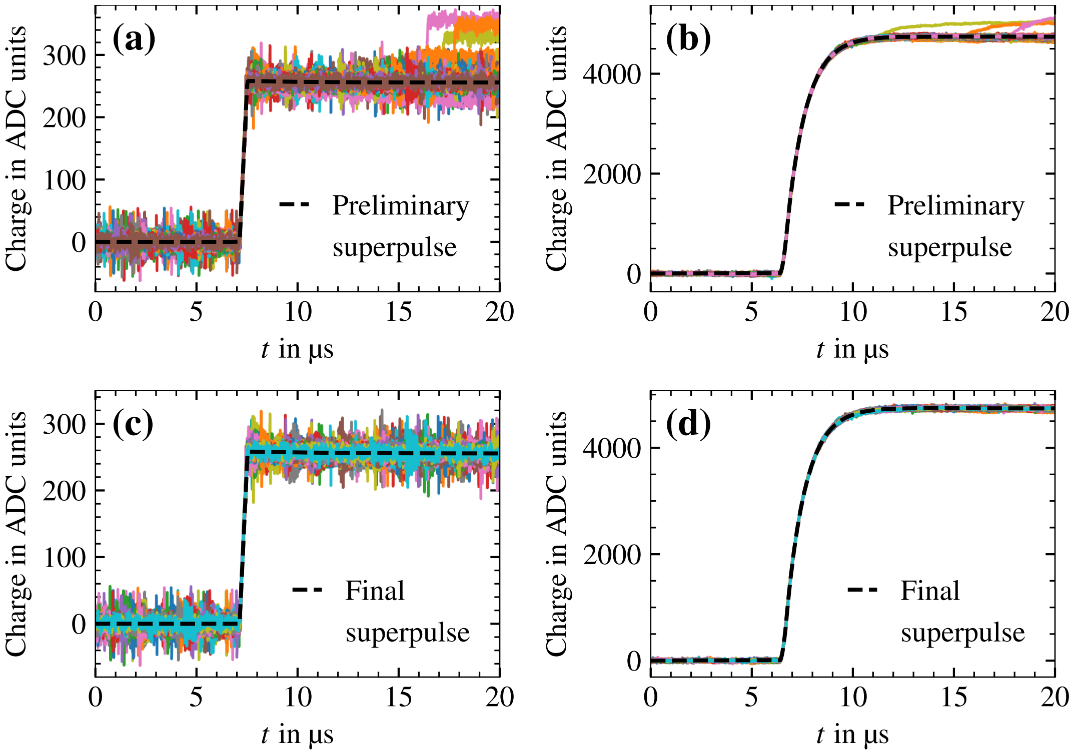

Figure 8.5: Example pulses passing the amplitude and frequency cut for (a) $V_B = -3000\,\mathrm{V}$ and (b) $V_B = -300\,\mathrm{V}$. Final selection of pulses for (c) $V_B = -3000\,\mathrm{V}$ and (d) $V_B = -300\,\mathrm{V}$ after the similarity cut. Shown as black dashed lines are the preliminary superpulses in (a) and (b), and the final superpulses in (c) and (d).

The events that passed the amplitude, frequency and similarity cuts comprise the final selection of pulser events. Their pulses are averaged to obtain the final superpulse for the respective V_B, see Figs. 8.5c and 8.5d, from which M_0 and Q_{out} were determined. The usage of superpulses provided more accurate Q_{out} values than averaging individually determined Q_{out}, especially at low V_B, where the noise level is substantial.

8.2.3 Determination of the capacitance values

The tail of the final superpulses in Fig. 8.5 should ideally be flat for the fully-depleted detector and follow an exponential function for the partially depleted detector as shown in Eq. (7.14). When zooming into the tails of the final superpulses in Fig. 8.6, ringing is visible which is well described by a damped oscillation. The amplitude of this ringing is less than 0.5% of the final pulse amplitude M_0. However, it was considered when composing a fit function to extract M_0 from the tail of the final superpulses:

$$Q_0(t) = \begin{cases} M_0 \cdot \left(1 + A \cdot \exp(-\frac{t}{\tau_r}) \sin(\omega t + \Phi)\right), & \text{if } |V_B| > |V_D|, \\ \underbrace{M_0 \cdot (1 - \exp(-\frac{t - t_0}{\tau_u}))}_{\text{Tail}} \cdot \underbrace{\left(1 + A \cdot \exp(-\frac{t}{\tau_r}) \sin(\omega t + \Phi)\right)}_{\text{Ringing}}, & \text{if } |V_B| < |V_D|, \end{cases} \tag{8.4}$$

where the fit parameters A, τ_r, ω and Φ denote the amplitude, the decay time, the angular frequency and the phase of the damped oscillation.

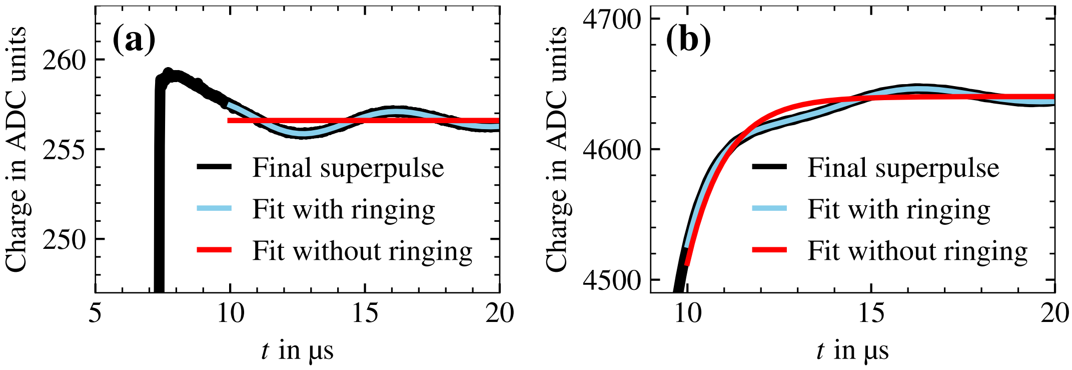

Figure 8.6: Zoom into the tails of the final superpulses shown in Figs. 8.5c and 8.5d for (a) $V_B = -3000\,\mathrm{V}$ and (b) $V_B = -300\,\mathrm{V}$. The fit results with and without the ringing factor in Eq. (8.4) are shown in blue and red, respectively.

The final pulse amplitudes are extracted by fitting the function in Eq. (8.4) to the tail of the pulses for $t > 10\,\mu\mathrm{s}$, see Fig. 8.6. This provides a more accurate result for M_0 compared to just taking the average in the tail window.

The fit results for M_0 of the final superpulses were converted to Q_{out} by multiplying them by the core calibration factor of $3.527 \cdot 10^{-17}\,\mathrm{C\,/\,ADC}$ units. The total measured capacitance $C_{\mathrm{tot}}^{\mathrm{meas}}$ was then determined by dividing by $V_{\mathrm{in}} = (1.630 \pm 0.028)\,\mathrm{mV}$. The resulting CV-curve for C_d^{meas} is shown in Fig. 8.7. Also shown are the values of $C_{\mathrm{tot}}^{\mathrm{meas}}$ before correcting for the coupling capacitor $C_C = 1.2\,\mathrm{nF}$ using Eq. (8.2). With decreasing depletion level, C_d increases and, therefore, the influence of $C_C = 1.2\,\mathrm{nF}$ on C_{tot} increases from less than 1% at full depletion to almost 16% at $V_B = -120\,\mathrm{V}$.

The simulation predicts a constant capacitance at full depletion of 5.54 pF. In the measurement, the capacitance values for V_B above V_D fluctuate around a mean value of 5.58 pF with a standard deviation of 0.17%. This mean value is 0.8% higher than the simulated value.

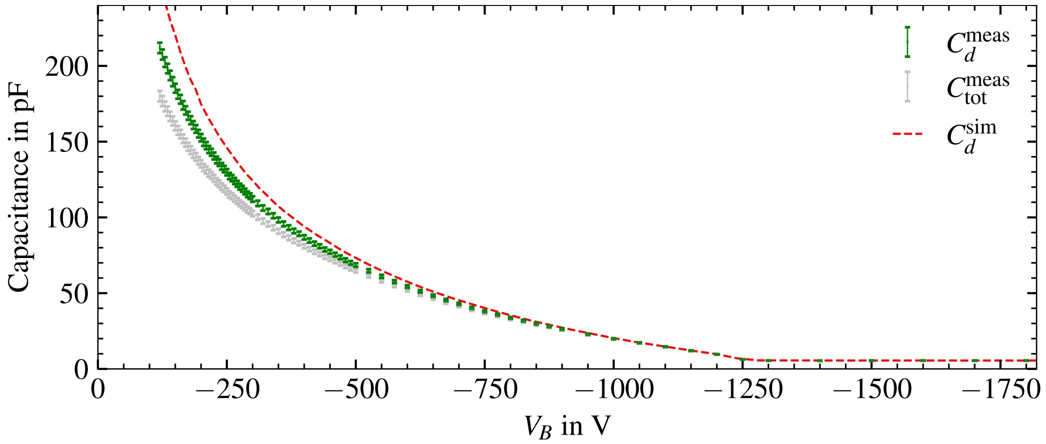

Figure 8.7: Measured CV-curve for the p-type segBEGe detector, $C_{\mathrm{tot}}^{\mathrm{meas}}$, and capacitance of the depleted volume, C_d^{meas}, correcting for $C_C = 1.2\,\mathrm{nF}$ using Eq. (8.2). Shown as a red dashed line is the simulated CV-curve, C_d^{sim}, from Fig. 6.11.

The systematic uncertainties, $\Delta C_{\mathrm{sys}}^{\mathrm{meas}}$, are mostly defined by the uncertainties on V_{in}, on $\bar{\tau}_0$ and on the core calibration factor. The 1.7% uncertainty on V_{in} results in a systematic relative uncertainty on C_d^{meas}, which is expected to be identical for all V_B. Variations of $\bar{\tau}_0$ result in systematic shifts of M_0 towards higher or lower ADC units. However, these deviations also result in a lower or higher core calibration factor, respectively, such that they are compensated and do not contribute significantly to $\Delta C_{\mathrm{sys}}^{\mathrm{meas}}$ compared to V_{in}.

The statistical uncertainties, $\Delta C_{\mathrm{stat}}^{\mathrm{meas}}$, result from the remaining noise level in the final superpulses and the uncertainties on the fit result for M_0. Based on the observed 0.17% fluctuation around the physically constant full-depletion capacitance, $\Delta C_{\mathrm{stat}}^{\mathrm{meas}}$ was estimated to be 10% of $\Delta C_{\mathrm{sys}}^{\mathrm{meas}}$. Thus, the uncertainties shown in Fig. 8.7 are dominated by $\Delta C_{\mathrm{sys}}^{\mathrm{meas}}$ and are highly correlated.

8.3 Fitting an impurity density profile to the measured CV-curve

The measured CV-curve was used to determine the impurity density profile of the p-type segBEGe detector. To do so, a parameterization for the impurity density profile had to be chosen. Then, CV-curves were simulated for different sets of parameters. The impurity density profile, for which the simulated CV-curve matches the measured CV-curve best, was chosen as the result.

In total, 98 capacitance values for bias voltages in the range from $-120\,\mathrm{V}$ to $-3000\,\mathrm{V}$ were extracted. Given a parameterization for the impurity density profile with a set of parameters, the CV-curve for all 98 bias voltages can be simulated using SSD.

The p-type segBEGe detector was implemented in SSD as described in chapter 6, assuming a segment contact thickness of 0.75 mm[*]. All simulations were run with refinement limits of $[0.2, 0.1, 0.05, 0.03, 0.02, 0.01]$ and a convergence limit of 10^{-7}. These refinement limits ensure that the numerically calculated potential values of neighboring grid points do not differ more than 1% of V_B for the electric potential, and 0.01 for the weighting potentials.

The values for the simulated capacitances, C_d^{sim}, are also subject to uncertainties. Systematic uncertainties, $\Delta C_{\mathrm{sys}}^{\mathrm{sim}}$, arise from uncertainties on the geometry of the detector, e.g. its radius R, height H and the thicknesses of the segment contacts, as well as from the simulation settings, e.g. the grid refinement or the convergence limit. However, they are small compared to the systematic uncertainty $\Delta C_{\mathrm{sys}}^{\mathrm{meas}}$ of 1.7%. Statistical uncertainties on the simulated capacitance values, $\Delta C_{\mathrm{stat}}^{\mathrm{sim}}$, are also negligible compared to the statistical uncertainties $\Delta C_{\mathrm{stat}}^{\mathrm{meas}}$.

The fit routine to determine the impurity density profile must account for the systematic and statistical uncertainties. The overall systematic uncertainty, ΔC_{sys}, is dominated by $\Delta C_{\mathrm{sys}}^{\mathrm{meas}}$ of 1.7%. It allows for a correlated, systematic shift of the values for C_d^{meas} which can be parameterized by a relative offset, Ξ. The statistical uncertainties, ΔC_{stat}, are dominated by $\Delta C_{\mathrm{stat}}^{\mathrm{meas}}$ and allow for random fluctuations in the residuals between the shifted values for C_d^{meas} and C_d^{sim}.

---

[*] The measured dead-layer thickness from radial scans is $(0.75 \pm 0.06)\,\mathrm{mm}$, see page 123.

The likelihood, $\mathcal{L}$, of observing the measured CV-curve $C_d^{\text{meas}}(V_B)$, given a simulated CV-curve $C_d^{\text{sim}}(V_B)$ for given parameters, can be defined as

$$\mathcal{L} = \prod_{V_B} \underbrace{\mathcal{N}(0, \Delta C_{\text{sys}}(V_B)/C_d^{\text{meas}}(V_B))(\Xi)}_{\text{Likelihood for } \Xi} \cdot \underbrace{\mathcal{N}(C_d^{\text{meas}}(V_B)\cdot(1+\Xi), \Delta C_{\text{stat}}(V_B))(C_d^{\text{sim}}(V_B))}_{\text{Likelihood for the capacitance value at } V_B} .$$

The goal is to find a set of parameters that result in a CV-curve $C_d^{\text{sim}}(V_B)$ with maximum likelihood $\mathcal{L}$. Mathematically, this is equivalent to finding the minimum of

$$-\ln(\mathcal{L}) = \sum_{V_B} \left(\frac{(\Xi \cdot C_d^{\text{meas}}(V_B))^2}{2\,\Delta C_{\text{sys}}(V_B)^2} + \frac{(C_d^{\text{sim}}(V_B) - C_d^{\text{meas}}(V_B)\cdot(1+\Xi))^2}{2\,\Delta C_{\text{stat}}(V_B)^2} \right) . \qquad (8.5)$$

The negative log-likelihood in Eq. (8.5) consists of an addition of logarithms rather than a multiplication of individual probabilities as in Eq. (8.3). This allows for a more efficient determination of the set of parameters with maximum likelihood when using an optimizer based on the gradient descent method, e.g. Optim.jl [199].

For each new set of parameters, the simulation of the CV-curve is redone. Starting with a given initial set of parameters, the optimizer estimates the gradients of $-\ln(\mathcal{L})$ by varying the parameters. It, then, updates the parameters to advance towards smaller values of $-\ln(\mathcal{L})$ until reaching a local minimum. If the negative log-likelihood has multiple local minima, different initial parameters can lead to different results. Therefore, fits are to be run with different sets of initial parameters to test that they always provide the same best-fit result.

The fit is essentially a frequentist maximum-likelihood fit with one improvement: The fit is performed in a transformed space to prevent the optimizer from moving to unphysical parts of the parameter space and to guide the optimizer toward faster convergence. A very conservative prior for the parameters is chosen which does not exclude any physically sensible parameters completely. The transformation function between this prior distribution and a standard multivariate normal distribution is applied to the parameter space during the maximum-likelihood search. This way, the optimizer runs in an unconstrained space. The likelihood function is not modified and the prior only reshapes the space. Thus, no bias beyond the exclusion of unphysical parameter values is introduced.

8.4 Parameterization of the impurity density profile

For the parameterization of the impurity density profile of the p-type segBEGe detector, the cylindrical detector coordinates r, φ and z introduced in Fig. 6.1a are used. In addition, the following assumptions about the parameterization, $\rho(r,\varphi,z)$, were made:

- The impurity density profile is assumed to be independent of φ, i.e. $\rho(r,\varphi,z) = \rho(r,z)$.
- The r and z-dependence are assumed to be factorizable, i.e. $\rho(r,z) = \rho_r(r)\cdot\rho_z(z)$.
- According to the detector manufacturer, the impurity density increases by 12.1% from the bottom to the top, see Tab. 6.1. This overall gradient is fixed for $\rho_z(z)$.

The z-dependence in the impurity density profile mostly influences the extent of the depleted volume in z. Different parameterizations for $\rho_z(z)$ resulting in a depletion voltage of $V_D = -1275\,\mathrm{V}$ were simulated. It was observed that the choice of the parameterization for the z-dependence does not have a significant influence on the simulated capacitance values, as long as it is monotonous. Therefore, $\rho_z(z) = (1 + \beta \frac{z}{H})$, i.e. a linear z-dependence with a fixed increase of $\beta = 12.1\%$, was chosen.

The detector manufacturer provided no information on the radial component $\rho_r(r)$. However, a simulation of the CV-curve assuming a constant value ρ_0 in r, chosen such that it matches the depletion voltage of $V_D = -1275\,\mathrm{V}$, the values of the capacitance at voltages below $-900\,\mathrm{V}$ are significantly overestimated, see Fig. 8.7. This means that the extent of the depleted volume is underestimated. As the detector depletes from the outside to the inside, this means that the impurity density at outer r is overestimated.

8.4.1 Piecewise constant parameterization

To get a first impression, a simplistic parameterization of $\rho_r(r)$ as a piecewise constant function with intervals of width $\Delta r = 5\,\mathrm{mm}$ was chosen:

$$\rho(r,z) = \rho_r(r) \cdot (1 + \beta \frac{z}{H}) \quad \text{with} \quad \rho_r(r) = \begin{cases} \rho_1, & \text{for } 0 \le r < \Delta r \\ \rho_2, & \text{for } \Delta r \le r < 2\Delta r \\ \vdots & \\ \rho_N, & \text{for } (N-1)\Delta r \le r \le R \end{cases}, \tag{8.6}$$

where $\beta = 12.1\%$ is fixed. The fit parameters ρ_k with $k \in \{1, \ldots, 8\}$ were restricted to negative values, corresponding to p-type germanium.

The result for $\rho_r(r)$ as obtained from the maximum-likelihood fit to the measured CV-curve is shown in Fig. 8.8a. It features an almost constant plateau at 97% of the manufacturer values for $r < 30\,\mathrm{mm}$ and decreases steeply to almost zero for $r > 30\,\mathrm{mm}$. The decrease in impurity density at large r requires the impurity density in the center of the detector to be higher than the previous scaling of 89% to still predict the full-depletion voltage of $V_D = -1275\,\mathrm{V}$.

In Fig. 8.8b, the simulated CV-curve for the best-fit result is compared to the measured CV-curve. The difference between the simulated and the measured value for the full-depletion capacitance is accounted for by the relative offset $\Xi = -0.8\%$. This relative offset is still well within the expected systematic uncertainty of 1.7%. The best-fit result predicts the measured CV-curve in the range between $-1050\,\mathrm{V}$ and $-550\,\mathrm{V}$ within less than two standard deviations. The prediction is more than 2σ above the measured CV-curve in the range from $-300\,\mathrm{V}$ to $-500\,\mathrm{V}$ and below by more than 2σ for V_B below $-180\,\mathrm{V}$. This means that the impurity density is underestimated close to the outer surface at $r \lesssim R$ and overestimated in the transition region between the constant plateau and the steep gradient around $r \approx 30\,\mathrm{mm}$. This shows the limits of this simplistic parameterization.

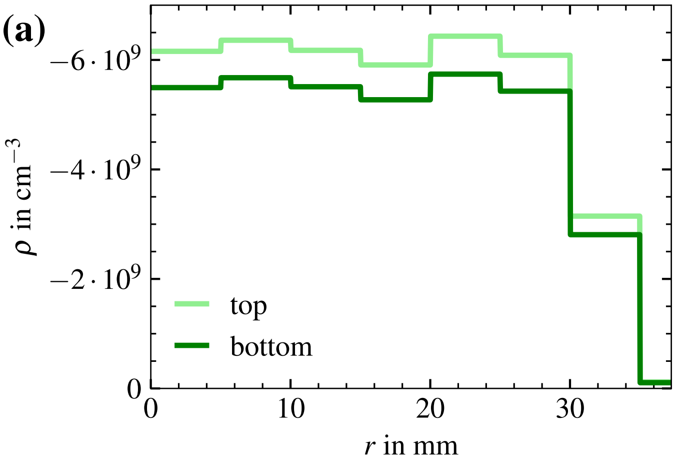

Parameter	Value
ρ_1	$-5.49\cdot10^9\,\mathrm{cm}^{-3}$
ρ_2	$-5.68\cdot10^9\,\mathrm{cm}^{-3}$
ρ_3	$-5.51\cdot10^9\,\mathrm{cm}^{-3}$
ρ_4	$-5.27\cdot10^9\,\mathrm{cm}^{-3}$
ρ_5	$-5.74\cdot10^9\,\mathrm{cm}^{-3}$
ρ_6	$-5.43\cdot10^9\,\mathrm{cm}^{-3}$
ρ_7	$-2.81\cdot10^9\,\mathrm{cm}^{-3}$
ρ_8	$-0.11\cdot10^9\,\mathrm{cm}^{-3}$

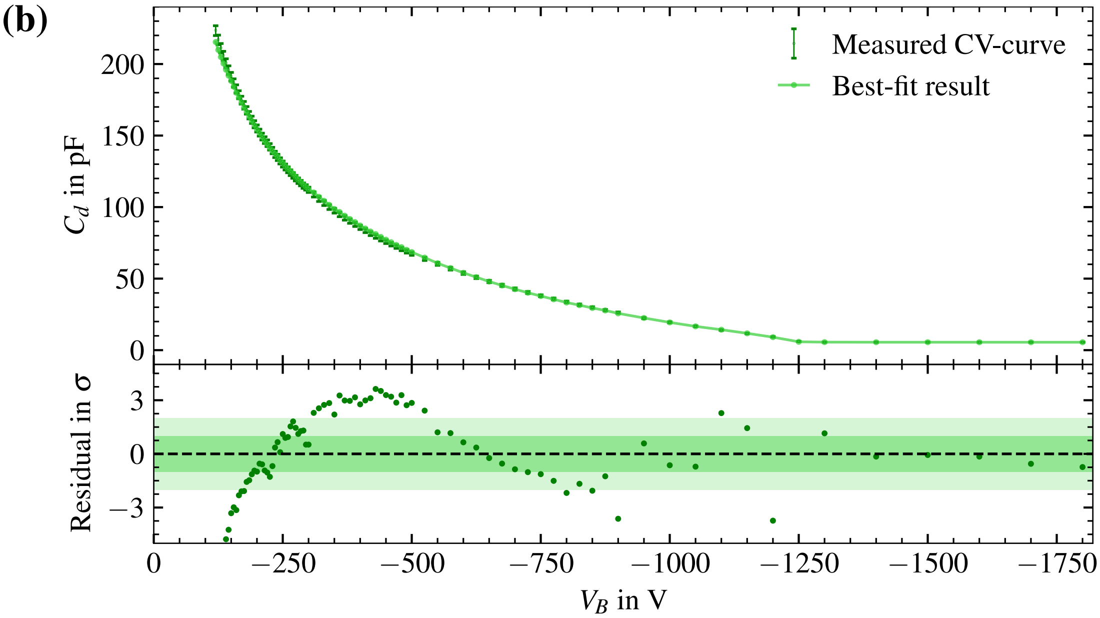

Figure 8.8: (a) Impurity density profile of the p-type segBEGe detector obtained from a maximum-likelihood fit to the measured CV-curve, see Eq. (8.5), using the parameterization in Eq. (8.6) with $\Delta r = 5\,\mathrm{mm}$. (b) Measured CV-curve for the p-type segBEGe detector with the best-fit result for the parameterization in Eq. (8.6).

8.4.2 Hyperbolic tangent parameterization

A smooth parameterization based on results in section 8.4.1 was built as

$$\rho(r,z) = \underbrace{(\rho_{\text{out}} + (\rho_{\text{in}} \cdot (1 - \alpha \cdot \frac{r}{R}) - \rho_{\text{out}})}_{\text{Linear } r\text{-dependence}} \cdot \underbrace{\frac{1}{2}(\tanh(-\frac{r - r_0}{\lambda}) + 1))}_{\text{Transition at } r = r_0} \cdot \underbrace{(1 + \beta \cdot \frac{z}{H})}_{\text{Linear } z\text{-dependence}} \ . \qquad (8.7)$$

with the fit parameters $\theta = (\rho_{\text{out}}, \rho_{\text{in}}, \alpha, r_0, \lambda)$ and fixed $\beta = 12.1\%$.

- The radial impurity density profile in the center of the detector was modeled as a linear function, where ρ_{in} is the impurity density value at $r = 0\,\text{mm}$ and α is the decrease of impurity density in % from the inside to the outside.
- A constant impurity density ρ_{out} was assumed in the very outer part of the detector to represent the unclear contact.
- The transition between $\rho_{\text{in}}(1 - \alpha \cdot \frac{r}{R})$ and ρ_{out} was modeled as a hyperbolic tangent function with fit parameters r_0 and λ, i.e. $\frac{1}{2}(\tanh(-\frac{r-r_0}{\lambda}) + 1)$, which approaches one for $r \ll r_0$ and zero for $r \gg r_0$.

The fit parameter ρ_{in} was restricted to negative values, corresponding to p-type germanium. The parameter r_0 was limited to values inside of the detector, i.e. $0 \leq r_0 \leq R$. Additional restrictions are $\alpha < 1$ and $\lambda > 0$.

The best-fit result for the parameterization in Eq. (8.7) is shown in Fig. 8.9a. The impurity density value in the center of the detector again corresponds to 97% of the values provided by the manufacturer. For the center of the detector, only a minor decrease of 0.8% from the inside to the outside is obtained. The transition between the high impurity density ρ_{in} in the inner part and the low impurity density ρ_{out} at the outer part of the detector is detected at $r_0 = 33.2\,\text{mm}$ with a width of $\lambda = 4.86\,\text{mm}$. The impurity density still decreases steeply at $r = R$ and ρ_{out} is not reached.

The best-fit result for the hyperbolic tangent parameterization in Eq. (8.7) provides a better estimate for the impurity density profile than the result for the piecewise constant parameterization in Eq. (8.6). The residuals are almost exclusively within 2σ, see Fig. 8.9b. The impurity density appears to be mildly overestimated for V_B between $-250\,\text{V}$ and $-500\,\text{V}$ and slightly underestimated for V_B below $-150\,\text{V}$.

The standard uncertainties, $\Delta\theta$, on the maximum-likelihood estimators, $\hat{\theta}$, were determined using the Hessian matrix, H, of the log-likelihood function, i.e.

$$\Delta\theta_i = \sqrt{H_{ii}^{-1}(\hat{\theta})} \quad \text{where} \quad H = -\frac{\partial^2 \ln(\mathcal{L})}{\partial\theta_i \partial\theta_j} \ . \qquad (8.8)$$

From these, the 2σ-uncertainty bands on the impurity density profile shown in Fig. 8.9a were calculated. The uncertainty on the impurity density profile for $r < 20\,\text{mm}$ is mostly defined by the uncertainty on ρ_{in} and, thus, at the permille level. For $r > 20\,\text{mm}$, where the strong radial dependence is observed, the uncertainty on the impurity density is significantly larger.

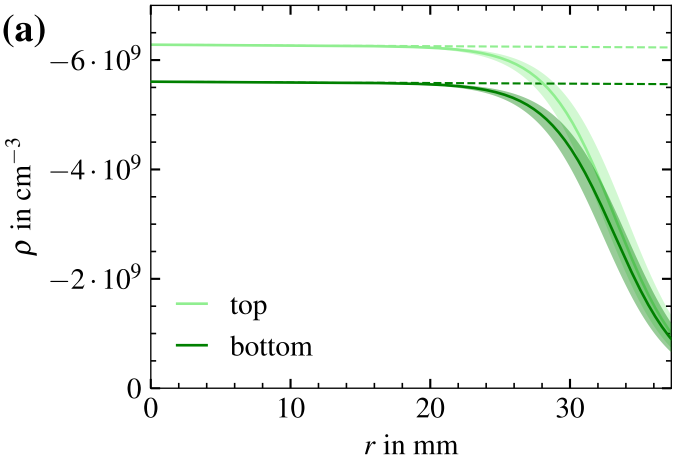

Parameter	Value
ρ_{in}	$(-5.61\pm0.01)\cdot10^9\ \text{cm}^{-3}$
ρ_{out}	$(-6.30\pm0.34)\cdot10^6\ \text{cm}^{-3}$
α	$(0.81\pm0.01)\ \%$
r_0	(33.2 ± 0.4) mm
λ	(4.86 ± 0.02) mm
β (fixed)	12.1 %

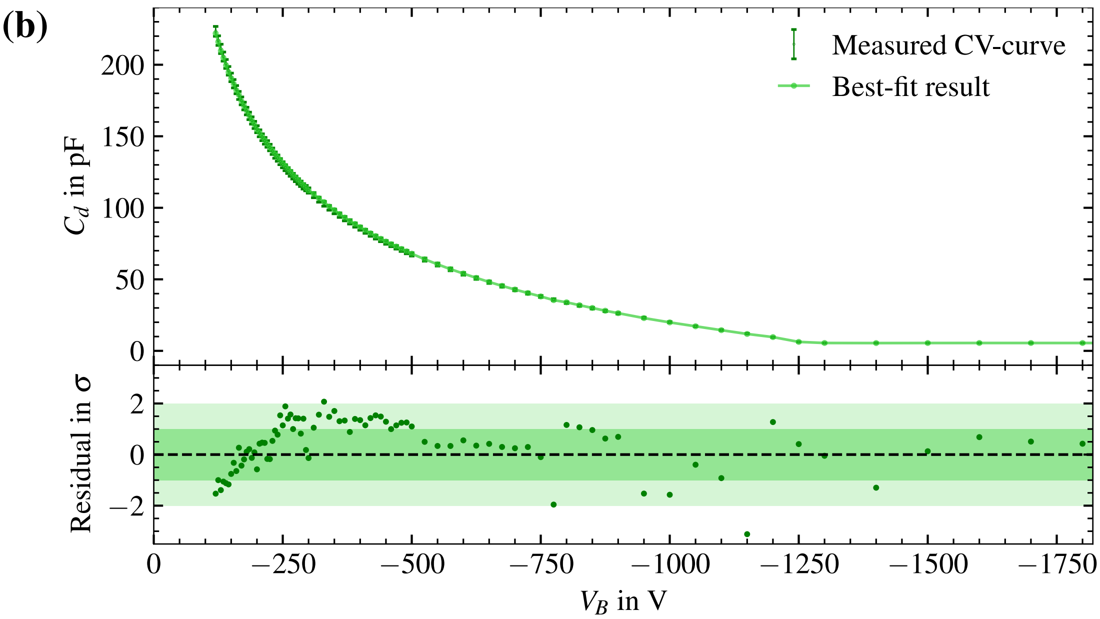

Figure 8.9: (a) Impurity density profile of the p-type segBEGe detector obtained from a maximum-likelihood fit to the measured CV-curve, see Eq. (8.5), using the parameterization in Eq. (8.7). The bands indicate 2σ-uncertainties on the best-fit result. Indicated as dashed lines are the linear functions describing the impurity density in the central part of the detector. (b) Measured CV-curve for the p-type segBEGe detector with the best-fit result for the parameterization in Eq. (8.7).

8.5 Implications for the p-type segBEGe detector

From the best-fit result for the impurity density parameterization in Eq. (8.7) shown in Fig. 8.9a, the electric field and the depletion behavior can be predicted using SSD.

8.5.1 Predicted depletion behavior

The predicted depletion volumes of the p-type segBEGe detector using the impurity density profile shown in Fig. 8.9a are shown in Fig. 8.10. Shown as reference are the boundaries obtained from the impurity density model with no r-dependence and a linear increase of 12.1% in z, scaling the manufacturer values for ρ_{top} and ρ_{bot} to 89% to match the depletion voltage.

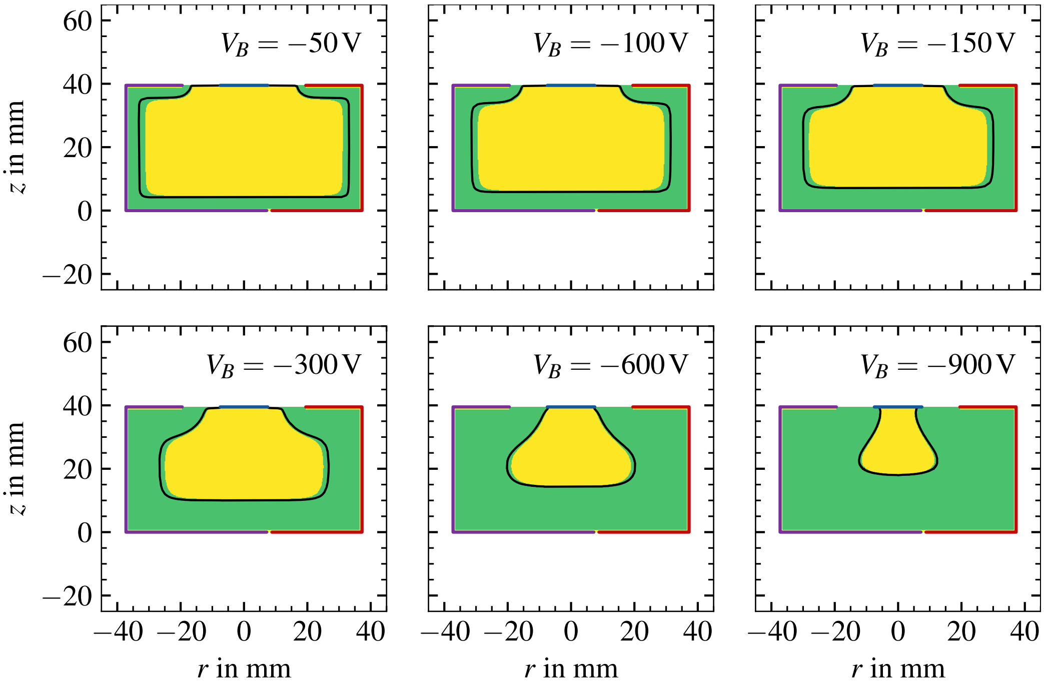

Figure 8.10: Depleted volumes of the p-type segBEGe detector as predicted by SSD using the impurity density profile shown in Fig. 8.9a for different bias voltages V_B. The depleted volumes are shown in green, the undepleted volumes are shown in yellow. The black lines depict the boundaries between depleted and undepleted volumes obtained from the values provided by the manufacturer scaled to 89%.

The z-dependence of the impurity density profile mostly influences the depletion from the bottom and from the top into the bulk. As the values for ρ_{bot} and ρ_{top} are almost identical for both impurity density models, the depletion in z is almost identical.

The r-dependence depicted in Fig. 8.9a results in faster depletion from the outside into the bulk. For V_B between $-50\,\text{V}$ and $-300\,\text{V}$, the depletion width for the best-fit increases by about 1 mm compared to the scaled manufacturer values. At $V_B = -600\,\text{V}$, this difference becomes smaller and basically disappears for $V_B = -900\,\text{V}$ and above. This agrees well with the observation that the simulated capacitances C_d^{sim} with the scaled impurity density values agree well with the measured capacitances C_d^{meas} for V_B above $-900\,\text{V}$, see Fig. 8.7.

8.5.2 Predicted electric field

The contributions of the best-fit result for the impurity density to the electric potential, $\phi_\rho(\vec{r})$, and the electric field, $\vec{\mathcal{E}}_\rho(\vec{r})$, are shown in Fig. 8.11. For $r < 15\,\mathrm{mm}$, $\phi_\rho(\vec{r})$ and $\vec{\mathcal{E}}_\rho(\vec{r})$ are almost identical to the ones shown in Figs. 6.5c and 6.5d, obtained from the scaled manufacturer values and assuming no r-dependence. However, the electric fields differ significantly in the outer part, especially for $r > 30\,\mathrm{mm}$, where the impurity density profile decreases significantly.

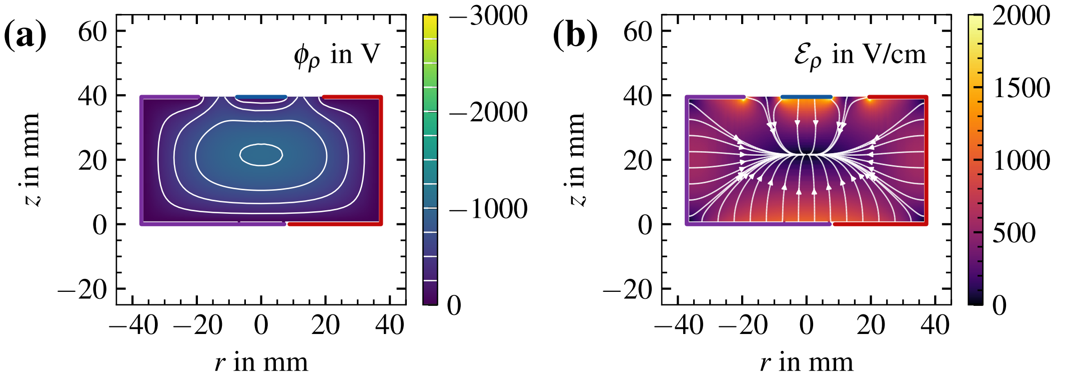

Figure 8.11: (a) Electric potential $\phi_\rho(\vec{r})$ and (b) electric field $\vec{\mathcal{E}}_\rho(\vec{r})$ resulting from the best-fit result for the impurity density profile shown in Fig. 8.9a as calculated with SSD for the r-z-plane at $\varphi = 30°$. The electric potential is shown with equipotential lines for 250 V levels. The electric field is shown with electric field lines.

The total electric field obtained from the best-fit result is shown in Fig. 8.12a. In all simulations, the measured dead-layer thickness of 0.75 mm was used. To account for the uncertainty on the impurity density profile, the electric field was calculated for multiple sets of parameters $(\rho_\mathrm{in}, \rho_\mathrm{out}, \alpha, r_0, \lambda)$ randomly drawn based on the Hessian matrix for the best-fit result. The resulting variations in the electric field are shown in Figs. 8.12b and 8.12c.

In the center of the detector at $r = 0\,\mathrm{mm}$, the electric field points upwards, i.e. $|\vec{\mathcal{E}}| = \mathcal{E}_z$, where $\mathcal{E}_z$ is the z-component of $\vec{\mathcal{E}}$. The z-dependence of $\mathcal{E}_z$ at $r = 0\,\mathrm{mm}$ is shown in Fig. 8.12b. It is basically identical to the dependence calculated from the scaled impurity density values provided by the manufacturer and assuming no r-dependence. The electric field features a minimal value of around 380 V/cm at $z = 21.5\,\mathrm{mm}$. It is strongest at the top, i.e. close to the core contact, where $\mathcal{E}_z \approx 1700\,\mathrm{V/cm}$. It also increases from the center towards the bottom, reaching a maximum value of around 1100 V/cm at the closed bottom end-plate of segment 4 at $z = 0\,\mathrm{mm}$.

At $z = 21.5\,\mathrm{mm}$ and $r > 20\,\mathrm{mm}$, $\vec{\mathcal{E}}$ points radially inwards and $\mathcal{E}_z \approx 0$, i.e. $|\vec{\mathcal{E}}| \approx \mathcal{E}_r$, where $\mathcal{E}_r$ is the r-component of $\vec{\mathcal{E}}$. The r-dependence of $\mathcal{E}_r$ and $|\vec{\mathcal{E}}|$ are shown in Fig. 8.12c. The total electric field strength at $z = 21.5\,\mathrm{mm}$ is around 400 V/cm for $r \lesssim 18\,\mathrm{mm}$ and increases slightly to 600 V/cm towards the outer surface of the detector. The electric field differs significantly from that obtained from the scaled manufacturer values, which is almost constant for $r < 20\,\mathrm{mm}$ and rises more steeply for $r > 25\,\mathrm{mm}$ to around 750 V/cm at the surface of the detector.

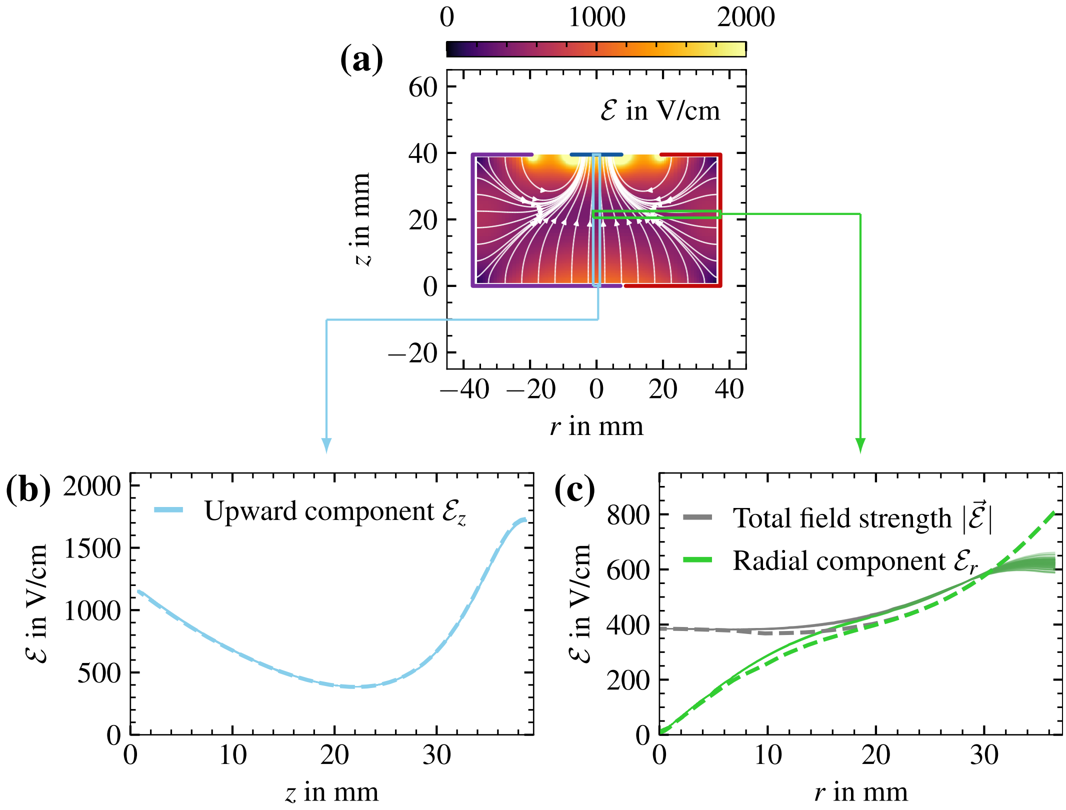

Figure 8.12: (a) Total electric field $\vec{\mathcal{E}}(\vec{r})$ resulting from the best-fit result for the impurity density profile shown in Fig. 8.9a as calculated with SSD for a bias voltage of $V_B = -3000\,\mathrm{V}$ for the r-z-plane at $\varphi = 30°$. (b) z-component of the electric field, $\mathcal{E}_z(z)$, in the center of the detector at $r = 0\,\mathrm{mm}$. (c) r-component, $\mathcal{E}_r(r)$, and total electric field strength, $|\vec{\mathcal{E}}(r)|$, at $z = 21.5\,\mathrm{mm}$. Predictions based on the best-fit result are shown as solid lines. Predictions based on the manufacturer values, scaled to 89% and assuming no r-dependence, are shown as dashed lines.

This difference in $\mathcal{E}_r(r)$ is especially important when analyzing charge-carrier drifts in the outer part of the detector. For events with energy deposits close to the outer surface of the detector, the initial inward drift of the holes is slower than what would be expected from an impurity density profile without an r-dependence. Likewise, the final part of the outward electron drift is slower in events where the electrons are collected on the segments at the outer surface.

The electric field strengths expected in the p-type segBEGe detector fall into the transition region between linear and saturated behavior of the drift velocities, see Fig. 4.1. Thus, the electron and hole drift velocities do not increase linearly with $\mathcal{E}$ but depend on both the mobility μ_0 in the linear region and the saturation drift velocity υ_{sat}.

8.6 Limitations of the result for the impurity density profile

The CV-curve was only measured down to $V_B = -120\,\text{V}$. Therefore, any maximum-likelihood fit to the measured CV-curve is not capable of testing the impurity density profile in volumes that are already depleted at $V_B = -120\,\text{V}$.

According to the SSD simulations, the detector is already depleted for $V_B = -120\,\text{V}$ at $r > 29.5\,\text{mm}$ and at $z < 6.8\,\text{mm}$, see Fig. 8.13. Therefore, multiple parameterizations for the impurity density profile can result in similar CV-curves as long as the impurity density profile is similar for $r < 29.5\,\text{mm}$ and results in a similar depleted volume for $V_B = -120\,\text{V}$ as shown in Fig. 8.13.

Another limitation is that the impurity density values are limited to negative values to model p-type germanium throughout the detector bulk. Any extension of the segment contacts into the bulk of the detector other than the measured dead-layer thickness of 0.75 mm is not modeled. Increasing the dead-layer thickness for the segment contacts in the simulation naturally shifts the p-n-junction towards the center of the detector, resulting in a higher full-depletion capacitance.

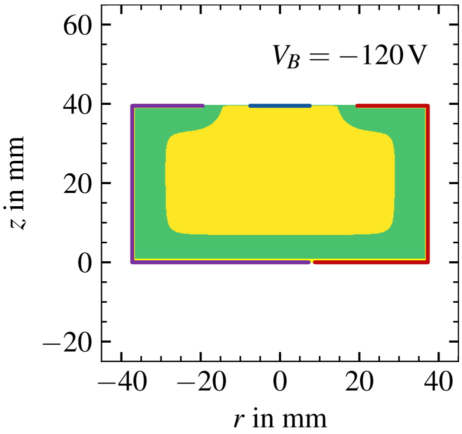

Figure 8.13: Depletion level of the p-type segBEGe detector at $V_B = -120\,\text{V}$, as calculated with SSD for the impurity density profile in Fig. 8.9a. The depleted volume is shown in green, the undepleted volume in yellow.

Maximum-likelihood fits based on the impurity density model in Eq. (8.7) were performed for different dead-layer thicknesses. Assuming that the measured capacitances are not subject to large systematic uncertainties, the dead-layer thickness would have to be 1.3 mm to match the simulated to the measured full-depletion capacitance. However, the exact choice of the dead-layer thickness does not significantly influence the results for the electric field, see Fig. 8.14.

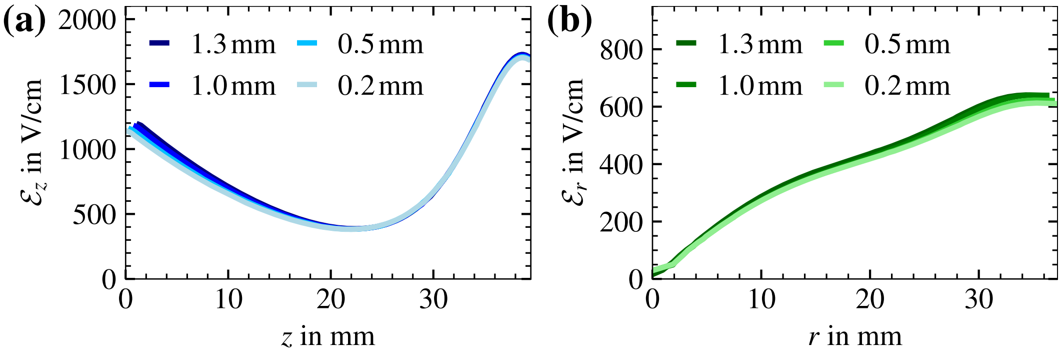

Figure 8.14: (a) $\mathcal{E}_z(z)$ at $r = 0\,\text{mm}$ and (b) $\mathcal{E}_r(r)$ at $z = 21.5\,\text{mm}$, as calculated with SSD for a bias voltage of $V_B = -3000\,\text{V}$ and different dead-layer thicknesses as listed in the legends.

9 Compton Scanner

The Compton Scanner is a novel experimental setup at the Max Planck Institute for Physics in Munich used to create pulse shape libraries for the bulk of germanium detectors. A detailed description of the Compton Scanner has already been published in 2022 [38]. At that time, it was equipped with a single pixelated camera and characterized based on measurements conducted on an n-type segBEGe detector [200]. Within the framework of this thesis, this setup was upgraded with a second camera [201] and measurements were conducted on the p-type segBEGe detector introduced in chapter 6. Most of the text in this chapter is quoted verbatim from the original publication [38] and updated to account for recent changes where necessary.

9.1 Basic working principle

In the Compton Scanner, the detector under test is irradiated vertically from the top with a collimated gamma beam. A schematic of a typical gamma trajectory is shown in Fig. 9.1. The figure also depicts the Cartesian coordinate system, x, y and z, used throughout this chapter. Gammas, which deposit part of their energy, E_{det}, through Compton scattering in the detector, are deflected by the Compton angle, θ, with

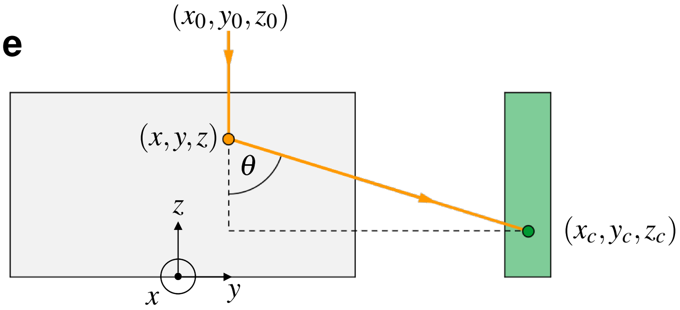

Figure 9.1: Schematic of a typical gamma trajectory in the Compton Scanner: The gamma is emitted by the source at (x_0, y_0, z_0), Compton scatters inside the detector at (x, y, z) and is fully absorbed in the camera at (x_c, y_c, z_c). The origin of the Cartesian coordinate system is located at the center of the bottom surface of the detector.

$$\cos(\theta) = 1 - \frac{m_e c^2 E_{\text{det}}}{E_{\text{in}} \left(E_{\text{in}} - E_{\text{det}}\right)} , \tag{9.1}$$

where E_{in} is the energy of the incoming gammas.

If a scattered gamma is fully absorbed in one of the cameras placed nearby, which measures both energy and position, the location of the scattering point in the detector under test, (x, y, z), can be reconstructed. Assuming there is exactly one scattering point on axis, i.e. $x = x_0$ and $y = y_0$, where (x_0, y_0, z_0) is the position of the center of source, the unknown z coordinate can be calculated as

$$z = z_\theta := z_c + \sqrt{(x_c - x_0)^2 + (y_c - y_0)^2} \cot(\theta) , \tag{9.2}$$

where z_θ is the z coordinate of the scattering point as reconstructed from the Compton angle θ and from the position of the hit in the camera, (x_c, y_c, z_c). The relation $z = z_\theta$ in Eq. (9.2) is true as long as the beam is parallel to the z axis.

Pulse shape libraries are created by moving the source to different positions x_0 and y_0. Note that with this setup, for any position of the source, data are collected for the whole range in z at the same time.

9.2 Requirements

The purpose of this Compton Scanner setup is to create pulse shape libraries from bulk events with an intrinsic spatial resolution of less than ± 1 mm in all dimensions. This volume is compatible with the volume of the charge clouds at energies around 2 MeV as expected in events from neutrinoless double-beta decay [110]. This results in a set of physical requirements on the components of the Compton Scanner:

- The gamma source should be monoenergetic, with a single gamma line at an energy that has a high penetration power into germanium and a high probability for Compton scattering. The gammas should predominantly scatter into an interval around 90°.
- The diameter of the collimated beam needs to be less than 2 mm throughout the detector volume to reach the target resolution in the x and y directions. The collimation of gammas with energies suitable for Compton scattering requires several centimeters of high-density material [202], e.g. lead or tungsten.
- For each position of the source, the data taking should only take up to a few hours, such that multiple detectors per year can be scanned at multiple temperatures. For this, a highly active source with an activity of several hundred MBq is required.
- The cameras need to have a spatial and energy resolution good enough to reconstruct z using Eq. (9.2) with an uncertainty of less than ± 1 mm.
- The Compton Scanner setup is to accommodate arbitrary detector cryostats, demanding it to be modular and to have a framework to mount and move the components. Enough space in the center of the setup is required where the detector cryostat can be installed.

In addition, the reconstruction based on Eq. (9.2) requires that the positions of the main components of the Compton Scanner, i.e. source, detector and cameras, are all known and aligned within a common coordinate system to much better than 1 mm.

9.3 Components

The individual components are mounted on a common frame as shown in Fig. 9.2. The frame consists of a circular base plate with four vertical MayTec aluminum profiles, two of which are connected via a fifth horizontal profile. The source and the camera are attached to a horizontal and a vertical translation motor stage (STANDA® 8MT50-200BS1-MEn1), respectively, which allow to move them with a precision of 5 µm. The base plate is fixed onto a rotational motor stage (STANDA® 8MRB450-360-60-MEn2), which allows to rotate it with a precision of 0.15°. The rotational motor stage is mounted on a 600 mm × 600 mm aluminum breadboard, with a 300 mm × 300 mm cutout in the center, which is located on a table with a circular hole. The detector in its cryostat is inserted through this hole. The Compton Scanner can accommodate cryostats with diameters of up to 130 mm. Two line lasers, attached to two adjacent vertical MayTec profiles, are used to roughly align the center of the Compton Scanner frame with respect to the center of the detector cryostat.

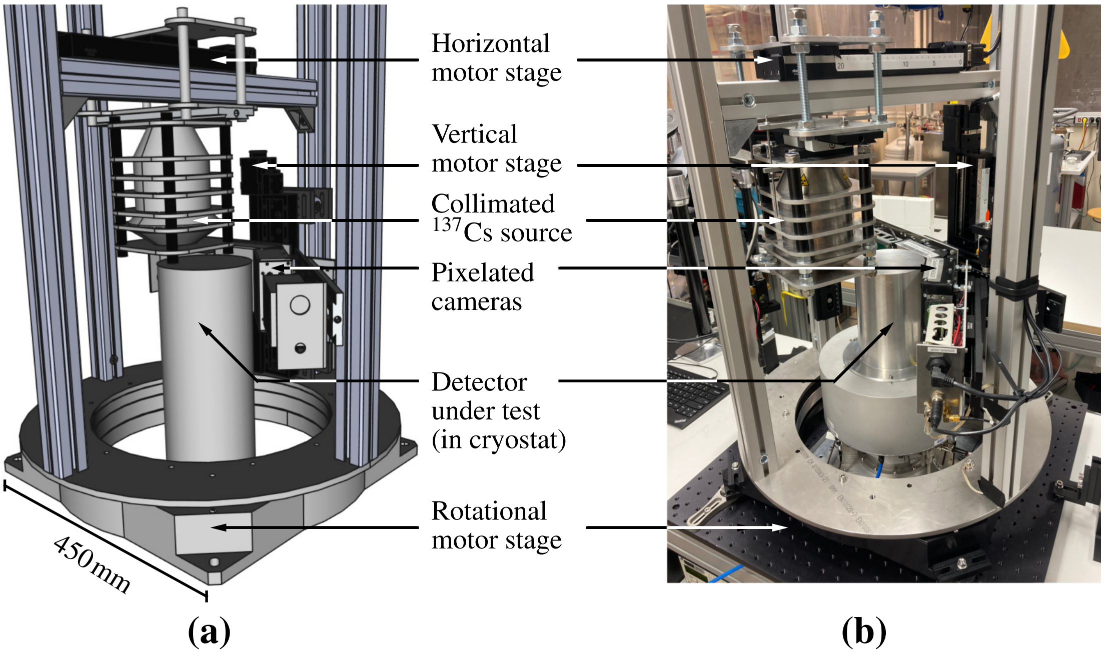

Figure 9.2: (a) 3D model and (b) photo of the Compton Scanner setup. The vertical motor is used to place the pixelated cameras at an optimal height with respect to the detector under test. The horizontal motor allows to move the ^{137}Cs source along the line which connects the centers of the detector cryostat and the reference point of the camera assembly. The rotational motor is used to rotate the whole frame, along with the pixelated cameras and the source, around the cryostat.

The source used in the Compton Scanner is a cylindrical 740 MBq ^{137}Cs source with an active diameter of 0.9 mm. It emits gammas with a characteristic energy of 661.660 keV [119] and fulfills the requirements listed in section 9.2. The emission of the gammas is isotropic. To create a narrow vertical beam, the source is embedded in a collimator.

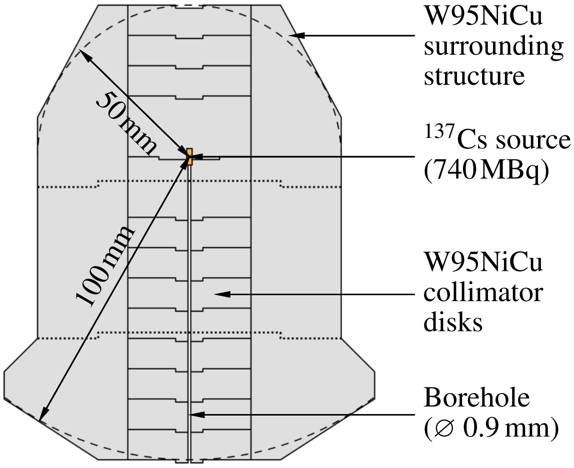

Figure 9.3: Schematic cross-section of the rotationally symmetric ^{137}Cs source collimator.

The collimator used in the Compton Scanner is shown in Fig. 9.3. It consists of 13 disks and a three-piece surrounding structure made out of W95NiCu tungsten alloy. Nine of the disks form a 100 mm long, massive collimator with a borehole of 0.9 mm in diameter. At the top, the collimator assembly provides a shielding of at least 50 mm of tungsten for radiation safety. The geometry of the collimator ensures that downwards but not vertically emitted 661.660 keV gammas have to pass through at least 100 mm of tungsten. This reduces the fraction of downward gammas that do not pass through the borehole to less than 10^{-7}.

The diameter of the borehole leads to an aperture angle of the collimated beam of 0.26°. The collimated source is mounted as close to the detector cryostat as possible in order to minimize the width of the beam reaching the detector. If the detector inside the cryostat is placed within 100 mm underneath the bottom of the collimator, the beam spot diameter is less than 1.8 mm.

The cameras used to detect the Compton scattered gammas are customized OEM modules produced by H3D, Inc. [203]. The cameras each consist of four pixelated cadmium-zinc-telluride (CdZnTe) detectors. The mean free path of 289 keV gammas in CdZnTe is around 11.2 mm [112]. Each detector is based on a $22 \times 22 \times 10\,\mathrm{mm}^3$ CdZnTe crystal. The four detectors are mounted inside an aluminum box in a 2×2 configuration with 2 mm gaps between them. For each CdZnTe detector, the $22 \times 22\,\mathrm{mm}^2$ surface facing the germanium detector is fully covered by the cathode. The back $22 \times 22\,\mathrm{mm}^2$ surface is covered by the anode which consists of 11×11 pixels with a center-to-center distance of 1.9 mm. This contact geometry allows for a three-dimensional reconstruction of the positions of the energy depositions (hits) in each camera. The lateral and depth position resolution of the cameras are both less than 0.5 mm full width at half maximum, FWHM. The sub-pixel lateral resolution is reached by considering the effect of charge sharing between neighboring pixels [204]. The depth resolution is achieved by comparing the anode and cathode pulse amplitudes [205].

The camera readout system, trigger and reconstruction algorithms are proprietary technology of H3D, Inc. [203]. The cameras were bought together with software providing a data stream consisting of deposited energy, time and position values for each event. The energy resolution of the pixelated cameras at energies relevant for Compton Scanner measurements were determined by irradiating the cameras directly with gammas emitted from a ^{133}Ba source, selecting only events with a single energy deposition. The resolution was observed to be homogeneous across the pixels, varying by less than 10%. The average values for the measured FWHM of the characteristic gamma peaks of ^{133}Ba are listed in Tab. 9.1.

Table 9.1: Absolute and relative energy resolution of the pixelated cameras used in the Compton Scanner, determined from events with the characteristic ^{133}Ba gamma energies [119] and only one energy deposition in the respective camera. The width of the peak, ΔE, corresponds to the FWHM.

E in keV	ΔE in keV	$\Delta E/E$
276.398	2.91	1.05%
302.853	2.83	0.93%
356.017	3.04	0.85%
383.851	3.11	0.81%

E in keV	ΔE in keV	$\Delta E/E$
276.398	2.74	0.99%
302.853	2.68	0.89%
356.017	2.89	0.81%
383.851	2.89	0.75%

9.4 Upgrade of the Compton Scanner with a second camera

At the time of the original publication [38], the Compton Scanner was equipped with a single pixelated camera, see Fig. 9.4. The vertical centers of the p-type segBEGe detector and the camera were aligned. Within the framework of this thesis, the Compton Scanner was upgraded with a second pixelated camera [201] to further increase the acceptance of Compton Scanner measurements.

The second camera was placed at the same height as the first one to maximize the number of detectable perpendicularly scattered gammas. Due to mechanical limitations, placing the second camera directly behind the first one was not possible. In total, four configurations to incorporate the second camera into the existing Compton Scanner setup were simulated using GEANT4 [177], see Fig. 9.5. The aim of this study was to find the optimal configuration to maximize the number of perpendicularly scattered gammas with a focus on increasing acceptance in the center of the bulk, where the acceptance is the lowest due to absorption of the scattered gammas.

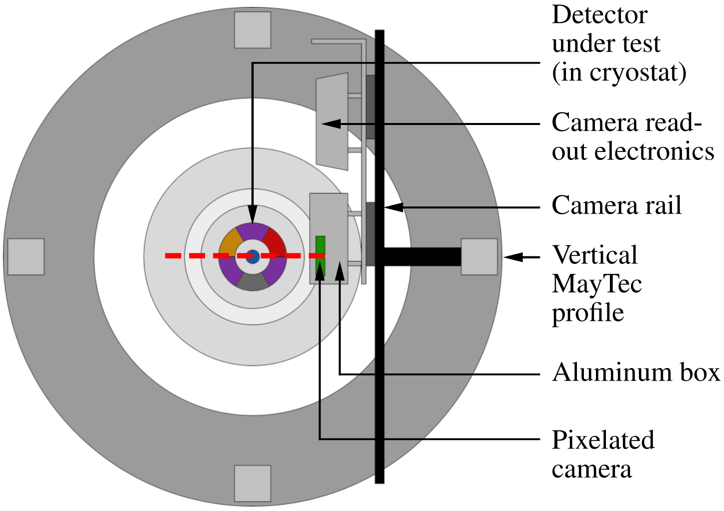

Figure 9.4: Top view of the geometry of the Compton Scanner setup with a single pixelated camera as presented in [38]. The axis of movement of the ^{137}Cs source is shown as a red dashed line.

The first two configurations are symmetric with respect to the axis of movement of the ^{137}Cs source. The vertical MayTec profiles restricted the choice of the angle between the cameras. For the upgrade, symmetric configurations with an angle between the cameras of 0° and 90° were considered, see Figs. 9.5a and 9.5b, respectively. In the other two configurations, the first camera was kept at its original position. The second camera was placed facing the center of the detector. Two such asymmetric configurations, with an angle between the cameras of 45° and 90°, were selected as upgrade candidates, see Figs. 9.5c and 9.5d.

For the initial camera configuration depicted in Fig. 9.4 and for the four upgrade candidates depicted in Fig. 9.5, 1 million ^{137}Cs decays were simulated for r between 0 mm and 36 mm in steps of 2 mm along the path of movement of the source. For each r, the number of events with exactly one Compton scatter in the germanium detector and fully-contained energy within the setup, i.e. with the scattered gamma being fully absorbed in either one of the cameras, were counted. For each two-camera configuration and each r, the increase in acceptance compared to the configuration with a single camera was determined. The results are shown in Fig. 9.6.

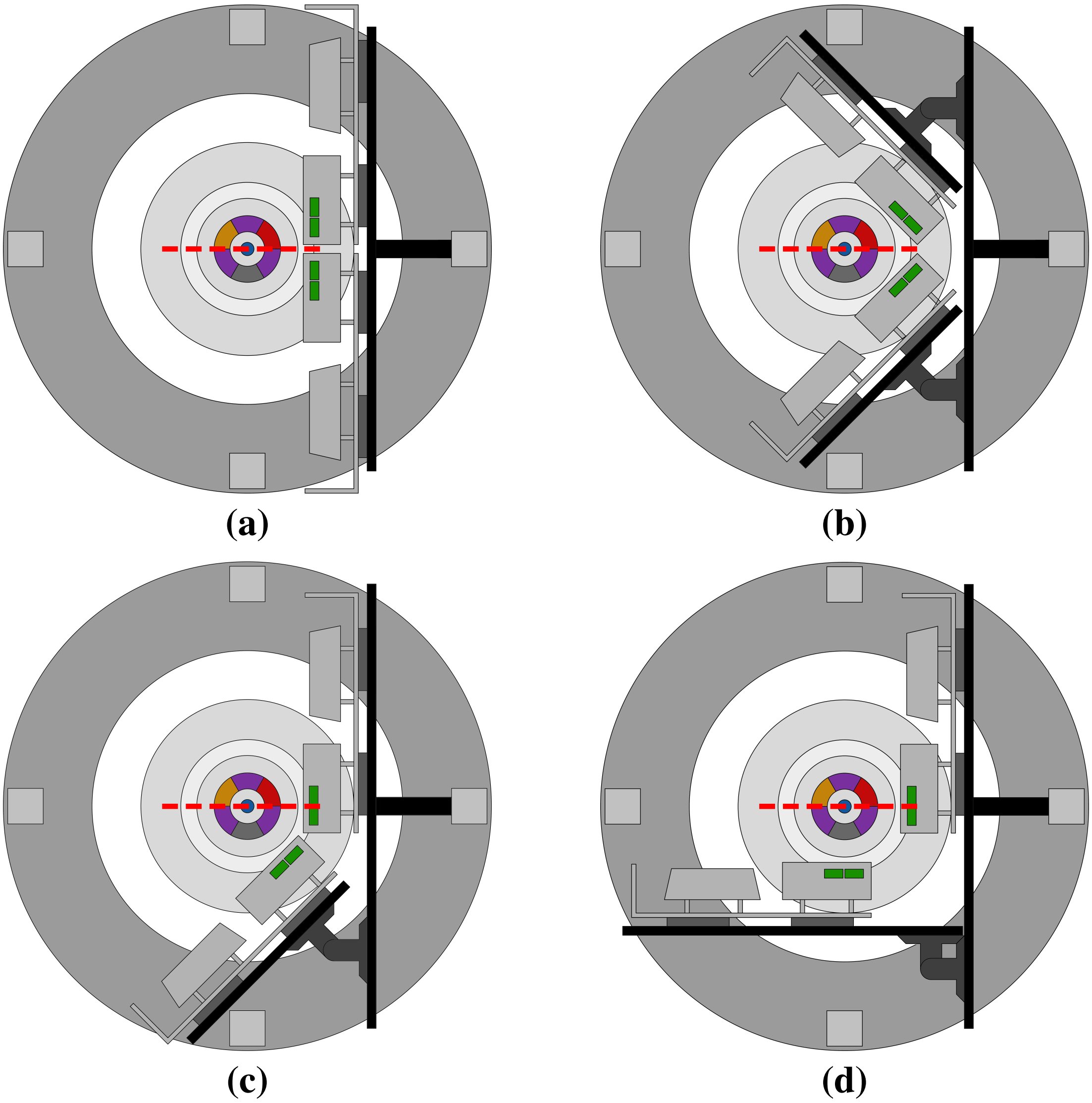

Figure 9.5: Top view of four possible geometries for placing the second pixelated camera to upgrade the Compton Scanner. The top row depicts symmetric, the bottom row asymmetric configurations with respect to the axis of movement of the source shown as a red dashed line. In the bottom row, one of the cameras is placed at its original position shown in Fig. 9.4.

The maximum increase in acceptance is achieved when the solid angle of acceptance is maximal and the scattered gammas have to pass through as little material as possible on their way to the cameras. For measurements at $r = 0\,\mathrm{mm}$, the camera in the original configuration and both cameras in the asymmetric configurations have a maximal solid angle of acceptance. Therefore, the acceptance in the asymmetric configurations is doubled compared to the single-camera configuration[*], see Fig. 9.6. For the symmetric configurations, the solid angle of acceptance for measurements at $r = 0\,\mathrm{mm}$ is not maximal and the increase in acceptance is only around 65%.

---

[*] In fact, the acceptance increase by slightly more than a factor of two. In addition to the doubled acceptance resulting from having two cameras with maximum acceptance, fully-contained events where the gamma Compton scatters in one camera and is fully absorbed in the other are counted as well.

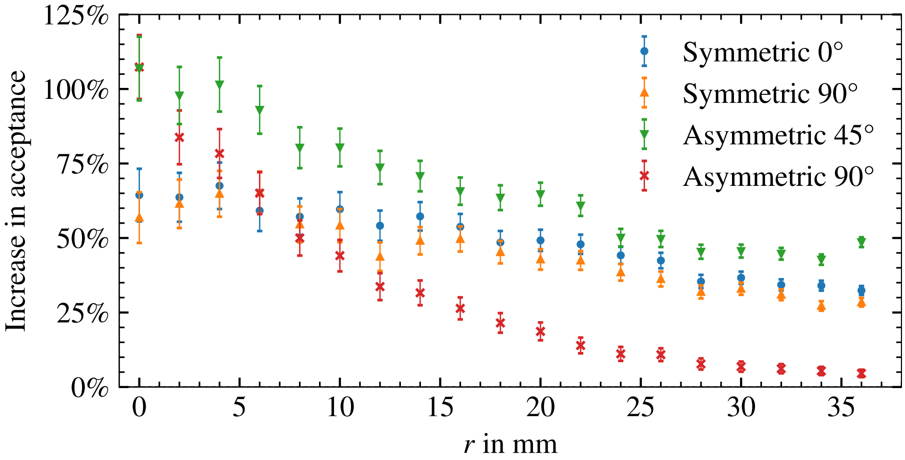

Figure 9.6: Increase in acceptance of the two-camera configurations shown in Fig. 9.5 compared to the single-camera setup shown in Fig. 9.4 as a function of the radius, r, at which the detector was irradiated.

During radial scans, the vertical beam moves from the center of the detector towards the rail on which the cameras are mounted. Therefore, the second camera should be placed as close to the rail as possible to also significantly increase the acceptance for measurements close to the surface of the detector. For the asymmetric configuration at an angle of 90°, the vertical beam moves away from the second camera when approaching the first one. The decrease in acceptance and the increased probability of additional interactions of the scattered gammas in the detector on their way to the camera significantly reduces the increase of acceptance with r to only 5% at $r = 36\,\text{mm}$. For the other camera configurations in Fig. 9.5, the collimated beam moves towards both cameras with r, increasing the solid angle of acceptance and decreasing the probability of additional interactions after the first Compton scatter in the detector. The increase in acceptance for measurements at $r = 36\,\text{mm}$ is significant, i.e. around 30% for the symmetric configurations and around 50% for the asymmetric configuration at an angle of 45°, see Fig. 9.6.

The asymmetric configuration with an angle between the cameras of 45° was found to have the highest increase of acceptance for all r. It was, thus, chosen as the optimal camera configuration for the Compton Scanner upgrade.

9.5 Data acquisition

The reconstruction of the scattering point for charge pulses measured in the Compton Scanner is only valid for events in which gammas emitted by the ^{137}Cs source Compton scatter in the detector and are absorbed in one of the cameras. These events have to be selected from all events recorded independently in the detector and the cameras.

A flowchart depicting the event selection and the z-reconstruction is shown in Fig. 9.7. The data streams from the detector under test and from the pixelated cameras were recorded independently and stored separately. There was no online event building. The p-type segBEGe detector recorded events with a rate of around 3.3 kHz. The rate of recorded events in the cameras varied between 100 Hz and 150 Hz, depending on the position of the source. After offline synchronization of the camera and detector data streams, events with coincident energy deposits in the detector and the cameras with a total recorded energy compatible with 661.660 keV were selected. For these events, the z coordinate of the scattering point was reconstructed from the position of the source, the hits in the cameras and the Compton angle θ.

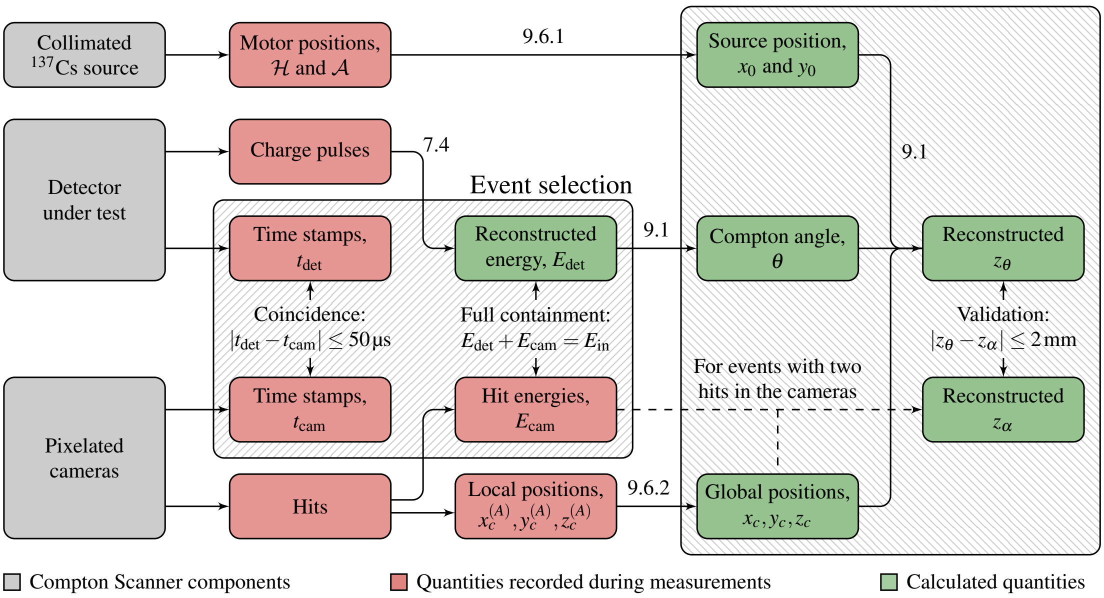

Figure 9.7: Flowchart of the Compton Scanner data processing, consisting of event selection and z-reconstruction. Arrows pointing to calculated quantities are labeled with the number of the section in which the respective calculation is explained in detail.

9.5.1 Synchronization of data streams

The camera and detector data streams were recorded with independent time stamps and had to be synchronized. For this, 50 ns long rectangular voltage pulses generated by each camera in time intervals of 2 ns were sent to the ADC also used in the detector read-out. From these pulses, the offset between time stamps of the detector ADC, t_{det}, and of the camera DAQ system, t_{cam}, was determined and corrected for. Detector and camera events with no respective counterpart within 50 µs in the cameras or detector were discarded. This resulted in a rate of coincident events of around 60 Hz when the detector was irradiated in the center, and of around 200 Hz when it was irradiated close to the edge of the detector.

9.6 Spatial alignment

The z-reconstruction requires the positions of the source and the cameras to be expressed in a common coordinate system. For this, all components were aligned with respect to the center of the Compton Scanner frame. In this section, the alignment of the components of the Compton Scanner is presented.

9.6.1 Spatial alignment of the detector

After inserting the K2 cryostat through the hole in the table, the center alignment was of the order of a few millimeters. Line lasers, which produced a laser cross at the center of the Compton Scanner frame, were used to further align the centers. Moving the rotational motor stage on the aluminum breadboard until the laser cross matched the center of the cryostat allowed for a center alignment to several hundreds of micrometers.

The position of the source was set by the horizontal stage position, $\mathcal{H}$, and the rotational stage angle, $\mathcal{A}$, in the local motor coordinate system shown in Fig. 9.8. The origin of this cylindrical coordinate system was located at the center of the Compton Scanner frame. The position of the source had to be expressed in the polar coordinates, r and φ, of the segBEGe detector coordinate system introduced in Fig. 6.1a. If the centers were perfectly aligned, the source position, $\mathcal{H}$, in the local motor coordinate system and r in the detector coordinate system would only differ by an offset, i.e. $r = \mathcal{H} - \mathcal{H}_0$. The same would apply to the rotational stage angle, $\mathcal{A}$, and the polar angle φ, i.e. $\varphi = \mathcal{A} - \mathcal{A}_0$. However, the unavoidable mismatch of the centers made the conversion from local motor coordinates to detector coordinates non-trivial and required further alignment measurements.

Figure 9.8 introduces the quantities that define a possible misalignment of the center of the Compton Scanner frame with respect to the center of the segBEGe detector. For a non-zero mismatch, $\Delta\mathcal{H}$, the detector edge is reached at different horizontal stage positions, $\mathcal{H}_e$, for different $\mathcal{A}$. There exists a rotational stage angle, $\Delta\mathcal{A}$, at which $\mathcal{H}_e$ reaches its maximum value, $\mathcal{H}_{e,1}$. Accordingly, the minimum, $\mathcal{H}_{e,2}$, is reached after a rotation of 180°. The misalignment quantities, $\Delta\mathcal{H} = \frac{1}{2}(\mathcal{H}_{e,1} - \mathcal{H}_{e,2})$ and $\Delta\mathcal{A}$, as well as the offset, $\mathcal{H}_0 = \frac{1}{2}(\mathcal{H}_{e,1} + \mathcal{H}_{e,2}) + R$, where R is the radius of the segBEGe detector, were determined from data.

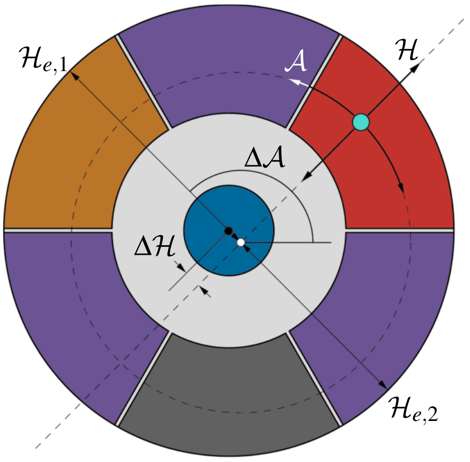

Figure 9.8: Schematic of the movement of the source in the local motor coordinate system of the Compton Scanner, $\mathcal{H}$ and $\mathcal{A}$. Also shown are the misalignment quantities, $\Delta\mathcal{H}$ and $\Delta\mathcal{A}$, that define the misalignment between the center of the Compton Scanner frame (white point) and the center of the segBEGe detector (black point).

An alignment scan was performed to determine $\Delta\mathcal{H}$ and $\Delta\mathcal{A}$. In this scan, $\mathcal{A}$ was increased from 0° to 360° in steps of 5°. For every $\mathcal{A}$, the horizontal motor stage was moved over a range of 11 mm in steps of 1 mm across the edge of the detector. At each point, a 1 min measurement was taken.

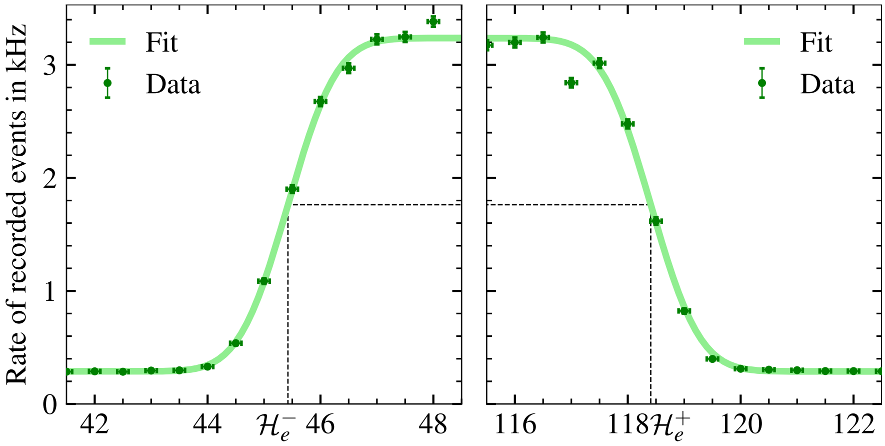

Figure 9.9: Rate of events in the p-type segBEGe detector as determined from 1 min measurements as a function of the horizontal motor position, $\mathcal{H}$, at $\mathcal{A} = 0°$, together with a fit of the data to the function in Eq. (9.3).

Figure 9.9 shows the rate of events, N, recorded in the p-type segBEGe detector as a function of $\mathcal{H}$ for $\mathcal{A} = 0°$. At low $\mathcal{H}$, the vertical beam does not intersect with the detector and only background events are observed. At higher $\mathcal{H}$, the beam is fully contained within the detector volume, resulting in a higher count rate. Once the detector edge on the other side is passed, the count rate drops again. The two detector edges, $\mathcal{H}_e^{\mp}$, can be determined by fitting the data to a Gauss error function, i.e.

$$N(\mathcal{H}) = \frac{N_0}{2} + \frac{N_0}{2}\mathrm{erf}\left(\pm\frac{\sqrt{2}(\mathcal{H}-\mathcal{H}_e^{\mp}(\mathcal{A}))}{R_b}\right) + B, \tag{9.3}$$

where R_b is the average 2σ-radius of the beam spot, N_0 is the event rate expected when the beam spot is fully contained throughout the detector and B is the rate of background events. The rate of events from the ^{137}Cs source was measured to be around 3 kHz, while the rate of background events was around 300 Hz. The average beam-spot radius was measured to be $R_b = (1.33 \pm 0.04)$ mm.

For cylindrical detectors, the relation between $\mathcal{H}_e^{\mp}$ and $\mathcal{A}$ as derived from the geometry depicted in Fig. 9.8 is [38]

$$\mathcal{H}_e^{\mp}(\mathcal{A}) = \mathcal{H}_0 - \Delta\mathcal{H}\cos(\mathcal{A}-\Delta\mathcal{A}) \mp \sqrt{\tilde{R}^2 - (\Delta\mathcal{H})^2\sin^2(\mathcal{A}-\Delta\mathcal{A})}\,. \tag{9.4}$$

with "$-$" for the edge around $\mathcal{H}_e^- \approx 45$ mm closer to the cameras and "$+$" for the edge around $\mathcal{H}_e^+ \approx 118$ mm further away from the cameras. The quantity $\tilde{R}$ describes the active radius of the detector, which is smaller than the crystal radius of $R = 37.25$ mm because of the thickness of the dead layer at the outer surface of the detector.

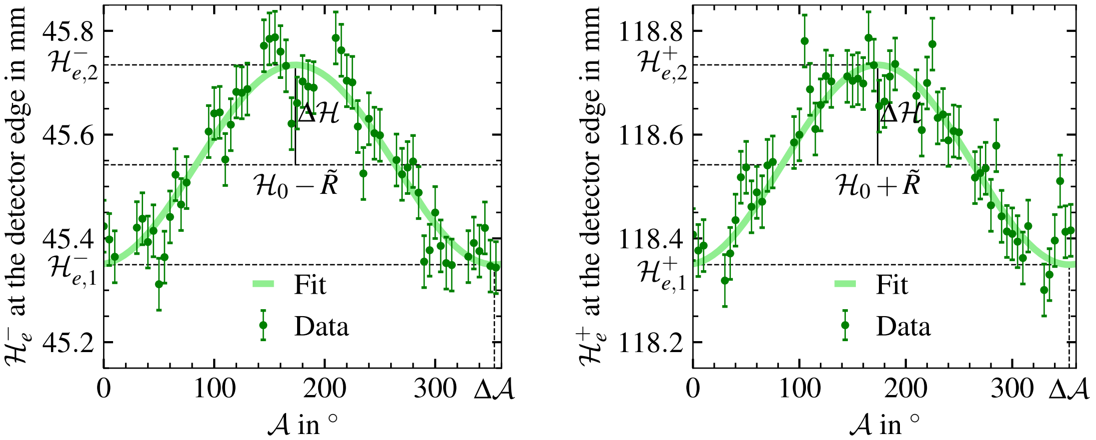

Figure 9.10: Horizontal stage position determined as the locations of the detector edges $\mathcal{H}_e^{\mp}$ depending on the rotational stage angle $\mathcal{A}$. The misalignment quantities $\Delta\mathcal{H}$ and $\Delta\mathcal{A}$ are indicated. The error bars correspond to the uncertainties obtained from the fits to determine $\mathcal{H}_e^{\mp}$.

The misalignment quantities were obtained from fitting the function in Eq. (9.4) to the measured $\mathcal{H}_e^{\mp}$, see Fig. 9.10. The center of the Compton Scanner frame was reached at $\mathcal{H}_0 = (82.0 \pm 0.6)$ mm. The mismatch of the centers was $\Delta\mathcal{H} = (0.19 \pm 0.06)$ mm at $\Delta\mathcal{A} = (353.5 \pm 3.9)^\circ$. The active radius of the detector was $\tilde{R} = (36.50 \pm 0.06)$ mm, implying a dead-layer thickness at the outer surface of (0.75 ± 0.06) mm. This supports the assumed thickness of the segment contacts of 0.75 mm in the simulation performed for the p-type segBEGe detector, see section 6.3.

For measurements with the Compton Scanner, the collimated source is moved only between the center of the detector and the detector edge closest to the cameras, i.e. in the range $\mathcal{H}_e^- \leq \mathcal{H} \leq \mathcal{H}_0$. The conversion of local motor coordinates with $\mathcal{H} \leq \mathcal{H}_0$ to r and φ becomes

$$r = \sqrt{|\mathcal{H} - \mathcal{H}_0|^2 + (\Delta\mathcal{H})^2 - 2\Delta\mathcal{H}|\mathcal{H} - \mathcal{H}_0|\cos(\mathcal{A} - \Delta\mathcal{A})}, \tag{9.5}$$

$$\varphi = \operatorname{asin}\left(\frac{|\mathcal{H} - \mathcal{H}_0|\sin(\mathcal{A} - \Delta\mathcal{A})}{r}\right) + \Delta\mathcal{A} - \mathcal{A}_0\,, \tag{9.6}$$

where $\mathcal{A}_0 = (173.0 \pm 1.5)^\circ$ is the offset between $\varphi = 0^\circ$ and the zero of the rotational motor stage. The value of $\mathcal{A}_0$ was previously determined by measuring the position of the segment boundaries in rotational motor coordinates [128]. In the following, for all Compton Scanner measurements on the p-type segBEGe detector, all motor stage positions were converted to detector coordinates using Eqs. (9.5) and (9.6).

9.6.2 Spatial alignment of the cameras

Based on the simulation studies presented in section 9.4, the second pixelated camera was installed on the rail next to the first one at an angle of approximately 45°, see Fig. 9.11. The first camera will be referred to as camera (A), the second one as camera (B). After the installation of camera (B), both cameras were kept at their fixed position on the camera rail. Thus, the relative alignment between the two cameras, i.e. the transformation between the coordinate systems of camera (A) and (B), remained unchanged for all measurements on the p-type segBEGe detector.

The cameras recorded hits in the local camera coordinates depicted in Fig. 9.11, i.e. $x^{(A)}$, $y^{(A)}$ and $z^{(A)}$ for camera (A) and $x^{(B)}$, $y^{(B)}$ and $z^{(B)}$ for camera (B). The origins of the coordinate systems are placed at the centers of the gaps between the camera crystals, aligned with the surfaces that face the camera rail. The $x^{(A)}$-axis points along the camera rail towards camera (B). The $z^{(A)}$-axis points perpendicular to the camera rail.

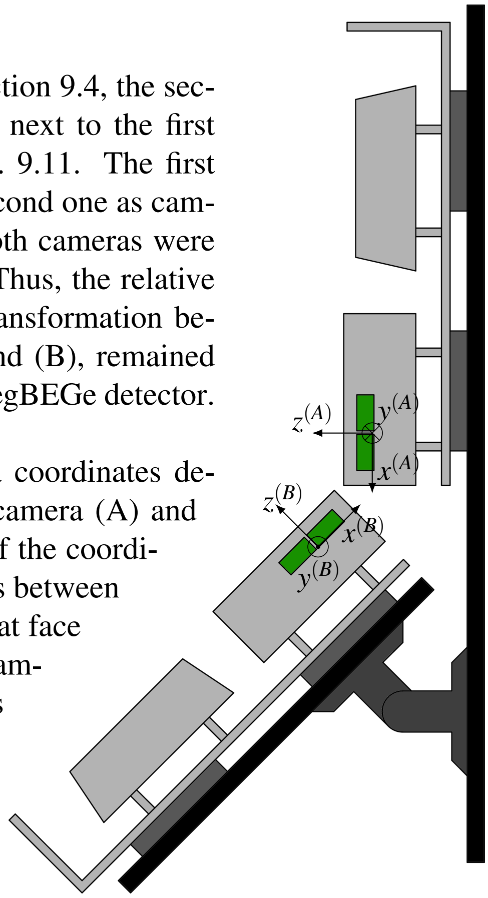

Figure 9.11: Schematic top view of the camera rail with the positions of the camera crystals depicted in green. The local coordinate systems of the two cameras are also shown.

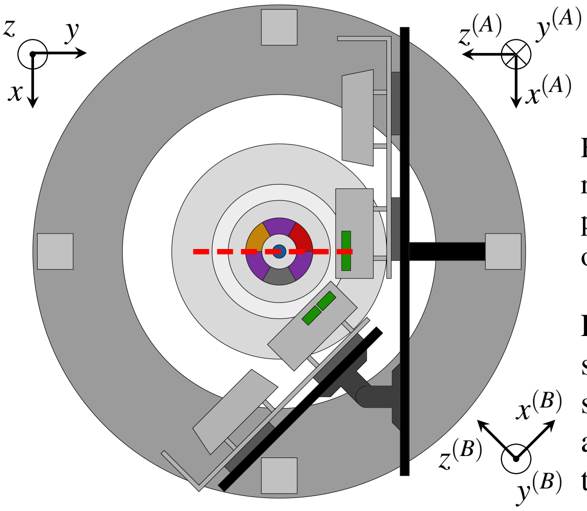

Figure 9.12: Top view of the Compton Scanner setup with the p-type segBEGe detector in the K2 cryostat and with two cameras installed. The axis of movement of the ^{137}Cs source is shown as a red dashed line. The global coordinate systems and local coordinate systems of the cameras are also shown.

For the measurements on the p-type segBEGe detector, the camera rail was installed with the surface of camera (A) at a shortest possible distance of 70.5 mm to the center of the Compton Scanner frame, see Fig. 9.12. The vertical motor stage was used to align the centers of the segBEGe detector and camera (A). The distance between the top of the detector and the bottom of the source collimator was 31 mm. The horizontal motor stage was installed such that the ^{137}Cs source could irradiate not only the detector but also camera (A) vertically from the top.

9.6.2.1 Spatial alignment of camera (A)

The orientation of the global coordinate system, x, y and z, is based on the orientation of the coordinate system of camera (A). The global x-axis is parallel to the $x^{(A)}$-axis, the global y-axis is antiparallel to the $z^{(A)}$-axis and the global z-axis is antiparallel to the $y^{(A)}$-axis, see Fig. 9.12.

Local coordinates of camera (A) are transformed to global coordinates as

$$\begin{bmatrix} x \\ y \\ z \end{bmatrix} = \begin{bmatrix} x^{(A)} \\ -z^{(A)} \\ -y^{(A)} \end{bmatrix} + \begin{bmatrix} \Delta x \\ \Delta y \\ \Delta z \end{bmatrix}, \tag{9.7}$$

where Δx, Δy and Δz are the components of the translation vector between the center of the camera and the center of the Compton Scanner frame.

The components Δx and Δy were determined experimentally by irradiating camera (A) directly. Figure 9.13 depicts measured beam spot positions in the local coordinates of camera (A) for a set of horizontal stage positions $\mathcal{H}$. From these beam spot positions, the axis of movement of the ^{137}Cs source was reconstructed. It was seen to be parallel to the $z^{(A)}$-axis with $\mathcal{H} = 0\,\mathrm{mm}$ being reached at $z^{(A)} = -1.46\,\mathrm{mm}$.

The center of the Compton Scanner frame is located at $\mathcal{H}_0 = 82.0\,\mathrm{mm}$, see section 9.6.1. In the local coordinate system of camera (A), this corresponds to $\Delta x = x^{(A)} = -4.50\,\mathrm{mm}$ and $\Delta y = z^{(A)} = 80.54\,\mathrm{mm}$.

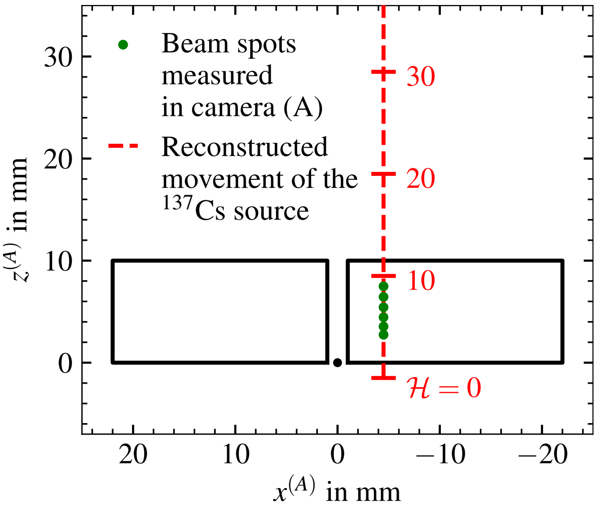

Figure 9.13: Measured beam spot positions in the local coordinate system of camera (A). Values for $\mathcal{H}$ are given on the red dashed line depicting the reconstructed axis of movement of the ^{137}Cs source.

The vertical motor stage was used to place the origin of camera (A) at the z of the center of the detector, i.e. $\Delta z = H/2 = 19.75\,\mathrm{mm}$. Thus, the translation vector in Eq. (9.7) for measurements on the p-type segBEGe detector is

$$\begin{bmatrix} \Delta x \\ \Delta y \\ \Delta z \end{bmatrix} = \begin{bmatrix} -4.50\,\mathrm{mm} \\ 80.54\,\mathrm{mm} \\ 19.75\,\mathrm{mm} \end{bmatrix}. \tag{9.8}$$

9.6.2.2 Spatial alignment of camera (B)

The coordinate system of camera (B) can be transformed to the camera (A) by inverting the signs of $x^{(B)}$ and $y^{(B)}$, rotating around the $y^{(B)}$-axis by an angle of 45°, and translating from the origin of camera (B) to the origin of camera (A), i.e.

$$\begin{bmatrix} x^{(A)} \\ y^{(A)} \\ z^{(A)} \end{bmatrix} = \underbrace{\begin{bmatrix} \cos(\alpha) & 0 & -\sin(\alpha) \\ 0 & 1 & 0 \\ \sin(\alpha) & 0 & \cos(\alpha) \end{bmatrix}}_{\text{rotate by } \alpha \text{ around } y^{(B)}} \underbrace{\begin{bmatrix} -1 & 0 & 0 \\ 0 & -1 & 0 \\ 0 & 0 & 1 \end{bmatrix}}_{\text{invert } x^{(B)} \text{ and } y^{(B)}} \begin{bmatrix} x^{(B)} \\ y^{(B)} \\ z^{(B)} \end{bmatrix} + \underbrace{\begin{bmatrix} \Delta x^{(A)} \\ \Delta y^{(A)} \\ \Delta z^{(A)} \end{bmatrix}}_{\text{translate origin (B) to (A)}} . \tag{9.9}$$

The relative alignment between the two cameras is defined by four quantities: the precise value of the angle $\alpha \approx 45°$ between the $x^{(A)}$- and $x^{(B)}$-axes and the translation vector, $\Delta x^{(A)}$, $\Delta y^{(A)}$ and $\Delta z^{(A)}$, which describes the translation between the origins of camera (A) and camera (B) in coordinates of camera (A).

The relative alignment between the two cameras was determined experimentally using the setup depicted in Fig. 9.14. After placing the camera rail in the center of the Compton scanner frame, the collimated ^{137}Cs source was moved across both cameras. This allowed each camera to be irradiated vertically from the top, i.e. parallel to the $y^{(A)}$- and $y^{(B)}$-axes, see Fig. 9.11. The position of the source was set by the horizontal stage position, $\mathcal{H}$. If one of the cameras was irradiated directly for a given $\mathcal{H}$, the position of the beam spot in the x-z-plane could be measured in the local coordinate system of that camera [201]. A selection of measured beam spot positions is listed in Tab. 9.2.

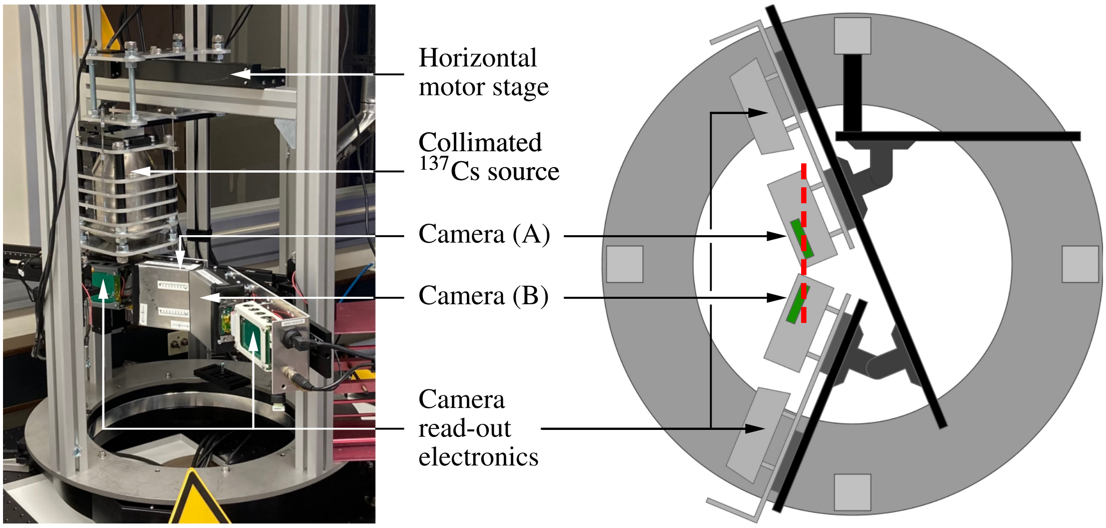

(a) **(b)**

Figure 9.14: (a) Photo and (b) schematic top view of the configuration of the camera rail used to determine the relative spatial alignment of the two cameras. In (b), the axis of movement of the ^{137}Cs source is shown as a red dashed line.

From the values in Tab. 9.2, two normalized vectors, $\vec{\mathcal{H}}^{(A)}$ and $\vec{\mathcal{H}}^{(B)}$, describing the movement of the ^{137}Cs source in the x-z-plane of the local coordinate systems are determined using linear regression:

$$\vec{\mathcal{H}}^{(A)} = \begin{bmatrix} 0.9088 \\ 0 \\ 0.4173 \end{bmatrix} \qquad \vec{\mathcal{H}}^{(B)} = \begin{bmatrix} 0.9354 \\ 0 \\ 0.3536 \end{bmatrix}$$

Inverting the signs of $x^{(B)}$ and $y^{(B)}$, the precise angle between by the two vectors is

$$\begin{aligned} \alpha &= 180^\circ - \mathrm{acos}(\vec{\mathcal{H}}^{(A)} \cdot \begin{bmatrix} -1 & 0 & 0 \\ 0 & -1 & 0 \\ 0 & 0 & 1 \end{bmatrix} \cdot \vec{\mathcal{H}}^{(B)}) \\ &= (45.37 \pm 0.12)^\circ \end{aligned} \tag{9.10}$$

which is close to the envisioned 45° angle. The uncertainty given is purely statistical.

Table 9.2: Measured beam spot position in the x-z-plane of the camera coordinate systems for different horizontal stage positions, $\mathcal{H}$. The uncertainty on $\mathcal{H}$ is 0.05 mm and on x_0 and z_0 as measured by the cameras is 0.1 mm.

$\mathcal{H}$ in mm	$x_0^{(A)}$ in mm	$z_0^{(A)}$ in mm
76.3	15.9	8.4
79.3	13.2	7.2
81.3	11.4	6.4
84.3	8.7	5.1

$\mathcal{H}$ in mm	$x_0^{(B)}$ in mm	$z_0^{(B)}$ in mm
34.4	11.3	3.0
36.4	13.2	3.7
38.4	15.1	4.5
40.4	16.9	5.1

Based on $\vec{\mathcal{H}}^{(A)}$, the beam spot positions in the coordinate system of camera (A) can be predicted for a given $\mathcal{H}$, see Fig. 9.15. Doing this for the values of $\mathcal{H}$ in Tab. 9.2, for which camera (B) was directly irradiated, allows to find $\Delta x^{(A)}$ and $\Delta z^{(A)}$. The values

$$\Delta x^{(A)} = (64.13 \pm 0.03)\,\mathrm{mm} \quad \text{and} \quad \Delta z^{(A)} = (31.86 \pm 0.02)\,\mathrm{mm} \tag{9.11}$$

were determined such that the transformed beam spot positions measured in camera (B) result in the least mean squared difference to the positions expected from $\mathcal{H}$. Again, the uncertainties provided are purely statistical. The beam spot positions measured in camera (B), transformed to the coordinate system of camera (A) using Eq. (9.9), $\alpha = (45.37 \pm 0.12)^\circ$ and the determined values for $\Delta x^{(A)}$ and $\Delta z^{(A)}$, are shown in Fig. 9.15. As the beam is parallel to the $y^{(A)}$- and $y^{(B)}$-axes, $\Delta y^{(A)}$ cannot be determined from this particular analysis.

The missing alignment quantity $\Delta y^{(A)}$ describes the difference in height of the cameras on the rail depicted in Fig. 9.11. As the cameras were installed at approximately the same height on the camera rail, $\Delta y^{(A)}$ is expected to be close to zero. The value of $\Delta y^{(A)}$ was determined from the same dataset as used for Fig. 9.15, selecting events where the characteristic 661.660 keV gammas Compton scattered exactly once in one camera and were fully absorbed in the other. For these events, $y^{(A)}$ can be both directly measured in camera (A), i.e. $y^{(A)}_{\mathrm{meas}}$, and reconstructed from the hit in camera (B), i.e. $y^{(A)}_{\mathrm{rec}}$, as presented in section 9.1. For the latter, the coordinates from camera (B) have to be transformed to the coordinate system of camera (A) using Eq. (9.9). The value of $\Delta y^{(A)}$ is chosen such that the distribution of the difference $y^{(A)}_{\mathrm{rec}} - y^{(A)}_{\mathrm{meas}}$ is centered at zero.

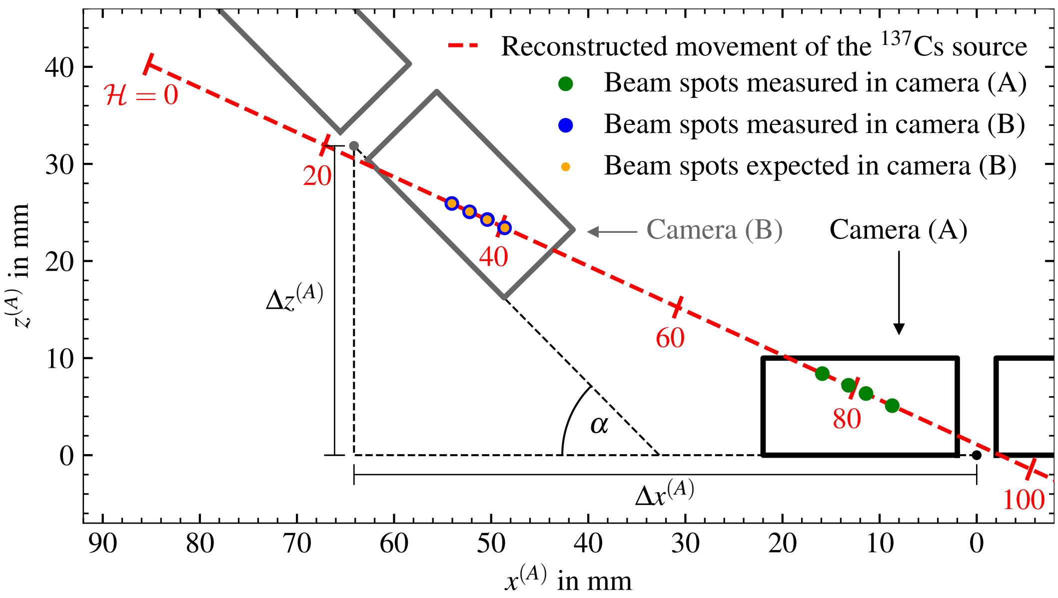

Figure 9.15: Measured beam spot positions in camera (A) and (B), as well as beam spot positions expected from the horizontal motor position, $\mathcal{H}$. Values for $\mathcal{H}$ are given on the red dashed line depicting the reconstructed axis of movement of the ^{137}Cs source. The coordinates of camera (B) are transformed using Eq. (9.9) with $\alpha = (45.37 \pm 0.12)^\circ$, $\Delta x^{(A)} = (64.13 \pm 0.03)\,\text{mm}$ and $\Delta z^{(A)} = (31.86 \pm 0.02)\,\text{mm}$.

After synchronizing the two data streams from the cameras, coincident events, i.e. events with time differences of less than 50 µs, were selected. Events were further selected if they comprised exactly one hit in each camera and if the total energies detected in cameras (A) and (B), $E^{(A)}_{\text{cam}}$ and $E^{(B)}_{\text{cam}}$, added up to the characteristic energy of the gammas emitted by the ^{137}Cs source, i.e. $E^{(A)}_{\text{cam}} + E^{(B)}_{\text{cam}} = (662 \pm 8)\,\text{keV}$. This selection ensured that most of the events originated from gammas which were emitted by the ^{137}Cs source, Compton scattered exactly once in the irradiated camera and were absorbed in the other.

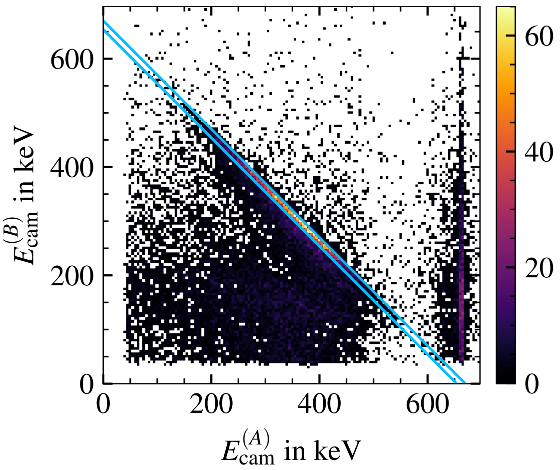

Figure 9.16: Distribution of energies, $E^{(A)}_{\text{cam}}$ in camera (A) and $E^{(B)}_{\text{cam}}$ in camera (B), for coincident events ($\Delta t < 50\,\mu\text{s}$) from a 10 min measurement at $\mathcal{H} = 79.3\,\text{mm}$. Both axes are divided into bins of 5 keV. The solid lines indicate the region containing events with a sum energy of $E^{(A)}_{\text{cam}} + E^{(B)}_{\text{cam}} = (662 \pm 8)\,\text{keV}$.

Figure 9.16 shows a correlation plot for $E^{(A)}_{\text{cam}}$ and $E^{(B)}_{\text{cam}}$ obtained from a 10 min measurement at $\mathcal{H} = 79.3\,\text{mm}$, where camera (A) was irradiated directly, see Fig. 9.15. Most events populate the diagonal line corresponding to fully-contained gammas from the ^{137}Cs source.

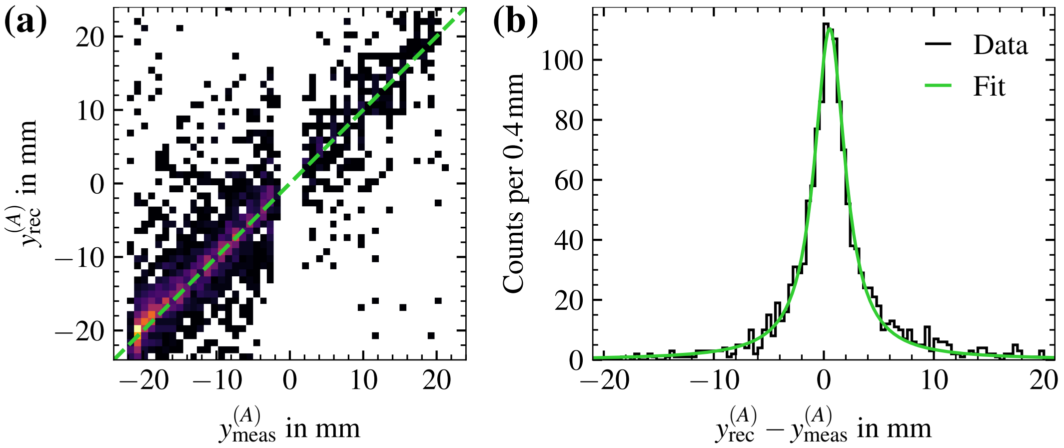

Figure 9.17: (a) Correlation between $y_{\mathrm{rec}}^{(A)}$ reconstructed using the hits in camera (B) and $y_{\mathrm{meas}}^{(A)}$ directly measured in camera (A) for a 10 min measurement at $\mathcal{H} = 79.3\,\mathrm{mm}$. For the former, coordinates of camera (B) were transformed using Eq. (9.9) with $\Delta y^{(A)} = 0\,\mathrm{mm}$. The green dashed line depicts $y_{\mathrm{rec}}^{(A)} = y_{\mathrm{meas}}^{(A)}$. (b) Distribution of the difference $y_{\mathrm{rec}}^{(A)} - y_{\mathrm{meas}}^{(A)}$, together with a fit of a Cauchy distribution, from which a median value of $(0.55 \pm 0.03)\,\mathrm{mm}$ and a FWHM of 3.21 mm were determined.

The hits in camera (B) were transformed to the coordinate system of camera (A) using Eq. (9.9) with $\Delta y^{(A)} = 0\,\mathrm{mm}$ and the values for α, $\Delta x^{(A)}$ and $\Delta z^{(A)}$ as listed in Eqs. (9.10) and (9.11). Then, the reconstructed

$$y_{\mathrm{rec}}^{(A)} = y^{(A)} + \sqrt{(x^{(A)} - x_0^{(A)})^2 + (z^{(A)} - z_0^{(A)})^2}\,\cot(\theta) \tag{9.12}$$

for the hits measured in camera (B) and $y_{\mathrm{meas}}^{(A)}$ from hits measured directly in camera (A) were compared for all selected events. The correlation between $y_{\mathrm{rec}}^{(A)}$ and $y_{\mathrm{meas}}^{(A)}$ for the same 10 min measurement at $\mathcal{H} = 79.3\,\mathrm{mm}$ is shown in Fig. 9.17a.

In Fig. 9.17b, the distribution of the differences $y_{\mathrm{rec}}^{(A)} - y_{\mathrm{meas}}^{(A)}$ for all selected events are shown. The distribution is well described by a Cauchy distribution with a median value of $(0.55 \pm 0.03)\,\mathrm{mm}$ and a FWHM of 3.21 mm. The median value describes how much the coordinate transformation from camera (B) to camera (A) overestimates $y^{(A)}$ when choosing $\Delta y^{(A)} = 0\,\mathrm{mm}$. From this, the missing alignment quantity was determined as

$$\Delta y^{(A)} = (-0.55 \pm 0.03)\,\mathrm{mm}\,, \tag{9.13}$$

where the uncertainty provided is purely statistical.

9.7 Intrinsic spatial resolution

The results of the alignment are input to the determination of the intrinsic spatial resolution. The intrinsic spatial resolution of the Compton Scanner configuration depicted in Fig. 9.12 was determined from Monte Carlo simulations performed with the simulation toolkit GEANT4 [177]. Two scenarios with different positions of the vertical beam were simulated:

(i) $r = 0$ mm, i.e. the vertical beam placed at the center of the detector and the Compton Scanner frame.

(ii) $r = 36$ mm, i.e. the vertical beam placed 36 mm away from the center of the Compton Scanner frame at a minimal distance of 34.5 mm to the surface of camera (A).

Only events with exactly one Compton scatter in the germanium detector and at least one hit in the pixelated camera were selected. The lateral and depth position resolutions of the camera of 0.5 mm FWHM were used in the Monte Carlo simulation for smearing the hit positions. The energy resolutions of cameras (A) and (B) of 0.85% and 0.81% FWHM at 356.017 keV, see Tab. 9.1, were added as uncertainty on the hit energies. The z coordinates were reconstructed for all selected events using Eqs. (9.1) and (9.2). The results are shown in Fig. 9.18.

$r = 0$ mm:

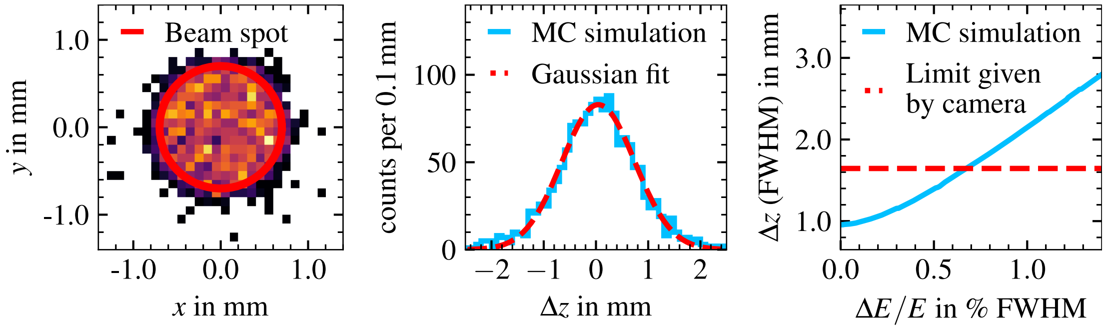

$r = 36$ mm:

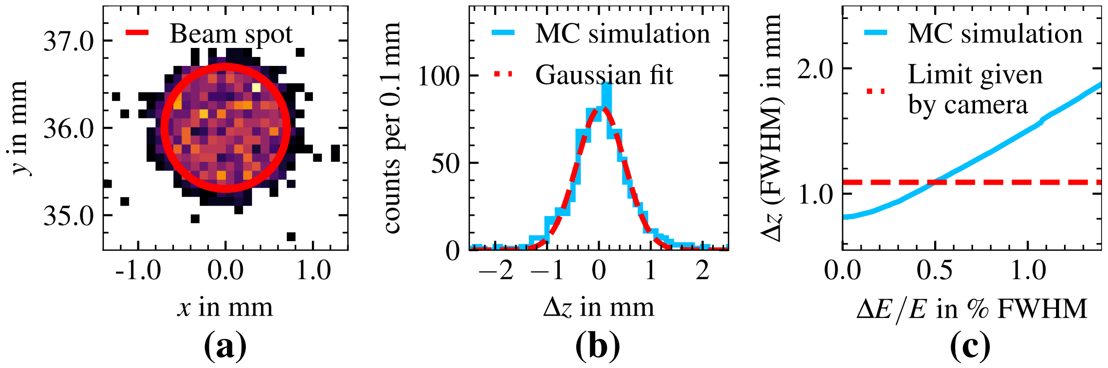

Figure 9.18: (a) Beam spot profile as determined from a Monte Carlo simulation performed with GEANT4 [177]. (b) Deviation, Δz, of the reconstructed z_θ using Eq. (9.2) from the true z in the simulation using the energy and spatial resolutions from the camera as listed in section 9.7. (c) FWHM of the Δz distribution, Δz (FWHM), as a function of the energy resolution, $\Delta E/E$, of the detector at 356.017 keV. The dashed line in (c) depicts the upper limit for the precision of the reconstruction, achieved when the energy reconstructed by the camera is used.

The size of the beam spot in the xy-plane does not depend on the xy-position of the source. The beam spot diameter at the top (bottom) of the detector was 1.23 mm (1.61 mm) for all radii, resulting in an average of 1.40 mm, see Fig. 9.18a. This agrees well with the diameters expected from the aperture of the beam.

During measurements, the Compton angles cannot be measured directly but are calculated from the energies deposited in the detector or in the camera. For cases in which a germanium detector has a poor energy resolution, E_{det} can be determined from the energy deposited in the camera, E_{cam}, via $E_{\text{det}} = E_{\text{in}} - E_{\text{cam}}$ with a resolution given by the uncertainties on E_{cam}. The resulting Gaussian distributions of the differences, Δz, between the reconstructed z_θ and the true z for this case are shown in Fig. 9.18b. The resolution for reconstructing z is 1.64 mm FWHM at $r = 0$ mm and 1.09 mm FWHM at $r = 36$ mm. This defines an upper limit for the intrinsic Δz resolution of the Compton Scanner configuration depicted in Fig. 9.12.

Alternatively, E_{det} can be determined directly from the core pulses recorded from the germanium detector. If the energy resolution of the detector is better than the resolution on E_{det} determined via E_{cam}, the intrinsic spatial resolution is further improved. The dependence of the Δz resolution on the energy resolution of the detector is shown in Fig. 9.18c. For the p-type segBEGe detector, the energy resolution at 356.017 keV is 0.42% FWHM, see Tab. 7.1. When reconstructing θ using the energy deposited in the segBEGe detector, the Δz resolution is improved to 1.29 mm FWHM at $r = 0$ mm and to 1.02 mm FWHM at $r = 36$ mm.

9.8 Data processing

9.8.1 Event selection

The event selection for the Compton reconstruction of z was performed using only coincident events. Events were selected if the energy in the segBEGe detector, E_{det}, as determined from the core pulse, see section 7.4, and the total energy detected in the pixelated cameras, E_{cam}, added up to the characteristic energy of the gammas from the ^{137}Cs source, i.e. $E_{\text{det}} + E_{\text{cam}} = (662 \pm 8)$ keV. This selection of fully-contained events ensured that most of the events originated from gammas emitted by the ^{137}Cs source and that the gammas did not undergo additional Compton scattering on their way from the segBEGe detector to the camera, e.g. off the cryostat wall or off the aluminum boxes of the pixelated cameras.

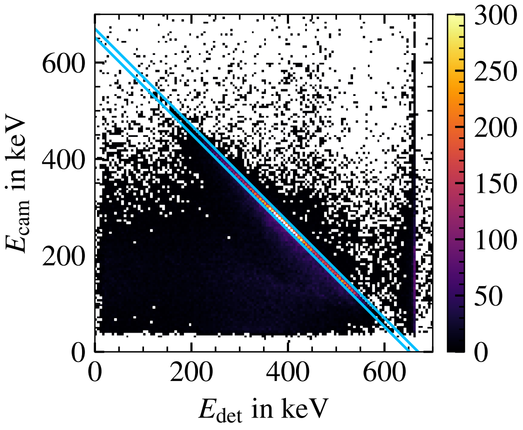

Figure 9.19: Distribution of energies measured in the core of the p-type segBEGe detector, E_{det}, and in the pixelated cameras, E_{cam}, for coincident events during a 10 min Compton Scanner measurement on the $\langle 110 \rangle$ axis in segment 3 at $r = 32.2$ mm. The solid lines indicate the region containing events with a sum energy of $E_{\text{det}} + E_{\text{cam}} = (662 \pm 8)$ keV.

Figure 9.19 shows a correlation plot for E_{det} and E_{cam} obtained from a 10 min measurement, for which the p-type segBEGe detector was irradiated at $r = 32.2\,\mathrm{mm}$, i.e. at a distance of around 5 mm to the edge. The diagonal line corresponds to fully-contained gammas from the ^{137}Cs source and is densely populated. The fraction of fully-contained events varies from 12% when irradiated in the center to 25% when irradiated close to the detector edge.

9.8.2 Reconstruction of the interaction point

The reconstruction of z presented in section 9.1 applies only to events in which the gamma Compton scatters exactly once in the detector, i.e. single-site events. Eq. (9.2) does not hold for events in which the gamma scatters multiple times in the detector, i.e. multi-site events. In these cases, the interaction point is misreconstructed and the pulses are attributed to the wrong z.

Misreconstructed pulses can be identified for events with two well-separated hits in the pixelated cameras. This approach was inspired by the procedures employed for Compton cameras used to image gamma sources [206–208]. The reconstruction of the origin of a gamma requires an assumption on which of the camera hits was the first hit, i.e. the Compton scatter. According to the Monte Carlo simulation, the first hit is expected to be the one with the lower energy. The Compton angle, α, between the path of the gamma entering the camera and the line connecting both hits, see Fig. 9.20a, is calculated using Eq. (9.1). This requires replacing θ by α, E_{in} by $E_{\mathrm{cam},1} + E_{\mathrm{cam},2}$, and E_{out} by $E_{\mathrm{cam},2}$, where $E_{\mathrm{cam},1}$ and $E_{\mathrm{cam},2}$ are the energy deposited in the first and the second hit in the camera, respectively. Geometrically, α and the line connecting the two hits define a Compton cone. The gamma entering the camera propagated along the surface of this Compton cone. Thus, the last interaction point of the gamma in the germanium detector has to lie on the surface of the Compton cone which intersects with the beam axis in up to two points, $z_{\alpha,1}$ and $z_{\alpha,2}$.

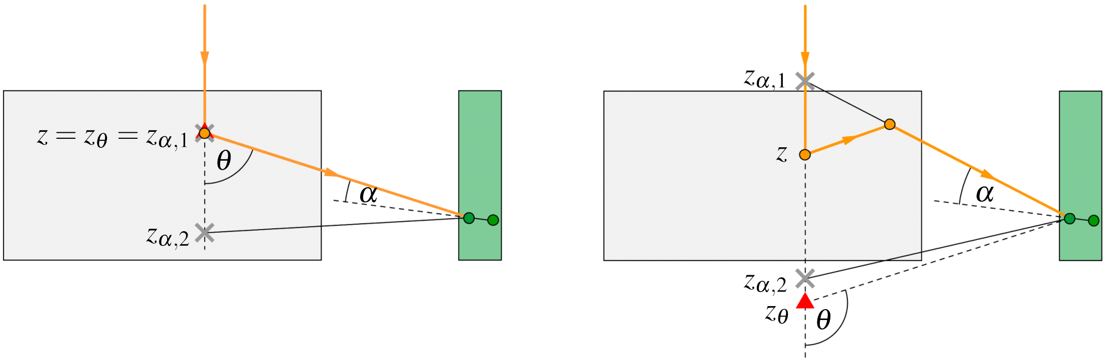

(a) **(b)**

Figure 9.20: Schematic of the trajectory of a fully-contained gamma for (a) a single-site event and (b) a multi-site event in the germanium detector. Interaction points in the germanium detector and in the camera are shown as dots, the reconstructed interaction point using Eq. (9.2) is shown as a triangle, and possible candidates obtained from the Compton cone using only camera information are shown as crosses. In (a), the dot, the triangle and one of the crosses overlap.

For single-site events, see Fig. 9.20a, there is only one interaction point in the germanium detector and it is located on the beam axis. The surface of the Compton cone intersects with the beam axis in this interaction point, i.e. $z = z_\theta = z_\alpha$, where z_α is either $z_{\alpha,1}$ or $z_{\alpha,2}$. For multi-site events, see Fig. 9.20b, the last interaction point in the germanium detector is typically not located on the beam axis. The surface of the Compton cone passes through the last interaction point of the gamma in the germanium detector and intersects with the beam axis in so-called ghost points. These ghost points are often outside of the germanium detector and typically none of them agrees with the misreconstructed interaction point, i.e. $z_\theta \neq z_\alpha$.

Reconstructing z_θ as described in section 9.1 and demanding one of the $z_{\alpha,i}$ to agree with z_θ within 2 mm allows to reject multi-site events without the need of pulse shape analysis. In the case that the reconstruction is rejected, the time order of the two hits is swapped. Only if both scenarios are rejected, the event is classified as a multi-site event and is discarded. The uncertainty of this validation is too large when the two hits in the cameras are too close to each other. The method works reliably for events with a minimum distance of 3 mm between the two hits. This distance is also larger than 1.5 times the center-to-center distance of the anode pixels which ensures that the cameras can reliably separate multiple hits from each other.

9.9 Event statistics

The increase in acceptance resulting from the upgrade of the Compton Scanner with a second camera was also determined from data. A radial scan was performed along the ⟨110⟩ axis in segment 3 in steps of 2 mm. For each r, the rate of validated two-hit events in the detector volume was determined for all events and for a selection of events with only hits in camera (A). The increase in acceptance is shown in Fig. 9.21.

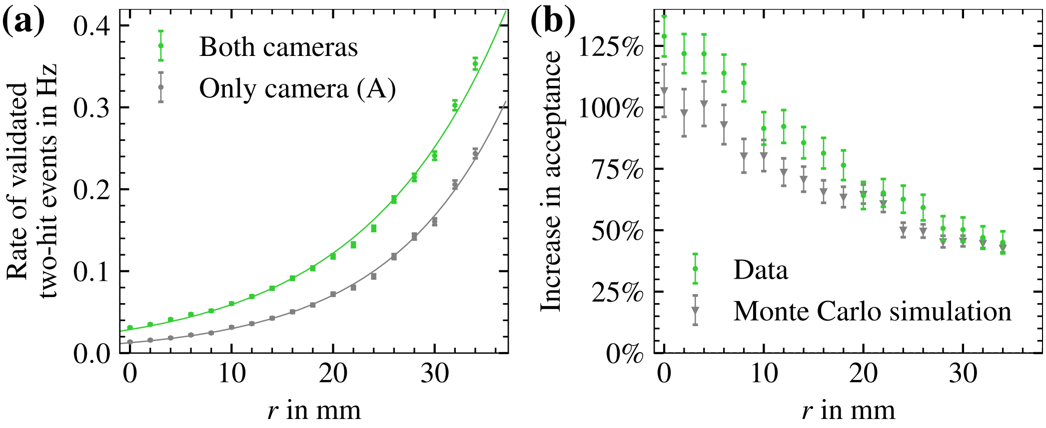

Figure 9.21: (a) Rate of validated two-hit events recorded with both cameras and selecting only events in camera (A) for reference. Also shown are exponential fits to the data. (b) Increase in acceptance as determined from the data and from the Monte Carlo simulation shown in Fig. 9.6.

In the center of the detector at $r = 0\,\mathrm{mm}$, the rate of validated two-hit events is 0.014 Hz for only camera (A) and 0.031 Hz for both cameras. This corresponds to an increase of acceptance of more than 120%. The rate of validated two-hit events increases exponentially with r, see Fig. 9.21a. Close to the edge of the detector, at $r = 34\,\mathrm{mm}$, the rate is more than 10 times higher than at the center. The setup with two cameras shows a rate of 0.35 Hz while, only using camera (A), the rate of validated two-hit events is 0.24 Hz.

In general, the increase in acceptance as determined from data is slightly higher than the expectation from Monte Carlo simulations, see Fig. 9.21b. An explanation is that the cameras cannot resolve some events with two hits in the same camera. If the two hits are less than 1 mm apart, the camera classifies the event as a one-hit event, for which the reconstructed z_θ cannot be validated, and which does not pass the event selection for Fig. 9.21. However, the predicted doubling of acceptance in the center and 50% increase close to the edge of the detector describes the data reasonably well.

10 Determination of the impurity density profile from depletion images

The impurity density profile of a given detector can be determined from capacitance measurements, see chapter 8. However, the measured capacitances only represent integrated values over the depleted volumes of the detector, see Eq. (3.22). Thus, the best-fit result for the impurity density profile is not necessarily unique. Different impurity density profiles might result in similar CV-curves, despite having differently shaped undepleted volumes. One way to resolve this ambiguity is to image the undepleted volumes of the detector for a set of bias voltages and to use them to independently determine the impurity density profile.

In this chapter, a novel method to image the undepleted volumes of a given detector using the Compton Scanner is presented. From the analysis of the images for different bias voltages, the impurity density profile of the p-type segBEGe detector is inferred. This allows for an independent validation of the impurity density profile obtained from capacitance measurements.

10.1 Basic working principle

If a germanium detector is operated well above its full-depletion voltage V_D, energy deposits in the bulk are detected with an efficiency of basically 100%. If it is operated below V_D, energy deposits in the undepleted volumes are theoretically not detected as the electron-hole pairs are not (fully) separated by the vanishing electric field. In reality, some events have been observed in undepleted volumes of silicon detectors [209]. However, the rate of recorded events in germanium is significantly lower in the undepleted volumes of a detector.

The Compton Scanner setup provides the possibility to reconstruct and validate the interaction points of single-site events recorded in the detector with two hits in the cameras, see section 9.8.2. The distribution of reconstructed and validated events is determined for the fully-depleted detector and for a set of bias voltages V_B below V_D. In the depleted volumes, the event rates are expected to be the same as at full depletion if the energy is reconstructed correctly. In the undepleted volumes, a deficiency of reconstructed events with respect to the fully-depleted detector is to be observed. Dividing the detector bulk into small volumes and determining volumes with high detection deficiencies should, thus, allow to image the undepleted volumes of the detector.

10.2 Data taking and processing

The data to image the undepleted volumes of the p-type segBEGe detector was taken along the $\langle 110 \rangle$ axis in segment 3 at $\varphi = 275.8^\circ$, see Fig. 10.1. The measurement times were increased exponentially towards the center of the detector to compensate for the observed exponential decrease in acceptance, see Fig. 9.21. Measurements were performed for bias voltages of $-900\,\mathrm{V}$, $-600\,\mathrm{V}$, $-300\,\mathrm{V}$, $-150\,\mathrm{V}$, $-100\,\mathrm{V}$ and $-50\,\mathrm{V}$. The reference data for the fully-depleted detector was taken at $V_B = -3000\,\mathrm{V}$.

The data acquisition was described in section 6.2 and is depicted in Fig. 6.3. As Compton Scanner events were not built at runtime, all events from the detector had to be recorded. For this measurement, charge pulses were recorded with 3000 samples each, corresponding to an extended pulse length of $12\,\mu\text{s}$. This was required to capture the exponential convergence towards the final pulse amplitude. An event rate of 3.3 kHz and 16 bits per sample caused data rates of almost 160 Mbit/s per read-out channel. The bandwidth of the network connection was too low to record the charge pulses from all contacts of the p-type segBEGe detector. The dead time of the measurement was kept $\ll 1\%$ by recording only core pulses.

Compton Scanner event building was described in section 9.5 with a schematic shown in Fig. 9.7. The measured pulse amplitudes from the core pulses were converted to energies by multiplying them with the V_B-dependent core calibration factor, see Fig. 10.2.

At V_B below -300 V, an additional r-dependence of the core calibration factor was observed. This is due to the difference in cross-talk from segment 3 and 4 to the core. For $r < 7$ mm, the electrons were collected on the closed bottom endplate of segment 4. The cross-talk from segment 4 to the core was significantly higher than from segment 3, where the electrons were collected for $r > 7$ mm. The reduced core pulse amplitudes when segment 4 collected the electrons were compensated by a higher core calibration factor. For bias voltages of -600 V and above, this effect was negligible and the core calibration factor was independent of the collecting segment.

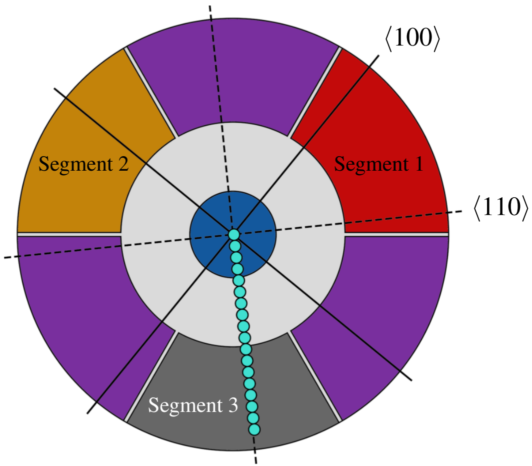

r in mm	0.2	2.2	4.2	6.2	8.2	10.2
t in min	1385	1200	1040	900	780	675

r in mm	12.2	14.2	16.2	18.2	20.2	22.2
t in min	585	510	440	380	330	285

r in mm	24.2	26.2	28.2	30.2	32.2	34.2
t in min	250	215	185	160	140	120

Figure 10.1: Top view of the scan points and a table of the measurement times, t, at the different radii, r, used to image the undepleted volumes of the p-type segBEGe detector. The solid and dashed black lines indicate the locations of the ⟨100⟩ and ⟨110⟩ axes, respectively.

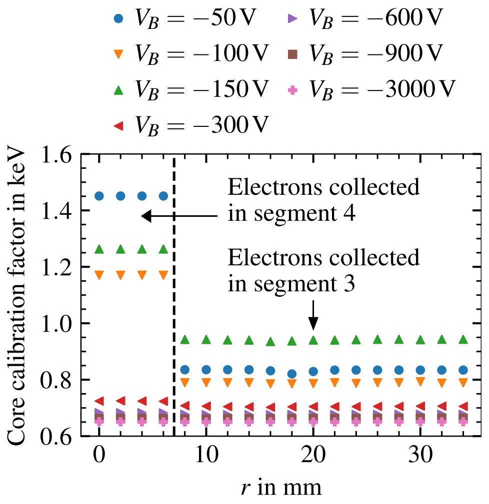

Figure 10.2: Core calibration factors for different r and V_B as listed in the legend.

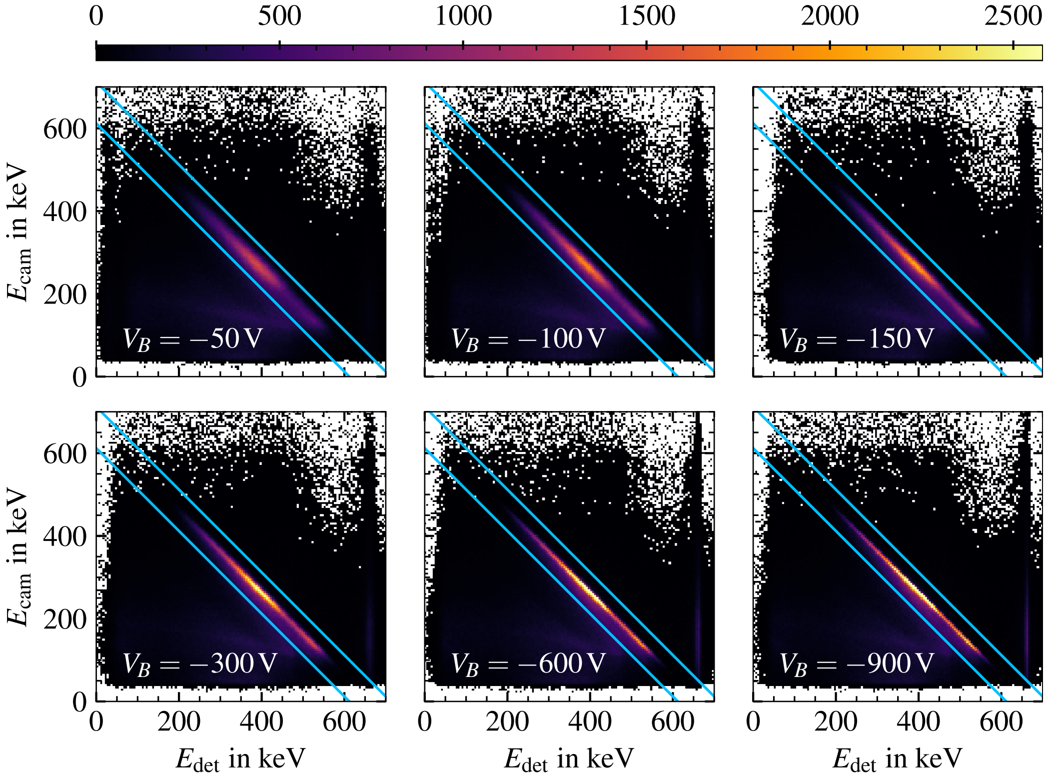

Figure 10.3: Correlation of the energies E_{det} and E_{cam} for coincident events ($\Delta t < 50\,\mu\mathrm{s}$) from a 120 min measurement at $r = 34.2\,\mathrm{mm}$ for different bias voltages V_B. The solid blue lines indicate the regions containing events with $E_{\mathrm{det}} + E_{\mathrm{cam}} = (662 \pm 50)\,\mathrm{keV}$.

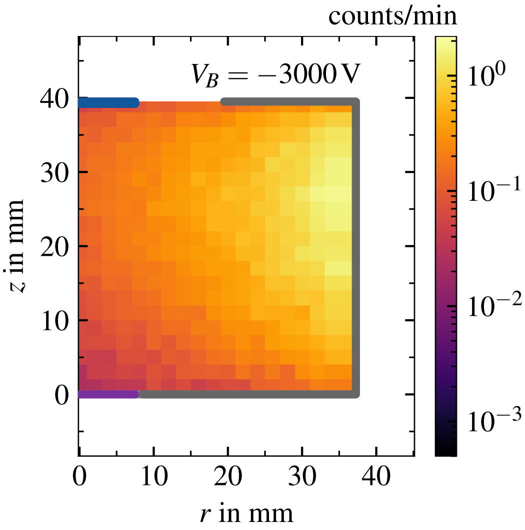

Figure 10.4: Rate of validated events with two hits in the cameras for $V_B = -3000\,\mathrm{V}$, determined from the data from the scan shown in Fig. 10.1.

Because of the poor energy resolution at low V_B, E_{det} as determined from the core contact of the p-type segBEGe detector was only used for a first-level event selection, i.e. $E_{\mathrm{det}} + E_{\mathrm{cam}} = (662 \pm 50)\,\mathrm{keV}$, see Fig. 10.3. This energy window of 100 keV was wide enough to select all fully-contained events. For further analysis, the detector energy was determined from $E_{\mathrm{det}} = 661.660\,\mathrm{keV} - E_{\mathrm{cam}}$. This minimized the influence of the different performance of the detector at different V_B.

The distribution of validated two-hit events in the r-z-plane at $\varphi = 275.8^{\circ}$ is shown in Fig. 10.4. The r coordinates are defined by the position of the ^{137}Cs source, which was moved in steps of 2 mm. The reconstructed z values were binned into 2 mm bins. Event rates were determined by dividing the number of events in each bin by the dead-time corrected measurement time at the respective r.

The collimated beam irradiates the detector from the top and the pixelated cameras are placed at the side of the detector. Therefore, the event rates are generally higher at the top and close to the outer surface of the detector. The maximum event rate of 1.75 counts/min is reached in the bin close to the surface at a height of $z \approx 28\,\mathrm{mm}$. For this bin, the product of the probabilities of a 661.660 keV gamma reaching this part of the detector, the scattered gamma escaping from the detector and being absorbed in the cameras is the highest. The lowest event rate of 0.025 counts/min is observed in the bin at the bottom center of the detector.

The distributions of validated events with two hits in the cameras for V_B below the full-depletion voltage are shown in Fig. 10.5. For all V_B, the highest event rate is observed in the same region as for the fully-depleted detector, see Fig. 10.4. However, bins towards the top center have significantly lower event rates than at $V_B = -3000\,\mathrm{V}$. At $V_B = -900\,\mathrm{V}$, the rate deficiency is concentrated in the upper half of the detector around $r = 0\,\mathrm{mm}$. With decreasing V_B, the region featuring a rate deficiency becomes larger in r and z.

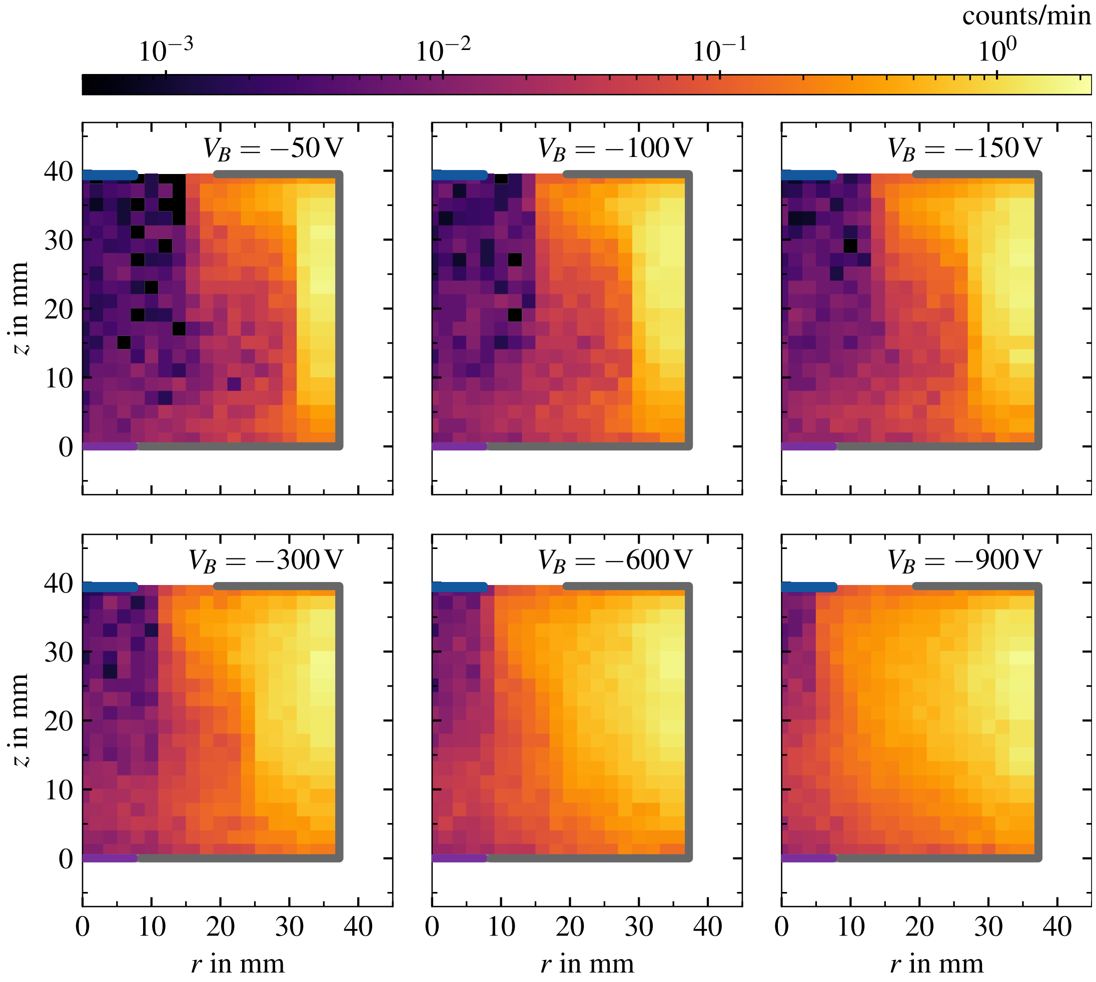

Figure 10.5: Rate of validated events with two hits in the cameras for V_B below the full-depletion voltage as listed in the legends, determined from the data from the scan shown in Fig. 10.1.

10.3 Determination of depletion images

The relative efficiency is defined as the ratio of the event rate at a given V_B to the rate at the reference voltage of $V_B = -3000\,\mathrm{V}$. Figure 10.6 depicts the relative efficiencies for the six event rate distributions shown in Fig. 10.5. These images will be called depletion images.

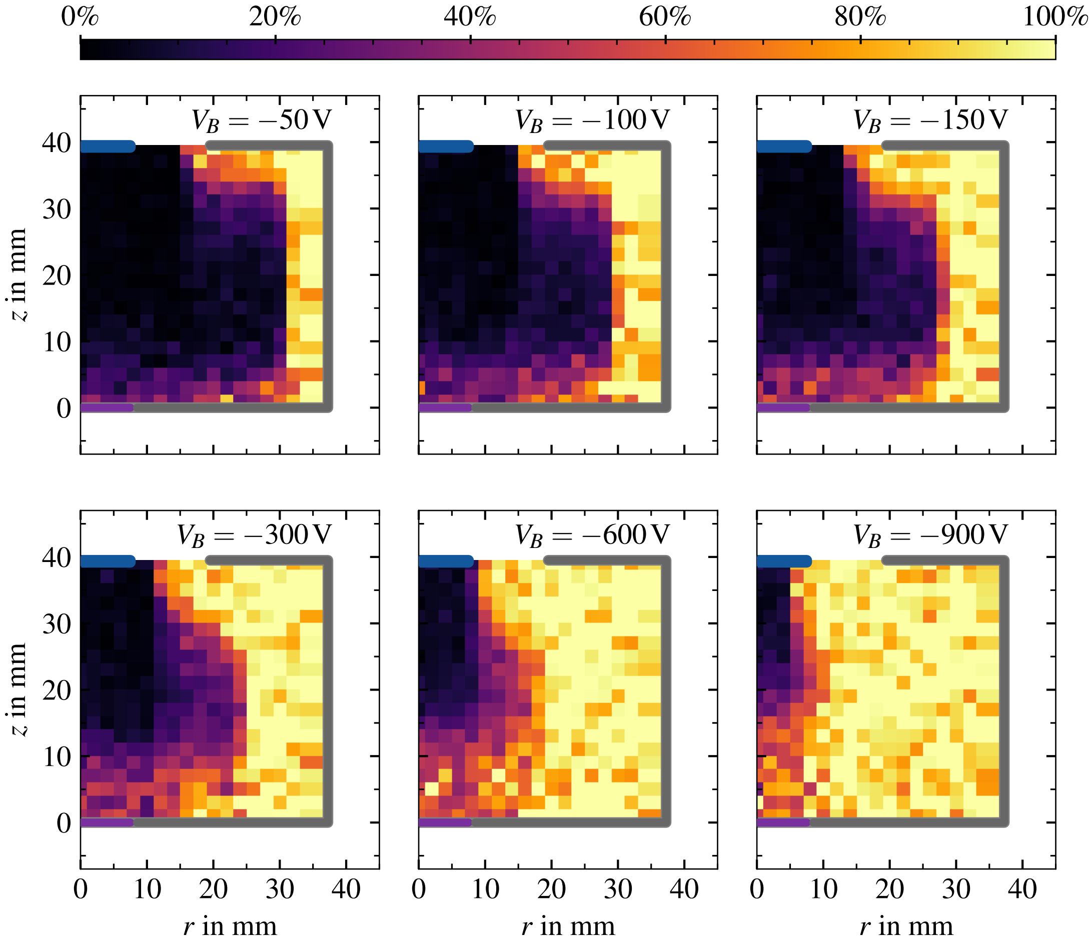

Figure 10.6: Depletion images as determined from the data shown in Figs. 10.4 and 10.5.

The values for the relative efficiency range from 0%, associated with undepleted volumes, up to 100%, associated with depleted volumes. In the depleted volumes at larger r, the relative efficiency fluctuates around the expected value of 100% with a standard deviation of around 10%.

At very low V_B, the transition between the depleted and undepleted volumes is abrupt in r. This is correlated precisely to specific positions of the beam. This requires the boundary between the depleted and undepleted volume to be very thin, i.e. $\ll 1\,\mathrm{mm}$. At higher V_B, the boundary in r is softened, indicating that some events in the undepleted volume survive.

The transition between the depleted and the undepleted volumes in z is soft for all V_B. In addition, presumably depleted volumes underneath the undepleted volume do not reach a relative efficiency of 100%. Both of these observations most likely arise from the nature of the z-reconstruction. The deviation of the reconstructed z_θ to the true z was observed to follow a Cauchy distribution, see Fig. 9.17b. Some events are reconstructed at a z_θ far away from their true z. These events are referred to as catastrophic events. At $r = 0\,\mathrm{mm}$, around half of the z-range of the detector is undepleted at $V_B = -900\,\mathrm{V}$, and more than 75% is undepleted for V_B below $-150\,\mathrm{V}$. This does not only lead to the observed rate deficiencies in the undepleted volume but also to a decrease in catastrophic events in the depleted volumes. As event rates are generally expected to be higher for larger values of z, see Fig. 10.4, the contamination with catastrophic events is expected to be higher for bins at lower z. This also explains why the relative efficiencies for volumes above the undepleted volume do not show large as deviations from 100%.

10.4 Fitting an impurity density profile to the depletion images

For the field calculation in SSD, the impurity density values around grid points $\vec{r}_{i,j,k}$ in undepleted volumes are scaled by factors $f_{i,j,k}$, see section 5.3. For each V_B, these $f_{i,j,k}$ describe the fraction of ionized impurities and would translate to the relative efficiencies depicted in Fig. 10.5 if the z-reconstruction was perfect and the boundary between the depleted and undepleted volumes was thin for all V_B.

The predicted depletion level of the detector can be determined and mapped onto a grid resembling the binning in Fig. 10.6 for a given impurity density model. The impurity density profile is determined from a fit, for which the predicted $f_{i,j,k}(V_B)$ describes the observed depletion images for all V_B best. In the fit,

- the impurity density profile was parameterized as given in Eq. (8.7), i.e. the hyperbolic tangent parameterization. The parameters ρ_{in}, ρ_{out}, α, r_0 and λ were limited such that they reproduce the full-depletion voltage of $V_D = -1275\,\mathrm{V}$.
- the bin at $\vec{r}_{i,j,k}$ is classified as depleted ($d_{i,j,k}(V_B) = 1$) or undepleted ($d_{i,j,k}(V_B) = 0$), depending on whether its measured relative efficiency exceeds a threshold of 50%.
- regions below the undepleted volume, where the relative efficiency significantly deviates from 100%, see Fig. 10.7a, are excluded.

The fit is performed by minimizing the loss function,

$$L = \sum_{V_B} \sum_{i,j,k} \left(f_{i,j,k}(V_B) - d_{i,j,k}(V_B) \right)^2 \,, \tag{10.1}$$

i.e. the sum over the squared differences between the simulated scale factors for the impurity density $f_{i,j,k}(V_B)$ and the measured depletion fraction commensurate $d_{i,j,k}(V_B)$ over all bins for all V_B. The result for the impurity density profile is shown in Fig. 10.7b. Uncertainties on the fit result were estimated from the variations of the parameter values when performing the fit with threshold values of 40% and 60%, accounting for the 10% standard deviation of the fluctuations seen in the depleted volumes.

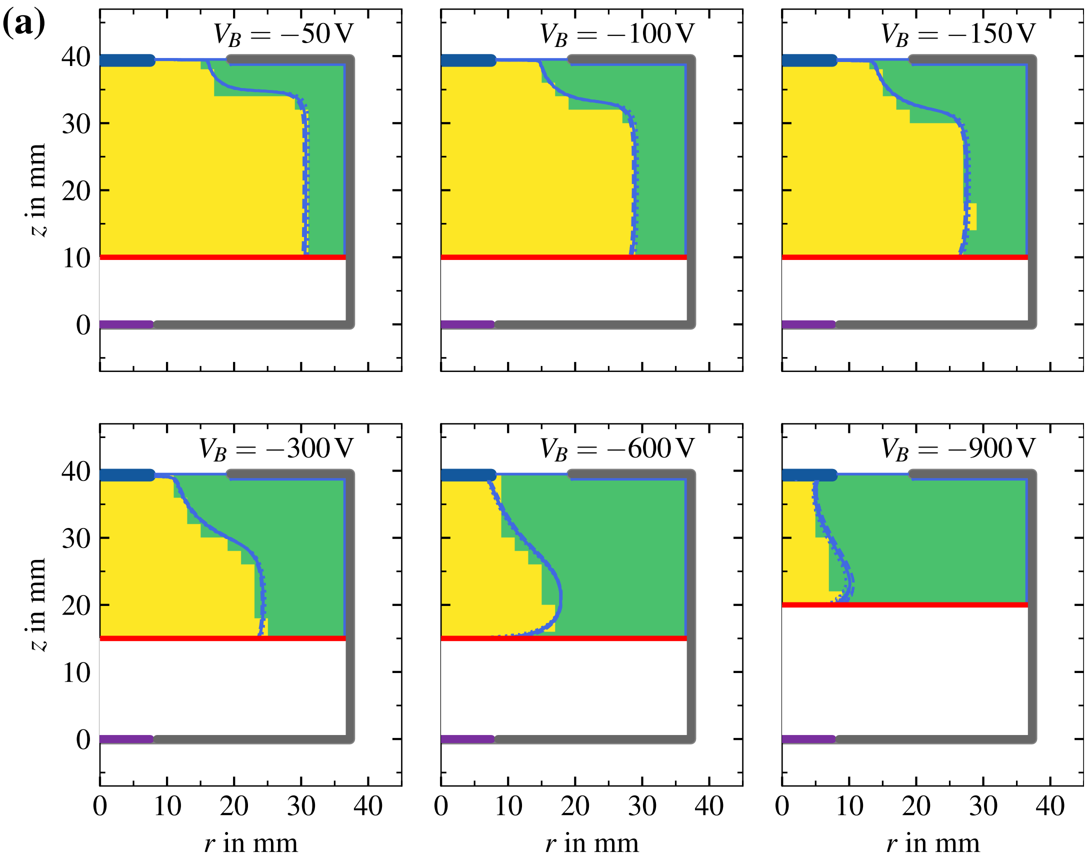

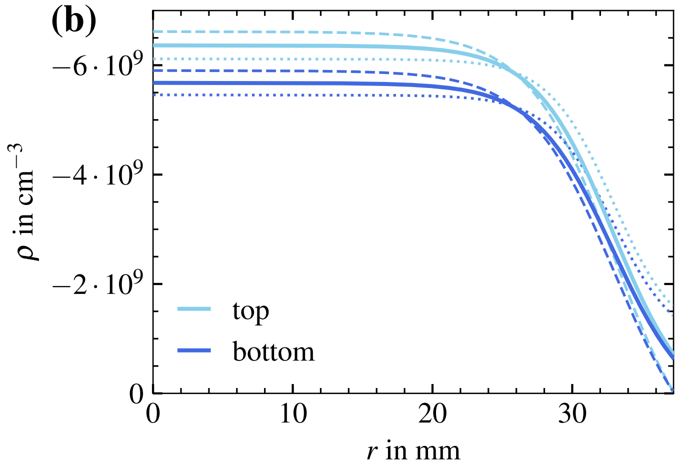

Parameter	Value
ρ_{in}	$(-5.68 \pm 0.22) \cdot 10^9\,\mathrm{cm}^{-3}$
ρ_{out}	$(+0.42^{+1.06}_{-1.10}) \cdot 10^9\,\mathrm{cm}^{-3}$
α	$(1.20^{+0.16}_{-0.13})\,\%$
r_0	$(32.9^{+0.3}_{-0.4})\,\mathrm{mm}$
λ	$(5.56^{+0.62}_{-0.92})\,\mathrm{mm}$
β (fixed)	$12.1\,\%$

Figure 10.7: (a) Classification of volumes of the p-type segBEGe detector into depleted (green) and undepleted (yellow) using a threshold of 50% on the depletion images for different V_B shown in Fig. 10.6. The horizontal red line shows the minimum z-value for each V_B included in the impurity density profile fit. (b) Impurity density profile of the p-type segBEGe detector obtained from minimizing the loss function in Eq. (10.1) for the hyperbolic tangent parameterization in Eq. (8.7) using a threshold value of 50% (solid), 40% (dotted) and 60% (dashed). In (a), the shapes of the undepleted volumes, obtained from the impurity density profile shown in (b), are indicated as blue lines.

10.5 Comparison to the result from capacitance measurements

The impurity density profile of the p-type segBEGe detector was determined in two completely independent ways. Either the profile was fitted to a measured CV-curve, see Fig. 8.9, or to measured depleted volumes at voltages below full depletion, see Fig. 10.7. The best-fit results for the hyperbolic-tangent parameterization in Eq. (8.7) are shown in Fig. 10.8 with the parameters listed in Tab. 10.1. In both fits, a linear z-gradient with a fixed increase of $\beta = 12.1\%$ from the bottom to the top was assumed.

Table 10.1: Best-fit result for the parameters in the hyperbolic-tangent parameterization in Eq. (8.7) for the impurity density profile of the p-type segBEGe detector, determined from fits to the measured CV-curve and from fits to measured depletion images.

Parameter	Values from CV-curve	Values from depletion images
ρ_{in}	$(-5.61 \pm 0.01) \cdot 10^9\,\text{cm}^{-3}$	$(-5.68 \pm 0.22) \cdot 10^9\,\text{cm}^{-3}$
ρ_{out}	$(-6.30 \pm 0.34) \cdot 10^6\,\text{cm}^{-3}$	$(+0.42^{+1.06}_{-1.10}) \cdot 10^9\,\text{cm}^{-3}$
α	$(0.81 \pm 0.01)\,\%$	$(1.20^{+0.16}_{-0.13})\,\%$
r_0	$(33.2 \pm 0.4)\,\text{mm}$	$(32.9^{+0.3}_{-0.4})\,\text{mm}$
λ	$(4.86 \pm 0.02)\,\text{mm}$	$(5.56^{+0.62}_{-0.92})\,\text{mm}$

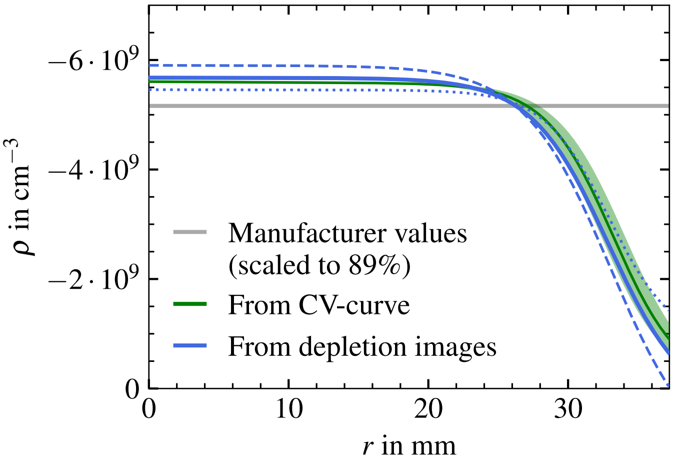

Figure 10.8: Impurity density profile of the p-type segBEGe detector for the parameters listed in Tab. 10.1 at the bottom of the detector, i.e. $z = 0\,\text{mm}$. For reference, the impurity density provided by the manufacturer and scaled to 89% to match the measured depletion voltage assuming no r-dependence is shown in gray.

The best-fit results for ρ_{in}, ρ_{out} and r_0 agree within uncertainties. Both methods predict an almost constant impurity density profile of approximately ρ_{in} for $r < 20\,\text{mm}$, and a significant decrease in the outermost centimeter to almost zero with an inflection point at $r_0 = 33\,\text{mm}$. In comparison with the manufacturer values on the impurity density scaled to 89%, the impurity density profile from both methods is significantly higher for $r \lesssim 25\,\text{mm}$ and lower for $r \gtrsim 28\,\text{mm}$.

In direct comparison, the impurity density profile fitted to the CV-curve is subject to smaller uncertainties, especially at small r. The impurity values at small r mostly influence the depletion levels of the detector at V_B close to the depletion voltage. The voltage closest to the depletion voltage at which the capacitance was measured was $V_B = -1250\,\mathrm{V}$, whereas the first depletion image was taken only at $V_B = -900\,\mathrm{V}$. In addition, the measured capacitances are subject to smaller statistical fluctuations than the relative efficiencies in the depletion images.

A drawback of the fit to the measured CV-curve is that the capacitances were only measured down to $V_B = -120\,\mathrm{V}$. Therefore, it is not sensitive to the exact form of the impurity density for $r \gtrsim 30\,\mathrm{mm}$, see section 8.6. An advantage of the fit to the depletion images is that smaller bias voltages were probed. Two depletion images were taken at $V_B = -50\,\mathrm{V}$ and $V_B = -100\,\mathrm{V}$, which is below the lowest bias voltage $V_B = -120\,\mathrm{V}$ at which the detector capacitance was measured. While the fit to the CV-curve has to extrapolate the impurity density to large values for r, it can be determined from the fit to the depletion images.

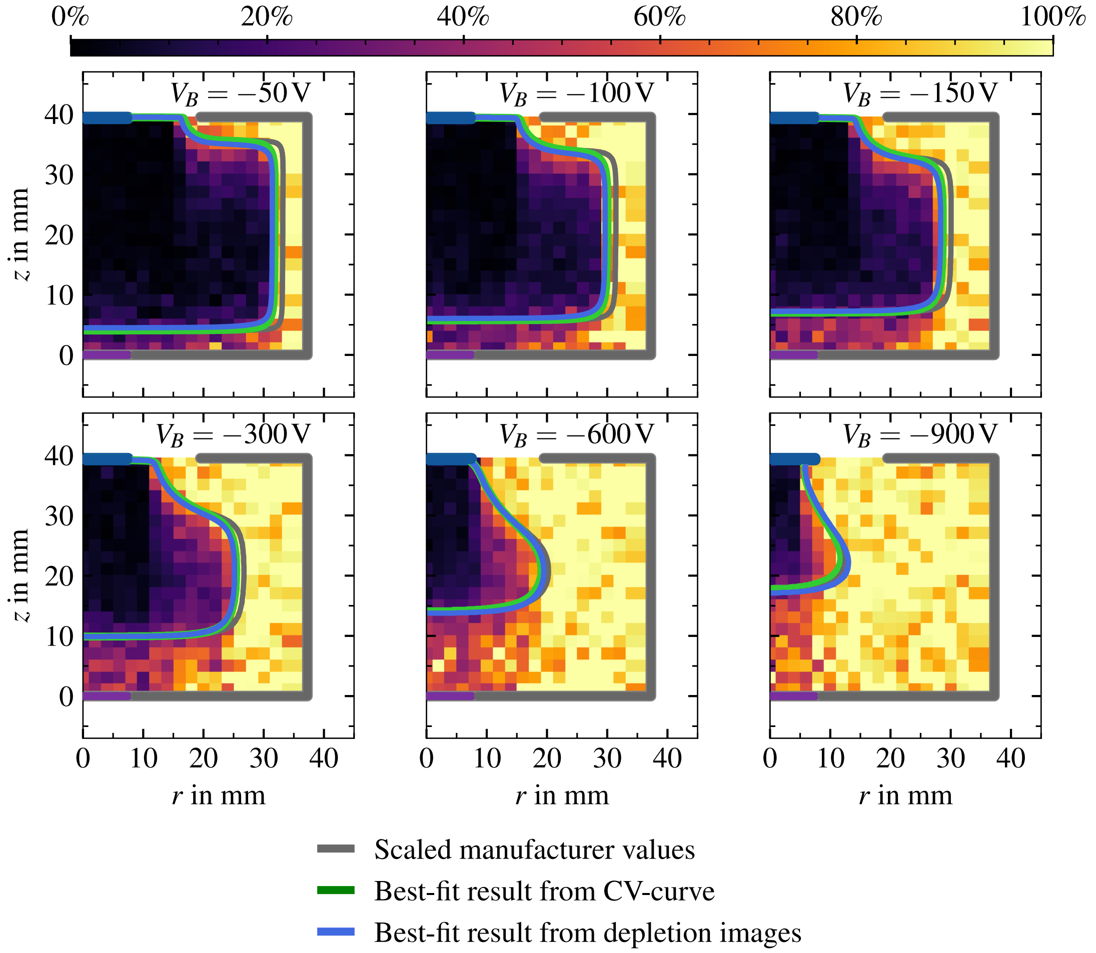

Figure 10.9: Depletion images shown in Figs. 10.6, together with predicted depleted volumes for the best-fit results of the impurity density.

In Fig. 10.9, the measured depletion images are shown together with the undepleted volumes predicted using the impurity density profiles shown in Fig. 10.8. The undepleted volumes agree for all three impurity density profiles for $V_B = -600\,\text{V}$ and above. This is expected because the fitted impurity density profiles are basically flat up to $r = 20\,\text{mm}$. For $V_B = -300\,\text{V}$ and below, the impurity profile using the scaled manufacturer values results in a depletion volume thinner in r compared to the fitted profiles. The predicted undepleted volumes using the impurity density profiles obtained from the capacitance measurements and from the depletion images agree very well. Even at $V_B = -50\,\text{V}$ and $V_B = -100\,\text{V}$, where no capacitance values were measured, the prediction using the impurity density profile from the capacitance measurements provides a significantly better agreement than the impurity density profile assuming no radial dependence.

10.6 Discussion

Both, the capacitance measurements and the depletion images imply an almost flat impurity density profile in the center of the detector and a strong radial decrease in the last centimeter close to the surface of the detector. This is not the first time that a strong radial decrease in the impurity density profile has been observed in a large-volume detector produced by Mirion Technologies [34]. There are several explanations for the observed impurity density, see also section 3.5.

The radial component of the impurity density profile could have been introduced during crystal growth:

- The solid-liquid interface during crystal growth is not necessarily flat [145].
  Outer parts of the crystal might have been grown before the inner parts. Impurities in the germanium melt with low segregation coefficients $k_S \ll 1$ would then have accumulated at later times in the crystal growth, resulting in a radially decreasing impurity density profile.
- During crystal growth, copper contamination could not be avoided.
  In n-type germanium detectors, copper contamination from the gas phase leads to so-called coring, i.e. the bulk being n-type and the surface being p-type [146]. In p-type germanium, copper contamination can also result in an r-dependence in the impurity density profile.

The radial component of the impurity density profile could have been introduced during the fabrication of the segment contacts:

- The n^+ segment contacts are fabricated by lithium diffusion.
  Lithium atoms diffusing up to 1 cm into the bulk of the detector could partly compensate for the p-type impurities in the center, resulting in a lower net impurity density at the surface compared to the bulk. However, if lithium atoms had diffused this deep into the bulk of the detector, it would have been impossible to realize the segmentation of the contacts. Therefore, this explanation is highly unlikely.
- The temperatures needed to fabricate lithium-diffused contacts facilitate copper contamination [149], which mostly accumulates close to the detector surface.

As the exact temperature history and the crystal growth conditions are not disclosed by the manufacturer, it is not possible to provide a certain explanation for the observed r-dependence of the impurity density profile. However, the excellent agreement between the impurity density profiles determined from capacitance measurements and from depletion images allows to confirm the existence of an r-dependence in the impurity density profile and to validate the predictions for the electric field of the p-type segBEGe detector presented in section 8.5, which will be used for pulse-shape studies in the last part of this thesis.

11 Creation of Compton pulse shape libraries

The charge-carrier mobilities in germanium can be determined from charge pulses if their origin and the electric field in the detector are known. The Compton Scanner makes it possible to reconstruct the origin of pulses. For each small volume inside the detector, the pulse shape from energy deposits within that volume can be determined from data. Such a set of pulse shapes is called pulse shape library. The electric field in the p-type segBEGe detector was determined from capacitance measurements and validated using Compton images of undepleted volumes.

Pulses from individual events are too noisy to be used in a pulse shape library, on which pulse shape analysis algorithms are to be trained. Thus, in the order of 100 pulses for each detector volume are necessary to form superpulses which are less affected by statistical fluctuations and electronic noise. The creation of a Compton pulse shape library for the bulk of a detector was described in section 5 of the publication introducing the Compton Scanner in 2022 [38]. Within the framework of this thesis, the creation of pulse shape libraries was further improved, especially by increasing the number of pulses in the center of the detector. As before, part of the text in this chapter is quoted verbatim from this publication [38] and updated to account for recent changes where necessary.

11.1 Events with one hit in the cameras

Figure 11.1 shows pulses from events with one hit in the cameras from a 140 min measurement at a typical detector temperature of 78 K, for which the detector was irradiated at $r = 18.2\,\mathrm{mm}$ and $\varphi = 275.8^\circ$, i.e. close to the $\langle 110 \rangle$ axis in segment 3. In total, 4142 events were reconstructed at $z = (21 \pm 1)\,\mathrm{mm}$. All pulses were shifted to a zero baseline and the tail of the pulses was corrected for the exponential decay of the charge in the preamplifiers, see chapter 7. In addition, the pulses were normalized by E_{det} as measured in the core. The pulses from any given event were collectively time-shifted such that the core pulses reached 50% of their final amplitude at the same time. Segment 3 is the collecting segment. The other segments show so-called mirror pulses which return to the baseline as soon as the charge carriers are collected at the contacts.

The shapes of the 4142 pulses recorded in the core vary significantly. At the same time, the lengths of the pulses recorded in segment 3 show a wide spread. These variations result from misreconstructed events which most probably are multi-site events in the segBEGe detector. Especially the multiple turning points observed in some core pulses are known to be an indication for multi-site events [30, 31]. As events with only one hit in the cameras do not allow for a validation of the reconstructed interaction point, it is expected that some events are assigned to the wrong z. The pulses from these events should not enter the averaging to create superpulses.

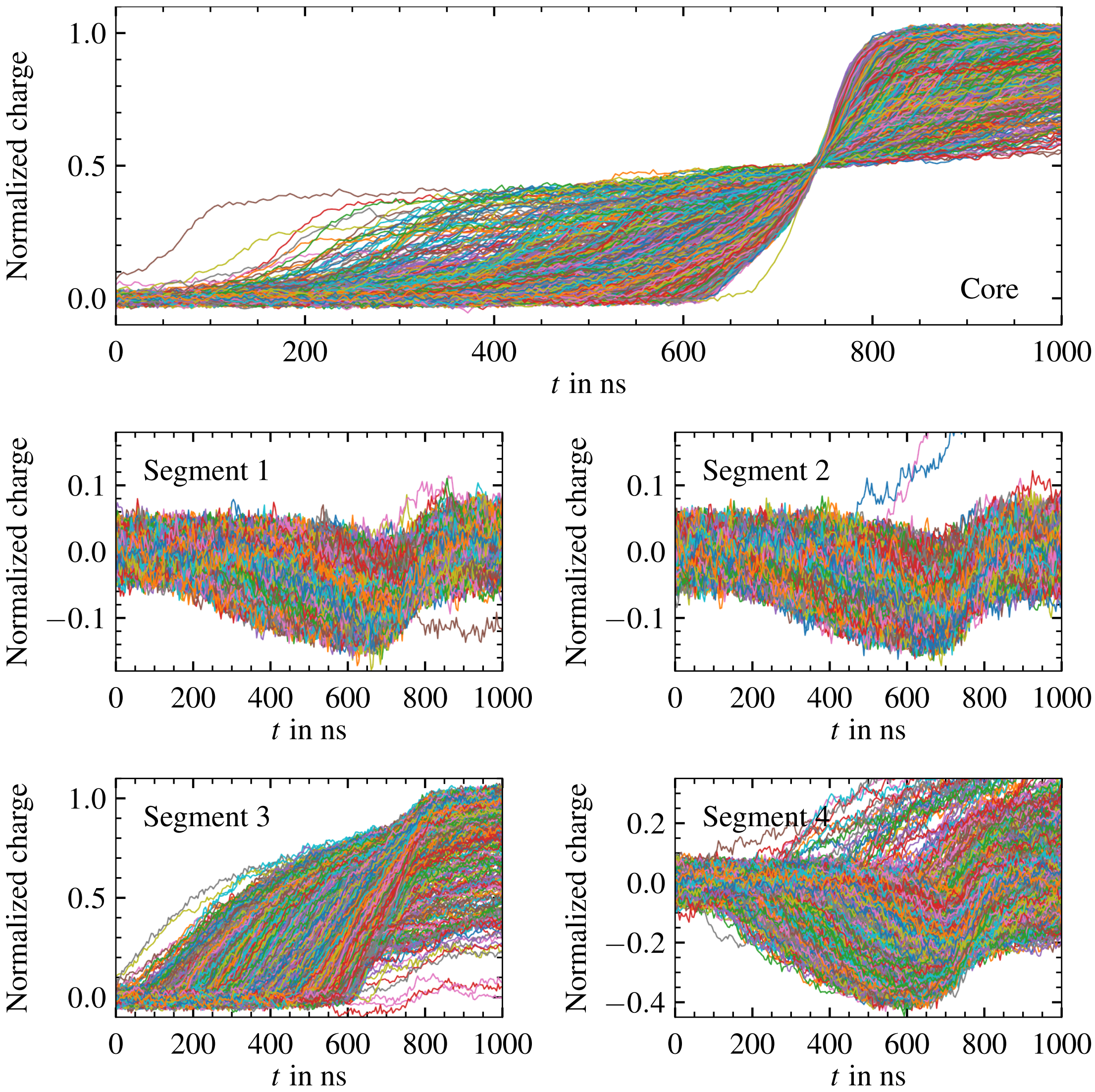

Figure 11.1: Individual pulses from events assigned to the interaction point at $r = 18.2\,\mathrm{mm}$, $\varphi = 275.8°$ and a reconstructed $z = (21 \pm 1)\,\mathrm{mm}$, with one hit in the pixelated cameras, from a $140\,\mathrm{min}$ Compton Scanner measurement at a detector temperature of $78\,\mathrm{K}$. All pulses are time-shifted such that the core pulses are aligned to 50% of their amplitude.

11.2 Events with two hits in the cameras

Events with two hits in the cameras, which additionally passed the Compton cone validation presented in section 9.8.2, were collected for all volumes. Figure 11.2 shows all pulses from validated events with two hits in the cameras for the same volume as considered for Fig. 11.1. From the same $140\,\mathrm{min}$ measurement, 74 pulses remain. In contrast to Fig. 11.1, most of the lengths and shapes of all pulses agree except for statistical fluctuations.

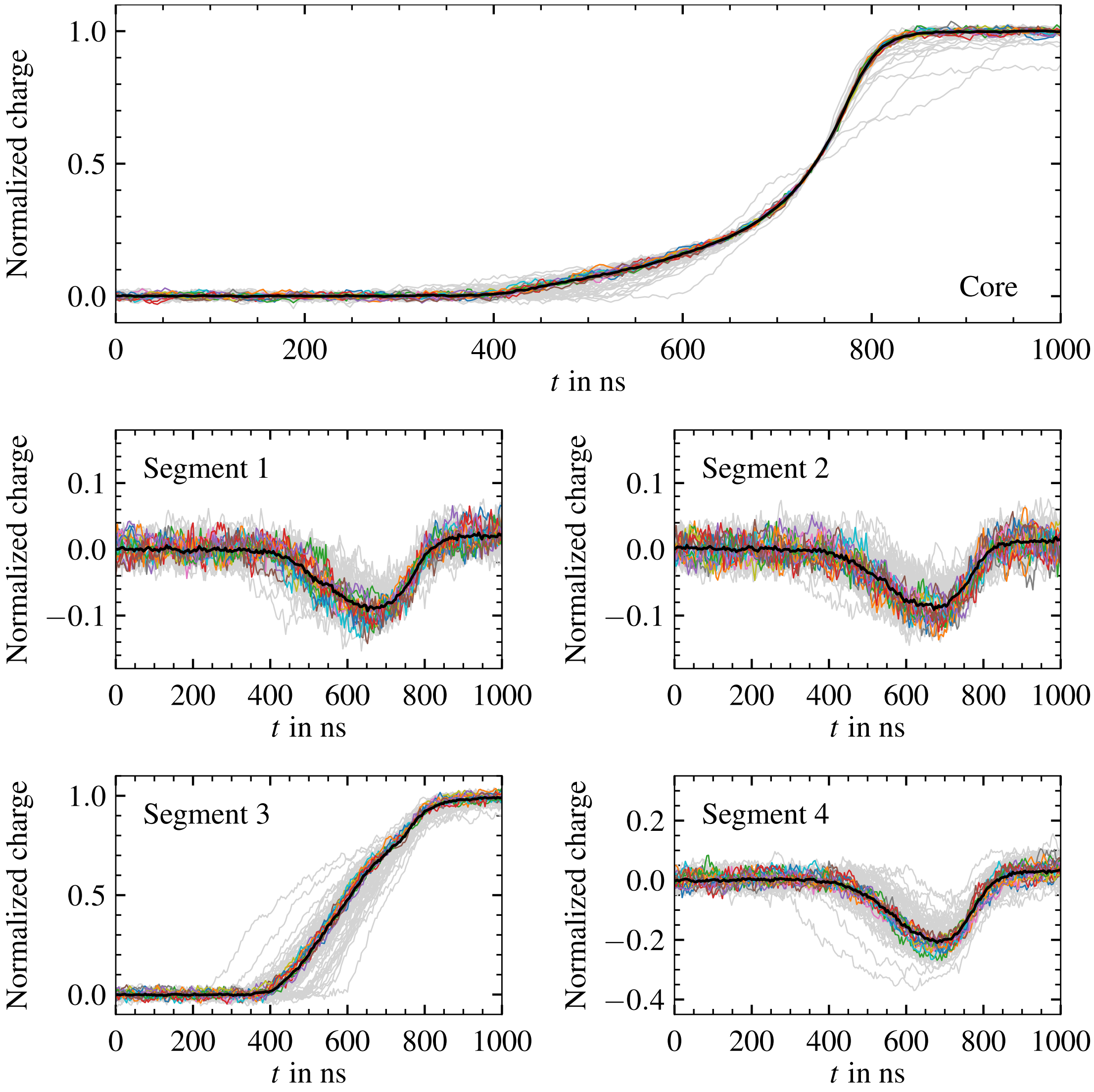

Figure 11.2: Individual pulses from events assigned to the interaction point at $r = 18.2\,\mathrm{mm}$, $\varphi = 275.8^\circ$ and a reconstructed $z = (21 \pm 1)\,\mathrm{mm}$, using only events with two hits in the pixelated cameras that passed the Compton cone validation, see section 9.8.2, from a 140 min Compton Scanner measurement at a detector temperature of 78 K. All pulses are time-shifted such that the core pulses are aligned to 50% of their amplitude. Shown as black lines are the median pulses. For each channel, pulses that do not agree with these intermediate reference superpulses with $\chi^2/\mathrm{ndf} \leq 3$ are shown in gray.

Some events with two hits in the cameras feature a significant deviation at the end of the core pulses or a significantly different rise time in the collecting segment 3, see Fig. 11.2. One way to discard these outlier events is to perform a self-similarity cut on the pulses from all two-hit events for a given detector volume. This requires the determination of intermediate reference superpulses for all channels.

Originally [38], the intermediate reference superpulses for the self-similarity cut were determined for each channel by taking the mean of the respective pulses from all events. This method of creating reference superpulses is reasonable for volumes in which the number of misreconstructed events is very small. However, the fraction of falsely validated events was seen to increase for smaller r. These outliers distort especially the beginning and the end of any superpulse formed by averaging.

The determination of intermediate superpulses for the self-similarity cut was improved to more effectively discard outliers. Assuming that at least half of the events are correctly validated, the median of all validated pulses for a given channel is a good first step in constructing an intermediate superpulse, see Fig. 11.2. Events with pulses that deviate by $\chi^2/\mathrm{ndf} \geq 10$ from the median pulse in the 1000 ns long signal window were classified as outliers and discarded, see Fig. 11.2. The reference superpulses were, then, determined as the mean of the remaining pulses. Only events where the pulses in the core and the collecting segment had a $\chi^2/\mathrm{ndf} \leq 3$ with respect to these intermediate superpulses were averaged to form the final two-hit superpulses for the given volume.

11.3 Final superpulses

The superpulses obtained using only events with two hits in the cameras are less noisy compared to the individual pulses. However, the limited number of pulse shapes is not sufficient to reduce the influence of noise enough to observe tiny features in the pulse shapes.

The superpulses from two-hit events were used as a reference to select the correctly reconstructed one-hit events. Events with one hit in the camera were selected if the individual pulses in all channels agreed within $\chi^2/\mathrm{ndf} \leq 2$ with the respective two-hit superpulses, see Fig. 11.3. The 348 pulses from one-hit events that passed the similarity cut are highlighted in Fig. 11.4. The final superpulses, determined as the mean of all pulses from selected one- and two-hit events, are also shown.

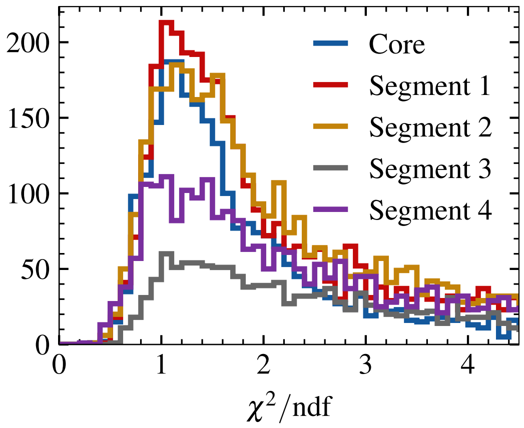

Figure 11.3: χ^2/ndf distribution of the pulses from all events with one hit in the cameras, see Fig. 11.1, with respect to the superpulses obtained from events with two hits in the cameras.

The individual pulses that enter the superpulse averaging have reconstructed z_θ-values which spread around a targeted z value, e.g. 21 mm for the pulses shown in Fig. 11.4. Due to the finite resolution of the Compton Scanner and the limited sample size of two-hit events, the actual z value of the final superpulses might differ from this targeted z value by up to 1 mm.

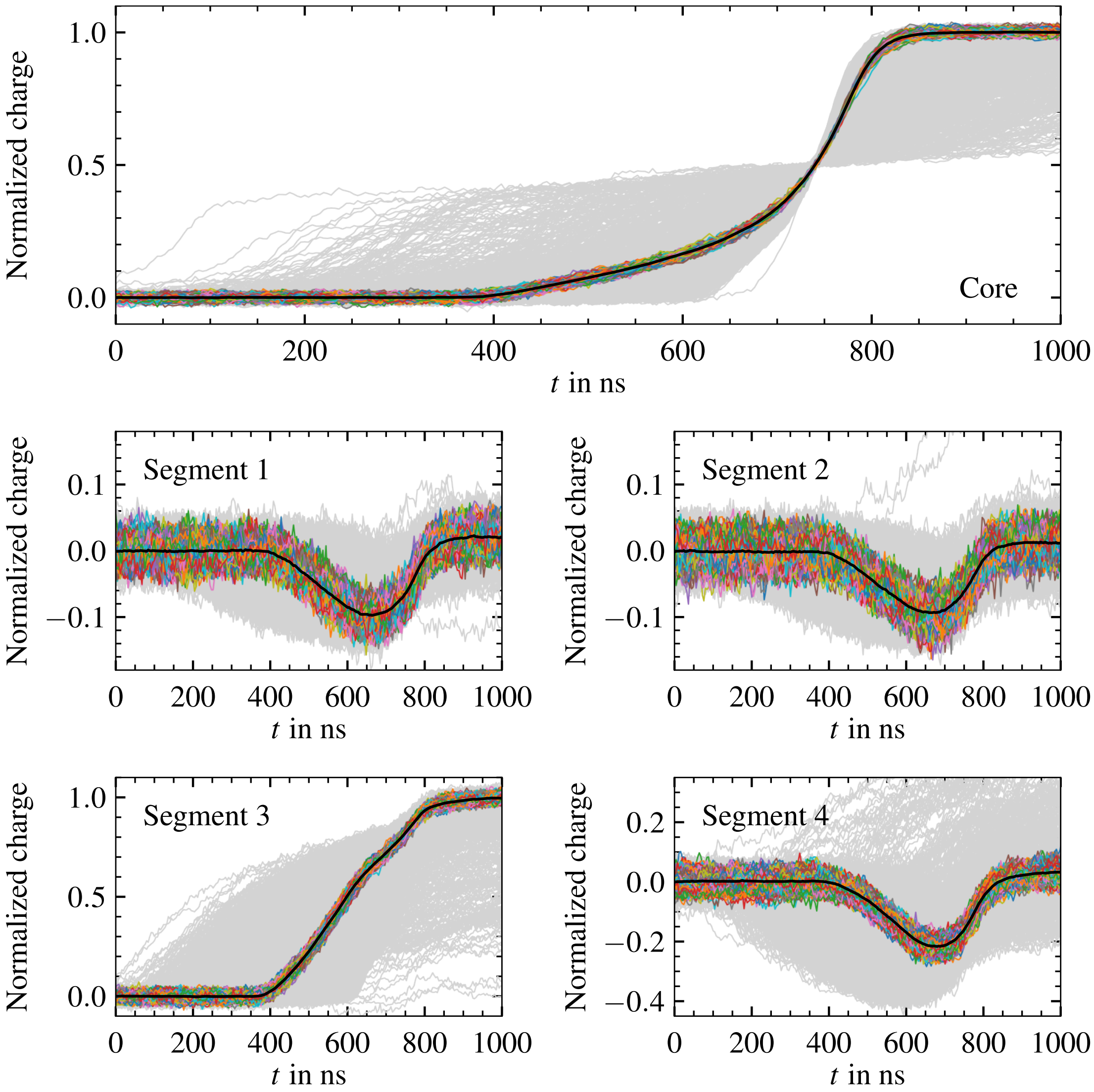

Figure 11.4: Pulses from events assigned to the interaction point at $r = 18.2\,\mathrm{mm}$, $\varphi = 275.8^\circ$ and a reconstructed $z = (21 \pm 1)\,\mathrm{mm}$, with one hit in the cameras and selected as described in section 11.3. All pulses are time-shifted such that the core pulses are aligned to 50% of their amplitude. Shown in gray are the pulses that did not agree with the two-hit superpulse with $\chi^2/\mathrm{ndf} \leq 2$. Shown in black are the final superpulses.

An estimate for the actual z value of the final superpulses is the most likely z_θ value of all similar events. An individual event is defined as similar if the pulses in the core and all segments agree with the respective superpulses with $\chi^2/\mathrm{ndf} \leq 3$ in the signal window. For these similar events, the distribution of z_θ follows a Cauchy distribution that peaks around the nominal z value. Figure 11.5 depicts the distribution of z_θ of events with pulses similar to the superpulses shown in Fig. 11.4. The actual z value is then determined as the median value, $\bar{z}_\theta$, of the Cauchy distribution fitted to the measured z_θ distribution. For the superpulses shown in Fig. 11.4, the actual z value of $\bar{z}_\theta = (21.35 \pm 0.05)\,\mathrm{mm}$ is slightly higher than the nominal z value of 21 mm.

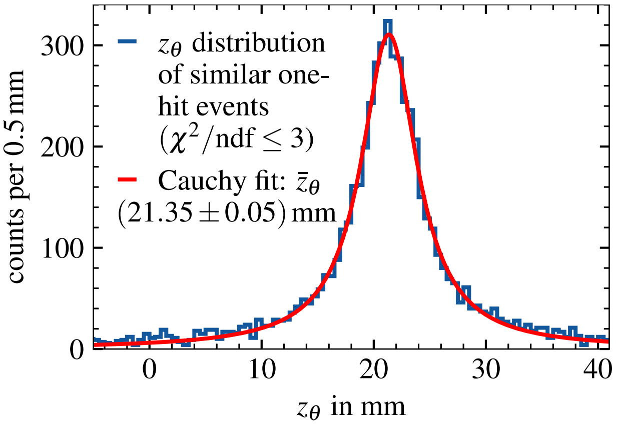

Figure 11.5: Distribution of the reconstructed z_θ values from all similar one-hit events from the 140 min measurement at $r = 18.2$ mm and $\varphi = 275.8°$, i.e all one-hit events with pulses that agree with the final superpulses determined for $z = (21 \pm 1)$ mm, see Fig. 11.4, with $\chi^2/\mathrm{ndf} \leq 3$. Also shown is a fit of a Cauchy distribution, from which a median value of $\bar{z}_\theta = (21.35 \pm 0.05)$ mm was determined.

11.4 First comparison of simulated to measured superpulses

The superpulses from the pulse shape library serve to test pulse shape simulations. Figure 11.6a depicts the distributions of $5-95\%$ rise times and A_0/E_0 as determined from the core contact, see section 6.3.2, for the p-type segBEGe detector at $\varphi = 275.8°$. Shown in Fig. 11.6b are simulation results from SSD, using the impurity density profile obtained from the capacitance measurement, see section 8.5, and the charge-drift models described in chapter 4. The simulated raw pulses were convolved with the preamplifier response functions to account for the bandwidths of the preamplifiers.

The general distributions of the $5-95\%$ rise times and A_0/E_0 are well predicted by this simulation. The smallest rise times are observed in the region forming a shell around the point contact. The largest rise time values are observed at the bottom and in the outer parts of the p-type segBEGe detector. The distribution of A_0/E_0 is basically constant over a large part of the detector and increases only in regions very close to the point contact. However, the $5-95\%$ rise times are generally underestimated and the values for A_0/E_0 are overestimated by approximately 10%. This implies that the charge-drift mobilities used in the simulation are too large by around 10%.

A better agreement between simulated and measured pulse shape library is achieved when scaling μ_0 for holes to 90% of the values listed in Tab. 4.1, see Fig. 11.6c. This agrees well with previous findings [210–212], where μ_0 values had to be scaled to between 85% and 90% to match the measured pulse lengths. For $r \geq 20$ mm or for $z \leq 20$ mm, the simulated A_0/E_0 distribution does not significantly deviate from the measured one for this change of input to the simulation. The rise time distribution is also well predicted in that part of the detector. However, at $r = 0$ mm, the simulation underestimates the rise times by up to 10%, and in the region just below the point contact, deviations of up to 42% in the rise times and down to -18% in the values for A_0/E_0 are observed, see Fig. 11.7.

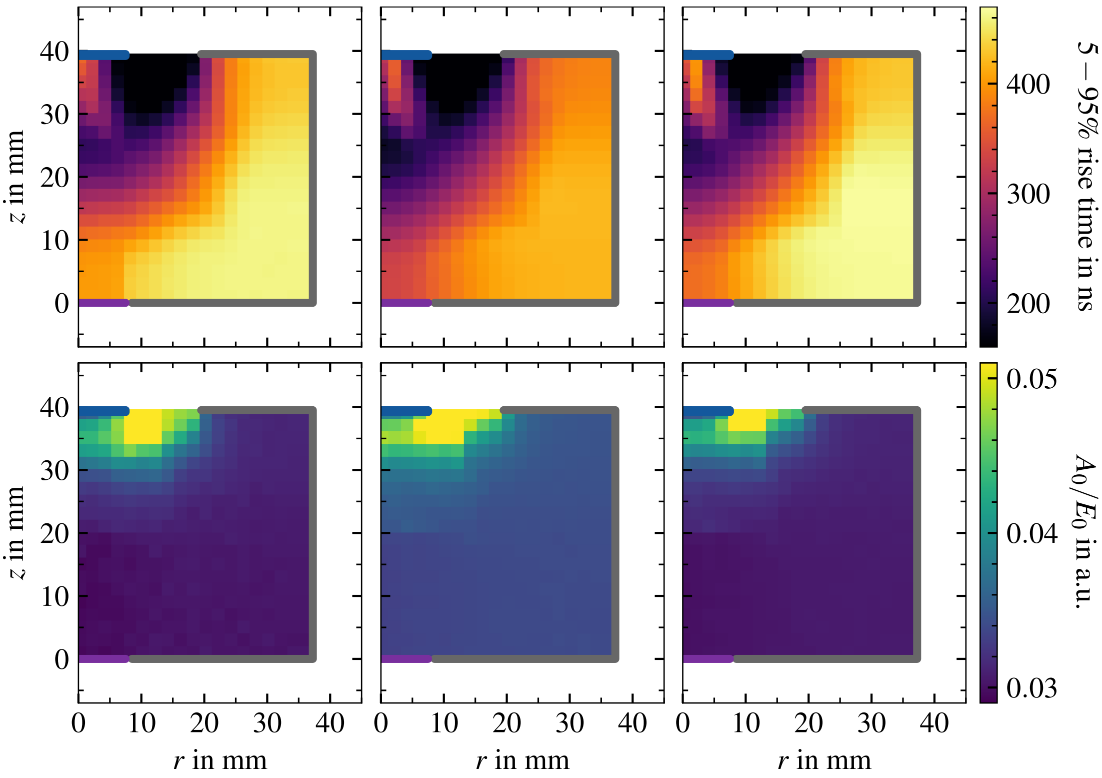

(a) **(b)** **(c)**

Figure 11.6: (Top) $5-95\%$ rise times and (bottom) A_0/E_0 for the $\langle 110\rangle$ axis in segment 3 at $\varphi = 275.8°$, as determined for the core contact: (a) from the superpulses obtained from Compton Scanner data at $T_0 = 78\,\mathrm{K}$, and (b) simulated with SSD using the mobility parameters listed in Tab. 4.1 and (c) with μ_0 for holes scaled to 90%. In all simulations, the electric field resulting from the capacitance measurements shown in Fig. 8.12 and the hole- and electron-drift models introduced in sections 4.4.1 and 4.4.2.3 were used.

The deviations depicted in Fig. 11.7 imply that simply scaling μ_0 for holes to 90% is not sufficient to fully predict the performance of the p-type segBEGe detector, despite significantly improving the agreement between simulation and data. In order to determine values for the longitudinal drift velocities along the $\langle 100\rangle$ and the $\langle 110\rangle$ axes and to test the charge-drift anisotropies for electric field strengths between 400 and 1200 V/cm, the superpulses in the high-quality pulse shape library obtained from Compton Scanner data are analyzed in more detail in the final part of this thesis.

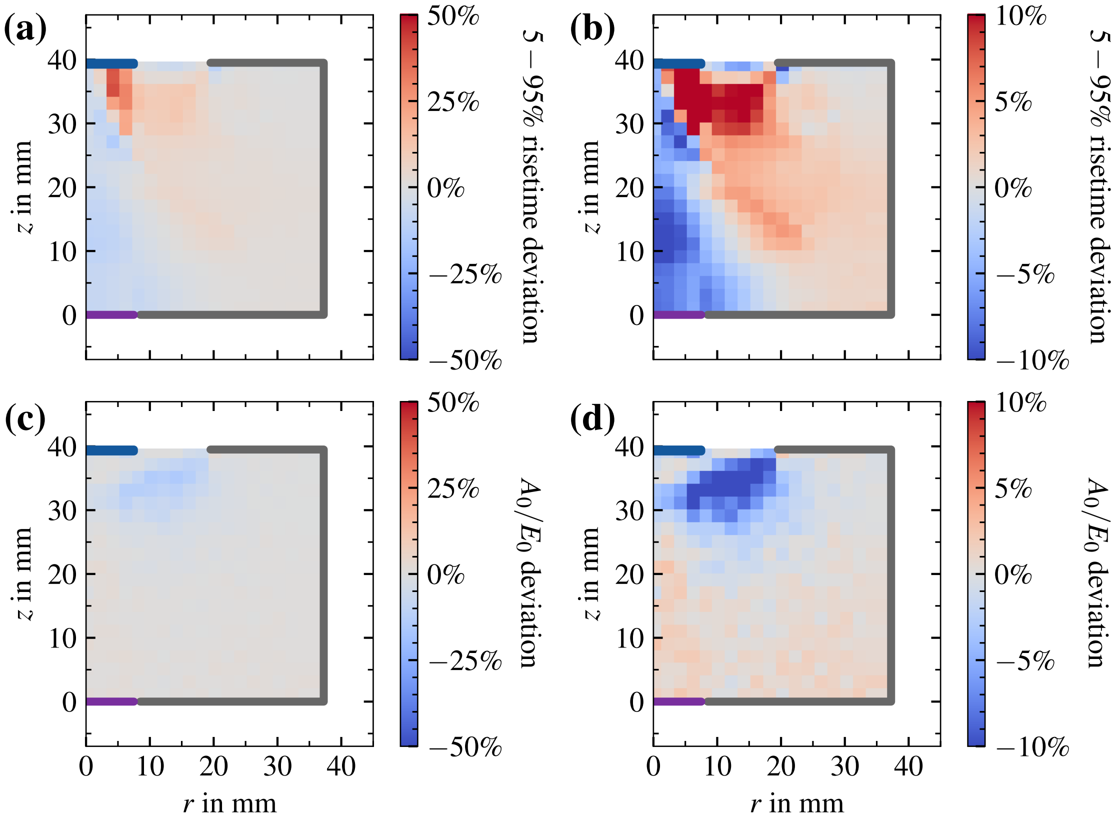

Figure 11.7: Relative deviation of the simulated (a) $5-95\%$ rise times and (b) A_0/E_0 values, using μ_0 for holes scaled to 90%, to the measured values as shown in Fig. 11.6.

12 Determination of charge-carrier mobilities

The longitudinal drift of electrons and holes can be studied in regions where the electric field is parallel to a crystallographic axis. In the p-type segBEGe detector, there are several regions where this is the case, see Fig. 8.12:

- In the center at $r = 0\,\text{mm}$, the electric field points upwards along the $[001]$ axis with an electric field strength of $400\,\text{V/cm} \lesssim \mathcal{E} \lesssim 1700\,\text{V/cm}$.
- At $z = 21.5\,\text{mm}$, the electric field for $r > 20\,\text{mm}$ points radially inwards and horizontal drifts along the $\langle 100\rangle$ and $\langle 110\rangle$ axes can be studied at electric field strengths of $470\,\text{V/cm} \lesssim \mathcal{E} \lesssim 620\,\text{V/cm}$.

In this chapter, the determination of the longitudinal drift velocities and corresponding mobilities of electrons and holes, as well as their temperature dependence, is presented for vertical and horizontal drifts along the $\langle 100\rangle$ and $\langle 110\rangle$ axes. The longitudinal anisotropy is used to test the assumptions made for the electron-drift model.

12.1 Longitudinal charge-carrier drift along the $[001]$ direction

For events at $r = 0\,\text{mm}$, the charge-carrier drift is fully vertical, i.e. longitudinal along the $[001]$ axis, see Fig. 12.1. The longest hole drift paths are obtained for events at the bottom of the detector, where the electrons are almost immediately collected on the closed bottom end-plate of segment 4 and the holes drift upwards through the whole detector. With increasing z, the hole drift path and, thus, the hole drift time becomes shorter, while the electron drift path becomes longer. This is shown exemplarily in Fig. 12.1 for two events at $z = 1\,\text{mm}$ and $z = 17\,\text{mm}$.

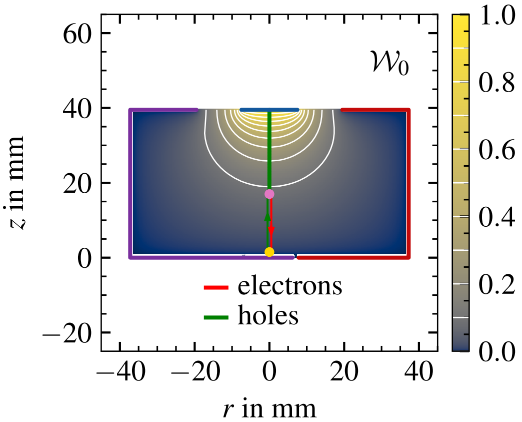

Figure 12.1: Electron and hole drift paths for two events at $r = 0\,\text{mm}$ as simulated with SSD. Lines depict the upward hole drift for the event at $z = 1\,\text{mm}$ (gold) and the downward electron drift for the event at $z = 17\,\text{mm}$ (pink). Also shown is the weighting potential $\mathcal{W}_0$ of the core contact.

The simulated pulses shown in Fig. 12.2 demonstrate the dependence of the drift time on the z-position of the event. The longest pulse is obtained for the event at $z = 1\,\text{mm}$, which features almost exclusively hole drift. With increasing z, the influence of the electron drift on the pulse shape increases, resulting in steeper slopes at the beginning of the pulses, see Fig. 12.2b. As long as the electrons are collected before the holes, i.e. $z < 21\,\text{mm}$, the pulses become shorter and end with a sharp rise. This sharp rise of the pulses shown in Fig. 12.2a results from the final approach of the holes to the core contact. For $z \geq 21\,\text{mm}$, the sharp rise is followed by a moderate slope associated with an ongoing downward drift of the electrons.

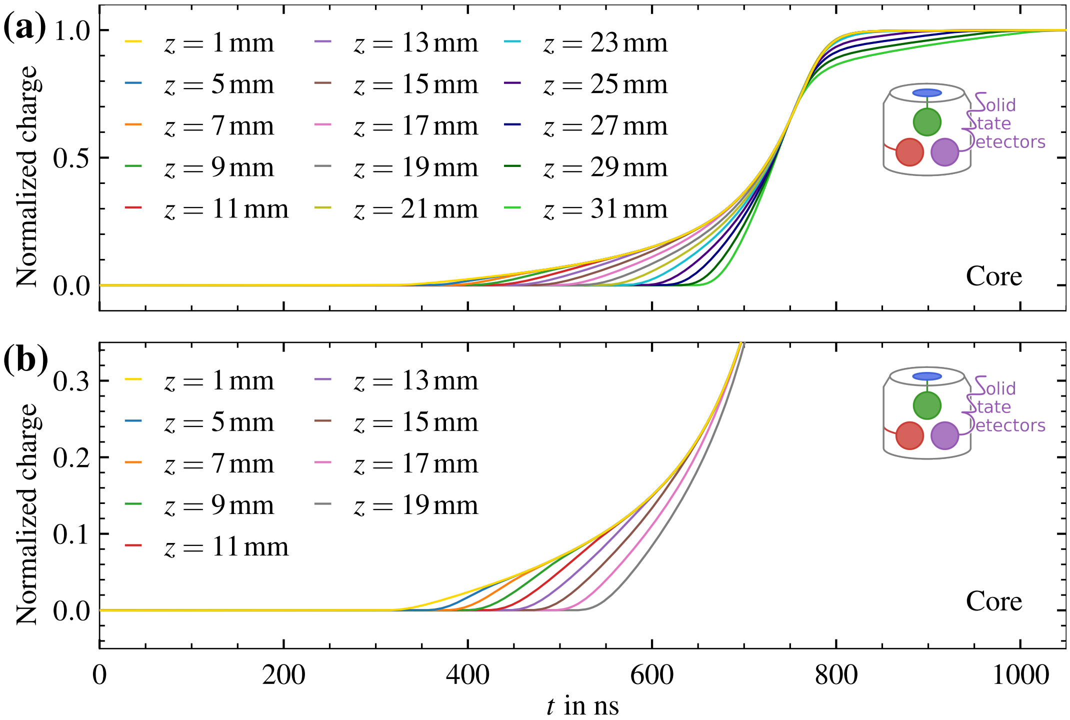

Figure 12.2: Simulated core pulses for events at $r = 0\,\mathrm{mm}$ and z as given in the legend using the electric field depicted in Fig. 8.12 and the mobility parameters listed in Tab. 4.1: (a) full amplitude and (b) zoom-in. The pulses are convolved with the response function of the core contact, normalized to their amplitude and time-aligned to 65% of their amplitude.

The exact shapes of the simulated pulses shown in Fig. 12.2 depend on

- the electric field $\vec{\mathcal{E}}(z)$ at $r = 0\,\mathrm{mm}$, see Fig. 8.12, which was determined from capacitance measurements and from depletion images,
- the weighting potential of the core contact for the fully-depleted detector, see Fig. 12.2, which depends only on the geometry of the detector and its contacts,
- the response function for the core read-out, see Fig. 7.9, which was determined from pulser measurements as described in section 7.3,
- the linear segment-to-core cross-talk, see Eq. (7.8), which was determined from background measurements as described in section 7.4.2,
- the differential segment-to-core cross-talk, which was set to be $-0.06/\mathrm{ns}$ for segment 4 and zero for all other segments based on the observation of segment-specific core rise times, see Appendix F on page 192, and
- the mobility parameters μ_0, $\mathcal{E}_0$ and β of the longitudinal electron and hole drift along the [001] direction used in $\upsilon_{L,e}^{100}(\mathcal{E})$ and $\upsilon_{L,h}^{100}(\mathcal{E})$, see Eq. (4.2). .

The parameters for $\upsilon_{L,e}^{100}(\mathcal{E})$ and $\upsilon_{L,h}^{100}(\mathcal{E})$ were determined from data taken at $r = 0\,\mathrm{mm}$ by finding sets of μ_0, $\mathcal{E}_0$ and β for electrons and holes that minimize the deviations between simulated and measured pulses.

12.1.1 Data taking and processing

Compton Scanner data was taken at $r = 0\,\mathrm{mm}$ with a measurement time of 100 h, see Fig. 12.3. The pulses from the core contact and the segments were recorded with a pulse length of 4.8 µs for all events registered in the core contact with an energy evaluated to be above 50 keV by the trigger. The pulses were processed as described in chapter 7. The z-reconstruction was performed for all events with one or two hits in the cameras as described in section 9.8. Then, pulse shape libraries were created as outlined in chapter 11.

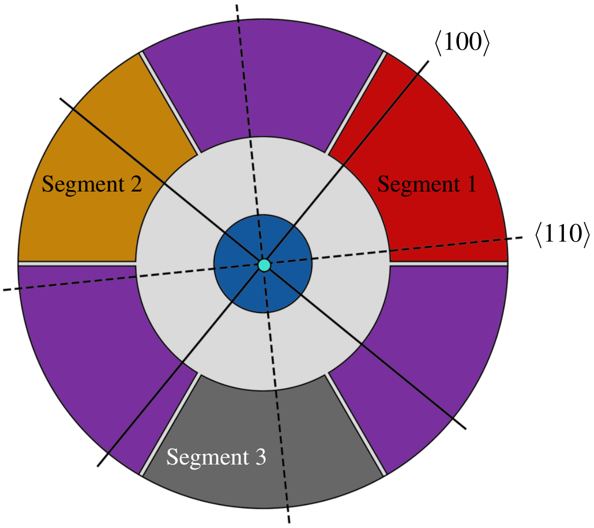

Figure 12.3: Top view of the scan point used to measure the longitudinal charge-carrier drift along the [001] axis. The solid and dashed black lines indicate the locations of the horizontal ⟨100⟩ and ⟨110⟩ axes, respectively.

Figure 12.4 depicts the Compton superpulses at $r = 0\,\mathrm{mm}$ for a detector temperature of 77.9 K. The trend predicted by the simulation in Fig. 12.2 is clearly observed in the data. However, the measured pulses are significantly longer than the simulated pulses. An additional feature observed in the data is that the pulses are not as evenly spread out in time as predicted by the simulation. This is due to the finite position resolution of the z-reconstruction and the limited number of two-hit events used as reference in the similarity cuts, which cause the superpulses to be representative of a z-value up to 1 mm different from the targeted z-value.

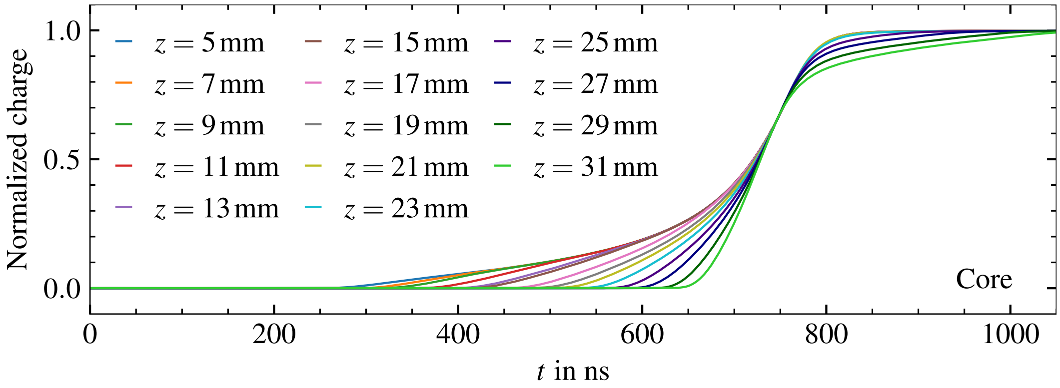

Figure 12.4: Measured core superpulses from events at $r = 0\,\mathrm{mm}$ and targeted z as given in the legend at a detector temperature of $T = 77.9\,\mathrm{K}$. The pulses are time-aligned to 65% of their amplitude.

12.1.2 Extraction of mobility parameters from pulses

Mobility parameters for the longitudinal drift along the [001] direction for electric field strengths of 400 V/cm $\lesssim \mathcal{E} \lesssim$ 1700 V/cm were extracted from the measured pulses shown in Fig. 12.4. The longitudinal drift velocities $v_{L,e}^{100}$ and $v_{L,h}^{100}$ were parameterized according to Eq. (4.2). For the electric field strengths tested here, the Gunn effect for electrons can be neglected. Thus, μ_n was set to zero.

The fit was built with six mobility parameters, i.e. μ_0, $\mathcal{E}_0$ and β for electrons and for holes. As the actual z can vary from the targeted z, additional nuisance parameters were added, allowing for variations around the targeted z of up to 2 mm. The fit routine adjusted the mobility parameters by minimizing the global χ^2/ndf between the simulated and the measured pulses in the rise-time window of 0.5 to 95%. The best-fit results for the mobility parameters are listed in Tab. 12.1 and shown in Fig. 12.6.

Simulated pulses based on these mobility values are compared to selected Compton superpulses in Fig. 12.5. The simulated pulses agree extremely well with the measured pulses throughout the whole pulse length. The largest deviations of up to 1.5% are seen right after the sharp rise, which is associated with the final upward drift of the holes at the highest electric field of $\mathcal{E} \approx$ 1700 V/cm. These deviations are reproducible for $z \leq$ 19 mm. The shape of the deviations implies that the bandwidth of the preamplifier read-out is slightly better than what is suggested by the core response function. The observed deviations could also be explained by small inaccuracies in the differential cross-talk matrix or in the electric field close to the core contact. However, the deviation has no influence on the result.

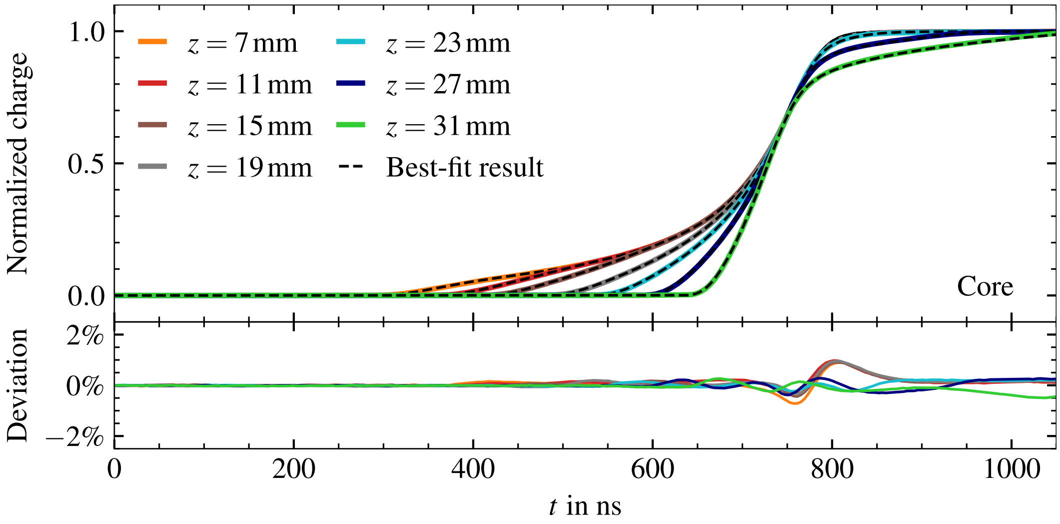

Figure 12.5: Comparison of simulated pulses based (dashed) on the best-fit result for the charge-carrier drift along the [001] direction listed in Tab. 12.1 to selected measured pulses (solid) from Fig. 12.4. Also shown are deviations as simulated minus the measured pulses.

Table 12.1: Best-fit values for the mobility parameters in Eq. (4.2) for electrons and holes along the [001]-direction for $400\,\mathrm{V/cm} \lesssim \mathcal{E} \lesssim 1700\,\mathrm{V/cm}$ determined for $T = 77.9\,\mathrm{K}$.

Charge carrier	Axis	μ_0 in $\frac{\mathrm{cm}^2}{\mathrm{Vs}}$	$\mathcal{E}_0$ in $\frac{\mathrm{V}}{\mathrm{cm}}$	β
Electrons	[001]	37511	507	0.805
Holes	[001]	56804	210	0.704

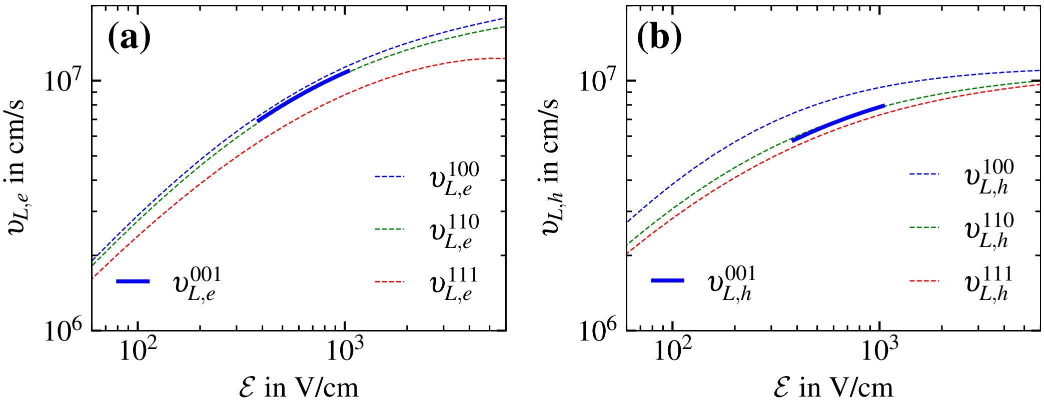

Figure 12.6: Longitudinal (a) electron- and (b) hole-drift velocity as a function of $\mathcal{E}$ along the [001] direction as determined from data (solid), in comparison to the curves obtained from the literature values [135] listed in Tab. 4.1 (dashed).

The drift velocities along the vertical [001] axis and along the $\langle 100 \rangle$ axis should be identical, as the two axes are equivalent by symmetry. The mobility parameters along the [001] axis obtained from fits to the Compton superpulses result in 4% slower electrons and 20% slower holes compared to what would be predicted by the literature values for the $\langle 100 \rangle$ axis listed in Tab. 4.1.

The drift velocities are extracted with uncertainties of approximately 1%. However, the conversion of drift velocities to mobility parameters requires dividing by $\mathcal{E}$. Any systematic uncertainty on $\mathcal{E}$ directly translates into a systematic uncertainty on the mobility parameters. If the true electric field strength, $\mathcal{E}$, would be a factor κ higher than the electric field strength, $\mathcal{E}_{\mathrm{sim}}$, assumed in the simulation, i.e. $\mathcal{E} = \kappa\mathcal{E}_{\mathrm{sim}}$, Eq. (4.2) is invariant under the following transformation:

$$\mu_0 = \mu_{0,\mathrm{sim}}/\kappa, \quad \mathcal{E}_0 = \kappa\mathcal{E}_{0,\mathrm{sim}}, \quad \beta = \beta_{\mathrm{sim}} \quad \text{and} \quad \mu_n = \mu_{n,\mathrm{sim}}/\kappa \tag{12.1}$$

However, the electron- and hole-drift velocities were determined in the same region of the detector. Thus, a 5% inaccuracy in the electric field might explain the deviation for the electrons, but not for the holes. In addition, the uncertainty on the electric field along the vertical [001] axis shown in Fig. 8.12b is too small to explain the deviations depicted in Fig. 12.6.

12.1.3 Temperature dependence determined from the vertical drift

The temperature dependence of the longitudinal drift mobilities along the [001] direction was studied by retaking the measurement presented in section 12.1.1 for different temperatures in the range between 77 K and 99 K, see Tab. 12.2. The mobility parameters were determined by fitting simulated pulses to the selected Compton superpulses at the same z locations as shown in Fig. 12.5.

Figure 12.7 depicts the resulting longitudinal electron and hole drift velocities along the [001] axis at the reference electric field strength of $\mathcal{E} = 500\,\text{V/cm}$. The electron-drift velocities are on average $(23.2 \pm 0.8)\%$ higher than the hole-drift velocities.

Table 12.2: Different Compton Scanner data sets: K2 controlling temperature, T_{CT}, detector temperature, T, and bias voltage, V_B, applied to the core contact. Uncertainties on the temperatures are $\Delta T = \pm 0.7\,\text{K}$.

Scan set	T_{CT} in °C	T in K	V_B in V
V78	−201.4	77.9	−3000
V80	−199.6	80.2	−3000
V83	−196.6	83.3	−3000
V87	−193.6	86.9	−3000
V89	−191.6	89.3	−3000
V95	−186.6	94.8	−3000
V98	−183.6	98.1	−3000

The electron- and hole-drift velocities decrease with increasing temperature. Fitting a power-law to the measured drift velocities, the temperature dependence at $\mathcal{E} = 500\,\text{V/cm}$ is $v_{L,e}^{100} \propto T^{-0.52}$ for the electrons and $v_{L,h}^{100} \propto T^{-0.53}$ for the holes. This T-dependence is significantly less pronounced than the expectation for scattering off acoustic phonons, see section 4.3, i.e. the theoretical prediction of $\mu_A \propto T^{-3/2}$ or the previously measured dependencies of $\mu_e \propto T^{-1.68}$ for electrons and $\mu_h \propto T^{-2.40}$ for holes [167–170].

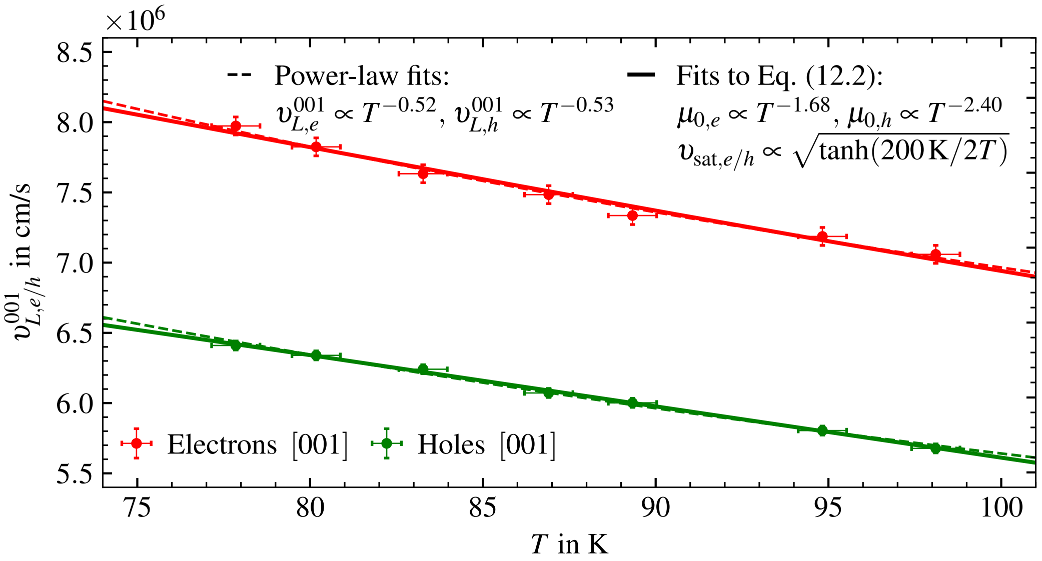

Figure 12.7: Temperature dependence of the electron and hole drift velocity along the [001] direction, determined from Compton superpulses taken at the temperatures T listed in Tab. 12.2 and evaluated at $\mathcal{E} = 500\,\text{V/cm}$. The lines depict fits of a power-law (dashed) and of the expressions in Eq. (12.2) (solid) to the data.

The difference between the temperature dependence of $\upsilon_{L,e/h}^{100}$ measured for this thesis and for previous publications at low electric field strengths is related to the saturation of the drift velocities at high electric fields. For $\mathcal{E} \lesssim 100\,\mathrm{V/cm}$, the drift velocities increase linearly with the electric field strength and the temperature dependence of the drift velocities is defined exclusively by the temperature dependence of $\mu_0 \propto T^{-p}$, i.e. $\upsilon_{L,e/h}^{100} \propto T^{-p}$. However, the electric field strengths in the p-type segBEGe detector are significantly higher, resulting in the drift velocities approaching saturation. In this case, the temperature dependence of the drift velocities is defined by an interplay between the T-dependence of μ_0 and of $\upsilon_{\mathrm{sat}} = \mu_0\mathcal{E}_0$.

Under the assumption that acoustic phonons are the dominant scattering centers and the temperature dependence of μ_0 in the linear region is approximately a power-law, e.g. $\mu_A \propto T^{-3/2}$ [161], this implies that υ_{sat} depends significantly less on T than μ_0. This is in agreement with previous findings [152].

In 1987, M.A. Omar and L. Reggiani [170] proposed the following parameterizations for the temperature dependence of μ_0 and of υ_{sat}, i.e.

$$\mu_0(T) = A \cdot T^{-p} \qquad\qquad \upsilon_{\mathrm{sat}}(T) = \mu_0(T)\mathcal{E}_0(T) = B \cdot \sqrt{\tanh(\theta/2T)}\,, \qquad (12.2)$$

where the values of $p = 1.68$ for electrons, $p = 2.40$ for holes and $\theta = 200\,\mathrm{K}$ were determined from data in the temperature range from 130 K to 300 K. The parameter A defines the absolute values of the low-field mobility μ_0, whereas the parameter B is a measure for the maximal saturation-drift velocity reached in the limit $T \to 0\,\mathrm{K}$.

Table 12.3: Best-fit results for the parameters A and B in Eq. (12.2) in the temperature range from 77 K to 99 K as extracted from the measured drift velocities evaluated at $\mathcal{E} = 500\,\mathrm{V/cm}$ shown in Fig. 12.7.

		A	B
Electrons	[001]	$2.741 \cdot 10^{6}\,\mathrm{K}^{1.68}\,\mathrm{cm^2/Vs}$	$11.38 \cdot 10^{6}\,\mathrm{cm/s}$
Holes	[001]	$8.672 \cdot 10^{7}\,\mathrm{K}^{2.40}\,\mathrm{cm^2/Vs}$	$8.43 \cdot 10^{6}\,\mathrm{cm/s}$

The parameters A and B were determined from a fit of Eq. (12.2) to the measured drift velocities, fixing $p = 1.68$ and $\beta = 0.805$ for electrons, $p = 2.40$ and $\beta = 0.704$ for holes and $\theta = 200\,\mathrm{K}$. The fit results are listed in Tab. 12.3. The resulting $\upsilon_{L,e/h}^{001}(\mathcal{E})$-dependence shows a similarly good agreement with the data than the fits based on a power-law, see Fig. 12.7.

The p-type segBEGe detector could not be operated stably at temperatures below 77 K due to the limited cooling power of the K2 cryostat, or above 100 K due to high leakage currents. This temperature range is not large enough to make accurate predictions for lower or higher temperatures. However, the expressions in Eq. (12.2) result in an upper bound on $\upsilon_{L,e}^{100}$ and $\upsilon_{L,h}^{100}$ at low T which would provide an explanation for the Boltzmann-like temperature dependence of rise times observed in an n-type coaxial germanium detector over a temperature range from 77 K to 130 K [35].

12.2 Longitudinal anisotropy between the $\langle 100 \rangle$ and $\langle 110 \rangle$ axes

The analysis in section 12.1 is limited to longitudinal drifts along the [001] axis and does not allow to study anisotropic effects and their temperature dependence. For this, events with drifts along the $\langle 100 \rangle$ and $\langle 110 \rangle$ axes have to be used.

At $z = 21.5\,\mathrm{mm}$, the electric field in the outer part of the detector points radially inwards. Thus, for events at $z = 21.5\,\mathrm{mm}$ and $r > 20\,\mathrm{mm}$, the first part of the hole drift and the whole electron drift is horizontal, see Fig. 12.8, i.e. along the $\langle 100 \rangle$ axis at $\varphi = 50.8°$ and along the $\langle 110 \rangle$ axis at $\varphi = 5.8°$. Here, events close to the mantle surface have the longest hole drift. The hole drift becomes shorter and the electron drift longer with decreasing r. The final part of the hole drift at $r < 20\,\mathrm{mm}$ is identical for all events.

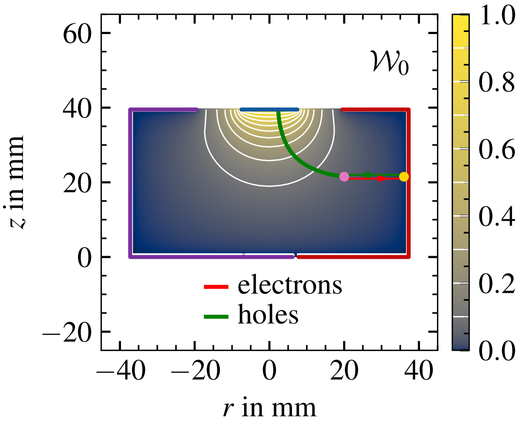

Figure 12.8: Electron and hole drift paths for two events at $z = 21.5\,\mathrm{mm}$ as simulated with SSD. Lines depict the inward hole drift for the event at $r = 36\,\mathrm{mm}$ (gold) and the outward electron drift for the event at $r = 20\,\mathrm{mm}$ (pink). Also shown is the weighting potential $\mathcal{W}_0$ of the core contact.

The corresponding core pulses are shown in Fig. 12.9. The longest pulse is obtained for the event at $r = 36\,\mathrm{mm}$, which is dominated by the hole drift. With decreasing r, the shorter hole drift and the simultaneous contribution from the outward electron drift result in shorter pulses and steeper slopes at the beginning of the pulse. The sharp rises at the end of the pulses are identical for all events because all the hole drift paths are identical at the end and because the electrons are collected before the holes reach the vicinity of the core contact.

If the pulses are time-aligned at the sharp rise at 65% of their final amplitude, the differences between the pulses from different r represent the electron and hole drift in the horizontal plane. The subtraction of pulses originating at smaller r from the pulse originating at $r = 36\,\mathrm{mm}$ is depicted in Fig. 12.10.

The subtraction results in triangular shapes with increasing lengths and amplitudes for decreasing r. The time at which a triangle leaves the baseline is associated with the charge-carrier creation for the event at $r = 36\,\mathrm{mm}$. The rising slope of the triangle is identical to the rise of the reference pulse at $r = 36\,\mathrm{mm}$, see Fig. 12.10a, due to the inwards drift of the holes. The maximum of each triangle is associated with the time at which the event at smaller r is created. From then on, the hole contribution to the charge pulses is identical and cancels when subtracted. Therefore, the falling slope is exclusively defined by the outward drift of the electrons. At the time, at which the triangle returns to its baseline, the electrons are collected on the segment contact. Therefore, the falling slopes agree if the triangles are time-aligned at the point of return to the baseline, see Fig. 12.10b.

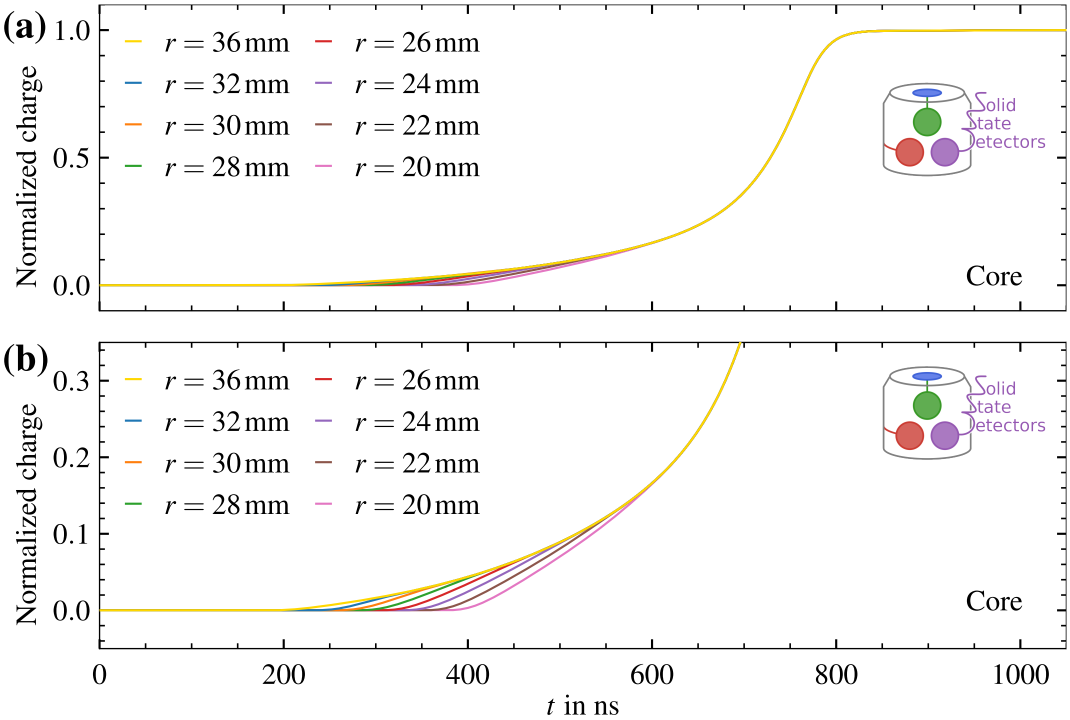

Figure 12.9: Simulated core pulses for events on the ⟨100⟩ axis at $\varphi = 50.8°$, $z = 21.5\,\mathrm{mm}$ and r as given in the legend, using the electric field depicted in Fig. 8.12, the mobility parameters listed in Tab. 4.1 and the hole- and electron-drift models introduced in sections 4.4.1 and 4.4.2.3: (a) full amplitude and (b) zoom-in. The pulses are convolved with the response function of the core contact, normalized and time-aligned to 65% of their amplitude.

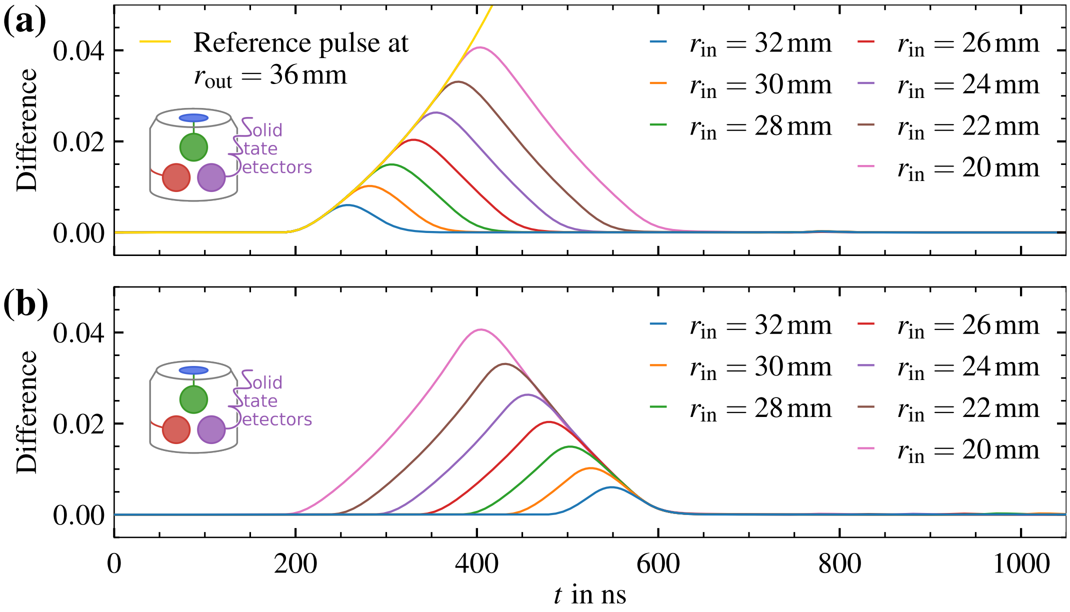

Figure 12.10: Subtraction of pulses as shown in Fig. 12.9 from the core pulse for an event at $r = 36\,\mathrm{mm}$, $\varphi = 50.8°$ and $z = 21.5\,\mathrm{mm}$ (gold). The resulting triangles are time-aligned to 0.005 on (a) the rising slope or (b) the falling slope.

The construction of triangles has the advantage that the change of the drift from inward to upward drift of the holes, which can only be described model-dependently, cancels and only the electron and hole drifts along the horizontal axes contribute. This allows to determine the mobility parameters for $\upsilon_{L,e}^{100}(\mathcal{E})$, $\upsilon_{L,h}^{100}(\mathcal{E})$, $\upsilon_{L,e}^{110}(\mathcal{E})$ and $\upsilon_{L,h}^{110}(\mathcal{E})$ for electric field strengths in the range $470\,\mathrm{V/cm} \lesssim \mathcal{E} \lesssim 620\,\mathrm{V/cm}$.

12.2.1 Data taking and processing

Data was taken in segment 1 on the ⟨110⟩ axis at $\varphi = 5.8°$ and on the ⟨100⟩ axis at $\varphi = 50.8°$, see Fig. 12.11. The measurement times per source position were increased towards the center of the detector to compensate for the loss in acceptance, see section 9.9.

For each source position, Compton superpulses were determined for the targeted z-value of 21.5 mm. Figure 12.12 depicts measured superpulses for this targeted value on the ⟨100⟩ axis for a detector temperature of $T = 77.9\,\mathrm{K}$. The measured pulses follow the predicted trend as shown in Fig. 12.9. However, the Compton superpulses are significantly longer than the simulated pulses.

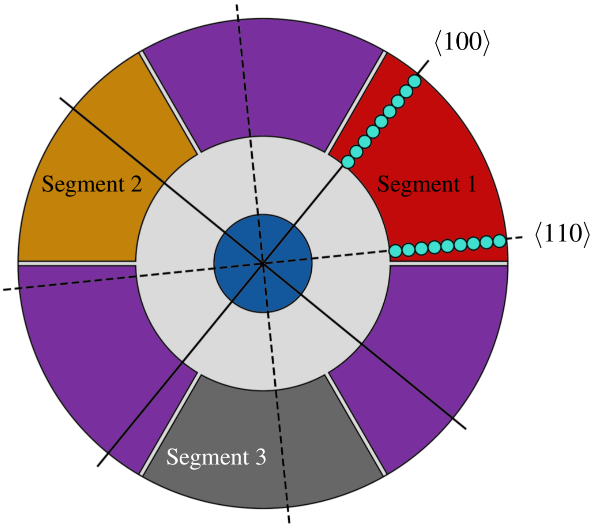

r in mm	20	22	24	26	28
t in min	330	285	250	215	185

r in mm	30	32	34	36
t in min	160	140	120	120

Figure 12.11: Top view of the scan points and a table of the measurement times, t, at the different radii, r, used to measure the horizontal charge-carrier drift. The solid and dashed black lines indicate the locations of the ⟨100⟩ and ⟨110⟩ axes, respectively.

Figure 12.13 depicts the result of the subtraction of pulses originating from smaller r from the reference pulse originating from $r = 36\,\mathrm{mm}$. These differences have similar triangular shapes as predicted by the simulation, see Fig. 12.10. The measured triangles return to a baseline value of zero. This implies that the contribution from the final hole drift from both events is indeed identical and cancels when subtracting the pulses from each other. Similar observations are made for the pulses and triangles extracted from the measurement on the ⟨110⟩ axis, see Figs. 12.14 and 12.15.

The triangles from the ⟨110⟩ axis are slightly longer than from the ⟨100⟩ axis. As the electric field is φ-symmetric, this difference is due to the longitudinal anisotropy of the charge-carrier mobilities, resulting in different longitudinal drift velocities along the ⟨100⟩ and ⟨110⟩ axes.

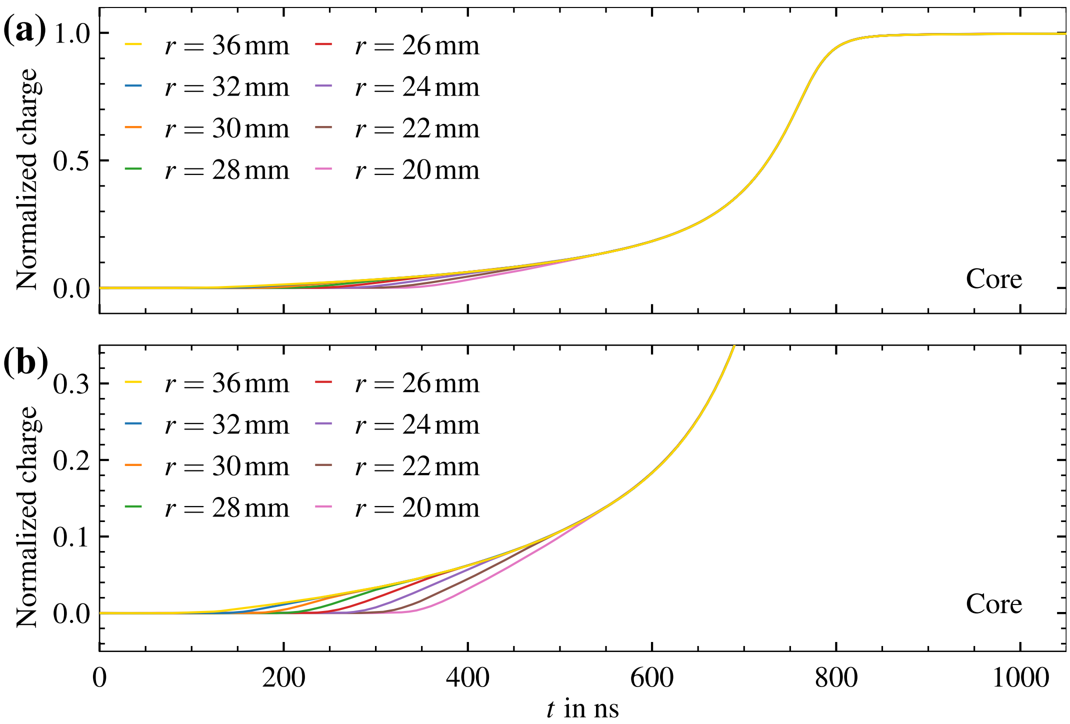

Figure 12.12: Core superpulses from events on the $\langle 100 \rangle$ axis at $\varphi = 50.8^\circ$, targeted $z = 21.5\,\mathrm{mm}$ and r as given in the legend, as measured with the Compton Scanner at a detector temperature of $T = 77.9\,\mathrm{K}$, (a) full amplitude and (b) zoom-in. The pulses are time-aligned to 65% of their amplitude.

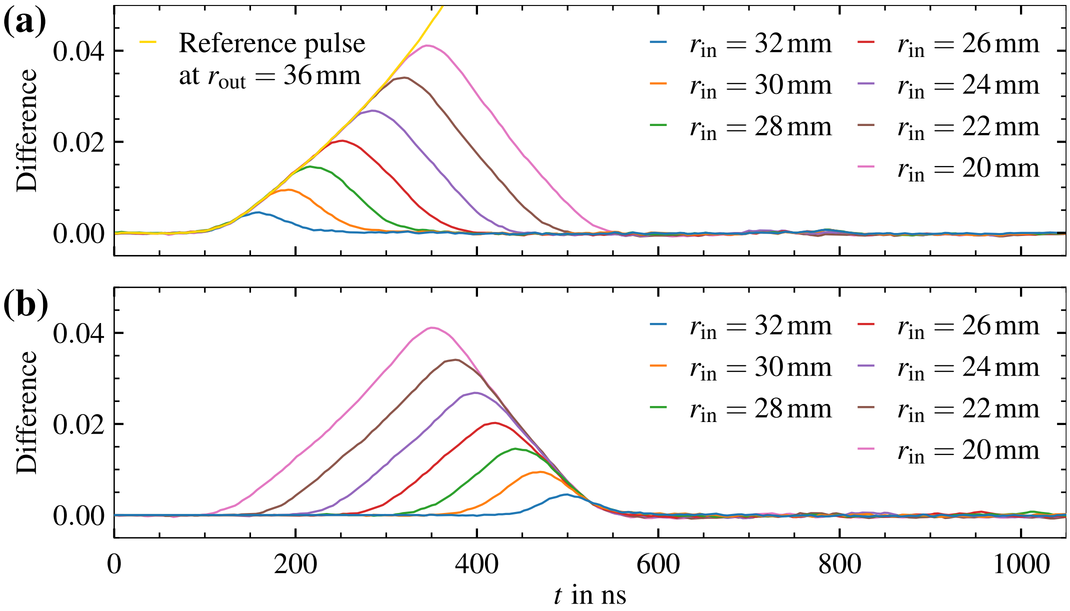

Figure 12.13: Subtraction of pulses on the $\langle 100 \rangle$ axis at $\varphi = 50.8^\circ$ as shown in Fig. 12.12 from the reference core pulse for the event at $r_{\mathrm{out}} = 36\,\mathrm{mm}$, $\varphi = 50.8^\circ$ and a targeted $z = 21.5\,\mathrm{mm}$. The resulting triangles are time-aligned to (a) 0.005 on the rising slope and (b) 0.003 on the falling slope.

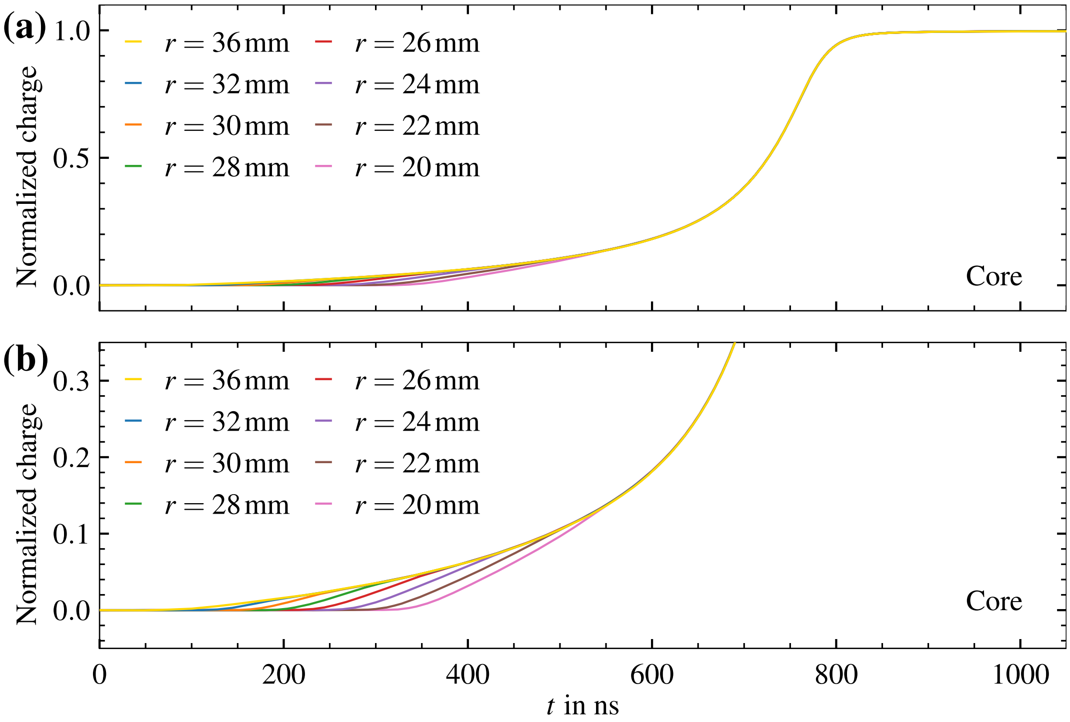

Figure 12.14: Core superpulses from events on the $\langle 110 \rangle$ axis at $\varphi = 5.8°$, targeted $z = 21.5\,\text{mm}$ and r as given in the legend, as measured with the Compton Scanner at a detector temperature of $T = 77.9\,\text{K}$, (a) full amplitude and (b) zoom-in. The pulses are time-aligned to 65% of their amplitude.

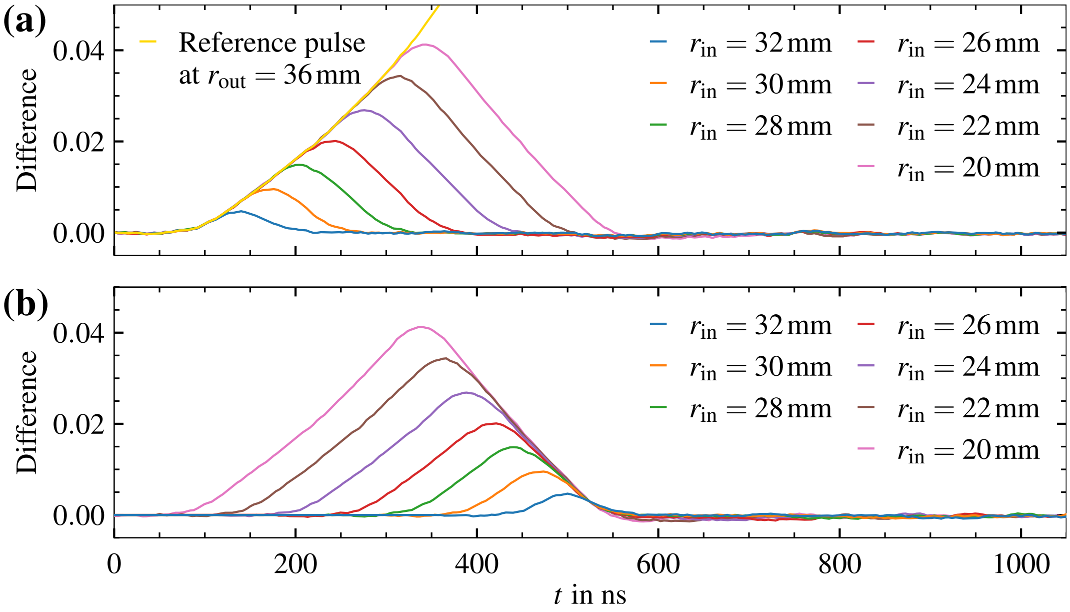

Figure 12.15: Subtraction of pulses on the $\langle 110 \rangle$ axis at $\varphi = 5.8°$ as shown in Fig. 12.14 from the reference core pulse for the event at $r_{\text{out}} = 36\,\text{mm}$, $\varphi = 5.8°$ and a targeted $z = 21.5\,\text{mm}$. The resulting triangles are time-aligned to (a) 0.005 on the rising slope and (b) 0.003 on the falling slope.

12.2.2 Extraction of mobility parameters from triangles

The drift velocities along the $\langle 100\rangle$ and $\langle 110\rangle$ axes were extracted from fits to the measured triangles shown in Figs. 12.13 and 12.15. The longitudinal drift velocities $v_{L,e}^{100}$ and $v_{L,h}^{100}$ were parameterized as in Eq. (4.2) with $\mu_n = 0$. Triangles were simulated as described at the beginning of section 12.2. The hole mobility parameters were extracted from the rising slope and the electron mobility parameters from the falling slope of the triangles.

The electric field strengths probed in this horizontal drift are in the range from 470 V/cm to 620 V/cm with the largest uncertainty of around 5% at the largest r, see Fig. 8.12c. This range of $\mathcal{E}$ is significantly smaller than the range assessed by the vertical [001] drift. It is so restricted that different sets of mobility parameters can result in similar triangles. Stable fits required fixing the values for β. The best-fit results obtained from the vertical drift were inserted for β and only μ_0 and $\mathcal{E}_0$ were free parameters. In addition, μ_0 was restricted to be equal for the $\langle 100\rangle$ and $\langle 110\rangle$ axes to ensure isotropic drift at low $\mathcal{E}$. For each measurement, the value of r was fixed to the source position and the value of z could vary up to ± 1 mm around the targeted z-value of 21.5 mm[*].

The mobility parameters were varied such that the global χ^2/ndf between the simulated and measured triangles above a threshold of 0.005 was minimal. This threshold was chosen to exclude the beginning and the end of the triangles from the fit because they are significantly influenced by differential cross-talk and the limited bandwidth of the preamplifiers. The results for the mobility parameters are listed in Tab. 12.4.

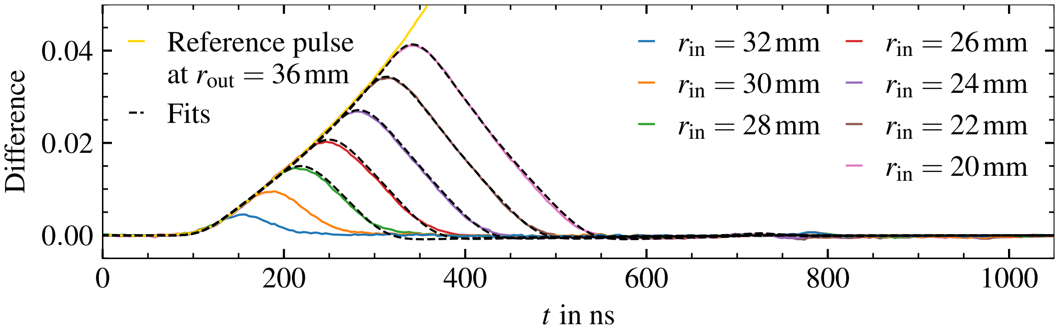

Figure 12.16: Comparison of simulated triangles based on the best-fit result for the charge-carrier drift along the $\langle 100\rangle$ direction to the measured triangles from Fig. 12.13. The measured triangle for $r_{\mathrm{in}} = 32$ mm did not enter the fit because it does not exceed the threshold of 0.005.

In Fig. 12.16, simulated triangles based on these mobility parameters are shown together with the measured triangles. The simulated curves describe the data well for all $r_{\mathrm{in}} \geq 20$ mm. The triangles return to their baseline at zero with a slight undershoot which arises from differential segment-to-core cross-talk.

---

[*] As the statistics were higher for the measurements along the horizontal than for the vertical direction and the z resolution is better for larger r, z was only allowed to vary by ± 1 mm instead of ± 2 mm. The pulses in Figs. 12.12 and 12.14 are quite evenly spread out in time, indicating that the targeted z-value was reached quite accurately.

The simulation predicts a slightly more convex rise than observed in the data. Two possible effects are:

- Outlier pulses passing the similarity cut can alter the beginning of the Compton superpulses, where the similarity cut is the least effective, up to the permille level.
- The largest uncertainty on the electric field of $\approx 5\%$ applies to the region where the triangles were determined, see Fig. 8.12c. The exact electric field might be slightly stronger close to the mantle surface and slightly weaker further inside. This could be due to a radial impurity density slightly less r-dependent as extracted from the capacitance measurements, which is not sensitive to the outermost part of the detector.

Table 12.4: Best-fit values for the mobility parameters in Eq. (4.2) for electrons and holes along the $\langle 100\rangle$ and $\langle 110\rangle$-direction for $470\,\mathrm{V/cm} \lesssim \mathcal{E} \lesssim 620\,\mathrm{V/cm}$ determined for $T = 77.9\,\mathrm{K}$. The β values were input to the fits.

Charge carrier	Axis	μ_0 in $\frac{\mathrm{cm}^2}{\mathrm{Vs}}$	$\mathcal{E}_0$ in $\frac{\mathrm{V}}{\mathrm{cm}}$	β (fixed)
Electrons	$\langle 100\rangle$	37995	504	0.805
	$\langle 110\rangle$	37995	422	0.805
Holes	$\langle 100\rangle$	56542	225	0.704
	$\langle 110\rangle$	56542	213	0.704

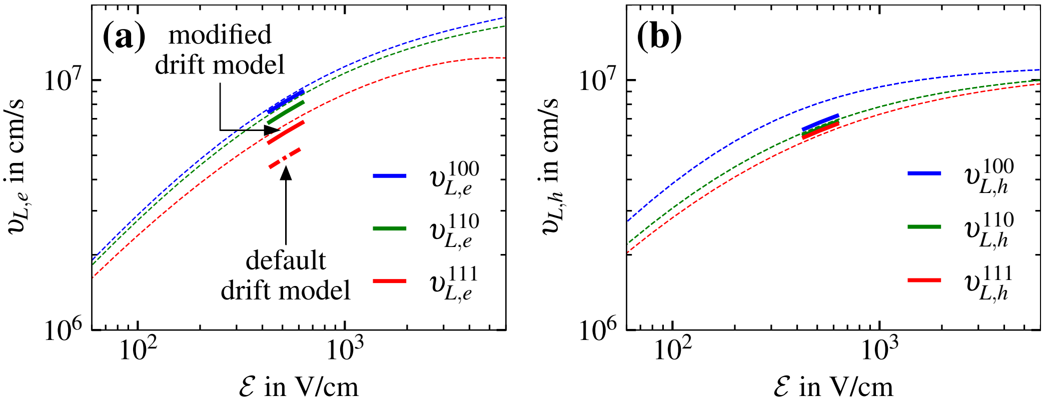

Figure 12.17: Longitudinal (a) electron- and (b) hole-drift velocity as a function of $\mathcal{E}$ along the $\langle 100\rangle$ and $\langle 110\rangle$ direction as determined from data taken at $T = 77.9\,\mathrm{K}$ and for $\langle 111\rangle$ as calculated using the charge drift models introduced in section 4.4 (solid). The electron-drift velocity along the $\langle 111\rangle$ direction was calculated using both the default electron-drift model from section 4.4.2.3 (dash-dotted) and the modified electron-drift model from section 4.4.2.4 (solid). The dashed lines depict the curves obtained from the literature values [135] at $T_0 = 78\,\mathrm{K}$ listed in Tab. 4.1 and shown in Fig. 4.1.

In general, the electrons are 3% slower and the holes are 17% slower than predicted using the literature mobility parameters at $T_0 = 78\,\mathrm{K}$ [135]. The longitudinal anisotropy between the $\langle 100\rangle$ and the $\langle 110\rangle$ axes is defined by the different values of $\mathcal{E}_0$. In the electric field range probed here, the longitudinal anisotropy at $T = 77.9\,\mathrm{K}$ is 10% for the electrons and 6% for the holes.

According to the values in Tab. 4.1, the anisotropy at $\mathcal{E} = 500\,\text{V/cm}$ is predicted to be 5.9% for the electrons and 21.5% for the holes. The longitudinal anisotropy observed here is significantly lower for holes and significantly higher for electrons. This agrees well with past observations [36, 128] of higher-amplitude rise-time oscillations for electrons and lower-amplitude rise-time oscillations for holes compared to the prediction using the literature values.

Using the charge drift models introduced in section 4.4, the drift velocities along the $\langle 111 \rangle$ axis can be calculated from $\upsilon_{L,e/h}^{100}$ and $\upsilon_{L,e/h}^{110}$.

The default electron-drift model predicts $\upsilon_{L,e}^{110} = 0.7858\,\upsilon_{L,e}^{100} + 0.2002\,\upsilon_{L,e}^{111}$, see section 4.4.2.3, i.e. a small anisotropy between the $\langle 100 \rangle$ and $\langle 110 \rangle$ axes and a large anisotropy between these axes and the $\langle 111 \rangle$ axis. The observation of a larger than predicted anisotropy between the $\langle 100 \rangle$ and $\langle 110 \rangle$ axes leads to the prediction of unphysically large anisotropies with respect to the $\langle 111 \rangle$ axis for both other axes, see Fig. 12.17a. Such low mobilities for the $\langle 111 \rangle$ axes have never been observed. This shows that the default electron-drift model does not describe the relation between the drift velocities along the different axes correctly.

The modified electron-drift model introduced in section 4.4.2.4 yield another relation between the drift velocities of $\upsilon_{L,e}^{110} = 0.3860\,\upsilon_{L,e}^{100} + 0.6901\,\upsilon_{L,e}^{111}$. This predicts $\upsilon_{L,e}^{111}$ to be only 6% smaller than the standard literature values compared to 38% for the default model. The literature values are based on measurements along the $\langle 111 \rangle$ axes and a 38% shift is highly unlikely.

The hole-drift model in section 4.4.1 predicts $\upsilon_{L,h}^{110} = \frac{1}{4}\upsilon_{L,h}^{100} + \frac{3}{4}\upsilon_{L,h}^{111}$. Combined with the small hole anisotropy of 6%, $\upsilon_{L,h}^{111}$ is slightly smaller but very similar to $\upsilon_{L,h}^{110}$, see Fig. 12.17b.

12.2.3 Charge-carrier drift between the axes

In the p-type segBEGe detector, the electric field lines are not parallel to a $\langle 111 \rangle$ axis long enough to measure $\upsilon_{L,e/h}^{111}$ and test the different predictions from the two charge-drift models shown in Fig. 12.17a. However, the two charge-drift models were tested by studying charge-carrier drifts between the axes.

An additional radial scan was taken at $T = 77.9\,\text{K}$ on the line bisecting the $\langle 100 \rangle$ and $\langle 110 \rangle$ axes in segment 1, see Fig. 12.18. From the on-axis measurements, mobility parameters for $\upsilon_{L,e/h}^{100}$ and $\upsilon_{L,e/h}^{110}$ were determined from the triangles as presented in section 12.2.2. Triangles were also created from the Compton superpulses taken off-axis, see Fig. 12.19.

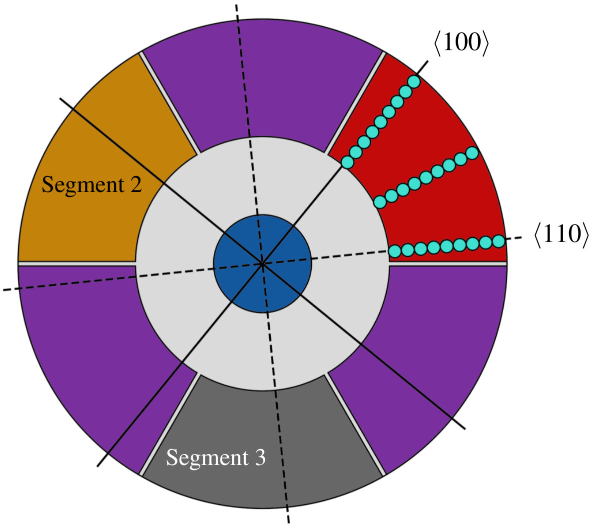

Figure 12.18: Top view of the scan points used to test the charge-drift models. The solid and dashed black lines indicate the locations of the $\langle 100 \rangle$ and $\langle 110 \rangle$ axes, respectively.

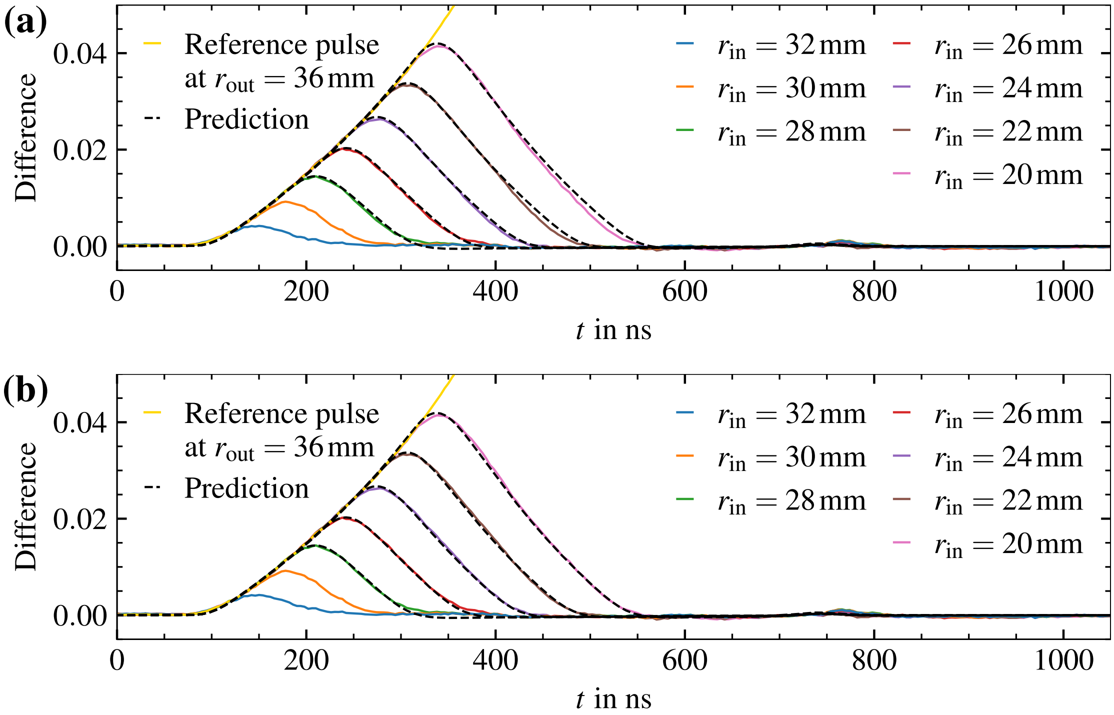

Figure 12.19: Comparison of predictions to measured triangles for drifts between the $\langle 100 \rangle$ and $\langle 110 \rangle$ axes in segment 1. The predictions are based on the best-fit result for the charge-carrier drift along the $\langle 100 \rangle$ and $\langle 110 \rangle$ direction at $T = 77.9\,\text{K}$ listed in Tab. 12.4, the hole-drift model introduced in section 4.4.1 and (a) the default electron-drift model introduced in section 4.4.2.3 and (b) the modified electron-drift model introduced in section 4.4.2.4.

The hole-drift anisotropy is small and the hole-drift between the $\langle 100 \rangle$ and $\langle 110 \rangle$ axis is quasi-longitudinal, i.e. there is almost no transverse anisotropy. Thus, the inner events are expected to follow the hole drift path of the event at $r_{\text{out}} = 36\,\text{mm}$ and the hole contribution cancels when the triangles are extracted by subtraction. Figure 12.19 depicts the measured triangles together with predictions based on the values listed in Tab. 12.4 and the charge-drift models presented in section 4.4.

The rising slopes of the triangles are defined by the horizontal inwards drift of the holes and are very well predicted by the hole-drift model presented in section 4.4.1. This implies that the hole-drift model provides a more accurate description of the small transverse anisotropy of the hole drift for $470\,\text{V/cm} \lesssim \mathcal{E} \lesssim 620\,\text{V/cm}$.

The falling slopes of the triangles are defined by the horizontal outwards drift of the electrons. Figures 12.19a and 12.19b depict simulated triangles using the default and the modified electron-drift model, see sections 4.4.2.3 and 4.4.2.4, respectively. The default electron-drift model underestimates the drift velocity of the electrons between the axes, resulting in slower falling slopes shown in Fig. 12.19a. The modified electron-drift model predicts faster electron drifts between the axes. The falling slopes of the measured triangles are significantly better predicted using the modified electron-drift model. This implies that the modified electron-drift model provides a more accurate description of the electron-drift anisotropy for $470\,\text{V/cm} \lesssim \mathcal{E} \lesssim 620\,\text{V/cm}$.

12.2.4 Temperature dependence determined from the horizontal drift

The determination of the mobility parameters from horizontal drifts was repeated at the same temperatures as for the vertical drift, see Tab. 12.5. The electron- and hole-drift velocities were again evaluated at a reference electric field strength of $\mathcal{E} = 500\,\text{V/cm}$ like in section 12.1.3.

All drift velocities and, thus, mobilities decrease with increasing T. The absolute differences between the electron- and hole-drift mobilities also decrease with the temperature. However, the longitudinal anisotropy between the $\langle 100\rangle$ and $\langle 110\rangle$ axes remains at $(10.0\pm0.5)\%$ for the electrons, while for holes it decreases from $(6.0\pm0.5)\%$ at 77.9 K to $(3.5\pm0.4)\%$ at 98.1 K. The values for the longitudinal anisotropy are in contradiction with the widely used charge-drift mobility values listed in Tab. 4.1, which predict a longitudinal anisotropy of 5.9% for electrons and 21.5% for holes. This is, however, in good agreement with the observations in recent publications [128, 192].

Table 12.5: Different Compton Scanner data sets: K2 controlling temperature, T_{CT}, detector temperature, T, and bias voltage, V_B, applied to the core contact. Uncertainties on the temperatures are $\Delta T = \pm 0.7\,\text{K}$.

Scan set	T_{CT} in °C	T in K	V_B in V
H78	−201.4	77.9	−3000
H80	−199.6	80.2	−3000
H83	−196.6	83.3	−3000
H87	−193.6	86.9	−3000
H89	−191.6	89.3	−3000
H95	−186.6	94.8	−3000
H98	−183.6	98.1	−3000

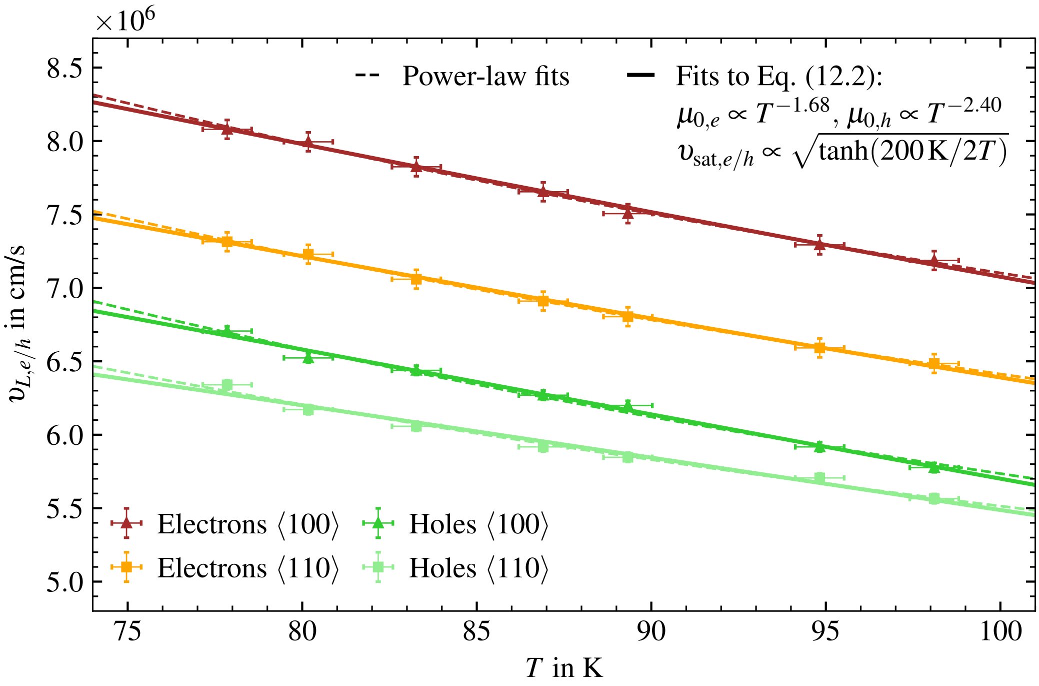

Figure 12.20: Temperature dependence of the electron- and hole-drift velocity along the horizontal $\langle 100\rangle$ and $\langle 110\rangle$ axes in segment 1, determined from Compton superpulses taken at the temperatures T listed in Tab. 12.5 and evaluated at $\mathcal{E} = 500\,\text{V/cm}$. The lines depict fits of a power-law (dashed) and of the expressions given in Eq. (12.2) (solid) to the data.

From a power-law fit to the measured drift velocities, the temperature dependence is determined as $\upsilon_{L,e}^{100} \propto T^{-0.52}$, $\upsilon_{L,e}^{110} \propto T^{-0.53}$, $\upsilon_{L,h}^{100} \propto T^{-0.61}$ and $\upsilon_{L,h}^{110} \propto T^{-0.53}$. The differences between the measured temperature dependencies and the expectation for the low-field mobility μ_0 resulting from scattering off acoustic phonons are again attributed to the onset of saturation effects below $\mathcal{E} = 500\,\mathrm{V/cm}$, see section 12.1.3.

Table 12.6: Best-fit results for the parameters A and B in Eq. (12.2) in the temperature range from 77 K to 99 K as extracted from the measured drift velocities evaluated at $\mathcal{E} = 500\,\mathrm{V/cm}$ shown in Fig. 12.20.

		A	B
Electrons	$\langle 100 \rangle$	$2.757 \cdot 10^6\,\mathrm{K}^{1.68}\,\mathrm{cm}^2/\mathrm{Vs}$	$11.64 \cdot 10^6\,\mathrm{cm/s}$
	$\langle 110 \rangle$	$2.423 \cdot 10^6\,\mathrm{K}^{1.68}\,\mathrm{cm}^2/\mathrm{Vs}$	$10.60 \cdot 10^6\,\mathrm{cm/s}$
Holes	$\langle 100 \rangle$	$6.712 \cdot 10^7\,\mathrm{K}^{2.40}\,\mathrm{cm}^2/\mathrm{Vs}$	$9.15 \cdot 10^6\,\mathrm{cm/s}$
	$\langle 110 \rangle$	$9.387 \cdot 10^7\,\mathrm{K}^{2.40}\,\mathrm{cm}^2/\mathrm{Vs}$	$8.09 \cdot 10^6\,\mathrm{cm/s}$

Figure 12.20 also depicts fits of the expressions in Eq. (12.2) to the measured drift velocities with fixed exponents $p = 1.68$ for electrons and $p = 2.40$ for holes, as well as $\theta = 200\,\mathrm{K}$. The results for the fit parameters are listed in Tab. 12.6.

The parameter A defines the absolute value of the low-field mobility. Under the assumption that the charge-carrier drift is isotropic at low electric field strengths, A should be identical for the $\langle 100 \rangle$ and the $\langle 110 \rangle$ axes. For the electrons, the fit results for A differ only by 12% between the two axes. For the holes, the deviation between the fit results for A for the two axes is more than 40%. In both cases, this reflects the difference in T-dependence of the drift velocities along the $\langle 100 \rangle$ and $\langle 110 \rangle$ axes which is much more pronounced for the holes. The assumption that the drift is isotropic at low $\mathcal{E}$ might not be correct at all T.

The parameter B defines the maximal saturation drift velocities in the limit $T \to 0\,\mathrm{K}$. For electrons, the values on the $\langle 100 \rangle$ axis is 10% higher than on the $\langle 110 \rangle$ axis. This is in good agreement with the observed longitudinal anisotropy of the electron drift of 10% between the $\langle 100 \rangle$ and $\langle 110 \rangle$ axes. For the holes, the fit results for B differ by 13%, which is significantly higher than the observed longitudinal anisotropy of the hole drift of between 3.5 and 6%. This is because, in the fit, the values for B partly compensate for the anisotropy in μ_0 as indicated by different values for A. The fit results listed in Tab. 12.6 describe the observed temperature dependencies for temperatures from 77 K to 99 K quite well. However, the resulting functional dependencies should be handled with care when extrapolating to higher or lower temperatures.

12.3 Final results on charge-carrier mobilities

Figure 12.21 depicts the measured electron- and drift velocities from the vertical and horizontal drifts at the reference electric field strength of $\mathcal{E} = 500\,\text{V/cm}$. The vertical [001] axis and the horizontal $\langle 100 \rangle$ axes are equivalent by symmetry. Therefore, $\upsilon_{L,e/h}^{001}$ and $\upsilon_{L,e/h}^{100}$ should be identical. However, throughout the whole temperature range from 77 K to 99 K, the values of $\upsilon_{L,e/h}^{100}$ extracted at $\mathcal{E} = 500\,\text{V/cm}$ are $(2.8 \pm 0.8)\%$ and $(2.0 \pm 0.5)\%$ higher for electrons and holes, respectively.

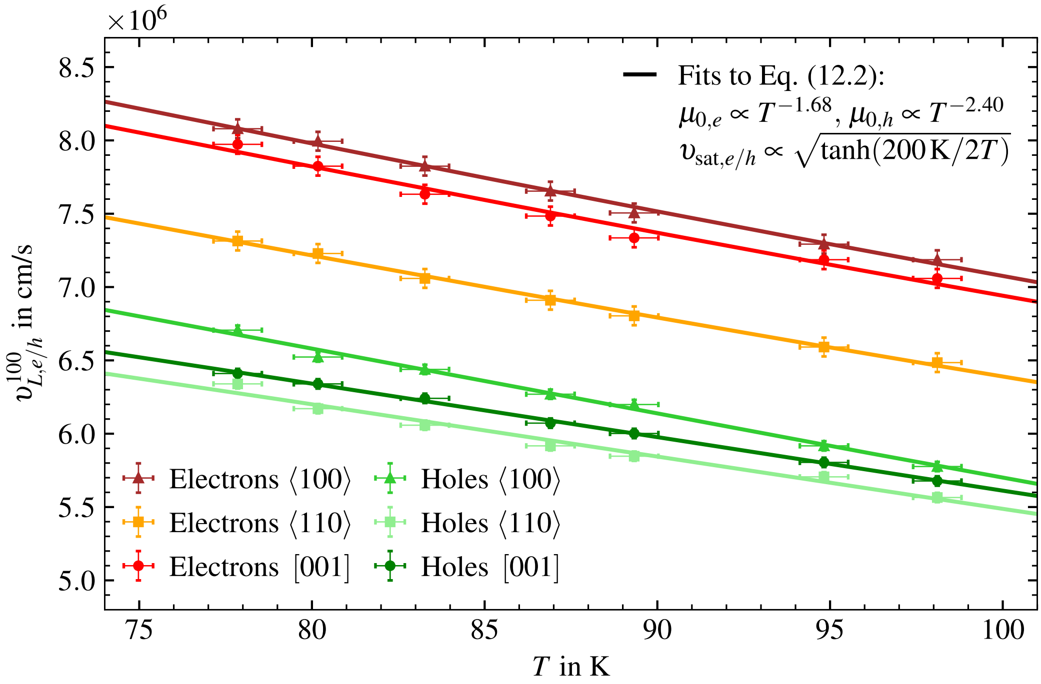

Figure 12.21: Temperature dependence of electron- and hole-drift velocities along the horizontal $\langle 100 \rangle$ and $\langle 110 \rangle$ axes in segment 1 and the vertical [001] axis in segment 4 at the temperatures T listed in Tab. 12.5 and evaluated at $\mathcal{E} = 500\,\text{V/cm}$. The solid lines depict fits of the expressions given in Eq. (12.2) to the data.

In the outer region, where the horizontal drift was measured, the electric field strength has its highest uncertainty of up to 5%. This is significantly higher than the uncertainties on the drift velocities extracted from the triangles of approximately 1%. Therefore, the systematic uncertainty on the mobility parameters results mostly from the systematic uncertainty on $\mathcal{E}$, see Eq. (12.1).

Table 12.7 summarizes the mobility parameters as extracted from the vertical [001] drift and the horizontal $\langle 100 \rangle$ drift. For the electrons, the values of $\mathcal{E}_0$ are almost identical for the [001] and $\langle 100 \rangle$ axes, but the value of μ_0 is noticeably smaller, resulting in smaller values for $\upsilon_{L,e}^{001}$ compared to $\upsilon_{L,e}^{100}$. For the holes, μ_0 is slightly higher but $\mathcal{E}_0$ is significantly lower for the vertical [001] drift compared to the horizontal $\langle 100 \rangle$ drift. In combination, this also yields smaller values for $\upsilon_{L,h}^{001}$ compared to $\upsilon_{L,h}^{100}$ for the holes.

In the temperature range from 77 K to 99 K, the electrons drift $(22.2 \pm 1.4)\%$ faster on the horizontal $\langle 100 \rangle$ axis than the holes. This agrees well with the $(23.2 \pm 0.8)\%$ determined from the vertical [001] drift, see section 12.1.3.

Table 12.7: Best-fit values for the mobility parameters in Eq. (4.2) for electrons and holes along the [001] and the $\langle 100 \rangle$ direction, determined for $T = 77.9\,\mathrm{K}$.

Charge carrier	Axis	μ_0 in $\frac{\mathrm{cm}^2}{\mathrm{Vs}}$	$\mathcal{E}_0$ in $\frac{\mathrm{V}}{\mathrm{cm}}$	β (fixed)
Electrons	[001]	37511	507	0.805
	$\langle 100 \rangle$	37995	504	0.805
Holes	[001]	56804	210	0.704
	$\langle 100 \rangle$	56542	225	0.704

The difference in absolute values along the $\langle 100 \rangle$ axis can have multiple origins:

- The model for differential segment-to-core cross-talk in the simulation could be inaccurate. However, different values for the differential cross-talk from segment 4 to the core could only improve the agreement for one type of charge carrier by worsening it for the other. Thus, any adjustment of the cross-talk model would not improve the agreement.
- The dead-layer thickness of the segments was set to 0.75 mm in the simulation, as determined from a radial scan at the mantle surface of the detector, see section 9.6.1. A different dead-layer thickness at the bottom of the detector would have an influence on the strength of the upward electric field. However, the region along the vertical [001] axis, at which $\mathcal{E} = 500\,\mathrm{V/cm}$, is not significantly influenced by variations in the dead-layer thickness of up to 0.5 mm, see section 8.6. Significantly higher variations in the dead-layer thickness are technically not possible.
- In all impurity density fits, a linear increase in impurity density from the bottom to the top of the detector of 12.1% was assumed. A deviation from this z-gradient would influence the electric field, mostly in the center and partly close to the mantle surface. However, the deviation required to fully explain the discrepancy between $v_{L,e}^{001}$ and $v_{L,e}^{100}$ would be so significant that the excellent agreement in the capacitances and depletion images between measurement and simulation would be lost.
- The uncertainties on the electric field strengths obtained from capacitance measurements allow for deviations in the outer part of the detector of up to 5%, see Fig. 8.12c. It is likely that the electric field strengths for the horizontal drifts are underestimated in the simulation and that the data shown in Fig. 12.21 was taken at a slightly higher electric field strength than 500 V/cm.

As the best-fit result for the electric field from the capacitance measurement has a smaller systematic uncertainty along the vertical [001] axis than for the horizontal $\langle 100 \rangle$ axis, see Fig. 8.12, the absolute values of the mobility parameters along the [001] direction are considered as the final result for these axes.

As there is no φ-dependence in $\mathcal{E}(\vec{r})$, the radial profile of the electric field on the $\langle 100 \rangle$ and $\langle 110 \rangle$ axis in segment 1 is identical. Thus, the velocities extracted for the $\langle 110 \rangle$ axis should be scaled down by the same factor as observed for the $\langle 100 \rangle$ axis. The mobilities extracted are listed in Tab. 12.8 and depicted in Fig. 12.22.

Table 12.8: Final results on the mobility parameters in Eq. (4.2) for electrons and holes for $T = 77.9\,\mathrm{K}$.. Values for the [001] axis are taken from Tab. 12.1, whereas values for the $\langle 110\rangle^*$ axis were determined by scaling $\upsilon^{110}_{L,e/h}$ by the same factor needed for $\upsilon^{100}_{L,e/h}$ to match $\upsilon^{001}_{L,e/h}$ and repeating the fit to the triangles presented in chapter 12.

Charge carrier	Axis	μ_0 in $\frac{\mathrm{cm}^2}{\mathrm{Vs}}$	$\mathcal{E}_0$ in $\frac{\mathrm{V}}{\mathrm{cm}}$	β
Electrons	[001]	37511	507	0.805
	$\langle 110\rangle^*$	37511	425	0.805
Holes	[001]	56804	210	0.704
	$\langle 110\rangle^*$	56804	196	0.704

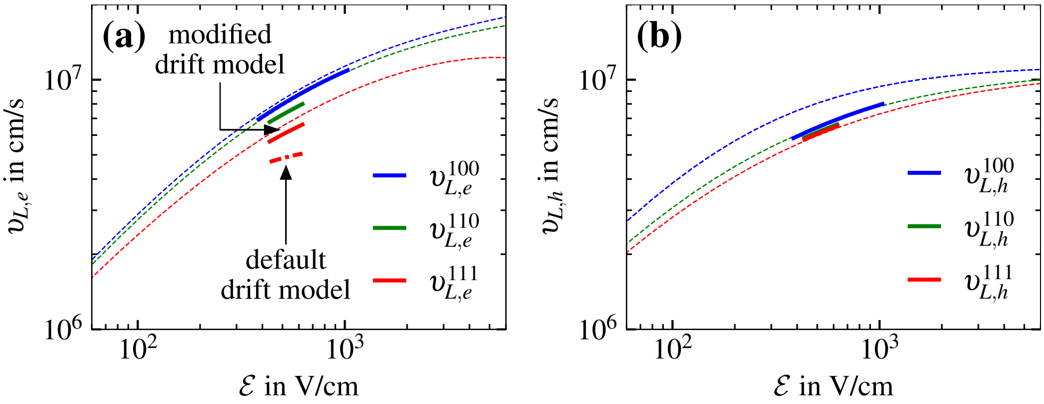

Figure 12.22: Longitudinal (a) electron- and (b) hole-drift velocity as a function of $\mathcal{E}$ along the $\langle 100\rangle$ and $\langle 110\rangle$ direction as calculated using the mobility parameters in Tab. 12.8 and the charge drift models introduced in section 4.4 (solid). The electron-drift velocity along the $\langle 111\rangle$ direction was calculated using both the default electron-drift model from section 4.4.2.3 (dash-dotted) and the modified electron-drift model from section 4.4.2.4 (solid). The dashed lines depict the curves obtained from the literature values [135] at $T_0 = 78\,\mathrm{K}$ listed in Tab. 4.1 and shown in Fig. 4.1.

12.4 Final comparison of simulated to measured superpulses

The final results on the mobility parameters were tested using the pulse shape library collected with the Compton Scanner on the $\langle 110\rangle$ axis in segment 3 at $\varphi = 275.8°$, see section 11.4. The distributions of $5-95\%$ rise times and A_0/E_0 as determined from the core pulses are shown in Fig. 12.23a. Also shown are predictions for these distributions based on the mobility parameters listed in Tab. 12.8 and using the default and modified electron-drift model in Figs. 12.23b and 12.23c, respectively. The general trend and the absolute values of the rise times and A_0/E_0 values are well described using either the default or the modified electron-drift model. However, significant differences are observed for the vicinity of the core contact.

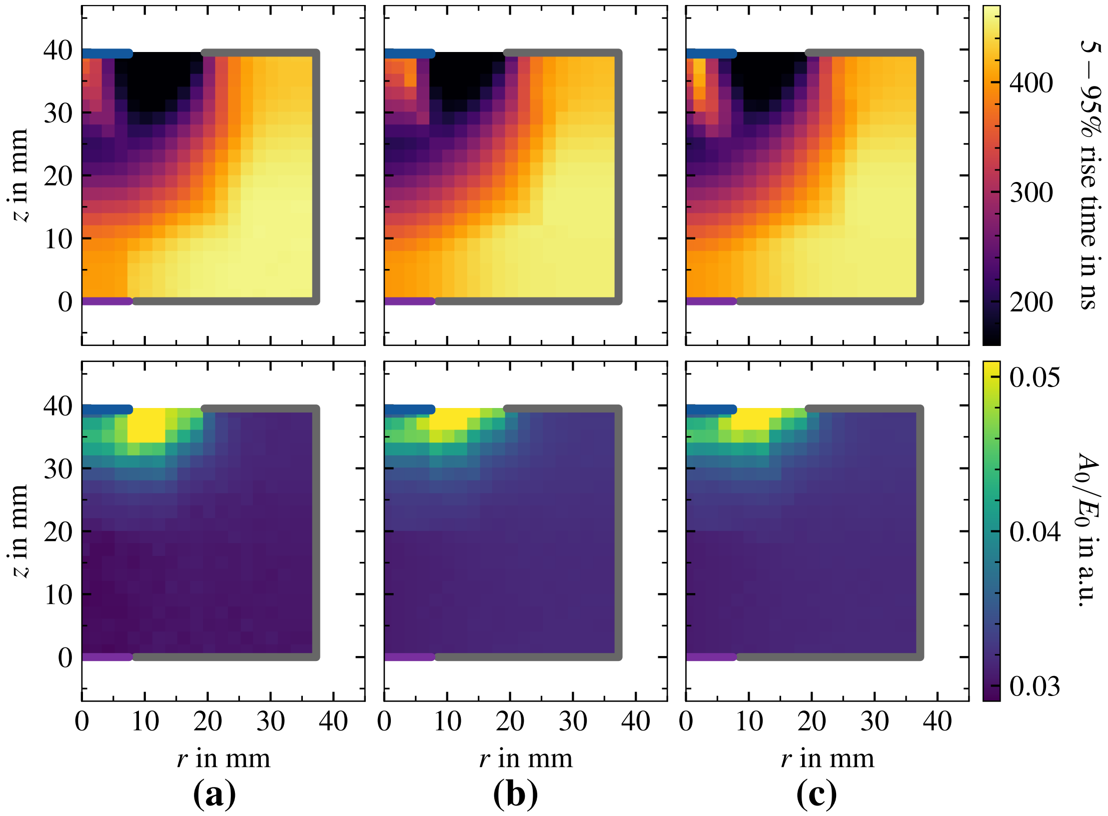

Figure 12.23: (Top) $5-95\%$ rise times and (bottom) A_0/E_0 for the $\langle 110 \rangle$ axis in segment 3 at $\varphi = 275.8^\circ$, as determined for the core contact (a) from the superpulses in the pulse shape library obtained from Compton Scanner data at $T_0 = 78\,\mathrm{K}$, and simulated with SSD using the electric field resulting from the capacitance measurements, see Fig. 8.12, using the mobility values listed in Tab. 12.8 and (b) the default electron-drift model from section 4.4.2.3 and (c) the modified electron-drift model from section 4.4.2.4.

Figure 12.24 shows the relative deviation of the simulated values from the data. In the lower and outer parts of the detector, the average $5-95\%$ rise time and A_0/E_0 values extracted from the core pulses are both well predicted by the simulation. For events in these regions, the weighting potential of the core contact is weak and the electrons are collected on the segments before the holes reach the vicinity of the core contact. Thus, the contribution of the electron drift to the core pulses is too small to noticeably influence the rise time or the A_0/E_0 values. The good agreement between simulation and data implies that the hole drift is accurately described by the hole mobility parameters in Tab. 12.8 and the hole-drift model presented in section 4.4.1.

The rise time values for events originating in the vicinity of the core contact are not so well predicted by either of the two electron-drift models. For the default electron-drift model, the core rise times at $r = 4\,\mathrm{mm}$ and $r = 6\,\mathrm{mm}$ are up to 58% higher than the data. Using the modified electron-drift model, the maximum deviation is 36% at $r = 6\,\mathrm{mm}$ and $z = 33\,\mathrm{mm}$, see Figs. 12.24a and 12.24b.

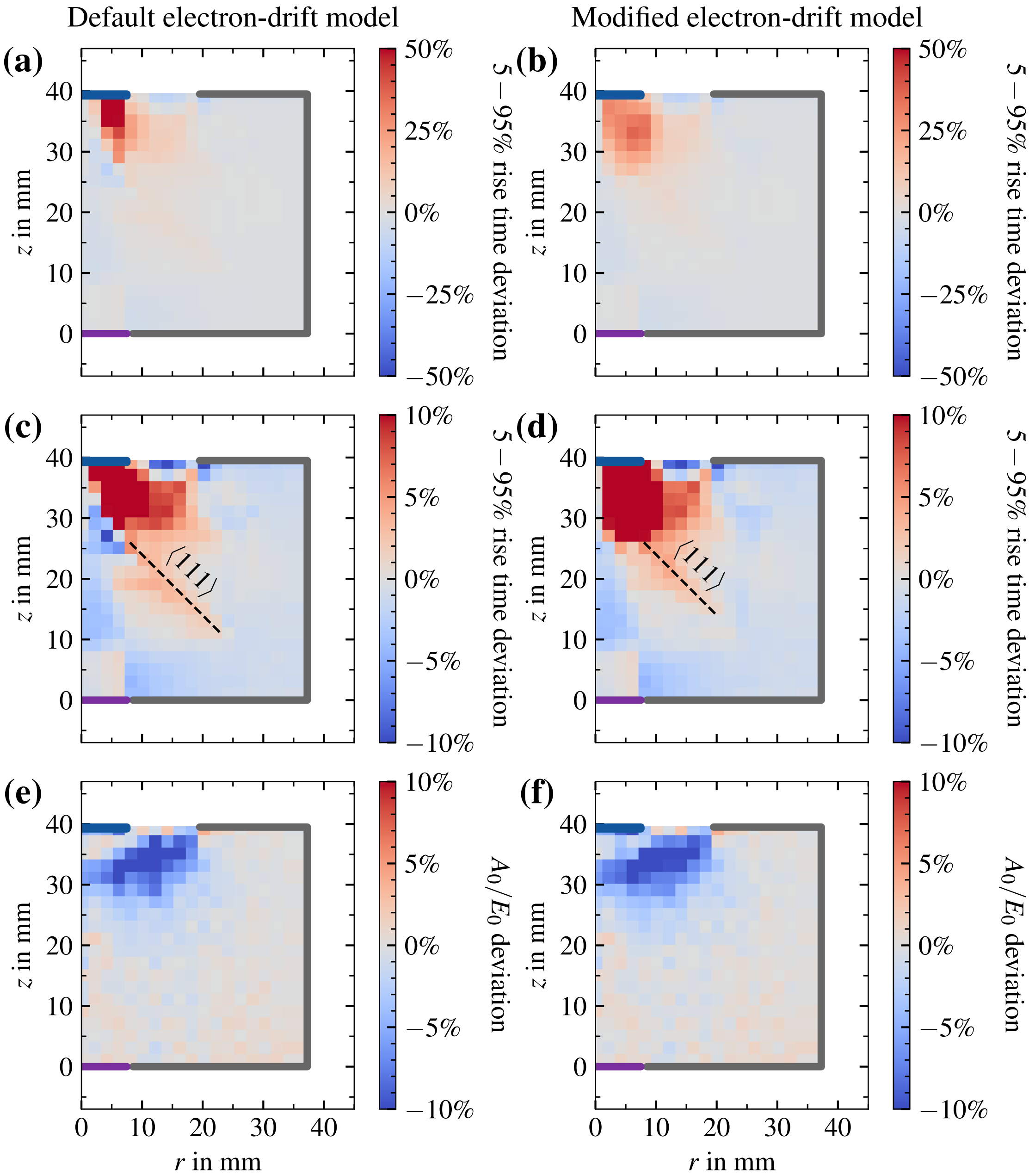

Figure 12.24: Relative deviation of the predicted (top) 5 − 95% rise time and (bottom) A_0/E_0 values using the final results on the mobility parameters listed in Tab. 4.1 and (left) the default and (right) the modified electron-drift model, with respect to the measured values. The distributions in the top and middle rows are identical shown with different color bar limits.

In Figs. 12.24c and 12.24d, the color bar limits are adjusted to reveal a diagonal line parallel to a $\langle 111 \rangle$ axis where the simulation predicts 5% longer rise times than measured. The electrons in these events are predicted to drift parallel to this $\langle 111 \rangle$ axis. The effect is more pronounced for the default than for the modified electron-drift model. However, $\upsilon_{L,e}^{111}$ seems still to be underestimated by the modified electron-drift model. It is most likely closer to the literature values for the $\langle 111 \rangle$ axis, see Fig. 12.22.

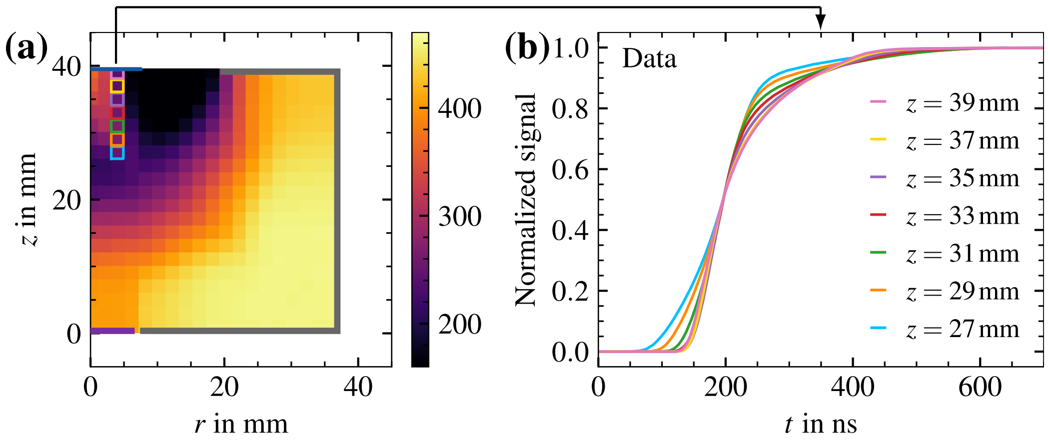

Figure 12.25: (a) $5-95\%$ rise times for the $\langle 110 \rangle$ axis in segment 3 at $\varphi = 275.8^\circ$ as measured in the core contact. (b) Superpulses for events at $r = 4$ mm and a targeted z as given in the legend as constructed from Compton Scanner data, time-aligned to 50% of their amplitude. The boxes in (a) depict the origins of the pulses with the same color as in (b).

The A_0/E_0 values are underestimated by both electron-drift models in the region forming a shell around the core contact, by up to -15% at $r = 10$ mm and $z = 35$ mm, Figs. 12.24e and 12.24f. Larger rise times and smaller A_0/E_0 values imply that the electrons leave the vicinity of the core contact faster and are collected on the segments earlier than predicted. This means that either the electron-drift velocity is underestimated by the simulation or the electrons take a shorter drift path than predicted. Both of these conclusions can arise from an inaccurate description of the longitudinal electron-drift velocity along the $\langle 111 \rangle$ axis.

Figure 12.25 depicts the measured superpulses from events originating at $r = 4$ mm and targeted $z \geq 27$ mm, where a large deviation in the $5-95\%$ rise time and A_0/E_0 values between simulation and measurement is observed. All superpulses start with a sharp rise followed by a moderate slope. The sharp rise is caused by the holes approaching the core contact, while the moderate slope is caused by the electrons drifting away from the core contact, see section 12.1. In all of the events, the holes are collected on the core contact before the electrons are collected on the segments.

The electron- and hole-drift times can be estimated from the pulses in Fig. 12.25b. The times at which the pulses leave the baseline are associated with the creation of the electron-hole pairs. For each pulse, the holes are collected on the core contact when the steepest slope is reached and the electrons are collected on the segments when the pulses reach their final amplitude.

The longest hole-drift time of approximately 150 ns is observed for $z = 27$ mm. With increasing z, the first part of the pulse becomes steeper until reaching the steepest slope at $z = 35$ mm. At $z \geq 37$ mm, the sharp rise is slightly less pronounced. The length of the final part of the pulse increases until reaching its maximum at $z = 31$ mm and becomes noticeably shorter for even higher z. The latter implies that the electron-drift times become significantly shorter for the events at $z > 31$ mm.

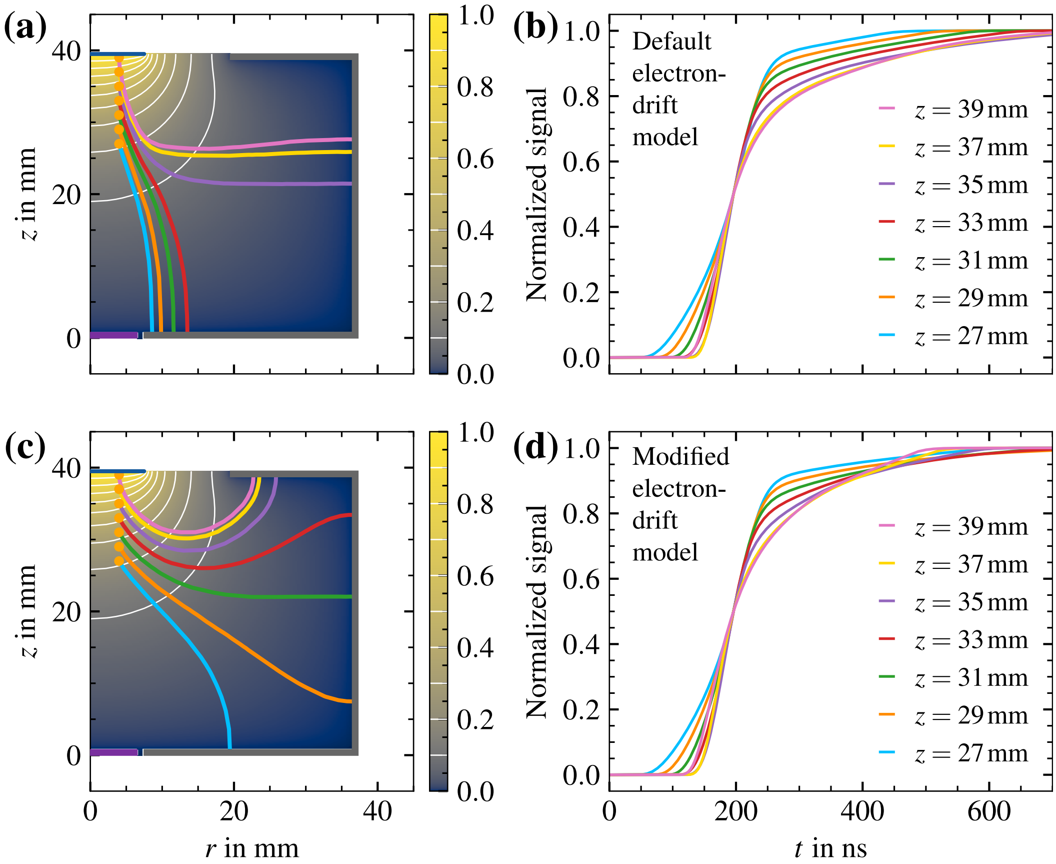

Figure 12.26: Electron-drift paths for events originating at $r = 4$ mm on the $\langle 110 \rangle$ axis in segment 3 at $\varphi = 275.8°$ and z from 27 mm to 39 mm in 2 mm steps as simulated using the mobility parameters listed in Tab. 12.8 and (a) the default electron-drift model from section 4.4.2.3 and (c) the modified electron-drift model from section 4.4.2.4. The hole-drift paths are not shown. Shown in (b) and (d) are the corresponding core pulses, time-aligned to 50% of their amplitude.

Figure 12.26 depicts the simulated electron-drift paths and pulse shapes corresponding to the measured pulses shown in Fig. 12.25. For the simulations, the electric field shown in Fig. 8.12, the mobility parameters listed in Tab. 12.8, and either the default or the modified electron-drift model were used.

The choice of the electron-drift model has a very significant impact on the electron-drift paths and, thus, the shapes of the final part of the pulses. The electrons from the event at $r = 4$ mm and $z = 27$ mm are predicted to be collected on the bottom plate of segment 3 by both models, see Figs. 12.26a and 12.26c. However, the electrons are collected at $r = 20$ mm using the modified electron-drift model compared to $r = 8$ mm for the default electron-drift model. The longer electron-drift path results in a longer pulse using the modified electron-drift model, see Figs. 12.26b and 12.26d.

For 29 mm $\leq r \leq$ 33 mm, the default electron-drift model predicts the electrons to be collected on the bottom surface, see Fig. 12.26a, while the modified electron-drift model predicts a collection on the mantle surface, see Fig. 12.26c. Again, the longer electron-drift paths using the modified electron-drift model result in longer pulses with respect to the default electron-drift model, see Figs. 12.26b and 12.26d.

For $r \geq 35\,\mathrm{mm}$, the default electron-drift model predicts the electrons to be collected on the mantle surface, see Fig. 12.26a. In fact, the default electron-drift model never predicts electrons from events at $r = 4\,\mathrm{mm}$ to be collected on the top plate of segment 3. This results in longer pulses with respect to $r \leq 33\,\mathrm{mm}$, see Fig. 12.26b. The modified electron-drift model predicts the electrons to be collected on the top plate of segment 3, see Fig. 12.26c. With increasing z, the electrons are collected closer to the core contact, resulting in the final part of the pulse to become significantly shorter, see Fig. 12.26d. This results in the cross-over between the pulses at $r = 27\,\mathrm{mm}$ and $r = 39\,\mathrm{mm}$ when time-aligning all pulses to 50% of their final amplitude. This prediction of the modified electron-drift model agrees with the data while the default electron-drift model completely fails at this point.

The simulated pulses shown in Fig. 12.26d generated with the modified electron-drift model correctly feature the cross-over as measured and depicted in Fig. 12.25b. This implies that the electrons in the uppermost events at $r = 4\,\mathrm{mm}$ are collected on the top surface of segment 3. The default electron-drift model cannot predict the cross-over observed in the data and does not accurately describe the anisotropic electron-drift in germanium. The cross-over is qualitatively well described using the modified electron-drift model. However, the simulated pulses are still 20% longer than observed in the data. This suggests that the simulation underestimates the electron-drift velocity along some part of the drift or predicts too long electron-drift paths.

The observation of higher rise times along the diagonal line in Fig. 12.24 already suggests that $\upsilon_{L,e}^{111}$ is underestimated and is most likely closer to the measured literature values listed in Tab. 4.1. The assumptions in the electron-drift model and small variations in the values for $\upsilon_{L,e}^{100}$ and $\upsilon_{L,e}^{110}$ have a strong influence on the exact values of $\upsilon_{L,e}^{111}$ in the simulation. At $r = 4\,\mathrm{mm}$, the electron-drift paths all feature a significant contribution from drifts along the $\langle 111 \rangle$ direction, see Fig. 12.26c. Therefore, any underestimate of $\upsilon_{L,e}^{111}$ in the simulation will have a large influence on the pulse shapes originating from regions close to the core contact.

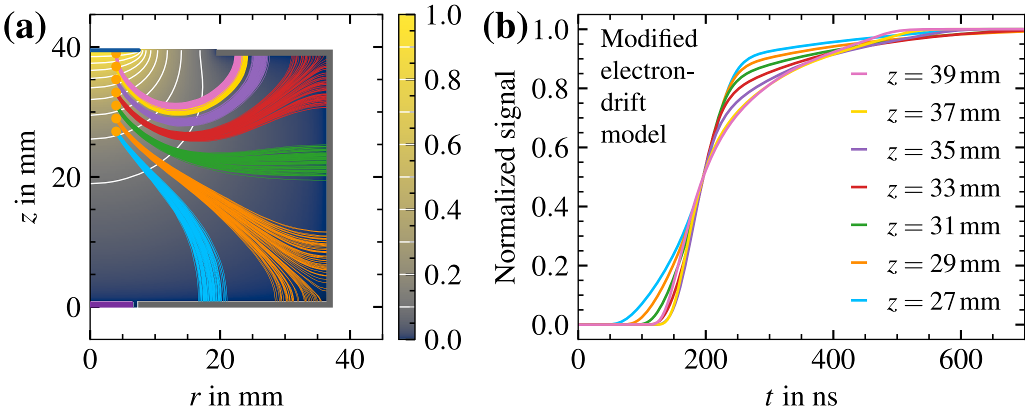

Figure 12.27: (a) Electron-drift paths for the same events as in Fig. 12.26 simulated for charge clouds consisting of 100 charges each, using the mobility parameters listed in Tab. 12.8 and the modified electron-drift model from section 4.4.2.4. (b) Corresponding charge pulses, time-aligned to 50% of their amplitude.

The electron-drift paths also heavily depend on the exact position of the energy deposit. Figure 12.27 depicts the electron-drift paths and pulses for the same events as in Fig. 12.26 but with each event being simulated as a charge cloud consisting of 100 electrons and with an initial radius of 0.2 mm. The electron cloud diverges during the drift towards the segment contacts and, for some events, the electrons reach the segment contact up to 1 cm apart. However, the charge-cloud divergence happens mostly in regions where the core weighting potential is weak. Thus, the influence on the pulse shapes is negligible.

Finally, it should be noted that the strong dependence of the pulse shape on the position of the event could have an influence on the determination of Compton superpulses as presented in chapter 11. In the vicinity of the core contact, significant changes in the pulse shapes occur already at length scales smaller than the position resolution of the Compton Scanner. Thus, differently shaped pulses enter the determination of intermediate superpulses as explained in sections 11.2, which might have an influence on the quality of the final superpulses. However, averaging differently shaped pulses would result in the first and last parts of the pulses being washed out and the overall pulse becoming longer. As this was not observed in the data, the effect must be small.

12.5 Conclusion

In conclusion, the hole drift in high-purity germanium seems to be accurately described by the mobility parameters listed in Tab. 12.8 and the general hole-drift model presented in section 4.4.1. The anisotropy of the electron drift is not well described by the default-electron drift model from section 4.4.2.3. The modifications to the electron-drift model proposed in section 4.4.2.4 result in better prediction of the data, especially qualitatively for events close to the point contact. Quantitatively, the largest deviations are observed for events with a long electron drift along the $\langle 111 \rangle$ direction. This implies that the modified electron-drift model does not perfectly predict the electron-drift velocity along the $\langle 111 \rangle$ axis and, thus, the anisotropy between the $\langle 111 \rangle$ axis and all other axes. A more accurate description of the electron drift would require further electron-drift models to be tested against data, ideally using further detectors with different geometries to probe a wider range of electric field strengths.

In p-type point-contact detectors, the electron drift significantly influences pulse-shape quantities as the $5-95\%$ rise times and A_0/E_0 for events close to the point contact. Therefore, an improved model of the electron drift and its anisotropy is essential to accurately predict pulse shapes for these events. The findings on the electron-drift model should, in principle, be applicable to all high-purity germanium detectors. This is especially important for simulation studies for the LEGEND experiment to tune pulse-shape discrimination techniques to accurately estimate cut efficiencies and fiducial volumes of the detectors, and to improve background suppression while preserving a high signal efficiency in regions close to the point contact. The thereby-increased discovery sensitivity would allow for exploring lower values of $\langle m_{\beta\beta} \rangle$ with the same exposure.

13 Summary and outlook

The search for neutrinoless double-beta decay is the most promising endeavor to search for a lepton-number-violating effect beyond the Standard Model. The real challenge for state-of-the-art germanium-based experiments is to reduce background, which, on the analysis side, is met with pulse-shape discrimination. These techniques have to be tested and tuned on pulse shape libraries, either measured under controlled conditions or simulated with validated models.

The pulse-shape studies performed for this thesis were based on data from a p-type segmented point-contact germanium detector. The geometry of this test detector resembles one of the detector geometries used in the LEGEND experiment but its segmentation provides additional information on the event topology. The goals to obtain an accurate description of the electric field in the detector and to determine electron and hole mobilities in germanium, as well as the anisotropy and temperature dependence of the mobilities, were achieved. The results improve the input to pulse shape simulation frameworks and, thus, improve background identification techniques for rare-event searches using germanium detectors.

The electric field in a germanium detector and the mobilities of the charge carriers determine the shape of the pulses coming from the detector. It is important to realize that the electric field in most of the volume of a point-contact detector is dominated by the density of ionized impurities and their distribution. Therefore, an accurate description of the electric field heavily relies on an accurate description of the impurity density profile in the bulk of the detector, which is not provided by the detector manufacturer.

The impurity density profile of the test detector was determined from a sequence of measurements of the capacitance of the partially depleted detector. It was found that the measured dependence of the capacitance on the bias voltage cannot be reproduced by simulations for impurity density profiles with only a gradient in z. An impurity density profile with an additional r-dependence, which was found to be almost constant in the center of the detector and to have a strong radial decrease towards the outer surface, was needed. The electric field close to the mantle surface of the detector was determined to be up to 25% lower than under the assumption of no radial dependence.

For the first time, images of the undepleted volumes of a segmented point-contact germanium detector were taken with the Compton Scanner at the Max Planck Institute for Physics in Munich. This experimental setup was commissioned within the framework of this thesis to determine the origin of events in the full detector volume with a resolution of ± 1 mm FWHM in each spatial dimension. To accomplish this, the Compton Scanner underwent a hardware and software upgrade, resulting in an increase of acceptance by 100% in the center and by 50% in the outer part of the detector. The depletion images confirm the existence of a radial component of the impurity density profile. The profiles determined from fits are very compatible for the two methods.

The Compton Scanner was also used to collect high-quality pulse shape libraries consisting of superpulses from events with charge-carrier drifts along the vertical [001] axis, and the horizontal $\langle 100 \rangle$ and $\langle 110 \rangle$ axes. Pulses simulated with the software package SolidStateDetectors.jl were compared to selected superpulses to determine the mobilities of electrons and holes in germanium. The vertical drift allowed to determine absolute values of mobilities over a wide range of electric field strengths while the horizontal drift allows to study the anisotropy between the axes.

At the reference temperature of 78 K, the measured hole mobility was 20% lower and the measured electron mobility approximately 3% lower than the values widely used in simulations so far. This is, however, in good agreement with the observations in recent publications. At an electric field strength of 500 V/cm, the longitudinal anisotropy between the $\langle 100 \rangle$ and the $\langle 110 \rangle$ direction was measured to be 6% for holes and 10% for electrons. While the widely used hole-drift model provided a good description of the measured transverse anisotropy of the hole-drift, the anisotropy of the electron-drift was significantly underestimated by the widely used electron-drift model. A modification of the electron-drift model that incorporates the proportionality on the effective electron mass expected for scattering off acoustic phonons was developed and tested. While this modified electron-drift model mildly underestimates the electron-drift velocity along the $\langle 111 \rangle$ direction, it describes the measured transverse anisotropy of the electron drift in germanium significantly better. This is especially relevant to accurately simulate pulse shapes for events close to the point contact in p-type germanium detectors.

The temperature dependence of the drift velocities determined at a reference electric field strength of 500 V/cm is $\propto T^{-0.52}$ for electrons and $\propto T^{-0.53}$ for holes. These exponents are significantly smaller than the theoretically expected $T^{-3/2}$-dependence of the mobility resulting from scattering off acoustic phonons. The deviation is well explained by saturation effects limiting the electron- and hole-drift velocities for electric field strengths above 100 V/cm. These saturation effects are shown to be significantly less temperature-dependent than scattering at low electric field strengths. Both the measured transverse anisotropy of the electron drift and the measured temperature dependence provide strong evidence for acoustic phonons being the main scattering centers and the main limitation for the drift mobilities.

The methods presented in this thesis are applicable to all detectors in the LEGEND experiment. The presence of a radial component in the impurity density profile observed in this thesis and in previous works [34] emphasizes the need to determine the r-dependencies of the impurity density profiles of all LEGEND detectors in order to accurately simulate electric fields. These radial components can be determined from capacitance measurements, which can easily be taken in a few hours and should become part of the standard characterization measurements upon detector acceptance. Compton Scanner measurements would only be required for detectors, for which no r-dependence in the impurity density profile describes the measured capacitance-voltage curve well and for which more insight into the impurity density would be needed.

The updated values of the longitudinal charge-drift velocities along the $\langle 100\rangle$ and $\langle 110\rangle$ axes and the modified electron-drift model are material properties and should, in principle, be applicable to all LEGEND detectors. The latter would be especially important to better predict pulse shapes from events close to the point contact in p-type germanium detectors. This is essential to tune pulse-shape discrimination techniques to further decrease the background level without decreasing the signal efficiency in regions close to the point contact, increasing the fiducial volume of the detectors and further-increasing the discovery sensitivity with the same exposure. This is essential for the LEGEND experiment to reach the goal of probing values more than 10^{28} years for the half-life of neutrinoless double-beta decay in ^{76}Ge.

Acknowledgements

I would like to close this thesis by thanking all the wonderful people who motivated, encouraged and supported me during my time as a PhD student.

First of all, I would like to thank Allen Caldwell for offering me the possibility to pursue my PhD program in the germanium detector group at the Max Planck Institute for Physics and for taking the time to give me valuable feedback on my thesis draft. I would also like to thank the rest of my PhD defense committee at TUM, Alejandro Ibarra and Lothar Oberauer.

A very special thanks goes to Iris Abt for the extensive number of hours spent discussing results, proofreading my thesis with greatest care, the *wonderful* business trips to conferences and summer schools and the guidance and advice for future career possibilities.

Thanks to all current members of the LEGEND group at the Max-Planck-Institute: Oliver Schulz for all questions regarding programming and fitting and making the best hot chocolate when times got tough, Xiang Liu and Chris Gooch for helping with lab-relating questions and for listening to my analysis updates in the weekly group meetings, Brennan Hackett for encouraging me to write my thesis in times of low motivation and proofreading parts of my thesis, and Arthur Butorev for being the best possible support I could have wished for, both work-wise and emotionally, especially during the last months before submitting.

I would also like to thank former members and fellows of the group: Lukas Hauertmann and Martin Schuster for introducing me to lab work and programming in julia when I started in the group and taking great care of me during the Corona lock-downs, David Hervas Aguilar for his collaboration and time spent on the Compton Scanner and Florian Henkes for the all-night productive programming sessions to get things done in preparation for my thesis and the LEGEND collaboration meetings.

I am also very grateful for all the young people I got to mentor and who have contributed to the successful completion of this thesis: Jan Plößner for contributing to the hardware upgrade of the Compton Scanner, Sebastian Ruffert for assisting in the development of SSD, Julia Penner and Johanna Lührs for helping with the measurement and analysis of capacitance-voltage curves and depletion images.

Thanks to my phone buddies, Jonas Grage and Georg Noffz, for being there when I needed someone to listen and for giving great advice when I needed it the most.

And last but definitely not least, I would like to thank my family and especially my parents for supporting me throughout my life and especially during my time in Munich. Thanks for your everlasting support – I am more than thankful to have you in my life!

Appendix

A Depletion widths in simple-geometry detectors

In this appendix, the dependence of the depletion width, w, of an infinite-extension planar detector with height H and an infinitely long cylindrical detector with radius R on the applied voltage, V_B, and the density of electrically active impurities, N_I, is derived. For simplicity, N_I is assumed to be constant throughout the detector volume.

A1 Infinite-extension planar detector

Assume a planar detector that extends infinitely in x and y and is contacted at $z = 0$ and at $z = H$, which depletes from the bottom to the top. The depletion width, w, is defined as the height z, below which the detector is depleted, i.e.

$$\rho(\vec{r}) = \begin{cases} eN_I, & \text{if } 0 < z < w \\ 0, & \text{if } w < z < H \end{cases} . \tag{A.1}$$

The undepleted volume is conductive and the electric field vanishes. Therefore, the electric potential is constant in the undepleted volume, i.e. $\phi(z > w) = V_B$, where V_B is the potential applied to the top contact at $z = H$. In the depleted volume, the ionized impurities lead to space charges that contribute to the electric potential:

$$\Delta\phi(\vec{r}) = -\frac{\rho(\vec{r})}{\varepsilon_0 \varepsilon_r(\vec{r})} \qquad \phi(z \geq w) = V_B \qquad \phi(z = 0) = 0 \, , \tag{A.2}$$

where $\rho(\vec{r})$ is the charge density resulting from ionized impurities, ε_0 is the vacuum permittivity and $\varepsilon_r(\vec{r})$ is the relative permittivity at a given position $\vec{r}$. The bottom contact of the detector is grounded.

Solving Eq. (A.2) using the impurity density requirement in Eq. (A.1) results in

$$\phi(z) = -\frac{eN_I}{2\varepsilon_0\varepsilon_r} z^2 + \left(\frac{eN_I w}{2\varepsilon_0\varepsilon_r} + \frac{V_B}{w} \right) z \, . \tag{A.3}$$

The electric field at the boundary between depleted and undepleted volumes vanishes, i.e.

$$0 = \frac{\partial \phi}{\partial z}(z = w) = -\frac{eN_I w}{2\varepsilon_0\varepsilon_r} + \frac{V_B}{w} \, . \tag{A.4}$$

The bias voltage needed to obtain a given depletion width becomes

$$V_B(w) = \frac{eN_I w^2}{2\varepsilon_0\varepsilon_r} \, . \tag{A.5}$$

To deplete the whole detector, i.e. for $w = H$, the full-depletion voltage, V_D, is

$$V_D = V_B(w = H) = \frac{eN_I H^2}{2\varepsilon_0\varepsilon_r} \, . \tag{A.6}$$

Solving Eq. (A.5) for w results in

$$w(V_B) = \sqrt{\frac{2\varepsilon_0\varepsilon_r V_B}{eN_I}} \, . \tag{A.7}$$

A2 Infinitely long cylindrical detector

A cylindrical detector is contacted at the mantle surface at $r = R$ and depletes from the outside towards the inside. The depletion width, $R - w$, is defined as the radius, below which the detector is undepleted, i.e.

$$\rho(\vec{r}) = \begin{cases} 0, & \text{if } 0 < r < w \\ eN_I, & \text{if } w < r < R \end{cases} . \tag{A.8}$$

For $r < w$, the electric field is zero, resulting in a constant electric potential of $\phi(r \leq w) = V_B$. In the depleted volume, $\phi(\vec{r})$ can be determined by solving Gauss' law:

$$\Delta\phi(\vec{r}) = -\frac{\rho(\vec{r})}{\varepsilon_0 \varepsilon_r(\vec{r})} \qquad \phi(r \leq w) = V_B \qquad \phi(r = R) = 0 \,, \tag{A.9}$$

where $\rho(\vec{r})$ is the charge density resulting from ionized impurities, ε_0 is the vacuum permittivity and $\varepsilon_r(\vec{r})$ is the relative permittivity at a given position $\vec{r}$. The mantle contact of the cylindrical detector is grounded.

Solving Eq. (A.9) using the impurity density requirement in Eq. (A.8), assuming no φ- and z-dependence of $\phi(\vec{r})$ in cylindrical coordinates results in

$$\phi(r) = -\frac{eN_I}{4\varepsilon_0\varepsilon_r}(r^2 - R^2) + \left(V_B - \frac{eN_I}{4\varepsilon_0\varepsilon_r}\left(R^2 - w^2\right)\right)\frac{\ln(r/R)}{\ln(w/R)} \,. \tag{A.10}$$

The electric field at the boundary between depleted and undepleted volumes vanishes, i.e.

$$0 = \frac{\partial\phi}{\partial r}(r = w) = -\frac{eN_I w}{2\varepsilon_0\varepsilon_r} + \left(V_B - \frac{eN_I}{4\varepsilon_0\varepsilon_r}\left(R^2 - w^2\right)\right)\frac{1}{w\ln(w/R)} \,. \tag{A.11}$$

The bias voltage needed to obtain a given depletion width becomes

$$V_B(w) = \frac{eN_I}{4\varepsilon_0\varepsilon_r}\left(R^2 + w^2\left(2\ln(w/R) - 1\right)\right) \,, \tag{A.12}$$

with a full-depletion voltage of

$$V_D = V_B(w = 0) = \frac{eN_I R^2}{4\varepsilon_0\varepsilon_r} \,. \tag{A.13}$$

Solving Eq. (A.12) for w results in

$$w(V_B) = R\sqrt{\exp\left(W_{-1}\left(\frac{1}{\mathrm{e}}\left(\frac{4\varepsilon_0\varepsilon_r V_B}{eN_I R^2} - 1\right)\right) + 1\right)} \tag{A.14}$$

where e is Euler's number and $W_{-1}(x)$ describes the -1 branch of the Lambert-W function [213] which satisfies $W_{-1}(x)\exp(W_{-1}(x)) = x$ with $-\frac{1}{\mathrm{e}} \leq x \leq 0$ and $W_{-1}(x) \leq -1$.

B Derivation of the diffusion equation

In this appendix, Eq. (4.41) is derived from Eq. (4.38). For a spherical coordinate system with an origin at the center of the charge cloud and $n_{e/h}(\vec{r},t)$ with only radial dependence, i.e. $n_{e/h}(\vec{r},t) = n_{e/h}(r,t)$, the total charge, $Q(r,t)$, contained in a sphere, $S(r)$, with radius r is given by

$$Q(r,t) = \pm e \iiint\limits_{S(r)} \mathrm{d}^3 r \, n_{e/h}(r,t) = \pm e \int\limits_0^r \mathrm{d}r \, n_{e/h}(r,t) 4\pi r^2 \, , \tag{B.1}$$

with + for holes and − for electrons.

Equation (B.1) allows to express $n_{e/h}(r,t)$ and $\frac{\partial}{\partial r} n_{e/h}(r,t)$ in terms of $Q(r,t)$:

$$\begin{gathered} \frac{\partial Q}{\partial r} = \pm n_{e/h}(r,t) \, 4\pi e r^2 \\ \Rightarrow \;\; n_{e/h}(r,t) = \pm \frac{1}{4\pi e r^2} \frac{\partial Q}{\partial r} \quad \text{and} \quad \frac{\partial}{\partial r} n_{e/h}(r,t) = \pm \frac{1}{4\pi e r^2} \frac{\partial^2 Q}{\partial r^2} \mp \frac{2}{4\pi e r^3} \frac{\partial Q}{\partial r} \, . \end{gathered} \tag{B.2}$$

Starting with Eq. (4.38), the charge-carrier density, $n_{e/h}(\vec{r},t)$ can be substituted by the charge $Q(\vec{r},t)$ performing a volume integral over $S(r)$:

$$\begin{aligned} 0 &= \pm e \iiint\limits_{S(r)} \mathrm{d}^3 r \, \frac{\partial}{\partial t} n_{e/h}(r,t) \pm e \iiint\limits_{S(r)} \mathrm{d}^3 r \, \vec{\nabla}(-D_{e/h}(r) \vec{\nabla} n_{e/h}(r,t) + n_{e/h}(r,t) \mu_{e/h}(r) \vec{\mathcal{E}}(r,t)) \\ &= \pm e \iiint\limits_{S(r)} \mathrm{d}^3 r \, \frac{\partial}{\partial t} n_{e/h}(r,t) \pm e \iint\limits_{\partial S(r)} \mathrm{d}\vec{A} \, (-D_{e/h}(r) \, \vec{e}_r \frac{\partial}{\partial r} n_{e/h}(r,t) + n_{e/h}(r,t) \mu_{e/h}(r) \vec{\mathcal{E}}(r,t)) \\ &\overset{\text{(B.1)}}{=} \frac{\partial}{\partial t} Q(r,t) \pm 4\pi e r^2 \vec{e}_r \cdot (-D_{e/h}(r) \, \vec{e}_r \frac{\partial}{\partial r} n_{e/h}(,t) + n_{e/h}(,t) \mu_{e/h}(r) \vec{\mathcal{E}}(r,t)) \\ &= \frac{\partial}{\partial t} Q(r,t) \pm 4\pi e r^2 (-D_{e/h}(r) \frac{\partial}{\partial r} n_{e/h}(r,t) + n_{e/h}(,t) \mu_{e/h}(r) \mathcal{E}_r(r,t)) \\ &\overset{\text{(B.2)}}{=} \frac{\partial}{\partial t} Q(r,t) - D_{e/h}(r) \left(\frac{\partial^2}{\partial r^2} Q(r,t) - \frac{2}{r} \frac{\partial}{\partial r} Q(r,t) \right) + \frac{\partial}{\partial r} Q(r,t) \mu_{e/h}(r) \mathcal{E}_r(r,t) \\ &\overset{\text{(4.40)}}{=} \frac{\partial}{\partial t} Q(r,t) - D_{e/h}(r) \left(\frac{\partial^2}{\partial r^2} Q(r,t) - \frac{2}{r} \frac{\partial}{\partial r} Q(r,t) \right) - Q(r,t) \frac{\partial}{\partial r} Q(r,t) \frac{\mu_{e/h}(r)}{4\pi \varepsilon_0 \varepsilon_r r^2} \\ &= -\frac{1}{D_{e/h}(r)} \frac{\partial}{\partial t} Q(r,t) + \frac{\partial^2}{\partial r^2} Q(r,t) - \frac{2}{r} \frac{\partial}{\partial r} Q(r,t) + Q(r,t) \frac{\partial}{\partial r} Q(r,t) \frac{\mu_{e/h}(r)}{D_{e/h}(r)} \frac{1}{4\pi \varepsilon_0 \varepsilon_r r^2} \\ &\overset{\text{(4.37)}}{=} -\frac{1}{D_{e/h}(r)} \frac{\partial}{\partial t} Q(r,t) + \underbrace{\frac{\partial^2}{\partial r^2} Q(r,t) - \frac{2}{r} \frac{\partial}{\partial r} Q(r,t)}_{\text{Diffusion}} - \underbrace{Q(r,t) \frac{\partial}{\partial r} Q(r,t) \frac{e}{k_B T} \frac{1}{4\pi \varepsilon_0 \varepsilon_r r^2}}_{\text{Coulomb self-repulsion}} \, . \end{aligned}$$

C Example configuration file for SolidStateDetectors.jl

In this appendix, the configuration file that defines the example p-type inverted-coaxial point-contact detector for the SolidStateDetectors.jl simulations in section 5 is listed.

```
name: Public Inverted Coax
units:
  length: mm
  angle: deg
  potential: V
  temperature: K
grid:
  coordinates: cylindrical
  axes:
    r:
      to: 40
      boundaries: inf
    phi:
      from: 0
      to: 0
      boundaries: periodic
    z:
      from: -10
      to: 90
      boundaries:
        left: inf
        right: inf
medium: vacuum
detectors:
  - semiconductor:
      material: HPGe
      temperature: 78
      impurity_density:
        name: cylindrical
        z:
          init: -1e7
          gradient: -1e5
      geometry:
        difference:
          - tube:
              r: 35
              h: 80
              origin:
                z: 40
          - cone:
              r:
                bottom:
                  from: 35
                  to: 36
                top:
                  from: 23.71
                  to: 36
              h: 64
              origin:
                z: 52
          - tube:
              r: 5
              h: 80
              origin:
                z: 65
```

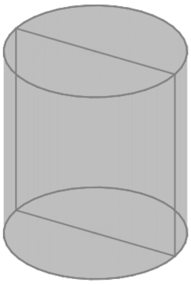

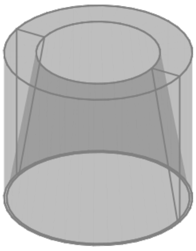

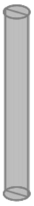

```
contacts:
  - material: HPGe
    id: 1
    potential: 0
    geometry:
      tube:
        r: 3
        h: 2
        origin:
          z: 1
  - material: HPGe
    id: 2
    potential: 3500
    geometry:
      union:
        - tube:
            r:
              from: 15
              to: 35
            h: 0
        - tube:
            r:
              from: 35
              to: 35
            h: 20
            origin:
              z: 10
        - cone:
            r:
              bottom:
                from: 35
                to: 35
              top:
                from: 24.42
                to: 24.42
            h: 60
            origin:
              z: 50
        - tube:
            r:
              from: 5
              to: 24.42
            h: 0
            origin:
              z: 80
        - tube:
            r:
              from: 5
              to: 5
            h: 55
            origin:
              z: 52.5
        - tube:
            r: 5
            h: 0
            origin:
              z: 25
```

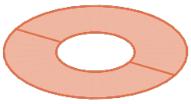

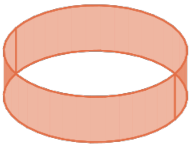

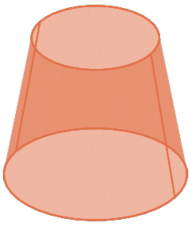

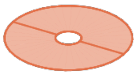

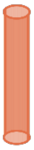

D Simulation of undepleted volumes in the segBEGe detector

The p-type segBEGe detector depletes from the segments into the bulk of the detector in three parts: from the bottom up, from the top down and from the outside in.

For low bias voltages well below the full-depletion voltage, i.e. $V_B \ll V_D$, these three parts can be treated as being almost independent. The depletion from the bottom and the top surface can each be approximated as in a planar parallel plate capacitor, see Appendix A1, and the depletion from the outside can be treated as in a cylindrical detector, see Appendix A2.

If the impurity is expected to be $\rho(z) = \rho_{\text{bot}} + (\rho_{\text{top}} - \rho_{\text{bot}})\, z/H$, i.e. constant in r and linear in z with ρ_{bot} at the bottom surface and ρ_{top} at the top surface of the detector, the depletion widths for all three parts becomes

$$
\begin{aligned}
&w_{\text{bot}}(V_B) = \sqrt{\frac{2\varepsilon_0\varepsilon_r V_B}{\rho_{\text{bot}}}}\,, \quad w_{\text{top}}(V_B) = H - \sqrt{\frac{2\varepsilon_0\varepsilon_r V_B}{\rho_{\text{top}}}} \quad \text{and} \\
&w_{\text{out}}(V_B, z) = R\,\sqrt{\exp(W_{-1}\left(-\frac{1}{\mathrm{e}} + \frac{4\varepsilon_0\varepsilon_r V_B}{\mathrm{e}R^2(\rho_{\text{bot}} + (\rho_{\text{top}} - \rho_{\text{bot}})\, z/H)}\right) + 1)}\ .
\end{aligned}
\tag{D.1}
$$

If $\rho_{\text{top}} > \rho_{\text{bot}}$, the detector depletes faster from the bottom than from the top, i.e. $w_{\text{top}} < w_{\text{bot}}$. In addition, the depletion from the outside has a z-dependence that arises from the z-dependence of $\rho(\vec{r})$.

Figure D.1 depicts simulation results for the depleted volumes of the p-type segBEGe detector at different V_B together with the analytical estimates for the depletion widths shown in Eq. (D.1), assuming only a linear z-gradient for $\rho(r)$.

For V_B below $-450\,\text{V}$, the expressions in Eq. (D.1) describe the results of the full simulation well. The shape of the undepleted volume is almost perfectly described except for the rounded corners.

For $V_B = -600\,\text{V}$, the outer edge of the undepleted volume stops being vertical over the z range. While w_{out} still describes the radial extent of the undepleted volume well at $V_B = -450\,\text{V}$, it is not a good estimate for V_B above $-600\,\text{V}$.

The bottom edge is well described by w_{bot} until $V_B = -900\,\text{V}$. For $V_B = -1050\,\text{V}$, the bottom edge of the undepleted volume deviates from the flat geometry and the lowest point is not well described by w_{bot}. For $V_B = -1200\,\text{V}$ and above, neither w_{bot}, w_{top} nor w_{out} are good estimates for the geometry of the simulated undepleted volume.

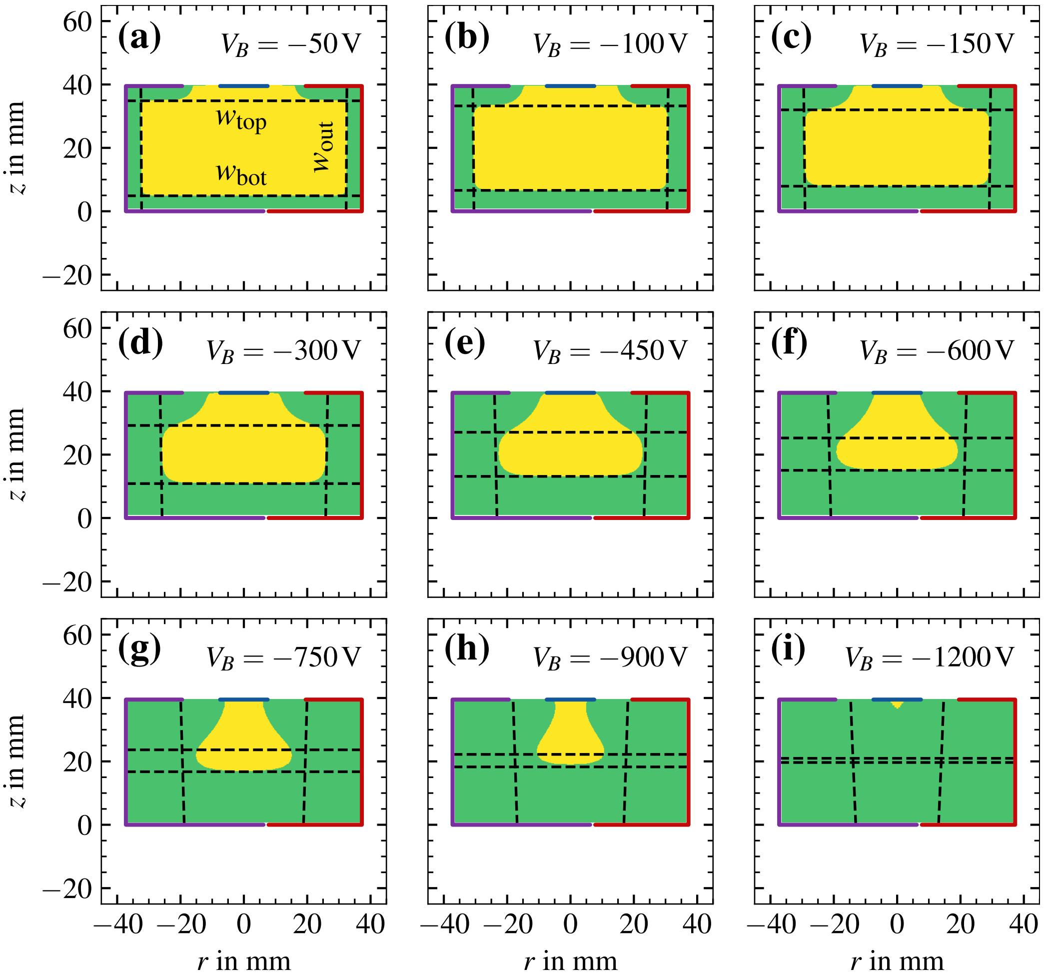

Figure D.1: Depletion volumes of the p-type segBEGe detector as predicted by SSD using all values listed in Tab. 6.1 scaled to 89%, assuming only a linear z-gradient for the impurity density profile for different V_B applied to the core contact. The depleted volumes are shown in green, the undepleted volumes are shown in yellow. The dashed lines depict depletion width estimates, w_{bot}, w_{top} and w_{out}, calculated using Eq. (D.1).

E Similarity between charge pulses

In this appendix, one method to quantify the similarity between two pulses is presented.

The pulses from all contacts of the segBEGe detector, S_i with $i \in \{0,1,2,3,4\}$, are sampled by the STRUCK ADC in steps of 4 ns. Hence, the continuous pulse shapes, $Q_i(t)$, are stored as sets of points, $(Q_{i,n})_{n\in N}$, where N is a set of discretized times.

Two pulses are defined to be similar if they agree with each other in the signal window within a few standard deviations of their noise levels. The noise level of a pulse is defined by the standard deviation, $\sigma(Q_i)$, of the sampled values of the pulse in the baseline window from the mean baseline value, $\overline{Q}_i$. The baseline window consists of a set of discretized times, $n \in \{1,\ldots,B\}$. This results in

$$\sigma(Q_i)^2 = \frac{1}{B-1}\sum_{n=1}^{B}\left(Q_{i,n}-\overline{Q}_i\right)^2 \quad \text{with} \quad \overline{Q}_i = \frac{1}{B}\sum_{n=1}^{B} Q_{i,n}. \tag{E.1}$$

A measure for the deviation between two pulses, $Q_i(t)$ and $q_i(t)$, is the χ^2 value. In the signal window, $n \in \{B+1,\ldots,B+S\}$, it is given by

$$\chi^2 = \sum_{n=B+1}^{B+S} \frac{(Q_{i,n}-q_{i,n})^2}{\sigma(Q_i)^2+\sigma(q_i)^2}. \tag{E.2}$$

The expression in Eq. (E.2) effectively sums up the squared differences at all sampled times in units of the combined variance of the two pulses. Divided by the degrees of freedom, $\mathrm{ndf} = S-1$, this gives a value which indicates how many standard deviations of the noise levels the two pulses differ from each other:

$$\frac{\chi^2}{\mathrm{ndf}} = \frac{1}{S-1}\sum_{n=B+1}^{B+S} \frac{(Q_{i,n}-q_{i,n})^2}{\sigma(Q_i)^2+\sigma(q_i)^2}. \tag{E.3}$$

The relation $\chi^2/\mathrm{ndf} \leq 1$ can be identified with the 1σ-interval of a Gaussian distribution, i.e. when cutting on $\chi^2/\mathrm{ndf} \leq 1$, around 68% of similar pulses are expected to pass the cut and around 32% are discarded. Pairs of pulses that are visibly similar usually show values of $\chi^2/\mathrm{ndf} \leq 3$. Pairs of pulses that are clearly seen not to be similar have values of χ^2/ndf that are usually orders of magnitude higher.

F Determination of the position of the crystal axes

The text in this section is quoted verbatim from my Master's thesis [128]:

The positions of the crystal axes were determined by looking at the pulse shapes resulting from hits close to the mantle and at the center height of the detector, i.e. $r \lesssim R$ and $z \approx H/2$. According to the simulation results shown in Fig. 6.7a, the charge carrier trajectories resulting from those hits are expected to move almost horizontally in the x-y-plane to the center of the detector bulk before drifting in z-direction. As the electric field does not change with φ, the horizontal part of the charge drift is expected to be the fastest when the charge carriers move along the $\langle 100 \rangle$ axis and the slowest when they move along the $\langle 110 \rangle$ axis. Thus, the two axes are also referred to as fast and slow axis, respectively.

Figure F.1a shows the scan points to determine the position of the crystal axes of the p-type segBEGe detector. The detector was irradiated 5.5 mm away from the mantle and in steps of 5°, taking into account the misalignment results in section 9.6.1. At each scan point, a total 1 h of data were taken to determine the superpulses at $z = (21 \pm 1)\,\mathrm{mm}$ using the reconstruction algorithm presented in section 11. A measure for the speed of the drift is the rise time, t_r, which is the time, in which the pulse rises from 5 to 95% of its amplitude. The determination of t_r for the core superpulse at $r = 31.7\,\mathrm{mm}$ and $\varphi = 12.2°$ is depicted in Fig. F.1b.

Figure F.1c depicts t_r as a function of φ. As expected, the rise time values oscillate with a periodicity of 90°. The function shows discontinuities at the segment boundaries which result from segment-to-core cross-talk at pulse shape level, see section 3.4.4. The discontinuities cannot be compensated by only correcting for linear cross-talk with the cross-talk matrix C obtained from the background measurement, see Eq. (7.12). This implies that the differential segment-to-core cross-talk is not negligible in the flat part of the core signal. To determine the position of the $\langle 110 \rangle$ axis, φ_{110}, Fig. F.1c is divided into six parts of 60°, which are each fitted to

$$t_r(\varphi) = A \cos\left(\frac{2\pi}{90^\circ}(\varphi - \varphi_{110})\right) + O, \tag{F.1}$$

where A and O describe the amplitude and the offset of the oscillation, respectively, and φ_{110} describes the angle at which the rise time reaches its maximum, i.e. when the charge carriers drift along the slow $\langle 110 \rangle$ axis. For the fitting procedure, A and O are chosen to be completely independent for the different partial fits. However, φ_{110} is forced to be the same for all parts of the fit to obtain a combined result. For the p-type segBEGe detector, the slow axis is situated at $\varphi_{110} = (5.8 \pm 1.8)°$.

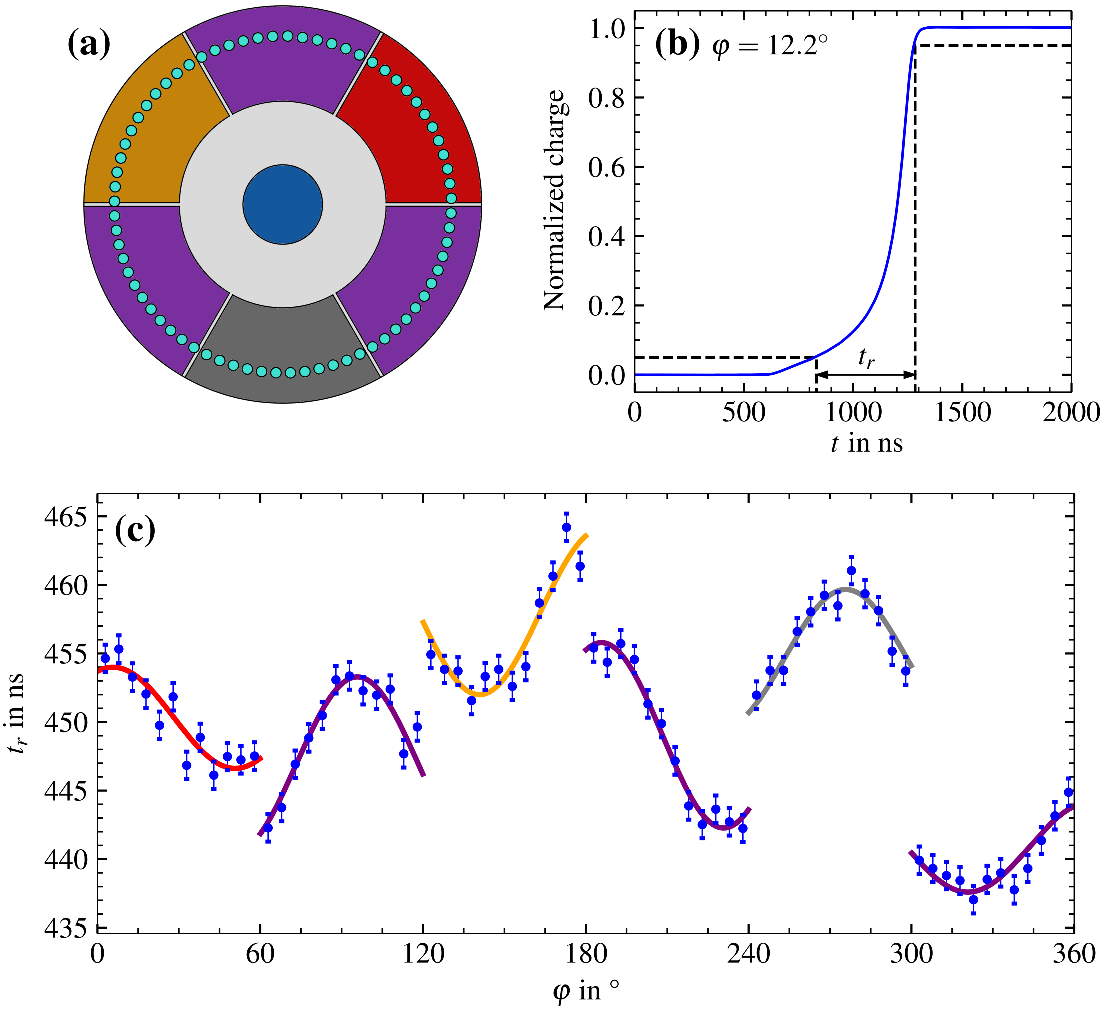

Figure F.1: (a) Scan points to determine the position of the crystal axes of the p-type segBEGe detector. The run was taken at a crystal temperature of $T = 85\,\mathrm{K}$ and with an operating voltage of $V_B = -3000\,\mathrm{V}$. (b) Illustration of the determination of the 5 to 95% rise time, t_r, of the core superpulse at $r = 31.7\,\mathrm{mm}$, $\varphi = 12.2°$ and $z = (21 \pm 1)\,\mathrm{mm}$. (c) Core rise time t_r as a function of φ. Partial fits to t_r in each segment are shown in the color of the respective segment.

References

[1] J. Eberth and J. Simpson, *From Ge(Li) detectors to gamma-ray tracking arrays – 50 years of gamma spectroscopy with germanium detectors*, Prog. Part. Nucl. Phys. **60**, 283 (2008).

[2] TEXONO COLLABORATION, *Limits on spin-independent couplings of WIMP dark matter with a p-type point-contact germanium detector*, Phys. Rev. Lett. **110**, 261301 (2013).

[3] CoGeNT COLLABORATION, *CoGeNT: A search for low-mass dark matter using p-type point contact germanium detectors*, Phys. Rev. D **88**, 012002 (2013).

[4] SUPERCDMS COLLABORATION, *Search for Low-Mass Weakly Interacting Massive Particles with SuperCDMS*, Phys. Rev. Lett. **112**, 241302 (2014).

[5] CDEX COLLABORATION, *Limits on Light Weakly Interacting Massive Particles from the First 102.8 kg × day Data of the CDEX-10 Experiment*, Phys. Rev. Lett. **120**, 241301 (2018).

[6] EDELWEISS COLLABORATION, *First Germanium-Based Constraints on Sub-MeV Dark Matter with the EDELWEISS Experiment*, Phys. Rev. Lett. **125**, 141301 (2020).

[7] V. Belov *et al.*, *The νGeN experiment at the Kalinin Nuclear Power Plant*, J. Instr. **10**, P12011 (2015).

[8] CONUS COLLABORATION, *Constraints on Elastic Neutrino Nucleus Scattering in the Fully Coherent Regime from the CONUS Experiment*, Phys. Rev. Lett. **126**, 041804 (2021).

[9] COHERENT COLLABORATION, *The COHERENT Experimental Program* `[arXiv:2204.04575]` (2022).

[10] GERDA COLLABORATION, *The* GERDA *experiment for the search of* $0\nu\beta\beta$ *decay in* ^{76}*Ge*, Eur. Phys. J. C **73**, 2330 (2013).

[11] MAJORANA COLLABORATION, *The Majorana Demonstrator Neutrinoless Double-Beta Decay Experiment*, Adv. High Energy Phys. **2014**, 365432 (2014).

[12] LEGEND COLLABORATION, *LEGEND-1000 Preconceptual Design Report* `[arXiv:2107.11462]` (2021).

[13] S. Paschalis *et al.*, *The performance of the Gamma-Ray Energy Tracking In-beam Nuclear Array GRETINA*, Nucl. Instr. Meth. A **709**, 44 (2013).

[14] S. Akkoyun *et al.*, *AGATA – Advanced GAmma Tracking Array*, Nucl. Instr. Meth. A **668**, 26 (2012).

[15] J.J. Valiente-Dobón *et al.*, *Conceptual design of the AGATA 2π array at LNL*, Nucl. Instr. Meth. A **1049**, 168040 (2023).

[16] N. Wall *et al.*, *The Miniball spectrometer*, Eur. Phys. J. A **49**, 40 (2013).

[17] L. Baudis *et al.*, *Gator: a low-background counting facility at the Gran Sasso Underground Laboratory*, J. Instr. **6**, P08010 (2011).

[18] Z. Zeng *et al.*, *The characteristics of a low background germanium gamma ray spectrometer at China JinPing underground laboratory*, Appl. Radiat. Isot. **91**, 165 (2014).

[19] P.R. Scovell *et al.*, *Low-background gamma spectroscopy at the Boulby Underground Laboratory*, Astropart. Phys. **97**, 160 (2018).

[20] J.P. Roques *et al.*, *The Use of Germanium Detectors in Space*, in *Handbook of X-ray and Gamma-ray Astrophysics*, edited by C. Bambi and A. Santangelo, Springer Nature Singapore, (2022), pp. 1–44.

[21] N. Hasebe *et al.*, *Gamma-ray spectrometer (GRS) for lunar polar orbiter SELENE*, Earth Planet Space **60**, 299 (2008).

[22] W.V. Boynton *et al.*, *The Mars Odyssey Gamma-Ray Spectrometer Instrument Suite*, Space Sci. Rev. **110**, 37 (2004).

[23] M. Burks *et al.*, *Thermal design and performance of the gamma-ray spectrometer for the MESSENGER spacecraft*, IEEE Symp. Conf. Rec. Nucl. Sci. **1**, 390 (2004).

[24] P.N. Peplowski, *Radioactive Elements on Mercury's Surface from MESSENGER: Implications for the Planet's Formation and Evolution*, Science **333**, 1850 (2011).

[25] D.J. Lawrence *et al.*, *Measuring the Elemental Composition of Phobos: The Mars-moon Exploration with GAmma rays and NEutrons (MEGANE) Investigation for the Martian Moons eXploration (MMX) Mission*, Earth Space Sci. **6**, 2605 (2019).

[26] N.R. Hines, *Designing and Testing the High-Purity Germanium Gamma-ray Spectrometer for the Dragonfly Mission to Titan*, (PhD thesis, Kansas State University, 2022).

[27] *The Compton Spectrometer and Imager Project for MeV Astronomy*, Band 37th International Cosmic Ray Conference (ICRC 2021), 2021.

[28] L.C. Johnson *et al.*, *Development of a Germanium Small-Animal SPECT System*, IEEE Trans. Nucl. Sci. **62**, 2036 (2015).

[29] G.F. Knoll, *Radiation Detection and Measurement*, 3rd edition, (John Wiley & Sons, New York, 2000), pp. 29–55, 353–456.

[30] MAJORANA COLLABORATION, *Multisite event discrimination for the* MAJORANA DEMONSTRATOR, Phys. Rev. C **99**, 065501 (2019).

[31] GERDA COLLABORATION, *Pulse shape discrimination for* GERDA *Phase I data*, Eur. Phys. J. C **73**, 2583 (2013).

[32] EDELWEISS COLLABORATION, *Pulse-Shape Analysis of Ionization Signals in Cryogenic Ge Detectors for Dark Matter*, J. Low Temp. Phys. **184**, 845 (2016).

[33] H. Gómez *et al.*, *Background reduction and sensitivity for germanium double beta decay experiments*, Astropart. Phys. **28**, 435 (2007).

[34] I. Abt *et al.*, *Bayesian inference of high-purity germanium detector impurities based on capacitance measurements and machine-learning accelerated capacitance calculations*, Eur. Phys. J. C **83**, 352 (2023).

[35] I. Abt *et al.*, *Measurement of the temperature dependence of pulse lengths in an n-type germanium detector*, Eur. Phys. J. Appl. Phys. **56**, 10104 (2011).

[36] I. Abt *et al.*, *Temperature dependence of the electron-drift anisotropy and implications for the electron-drift model*, J. Instr. **18**, P10030 (2023).

[37] I. Abt *et al.*, *Simulation of semiconductor detectors in 3D with SolidStateDetectors.jl*, J. Instr. **16**, P08007 (2021).

[38] I. Abt *et al.*, *A novel wide-angle Compton Scanner to study bulk events in germanium detectors*, Eur. Phys. J. C **82**, 936 (2022).

[39] C.F. von Weizsäcker, *Zur Theorie der Kernmassen*, Z. Physik **96**, 431 (1935).

[40] G. Gamow, *Mass defect curve and nuclear constitution*, Proc. R. Soc. Lond. A **126**, 632 (1930).

[41] E. Gapon and D. Iwanenko, *Zur Bestimmung der Isotopenzahl*, Naturwissenschaften **20**, 792 (1932).

[42] P. Vogel, B. Jonson, and P.G. Hansen, *Is there neutron-proton pairing in medium heavy nuclei?*, Phys. Lett. B **139**, 227 (1984).

[43] F. Boehm and P. Vogel, *Physics of Massive Neutrinos*, 2$^{\text{nd}}$ edition, (Cambridge University Press, Cambridge, 1992), pp. 160–192.

[44] J. Chadwick, *Intensitätsverteilung im magnetischen Spektrum der β-Strahlen von Radium B+C*, Verhandl. Dtsc. Phys. Ges. **16**, 383 (1914).

[45] W. Pauli, *Wissenschaftlicher Briefwechsel mit Bohr, Einstein, Heisenberg u.a. Band II: 1930–1939*, (Springer-Verlag, Berlin Heidelberg, 1985), p. 39.

[46] F. Reines and C.L. Cowan, *The Neutrino*, Nature **178**, 446 (1956).

[47] C.L. Cowan *et al.*, *Detection of the Free Neutrino: a Confirmation*, Science **124**, 103 (1956).

[48] G. Danby *et al.*, *Observation of High-Energy Neutrino Reactions and the Existence of Two Kinds of Neutrinos*, Phys. Rev. Lett. **9**, 36 (1962).

[49] DONUT COLLABORATION, *Observation of tau neutrino interactions*, Phys. Lett. B **504**, 218 (2001).

[50] M. Goeppert-Mayer, *Double Beta-Disintegration*, Phys. Rev. **48**, 512 (1935).

[51] S.R. Elliott, A.A. Hahn, and M.K. Moe, *Direct evidence for two-neutrino double-beta decay in* ^{82}Se, Phys. Rev. Lett. **59**, 2020 (1987).

[52] B. Pritychenko, *Systematic analysis of double-beta decay half lives*, Nucl. Phys. A **1033**, 122628 (2023).

[53] E. Fermi, *Versuch einer Theorie der* β*-Strahlen*, Z. Physik **88**, 161 (1934).

[54] E. Majorana, *Teoria simmetrica dell'elettrone e del positrone*, Nuovo Cim. **14**, 171 (1937).

[55] W.H. Furry, *On Transition Probabilities in Double Beta-Disintegration*, Phys. Rev. **56**, 1184 (1939).

[56] J. Schechter and J.W.F. Valle, *Neutrinoless double-*β *decay in SU(2)×U(1) theories*, Phys. Rev. D **25**, 2951 (1982).

[57] E. Takasugi, *Can the neutrinoless double beta decay take place in the case of Dirac neutrinos?*, Phys. Lett. B **149**, 372 (1984).

[58] M. Fukugita and T. Yanagida, *Baryogenesis without grand unification*, Phys. Lett. B **174**, 45 (1986).

[59] A. Salam, *On parity conservation and neutrino mass*, Nuovo Cim. **5**, 299 (1957).

[60] L. Landau, *On the conservation laws for weak interactions*, Nucl. Phys. **3**, 127 (1957).

[61] T.D. Lee and C.N. Yang, *Parity Nonconservation and a Two-Component Theory of the Neutrino*, Phys. Rev. **105**, 1671 (1957).

[62] E.C.G. Sudarshan and R.E. Marshak, *Chirality Invariance and the Universal Fermi Interaction*, Phys. Rev. **109**, 1860 (1958).

[63] R.P. Feynman and M. Gell-Mann, *Theory of the Fermi Interaction*, Phys. Rev. **109**, 193 (1958).

[64] ALEPH, DELPHI, L3, OPAL, SLD COLLABORATIONS, and LEP ELECTROWEAK WORKING GROUP, and SLD ELECTROWEAK AND HEAVY FLAVOUR GROUPS, *Precision electroweak measurements on the Z resonance*, Phys. Rep. **427**, 257 (2006).

[65] M.C. Gonzalez-Garcia and M. Yokoyama, *Neutrino Masses, Mixing and Oscillations*, pp. 285–311 in: R.L. Workman *et al.* (Particle Data Group)*, Review of Particle Physics*, Prog. Theor. Exp. Phys. **2022**, 083C01 (2022).

[66] B. Pontecorvo, *Neutrino experiments and the problem of conservation of leptonic charge*, Zh. Eksp. Teor. Fiz. **53**, 1717 (1967).

[67] Z. Maki, M. Nakagawa, and S. Sakata, *Remarks on the Unified Model of Elementary Particles*, Prog. Theor. Phys. **28**, 870 (1962).

[68] SNO COLLABORATION, *Direct Evidence for Neutrino Flavor Transformation from Neutral-Current Interactions in the Sudbury Neutrino Observatory*, Phys. Rev. Lett. **89**, 011301 (2002).

[69] KAMLAND COLLABORATION, *First Results from KamLAND: Evidence for Reactor Antineutrino Disappearance*, Phys. Rev. Lett. **90**, 021802 (2003).

[70] P.F. de Salas *et al.*, *Neutrino Mass Ordering from Oscillations and Beyond: 2018 Status and Future Prospects*, Front. Astron. Space Sci. **5**, 36 (2018).

[71] P.F. de Salas *et al.*, *2020 global reassessment of the neutrino oscillation picture*, J. High Energ. Phys. **2021**, 71 (2021).

[72] J. Lesgourgues and S. Pastor, *Massive neutrinos and cosmology*, Phys. Rep. **429**, 307 (2006).

[73] E. Di Valentino, S. Gariazzo, and O. Mena, *Most constraining cosmological neutrino mass bounds*, Phys. Rev. D **104**, 083504 (2021).

[74] KATRIN COLLABORATION, *Direct neutrino-mass measurement with sub-electronvolt sensitivity*, Nat. Phys. **18**, 160 (2022).

[75] M.J. Dolinski, A.W.P. Poon, and W. Rodejohann, *Neutrinoless Double-Beta Decay: Status and Prospects*, Annu. Rev. Nucl. Part. Sci. **69**, 219 (2019).

[76] I. Esteban *et al.*, *The fate of hints: updated global analysis of three-flavor neutrino oscillations*, J. High Energ. Phys. **2020**, 178 (2020).

[77] M. Agostini, G. Benato, and J.A. Detwiler, *Discovery probability of next-generation neutrinoless double-β decay experiments*, Phys. Rev. D **96**, 053001 (2017).

[78] M. Ettengruber *et al.*, *Discovering neutrinoless double-beta decay in the era of precision neutrino cosmology*, Phys. Rev. D **106**, 073004 (2022).

[79] A. Caldwell *et al.*, *Global Bayesian analysis of neutrino mass data*, Phys. Rev. D **96**, 073001 (2017).

[80] M. Agostini *et al.*, *Testing the inverted neutrino mass ordering with neutrinoless double-β decay*, Phys. Rev. C **104**, L042501 (2021).

[81] J. Kotila and F. Iachello, *Phase-space factors for double-β decay*, Phys. Rev. C **85**, 034316 (2012).

[82] B. Märkisch *et al.*, *Measurement of the Weak Axial-Vector Coupling Constant in the Decay of Free Neutrons Using a Pulsed Cold Neutron Beam*, Phys. Rev. Lett. **122**, 242501 (2019).

[83] J. Engel and J. Menéndez, *Status and future of nuclear matrix elements for neutrinoless double-beta decay: a review*, Rep. Prog. Phys. **80**, 046301 (2017).

[84] M. Hirsch, H.V. Klapdor-Kleingrothaus, and O. Panella, *Double beta decay in left-right symmetric models*, Physics Letters B **374**, 7 (1996).

[85] R.N. Mohapatra, *New contributions to neutrinoless double-beta decay in supersymmetric theories*, Phys. Rev. D **34**, 3457 (1986).

[86] M. Hirsch, H.V. Klapdor-Kleingrothaus, and S.G. Kovalenko, *New contributions to supersymmetric mechanism of neutrinoless double beta decay*, Phys. Lett. B **352**, 1 (1995).

[87] M. Hirsch, H.V. Klapdor-Kleingrothaus, and S.G. Kovalenko, *New leptoquark mechanism of neutrinoless double β decay*, Phys. Rev. D **54**, R4207 (1996).

[88] A. Ali, A.V. Borisov, and D.V. Zhuridov, *Angular distribution of electrons in neutrinoless double-beta decay and new physics*, Phys. Atom. Nuclei **70**, 1264 (2007).

[89] V. Tello *et al.*, *Left-Right Symmetry: From the LHC to Neutrinoless Double Beta Decay*, Phys. Rev. Lett. **106**, 151801 (2011).

[90] M. Duerr, M. Lindner, and A. Merle, *On the quantitative impact of the Schechter-Valle theorem*, J. High Energ. Phys. **2011**, 91 (2011).

[91] L. Maiani, *Selected Topics in Majorana Neutrino Physics*, Riv. del Nuovo Cim. **37**, 417 (2014).

[92] National Center for Biotechnology Information, *PubChem Compound Summary for CID 131708371, Germanium-76*, `https://pubchem.ncbi.nlm.nih.gov/compound/Germanium-76`, Accessed 25 June 2023.

[93] G. Cowan *et al.*, *Asymptotic formulae for likelihood-based tests of new physics*, Eur. Phys. J. C **71**, 1554 (2011).

[94] V.I. Tretyak and Y.G. Zdesenko, *Tables of Double Beta Decay Data – an Update*, Atom. Data Nucl. Data Tables **80**, 83 (2002).

[95] GERDA COLLABORATION, *Final Results of GERDA on the Search for Neutrinoless Double-β Decay*, Phys. Rev. Lett. **125**, 252502 (2020).

[96] MAJORANA COLLABORATION, *Final Result of the Majorana Demonstrator's Search for Neutrinoless Double-β Decay in* ^{76}Ge, Phys. Rev. Lett. **130**, 062501 (2023).

[97] CUPID-0 COLLABORATION, *Final Result on the Neutrinoless Double Beta Decay of* ^{82}Se *with CUPID-0*, Phys. Rev. Lett. **129**, 111801 (2022).

[98] CUPID COLLABORATION, *Final results on the $0\nu\beta\beta$ decay half-life limit of ^{100}Mo from the CUPID-Mo experiment*, Eur. Phys. J. C **82**, 1033 (2022).

[99] CUORE COLLABORATION, *Search for Majorana neutrinos exploiting millikelvin cryogenics with CUORE*, Nature **604**, 53 (2022).

[100] EXO-200 COLLABORATION, *Search for Neutrinoless Double-β Decay with the Complete EXO-200 Dataset*, Phys. Rev. Lett. **123**, 161802 (2019).

[101] KAMLAND-ZEN COLLABORATION, *Search for the Majorana Nature of Neutrinos in the Inverted Mass Ordering Region with KamLAND-Zen*, Phys. Rev. Lett. **130**, 051801 (2023).

[102] M. Agostini *et al.*, *Toward the discovery of matter creation with neutrinoless $\beta\beta$ decay*, Rev. Mod. Phys. **95**, 025002 (2023).

[103] SNO+ collaboration, *The SNO+ experiment*, J. Instr. **16**, P08059 (2021).

[104] B.J. Mount, M. Redshaw, and E.G. Myers, *Double-β-decay Q values of* ^{74}Se *and* ^{76}Ge, Phys. Rev. C **81**, 032501 (2010).

[105] NEMO COLLABORATION, *Technical design and performance of the NEMO 3 detector*, Nucl. Instr. Meth. A **536**, 79 (2005).

[106] SUPERNEMO COLLABORATION, *Probing new physics models of neutrinoless double beta decay with SuperNEMO*, Eur. Phys. J. C **70**, 927 (2010).

[107] CUPID COLLABORATION, *CUPID: The Next-Generation Neutrinoless Double Beta Decay Experiment*, J. Low Temp. Phys. **211**, 375 (2023).

[108] NEXO COLLABORATION, *nEXO: neutrinoless double beta decay search beyond 10^{28} year half-life sensitivity*, J. Phys. G: Nucl. Part. Phys. **49**, 015104 (2022).

[109] GERDA COLLABORATION, *Upgrade for Phase II of the* GERDA *experiment*, Eur. Phys. J. C **78**, 388 (2018).

[110] I. Abt *et al.*, *Background reduction in neutrinoless double beta decay experiments using segmented detectors – A Monte Carlo study for the GERDA setup*, Nucl. Instr. Meth. A **570**, 479 (2007).

[111] GERDA COLLABORATION, *Modeling of GERDA Phase II data*, J. High Energ. Phys. **2020**, 139 (2020).

[112] NIST XCOM, *Photon Cross Sections Data*, `https://physics.nist.gov/PhysRefData/Xcom/html/xcom1.html`, Accessed 20 March 2022.

[113] Center for X-Ray Optics and Advanced Light Source, *X-Ray Data Booklet*, 3rd edition, (Lawrence Berkeley National Laboratory, 2009), p. 1-3.

[114] O. Klein and Y. Nishina, *Über die Streuung von Strahlung durch freie Elektronen nach der neuen relativistischen Quantendynamik von Dirac*, Z. Physik **52**, 853 (1929).

[115] D.E. Groom and S.R. Klein, *Passage of Particles Through Matter*, p. 549 in: R.L. Workman *et al.* (Particle Data Group), *Review of Particle Physics*, Prog. Theor. Exp. Phys. **2022**, 083C01 (2022).

[116] R.M. Sternheimer, *The Density Effect for the Ionization Loss in Various Materials*, Phys. Rev. **88**, 851 (1952).

[117] C. Møller, *Zur Theorie des Durchgangs schneller Elektronen durch Materie*, Ann. Phys. **406**, 531 (1932).

[118] Particle Data Group, *Atomic and nuclear properties of germanium (Ge)*, `https://pdg.lbl.gov/2022/AtomicNuclearProperties/HTML/germanium_Ge.html`, Accessed 24 April 2023.

[119] R.B. Firestone *et al.*, *Table of Isotopes*, 8th edition, (John Wiley & Sons, New York, 1999).

[120] S.M. Sze and K.K. Ng, *Physics of Semiconductor Devices*, 3rd edition, (John Wiley & Sons, New York, 2007), p. 28.

[121] E. Schrödinger, *An Undulatory Theory of the Mechanics of Atoms and Molecules*, Phys. Rev. **28**, 1049 (1926).

[122] F. Bloch, *Über die Quantenmechanik der Elektronen in Kristallgittern*, Z. Physik **52**, 555 (1929).

[123] L. Brillouin, *Wave propagation in periodic structures: electric filters and crystal lattices*, 1st edition, (McGraw-Hill, New York, 1946), p. 153.

[124] M.L. Cohen and J.R. Chelikowsky, *Electronic Structure and Optical Properties of Semiconductors*, 1st edition, (Springer-Verlag, Berlin Heidelberg, 1988), p. 92.

[125] J.H. Crawford, H.C. Schweinler, and D.K. Stevens, *Magnetic Indications of Electronic Structure of the Conduction Band in Ge*, Phys. Rev. **99**, 1330 (1955).

[126] R.N. Dexter, H.J. Zeiger, and B. Lax, *Cyclotron Resonance Experiments in Silicon and Germanium*, Phys. Rev. **104**, 637 (1956).

[127] C. Poole, *Encyclopedic Dictionary of Condensed Matter Physics*, 1st edition, (Academic Press, Cambrigde, 2004), p. 517.

[128] F. Hagemann, *Dependence of signal development in germanium detectors on temperature and operating voltage*, (Master's thesis, Technische Universität Berlin, 2020).

[129] H.R. Verma, *Atomic and Nuclear Analytical Methods*, (Springer Verlag, Berlin Heidelberg, 2007), p. 254.

[130] H.R. Bilger, *Fano Factor in Germanium at 77°K*, Phys. Rev. **163**, 238 (1967).

[131] W. Schockley, *Currents to Conductors Induced by a Moving Point Charge*, J. Appl. Phys. **9**, 635 (1938).

[132] S. Ramo, *Currents induced by electron motion*, Proc. IRE **27**, 584 (1939).

[133] Z. He, *Review of the Shockley-Ramo theorem and its application in semiconductor gamma-ray detectors*, Nucl. Instr. Meth. A **463**, 250 (2001).

[134] I. Smolić and B. Klajn, *Capacitance Matrix Revisited*, Prog. Electromagn. Res. B **92**, 1 (2021).

[135] B. Bruyneel *et al.*, *Characterization of large volume HPGe detectors. Part II: Experimental results*, Nucl. Instr. Meth. A **569**, 774 (2006).

[136] I. Abt *et al.*, *Alpha-event and surface characterisation in segmented true-coaxial HPGe detectors*, Nucl. Instr. Meth. A **858**, 80 (2017).

[137] G. Yang *et al.*, *Study on the Properties of High Purity Germanium Crystals*, J. Phys.: Conf. Ser. **606**, 012013 (2015).

[138] W.G. Pfann, *Principles of Zone-Melting*, J. Met. **4**, 747 (1952).

[139] D.C. Curtolo, S. Friedrich, and B. Friedrich, *High Purity Germanium, a Review on Principle Theories and Technical Production Methodologies*, J. Cryst. Proc. Technol. **7**, 65 (2017).

[140] R.N. Hall, *Segregation of Impurities During the Growth of Germanium and Silicon*, J. Phys. Chem. **57**, 836 (1953).

[141] T. Taishi *et al.*, *Segregation of boron in germanium crystal*, J. Cryst. Growth **311**, 59 (2008).

[142] J.A. Spim, M.J.S. Bernadou, and A. Garcia, *Numerical modeling and optimization of zone refining*, J. Alloys Compd. **298**, 299 (2000).

[143] J. Czochralski, *Ein neues Verfahren zur Messung der Kristallisationsgeschwindigkeit der Metalle*, Z. Phys. Chem. **92**, 219 (1918).

[144] CRYTUR, *Crystal growing*, `https://www.crytur.cz/technologies/crystal-growing/`, Accessed 24 April 2023.

[145] M. Roth *et al.*, *Crystal-melt interface shape of Czochralski-grown large diameter germanium crystals*, J. Cryst. Growth **99**, 670.

[146] W.L. Hansen and E.E. Haller, *High-Purity Germanium Crystal Growing*, MRS Online Proceedings Library **16**, 1 (1982).

[147] J.P. Ponpon *et al.*, *Boron Implanted Contacts on High Purity Germanium*, pp. 420–429 in: I. Ruge and J. Graul (eds), *Ion Implantation in Semiconductors*, 1st edition, (Springer-Verlag, Berlin Heidelberg, 1971).

[148] R.H. Pehl and R.C. Cordi, *Lithium-Diffused n+ Contacts on High-Purity Germanium Detectors: How Thin Can They be Made-How Stable Are They?*, IEEE Trans. Nucl. Sci. **22**, 177 (1975).

[149] L. Van Goethem *et al.*, *Copper contamination of high purity germanium (HPGe) through Li-diffusion*, Nucl. Instr. Meth. A **240**, 365 (1985).

[150] R. Panth, *Characterization of high-purity germanium detectors with amorphous germanium contacts in cryogenic liquids*, Eur. Phys. J. C **80**, 667 (2020).

[151] S. Bertoldo *et al.*, *New method for the production of thin and stable, segmented n+ contacts in HPGe detectors*, Eur. Phys. J. A **57**, 177 (2021).

[152] L. Reggiani *et al.*, *Hole drift velocity in germanium*, Phys. Rev. B **16**, 2781 (1977).

[153] G. Ottaviani, C. Canali, and A.A. Quaranta, *Charge Carrier Transport Properties of Semiconductor Materials Suitable for Nuclear Radiation Detectors*, IEEE Trans. Nucl. Sci. **22**, 192 (1975).

[154] D.M. Caughey and R.E. Thomas, *Carrier mobilities in silicon empirically related to doping and field*, Proc. IEEE **55**, 2192 (1967).

[155] L. Mihailescu *et al.*, *The influence of anisotropic electron drift velocity on the signal shapes of closed-end HPGe detectors*, Nucl. Instr. Meth. A **447**, 350 (2000).

[156] C. Canali *et al.*, *Electron and hole drift velocity measurements in silicon and their empirical relation to electric field and temperature*, IEEE Trans. Electron Devices **22**, 1045 (1975).

[157] R. Barrie and R.R. Burgess, *Drift velocity of hot electrons in n-type germanium*, Can. J. Phys. **40**, 1056 (1962).

[158] G. Ottaviani *et al.*, *Hole drift velocity in high-purity Ge between 8 and 220 °K*, J. Appl. Phys. **44**, 2917 (1973).

[159] H.G. Reik and H. Risken, *Drift Velocity and Anisotropy of Hot Electrons in n Germanium*, Phys. Rev. **126**, 1737 (1962).

[160] A. Matthiessen and C. Vogt, *On the influence of temperature on the electric conducting-power of alloys*, Phil. Trans. R. Soc. **154**, 167 (1864).

[161] J. Bardeen and W. Shockley, *Deformation Potentials and Mobilities in Non-Polar Crystals*, Phys. Rev. **80**, 72 (1950).

[162] E. Conwell and V.F. Weisskopf, *Theory of Impurity Scattering in Semiconductors*, Phys. Rev. **77**, 388 (1950).

[163] C. Erginsoy, *Neutral Impurity Scattering in Semiconductors*, Phys. Rev. **79**, 1013 (1950).

[164] N. Sclar, *Neutral Impurity Scattering in Semiconductors*, Phys. Rev. **104**, 1559 (1956).

[165] E.E. Haller, W.L. Hansen, and F.S. Goulding, *Physics of ultra-pure germanium*, Adv. Phys. **30**, 93 (1981).

[166] E.E. Haller *et al.*, *Carbon in High-Purity Germanium*, IEEE Trans. Nucl. Sci. **29**, 745 (1982).

[167] L.P. Hunter, *Current Carrier Mobility Ratio in Semiconductors*, Phys. Rev. **91**, 579 (1953).

[168] M.B. Prince, *Drift Mobilities in Semiconductors. I. Germanium*, Phys. Rev. **92**, 681 (1953).

[169] F.J. Morin, *Lattice-Scattering Mobility in Germanium*, Phys. Rev. **93**, 62 (1954).

[170] M.A. Omar and L. Reggiani, *Drift velocity and diffusivity of hot carriers in germanium: Model calculations*, Solid-State Electronics **30**, 1351 (1987).

[171] B. Bruyneel *et al.*, *Characterization of large volume HPGe detectors. Part I: Electron and hole mobility parameterization*, Nucl. Instr. Meth. A **569**, 764 (2006).

[172] H. Nakagawa and S. Zukotynski, *Drift velocity of holes in germanium and silicon*, Can. J. Phys. **57**, 1233 (1979).

[173] L. Reggiani, *The anisotropy of the hot-hole drift velocity in Ge*, J. Phys. Chem. Solids **37**, 293 (1976).

[174] M.I. Nathan, *Anisotropy of the Conductivity of n-Type Germanium at High Electric Fields*, Phys. Rev. **130**, 2201 (1963).

[175] T. Comellato, M. Agostini, and S. Schönert, *Charge-carrier collective motion in germanium detectors for $\beta\beta$-decay searches*, Eur. Phys. J. C **81**, 76 (2021).

[176] E. Gatti *et al.*, *Dynamics of electrons in drift detectors*, Nucl. Instr. Meth. A **253**, 393 (1987).

[177] S. Agostinelli *et al.*, GEANT4 *– a simulation toolkit*, Nucl. Instr. Meth. A **506**, 250 (2003).

[178] V. Lazurik, V. Moskvin, and T. Tabata, *Average depths of electron penetration: use as characteristic depths of exposure*, IEEE Trans. Nucl. Sci. **45**, 626 (1998).

[179] M. Berger *et al.*, *ESTAR, PSTAR, and ASTAR: Computer Programs for Calculating Stopping-Power and Range Tables for Electrons, Protons, and Helium Ions*, 1999, Accessed 20 March 2022.

[180] C.G. Wohl *et al.*, *Review of particle properties*, Rev. Mod. Phys. **56**, S51 (1984).

[181] S.E. Boggs and S.N. Pike, *Analytical fitting of γ–ray photopeaks in germanium cross strip detectors*, Exp. Astron. **56**, 403 (2023).

[182] A.G. Requicha, *Representations for Rigid Solids: Theory, Methods, and Systems*, ACM Comput. Surv. **12**, 437 (1980).

[183] R.J. Cooper, D.C. Radford *et al.*, *A novel HPGe detector for gamma-ray tracking and imaging*, Nucl. Instr. Meth. A **665**, 25 (2011).

[184] L. Hauertmann, *Surface Characterization of Segmented Germanium Detectors with Alpha, Beta and Gamma Particles*, (PhD thesis, Technische Universität München, 2021).

[185] D. Young, *Iterative methods for solving partial difference equations of elliptic type*, Trans. Amer. Math. Soc. **76**, 92 (1954).

[186] B.A. Stickler and E. Schachinger, *Basic Concepts in Computational Physics*, 2nd edition, (Springer Nature Switzerland, 2016), pp. 271–295.

[187] Private communication with Mirion Technologies, Inc.

[188] GERDA COLLABORATION, *Characterization of 30 ^{76}Ge enriched Broad Energy Ge detectors for GERDA Phase II*, Eur. Phys. J. C **79**, 978 (2019).

[189] F.S. Goulding and D.A. Landis, *Signal Processing for Semiconductor Detectors*, IEEE Trans. Nucl. Sci. **29**, 1125 (1982).

[190] Canberra Eurisys S.A., *PSC823C operating manual*, `https://siliconpr0n.org/media/camac/1/PSC823.pdf`, Accessed 21 July 2023.

[191] Struck Innovative Systems, `https://www.struck.de/sis3316.html`.

[192] M. Schuster, *Temperature Dependence of Charge Carrier Drift in Germanium Detectors*, (PhD thesis, Technische Universität München, 2021).

[193] P. Holl *et al.*, *Deep learning based pulse shape discrimination for germanium detectors*, Eur. Phys. J. C **79**, 450 (2019).

[194] E.W. Weisstein, *Heaviside Step Function*, `https://mathworld.wolfram.com/HeavisideStepFunction.html`, Accessed 14 August 2023.

[195] E.E. Haller, W.L. Hansen, and F.S. Goulding, *Evaluation of High-Purity Germanium by Pulse Measurements on Detectors*, IEEE Trans. Nucl. Sci. **19**, 271 (1972).

[196] B. Birkenbach *et al.*, *Determination of space charge distributions in highly segmented large volume HPGe detectors from capacitance–voltage measurements*, Nucl. Instr. Meth. A **640**, 176 (2011).

[197] B. Bruyneel, B. Birkenbach, and P. Reiter, *Space charge reconstruction in highly segmented HPGe detectors through capacitance-voltage measurements*, Nucl. Instr. Meth. A **641**, 92 (2011).

[198] W. Riegler, *An application of extensions of the Ramo–Shockley theorem to signals in silicon sensors*, Nucl. Instr. Meth. A **940**, 453 (2019).

[199] P.K. Mogensen and A.N. Riseth, *Optim: A mathematical optimization package for Julia*, J. Open Source Softw. **3**, 615 (2018).

[200] I. Abt *et al.*, *Characterisation of an n-type segmented BEGe detector*, Nucl. Instr. Meth. A **925**, 172 (2019).

[201] J. Plößner, *Upgrade des Compton Scanners am MPP mit einer zweiten Kamera*, (Bachelor's thesis, Technische Universität München, 2021).

[202] R. Thoraeus, *Attenuation of Gamma Radiation from ^{60}Co, ^{137}Cs, ^{192}Ir, and ^{226}Ra in Various Materials Used in Radiotherapy*, Acta Radiol. **3**, 81 (1965).

[203] H3D, Inc., `https://h3dgamma.com/`.

[204] Y. Zhu, S.E. Anderson, and Z. He, *Sub-Pixel Position Sensing for Pixelated, 3-D Position Sensitive, Wide Band-Gap, Semiconductor, Gamma-Ray Detectors*, IEEE Trans. Nucl. Sci. **58**, 1400 (2011).

[205] Z. He *et al.*, *1-D position sensitive single carrier semiconductor detectors*, Nucl. Instr. Meth. A **380**, 228 (1996).

[206] S. Del Sordo *et al.*, *Progress in the Development of CdTe and CdZnTe Semiconductor Radiation Detectors for Astrophysical and Medical Applications*, Sensors **9**, 3491 (2009).

[207] C. G. Wahl *et al.*, *The Polaris-H imaging spectrometer*, Nucl. Instr. Meth. A **784**, 377 (2015).

[208] Y. Kim, T. Lee, and W. Lee, *Radiation measurement and imaging using 3D position sensitive pixelated CZT detector*, Nucl. Eng. Technol. **51**, 1417 (2019).

[209] L.J. Beattie *et al.*, *The electric field in irradiated silicon detectors*, Nucl. Instr. Meth. A **418**, 314 (1998).

[210] I. Abt *et al.*, *Pulse shape simulation for segmented true-coaxial HPGe detectors*, Eur. Phys. J. C **68**, 609 (2010).

[211] B. Bruyneel, B. Birkenbach, and P. Reiter, *Pulse shape analysis and position determination in segmented HPGe detectors: The AGATA detector library*, Eur. Phys. J. A **52**, 70 (2016).

[212] V.S. Prasher *et al.*, *Sensitivity of GRETINA position resolution to hole mobility*, Nucl. Instr. Meth. A **846**, 50 (2017).

[213] J. Lehtonen, *The Lambert W function in ecological and evolutionary models*, Methods Ecol. Evol. **7**, 1110 (2016).